



# Silk bionanocomposites : design, characterization and potential applications

Cristina Belda Marín

## ► To cite this version:

Cristina Belda Marín. Silk bionanocomposites : design, characterization and potential applications. Biomaterials. Université de Technologie de Compiègne, 2020. English. NNT : 2020COMP2570 . tel-03292347

**HAL Id: tel-03292347**

**<https://theses.hal.science/tel-03292347>**

Submitted on 20 Jul 2021

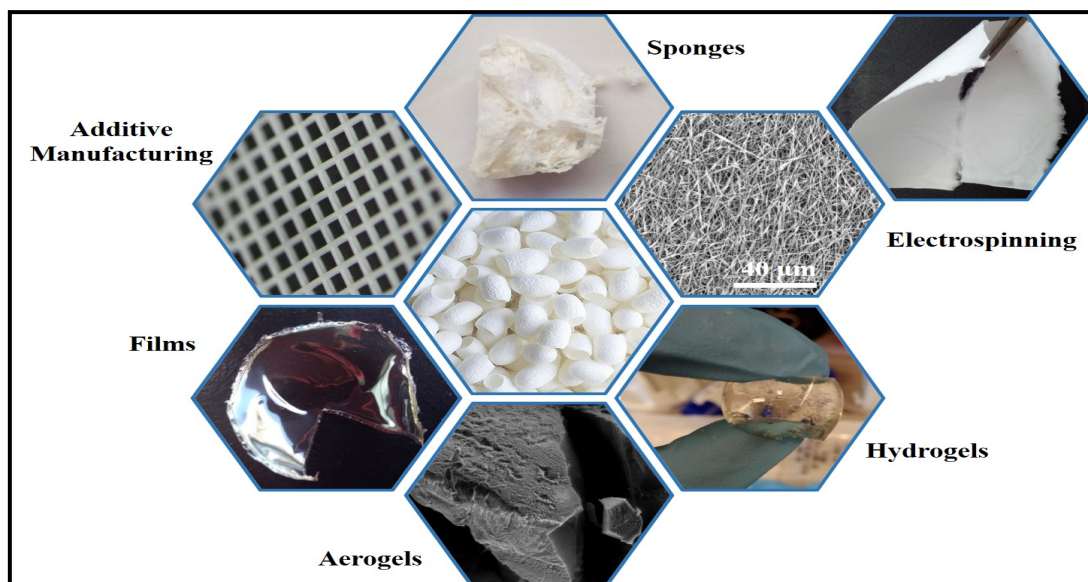
**HAL** is a multi-disciplinary open access archive for the deposit and dissemination of scientific research documents, whether they are published or not. The documents may come from teaching and research institutions in France or abroad, or from public or private research centers.

L'archive ouverte pluridisciplinaire **HAL**, est destinée au dépôt et à la diffusion de documents scientifiques de niveau recherche, publiés ou non, émanant des établissements d'enseignement et de recherche français ou étrangers, des laboratoires publics ou privés.

Par **Cristina BELDA MARÍN**

*Silk bionanocomposites : design, characterization  
and potential applications*

Thèse présentée  
pour l'obtention du grade  
de Docteur de l'UTC



Soutenue le 4 décembre 2020

**Spécialité :** Chimie et Biomatériaux : Transformations intégrées  
de la matière renouvelable (EA-4297)

D2570

École Doctorale Sciences pour l'Ingénieur ED71

**Thèse présentée pour l'obtention du grade de  
Docteur de l'Université de Technologie de Compiègne**

**Spécialité : Chimie et Biomatériaux**

**Par Cristina BELDA MARÍN**

# **Silk bionanocomposites : design, characterization and potential applications**

Soutenue le 4 décembre 2020

**Jury composé de:**

Rapporteurs

**Mme. Nadine MILLOT**

Professeur des Universités  
UBFG – Dijon - France

**M. Thibaud CORADIN**

Directeur de Recherche CNRS  
SU – Paris – France

Examineurs

**Mme. Claude JOLIVALT**

Professeur des Universités  
SU – Paris – France

**Mme. Isabelle PEZRON**

Professeur des Universités  
UTC – Compiègne - France

Membre invité

**M. Christophe EGLES**

Professeur des Universités  
UTC – Compiègne - France

Directeurs de thèse

**M. Jessem LANDOULSI**

Maître de conférences HDR  
SU – Paris – France

**M. Erwann GUÉNIN**

Professeur des Universités  
UTC – Compiègne - France





This PhD project was financed by Sorbonne  
Universités and the *Chaire de chimie verte et  
procédées*



Le projet « Chaire « Chimie et Procédés Verts » » est cofinancé dans le cadre du Fonds européen de développement économique et régional (FEDER) 2014/2020





*“A las dos mujeres más importantes de mi vida, mis queridas **Sagrario** y **Adriana**, por haber hecho de mi la persona que soy hoy. Donde quiera que estéis, sé que siempre estaréis conmigo y orgullosas de mi”*



# Acknowledgements

---

It has been for me a great pleasure to be able to accomplish this project in such a multidisciplinary field. Nevertheless, science is never done by oneself. This space is meant to acknowledge all the people who has participated to the realization of this work, not only by doing science but also for all of those who were there to handle my emotions providing the moral support that a PhD requires.

First of all, I would like to thank the entire jury for having accepted to judge and evaluate this work. Thank you **Pr. Nadine Millot** and **Dr. Thibaud Coradin** for accepting to review my work. Thank you as well **Pr. Claude Jolival** and **Pr. Isabelle Pezron** for judging this work.

I am also very thankful to my supervisor and my two PhD directors: **Christophe Egles**, **Jessem Landoulsi** and **Erwann Guénin**. Your support has been crucial for the good realization of this project, thank you as well for all the advices and suggestions. Thank you Christophe for taking me into the so exciting field of silk-based biomaterials. Thank you as well for setting the bases for this great collaboration between my two PhD directors. I appreciate the critical point of view of Jessem who drove me into a continuous improvement process. Of course, I could not forget Erwann for making nanoparticles so BIG in my life, for your patience to answer my so many questions, for all the advices and the trust that you have deposited on me. The three of you have always encouraged me to keep on going supporting my decisions and guiding me through not only the scientific world but also in daily life by providing personal support.

I am very grateful to **Andre Pauss**, **Isabelle Pezron**, **Cécile Legallais** and **Hélène Pernot** for welcoming me into their laboratories Transformations Intégrées de la Matière Renouvelable (TIMR) and BioMécanique et BioIngénierie (BMBI) at Université de Technologie de Compiègne (UTC) and Laboratoire de réactivité de surface (LRS) at Sorbone Université during the entire time of this work.

I would like to thank as well the entire team of **Pr. David Kaplan** at **Tufts University** for welcoming me into their laboratory for two months. Special thanks to Pr. David Kaplan for his so valuable ideas on working with silk hydrogels. Thank you as well **Sarah Vidal Yucha**, **Xuan Mu** and **Vincent Fitzpatrick** for taking the time to show me the hints of silk processing. Thank you Vincent for hosting me in your adorable apartment in Boston and for keeping science going by continuing our collaboration still today.

## *Acknowledgements*

Special thanks to the entire team of the **SAPC** at UTC, **François Oudet**, **Frederic Nadaud** and **Caroline Lefebvre**; providing the knowledge on electronic microscopy, so needed when working with nanoparticles. Special thanks to Caroline for her support and advice for the use of the transmission electron microscope as well as the confocal microscope.

The *in vivo* experiments presented within this work were conducted in collaboration with **NeuroSpin**. I appreciate very much collaborating with **Sébastien Meriaux**, **Françoise Geffroy** and **Erwan Selingue**. I am especially grateful to Françoise for her investment and incredible work on brain injections, histology and immunostaining procedures and for guiding me to achieve a better understanding in the neurobiology field.

This PhD has also been greatly impacted by many other persons within the three laboratories in which I have been working. Specially **Pascale Vigneron**, **Paul Quentin** from BMBI at UTC for their helpful tips and advices in the field of biology. Thank you **Vincent Humblot**, **Laetitia Valentin** and **Claude Jolival** from the LRS for dealing with me to adapt the well established microbiological procedures to my special support. Thank you to the technique team **Hervé Leclerc**, **Bruno Dautat** and **Michael Lefebvre** and the entire team of TIMR at UTC for their enriched discussions through the hallways and the coffee pauses.

Thank you **Franco Otaola** for providing adapted molds for my procedures but also for being, together with **Amal Essouiba**, my Spanish speaking colleagues providing a link to our so appreciated Latino culture. Special thoughts to all the PhD students I wish that all these projects get to a beautiful end. Thanks to my personal supporters, **Yancie Gagnon**, **Oceane Adriaio**, **Benjamin Dussaussoy** and **Sebastian Navarro** for all the encouraging words and moral support.

Last but not least, I cannot forget to thank my family. Firstly thanks to **Ismael** for following me all the way to Compiègne and for the unconditional everyday support. Thank you to my father **David** for making me the person I am today and for supporting all my decisions and encouraging me to keep up with my scientific career wherever it takes me around the globe. Thanks to all my siblings **Lucia**, **Marta** and **David** for their support. Thank you to my grandfather **David** for the wise knowledge “*Mas sabe el diablo por viejo que por diablo*”. Thank you **Mary Paz** for being there every time in spite of the distance. Finally, thanks to my scientific idol and cousin **Alex**, keep on scicling!

# List of abbreviations

---

Ag NPs	Silver nanoparticles
AO	Acridine orange
ATR-FTIR	Attenuated total reflectance Fourier Transformation infrared spectrometry
Au NPs	Gold nanoparticles
DLS	Dynamic light scattering
DMEM	Dulbecco's modified Eagle's Medium
EDX	Energy dispersive X-ray
FBS	Fetal bovine serum
FTIR	Fourier Transformation infrared spectrometry
GFAP	Glial-fibrillary acidic protein
HAP	Hydroxiapatite
HRP	Horseradish peroxidase
HR-TEM	High-resolution transmission electron microscopy
IBA 1	Ionized calcium-binding adaptor molecule 1
IONPS	Iron oxide nanoparticles
LB	Luria-Bertani medium
LSPR	Localized surface plasmon resonance
MADLS	Multi-angle dynamic light scattering
MB	Methylene blue
MEM	Minimal essential medium
MH	Mueller Hinton medium
MRI	Magnetic resonance imaging
MTS	[3-(4,5-dimethylthiazol-2-yl)-5-(3-carboxymethoxyphenyl)-2-(4-sulfophenyl)-2H-tetrazolium salt

NPs	Nanoparticles
O/N	Over night
OD	Optical density
PBS	Phosphate buffered saline
PDI	Polydispersity index
PDMS	Polydimethylsiloxane
PEO	Poly ethylene oxide
pI	Isoelectric point
RGD	arginine-glycine-aspartate
RT	Room temperature
SAED	Selected area electron diffraction
SEM	Scanning electron microscope
SF	Silk fibroin
SPR	Surface plasmon resonance
STEM	Scanning transmission electron microscopy
TEM	Transmission electron microscopy
TGA	Thermogravimetric analysis
VSM	Vibrating Sample Magnetometer
XPS	X-ray photoelectron spectroscopy
XRD	X-ray diffraction



# Index

---

General introduction.....	15
Chapter I: State of the art .....	19
1. Silk .....	21
1.1. Silk structure and extraction.....	21
1.2. Silk-based materials .....	25
1.3. Applications .....	31
2. Nano objects .....	37
2.1. Nanoparticle synthesis.....	39
2.2. Noble metal nanoparticles .....	40
2.3. Iron oxide nanoparticles .....	45
3. Silk-based bionanocomposites .....	47
3.1. Antibacterial activity .....	49
3.2. Tissue engineering.....	51
3.3. Hyperthermia.....	53
3.4. Imaging.....	55
3.5. Electronics and sensing .....	55
3.6. Catalysis .....	56
3.7. Depollution.....	57
4. Conclusion.....	59
Chapter II: Design and characterization of gold, silver and iron oxide silk-NPs bionanocomposites .....	79
1. Introduction .....	81
2. Materials and methods .....	82
2.1. Materials.....	82

2.2. Nanoparticle synthesis.....	82
2.3. Nanoparticle characterization.....	84
2.4. Silk fibroin dispersion preparation.....	87
2.5. Silk bionanocomposites synthesis.....	87
2.6. Hydrogel characterization.....	91
3. Results and discussion.....	96
3.1. Use of bisphosphonates as NPs stabilizing agents.....	96
3.2. Nanoparticle synthesis.....	97
3.3. SF extraction.....	99
3.4. SF/NPs dispersion.....	100
3.5. SF and SF / NPs electrospun mats.....	101
3.6. Hydrogels.....	103
3.7. Other silk-NPs bionanocomposites.....	117
4. Conclusion.....	120
Chapter III: Potential applications of silver, gold and iron oxide silk-NPs hydrogel bionanocomposites.....	125
1. Introduction.....	127
2. Antibacterial applications.....	128
2.1. Introduction.....	128
2.2. Materials and methods.....	129
2.3. Results and discussion.....	131
2.5. Conclusion.....	135
3. Magnetic properties and MRI applications.....	137
3.1. Introduction.....	137
3.2. Materials and methods.....	138
3.3. Results and discussion.....	142
3.4. Conclusion.....	152

4. Depollution.....	153
4.1. Introduction .....	153
4.2. Materials and methods .....	155
4.3. Results and discussion.....	158
4.1. Conclusion.....	166
General conclusion .....	173
Perspectives .....	177
Accomplishments .....	179
Annexes .....	181
1. Nanoparticle image analysis: Image J script .....	183
2. PDMS molds .....	184
3. Compression tests: stress / strain curves .....	185
4. Magnetic properties .....	186
5. Immunostaining.....	186
5.1. Lymphocytes CD8.....	186
5.2. Caspase .....	187
Résumé .....	189
Abstract .....	191



# General introduction

---

Polymeric materials have been largely developed in the last decades. The apparition of these materials, together with the multiple processing techniques developed for their preparation, have revolutionized several domains such as modern medicine for example. Polymers are easy to process allowing a good match between application requirements and materials' properties. As a result, these materials are used in the biomedical field for multiple applications including wound sutures, breast implants, contact lenses and drug delivery. Despite of their intensive use in the biomedical field, there are still two major drawbacks to overcome: biocompatibility and biodegradability.

The vast majority of solutions found to counteract these problems are based on the use of natural polymers such as cellulose, lignin or collagen. Cellulose is the natural polymer most widely used, however its production requires a great amount of field areas entering in competition with agriculture and therefore food production. Other natural polymers are now being developed to overcome this drawback such as chitosan (derived from crustaceous shells), alginate (derived from algae), or silk (either from spiders or silk worms).

The use of silk has long been present within the society. This material has been mainly developed for cloths and luxury tissues. Nevertheless, its enhanced mechanical properties together with its biocompatibility has driven the development of silk sutures. Although silk sutures have been used since long time ago, the development of silk materials has not been extensively explored until recently. Silk is a biocompatible, biodegradable material with enhanced mechanical properties that can be easily obtained from silk worms in high quantity. Moreover, the production and obtaining processes have been extensively studied and developed by the textile industry allowing the production of great amount of materials. Therefore, many different kinds of silk materials have been developed these last few years. However bringing further functionality to these materials and being able to thoroughly characterize them still remain challenging.

In parallel, the recent development of nanotechnologies has shown the application of nanoparticles in many different fields including biomedicine, catalysis, sensing and imaging. The combination of nanoparticles with biopolymers allows the acquisition of new properties, in many cases just by the addition of small quantities of nanomaterials. Nevertheless, although many studies have focused on the acquisition of nano-component derived applications, little is

known about the interaction within the two materials. Further investigations should be conducted to elucidate whether the inclusion of a nano-object within silk materials influences the inherent properties of the two components.

Previous studies have been conducted within the BMBI laboratory at UTC to develop a silk-based nerve graft. Electrical conductivity being crucial for nerve functionality, the addition of gold nanoparticles to the material to increase this parameter was evaluated within the frame of this work in collaboration with TIMR laboratory. Though proof of concept for the fabrication of a nanoparticle embedded silk material was obtained, no in-depth characterization and understanding of the silk and nanoparticle interaction was conducted during the frame of the project. Therefore, the present project financed by Sorbone Universités has been settled over these preliminary results and combine the expertise of three partners. Silk extraction and processing has long been studied by the Biomechanics and Bioengineering (BMBI) laboratory at the Université de Technologie de Compiègne (UTC). On the other hand, the laboratory of Integrated Transformations of Renewable Matter (TIMR) at UTC provides strong knowledge on nanoparticle synthesis, characterization and understanding. Finally, an expertise on material characterization and interface interaction is brought in by the Laboratoire de Réactivité de Surface (LRS) at Sorbonne Université. Thus, the main objectives of this project are to produce nanoparticles embedded silk materials; provide an in-depth characterization and understanding on the NPs dispersion within a silk fibroin dispersion and provide proof of concept of the acquisition of nanoparticle derived properties of the final material.

This manuscript is divided in three chapters. **Chapter 1** settles the background and provides a walkthrough the state of the development of silk-based nanocomposites. Firstly, a presentation of silk structure, properties and existing materials is provided. This section is followed by the description of nanobjects and in particular nanoparticle, synthesis and properties. This chapter finishes with a review of the production methods, properties and characterizations of existing silk-based nanocomposites.

Chapters 2 and 3 focus on the main results obtained within this project. For best understand the obtained results, the materials and methods used are explained within the first sections of these chapters. **Chapter 2** explores different synthesis procedures for silk-based nanocomposites. This chapter goes from the synthesis of gold, silver and iron oxide nanoparticles (chosen as model nanoparticles) to the inclusion, by different methodologies, into several silk materials and their characterization. A focus is made in the characterization of nanoparticle embedded silk hydrogels.

**Chapter 3** is focused on the characterization of the nanoparticle derived properties acquired by the silk nanocomposites. Herein the antibacterial activity, magnetic properties and catalysis activity are characterized for silver, iron oxide and gold embedded silk hydrogels respectively. This chapter is divided in three subsections presenting three applications that have been chosen as proof of concept: antibacterial materials, brain implantation of silk hydrogels followed by magnetic resonance imaging and depollution. For each section, a brief introduction allows the reader to best understand the background and interest of the given application. Moreover the materials and methods used within each section are presented separately to provide the reader with all the knowledge required for a good understanding of the results presented.

A general conclusion will provide the summary of the obtained results from the synthesis of nanoparticles to the application of the silk-based nanocomposites. Finally, the perspectives of this work are presented.





# Chapter I: State of the art

---



# 1. Silk

## 1.1. Silk structure and extraction

Silk is a biopolymer produced by many members of the arthropod family such as spiders, silk worms, flies and silverfish. Each arthropod produces silk components with a different amino acid composition, resulting in different structural properties <sup>1</sup>. Mechanical properties have been shown to be different, with spiders' silk being stronger than that of silk worms <sup>2</sup>. In addition, silk properties are influenced by other parameters, such as climate, environment and arthropod nutrition, giving rise to the possibility of having different silk types produced by the same species <sup>2-4</sup>.

Among the existing silks, spider and mulberry worm silks are the most commonly used for textiles and biomedical applications <sup>5</sup>. Although spider silk has greater tensile strength, toughness and extensibility, the cannibalistic nature of spiders makes the development of an industrial production with high yield impossible. *Bombyx mori* silkworms, on the other hand, were domesticated for industrial silk production several centuries ago. As such, silkworm silk is almost exclusively used, and for that reason only *B.mori* silk will be considered in the following sections.

### 1.1.1. *Bombyx mori*'s silk structure

Two main proteins form *B. mori* silk: fibroin and sericin. Silk fibers are composed of fibroin microfibrils assembled into filaments. Silk fibers are made up of two fibroin filaments each produced by one of the worm's salivary glands during spinning. Both filaments are then covered by sericin, an adhesive and hydrophilic protein, which ensures the structural unit <sup>6</sup> (Figure I.1).

Fibroin is an hydrophobic protein formed by two chains: a light chain (L-chain, ~26kDa); and a heavy chain (H-chain, ~390kDa) <sup>4,7</sup>. The two fibroin chains are covalently linked by a disulfide bond between two cysteines, forming a H-L complex. The formation of this complex is essential for the secretion of silk fibroin in great quantities from producing cells to the glands <sup>8</sup>.

The primary structure of silk fibroin (SF) is formed by highly repetitive sequences composed mainly of glycine (43%), alanine (30%) and serine (12%). Other amino acids such as tyrosine (5%), valine (2%) and tryptophan are present in smaller proportions <sup>3</sup>. The primary structure of the H-chain contains 12 repetitive hydrophobic domains interspersed with 11 non-repetitive hydrophilic regions.

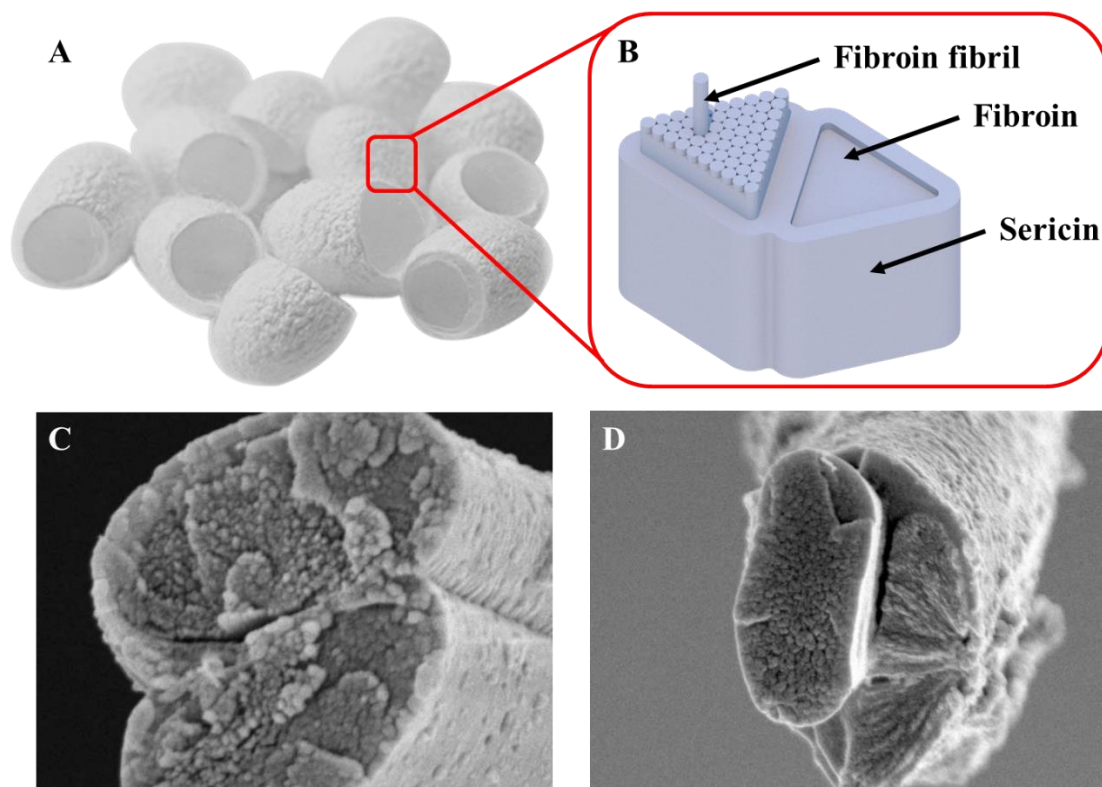


**Figure I.1.** (A, B) Schematic and (C, D) SEM images of silk fibers composing *Bombyx mori*'s silk cocoons showing sericin surrounding fibroin filaments. The later composed by fibrils. Adapted from Poza *et al* 2002 <sup>6</sup>.

Three different polymorphs of SF (silk I, II and III) exist according to its secondary structure. The silk I polymorph adopts a coiled structure and is found in the silk stored in the arthropods' glands. This conformation is also found in regenerated aqueous dispersions *in vitro*.

Silk II (Figure I.2 A) corresponds to the antiparallel  $\beta$ -sheet crystal structure obtained once silk has been spun. In the laboratory, this polymorph results from the mechanical / physical and chemical constraints exposure of silk I such as stirring, heating, exposure to methanol or water annealing procedures.

The formation of  $\beta$ -sheet structure is possible due to the rearrangement of the repetitive regions that form H-chain of SF and the intra and intermolecular interactions by hydrogen bonding, van Der Waals forces and hydrophobic interactions (Figure I.2 B). X-ray diffraction (XRD) analysis of the crystallinity regions of SF resulted in an antiparallel  $\beta$ -sheet structure <sup>9</sup>. The non-repetitive domains adopt a coiled conformation <sup>1,2,4</sup>.

Silk II excludes water from the structure giving strength to the protein filament and making it insoluble in water and other solvents like mild acids or bases. The third polymorph, silk III, adopts a helical structure <sup>1,4,5</sup>.

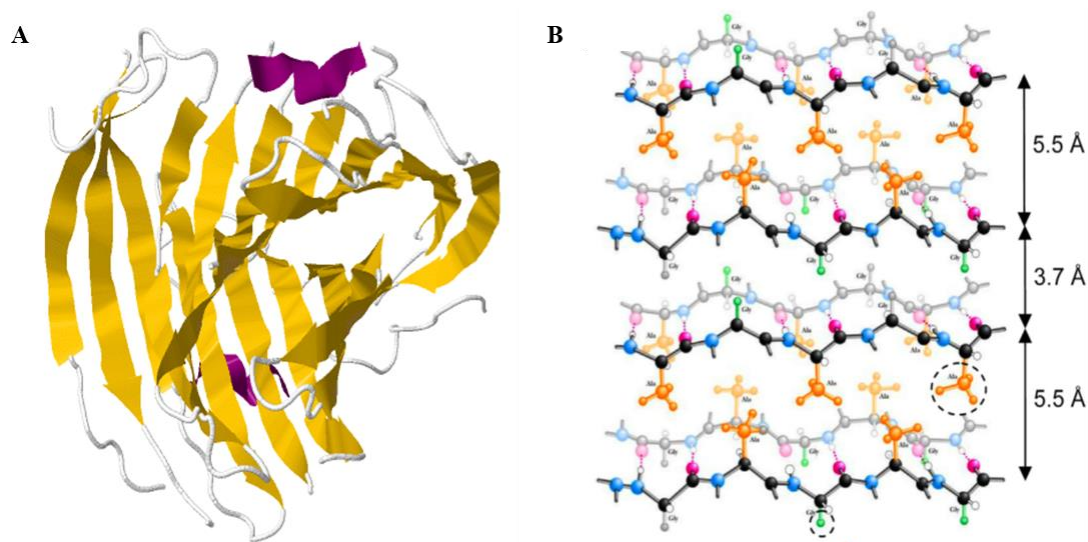


**Figure I.2.** (A) Silk fibroin H chain secondary structure and (B) antiparallel  $\beta$ -sheet formation. Adapted from Koh *et al* 2015<sup>3</sup>.

### 1.1.2. Silk fibroin biodegradation

Silk fibroin biodegradation has been proven by several authors to take place as well *in vitro* than *in vivo*. In both cases, this process is extremely dependent on the material final conformation and more specifically on the  $\beta$ -sheet content of the material<sup>10</sup>. As in other cases such as cellulose, crystalline regions are more stable and difficult to degrade. Therefore, tuning the crystalline content of silk fibroin materials results in tailored biodegradation rate of the material<sup>11</sup>. This property is of special interest for regenerative medicine and drug delivery applications, where material biodegradation plays a crucial role in its application.

*In vitro*, fibroin biodegradation occurs mainly due to enzymatic activity. Due to its proteic nature, silk fibroin has been shown to be hydrolyzed by protease XIV, collagenase IA and  $\alpha$ -chymotrypsin among others. This enzymatic mediated biodegradation is strongly dependent in the enzyme used: while the three enzymes cited are able to degrade amorphous regions only collagenase IA and the protease XIV are able to degrade crystalline regions, being the later most effective<sup>12</sup>.

*In vivo* silk fibroin biodegradation is probably due to synergistic activities of the immune, metabolic and circulatory systems, as well as the local tissue specific cells and proteinases. The exact mechanism is then dependent on the implanted tissue and the silk fibroin material its-self<sup>12</sup>.

The biodegradation of silk fibroin materials has been found to vary from several days up to several years. Therefore, although silk fibroin is said to be a biodegradable material, this property has to be evaluated for every material, synthesis procedure and application.

### 1.1.3. Regenerated silk fibroin extraction

Some studies have shown that sericin may induce an immunogenic response in the human body<sup>13</sup>, however SF has been approved by the FDA for medical use in the US<sup>14</sup>. Therefore sericin is removed from silk for biomedical applications<sup>13,15</sup>.

*Bombyx mori* silk cocoons are processed to obtain a regenerated SF dispersion. This procedure differs from the one used by the textile industry as the final objective is not to obtain silk fibers but a SF dispersion.

The idea is to bring silk (polymorphs II and III) to the initial state found in the glands of the worm (silk I) before being spun. This transformation can be achieved by denaturing SF proteins, which will result in a protein dispersion. The main procedure is described hereafter.

Briefly, silk cocoons are cut and boiled in a sodium carbonate ( $\text{Na}_2\text{CO}_3$ ) solution to remove the sericin (soluble in hot water) that glues together the SF filaments. Boiling time is a crucial parameter influencing the properties of obtained SF dispersion. Longer times will disrupt SF fibers to smaller molecular weight peptides. Boiling silk cocoons for 30 minutes will result in approximately 100 kDa fibroin proteins<sup>13</sup>. Once boiled, the resulting entangled cotton-like fibers are abundantly rinsed in abundant distilled water (to remove any remaining sericin), suspended in water and denatured to obtain the SF dispersion. Different solutions can be used for this purpose, giving rise to various procedures for SF regeneration, the most common denaturing agent used is lithium bromide (LiBr)<sup>1,13</sup>. LiBr allows the destabilization of hydrogen bonds found in silk II polymorph; allowing the shift to the silk I structure<sup>1</sup>.

Nevertheless, LiBr is a chemical hazard that can cause skin and eye irritation, encouraging the search for alternative solutions. Another solution used to dissolve and denature silk fibroin fibers is a ternary system composed of calcium chloride, ethanol and water<sup>16-19</sup>. Other solutions such as 1-butyl-3-methylimidazolium chloride (BMIM Cl), 1-butyl-2,3-dimethylimidazolium chloride (DMBIM Cl) and 1-ethyl-3-methylimidazolium chloride (EMIM Cl); have also been proven to dissolve and denature silk<sup>20</sup>.

After a dialysis stage, the resultant dispersion is around 6-8% w/v SF concentration and can be further concentrated up to 30% approximatively. Higher concentrations induce SF gelation. Regenerated SF dispersion should be handled with care as many procedures such as heating, stirring or pH variations will induce protein rearrangement forming  $\beta$ -sheet structures resulting in the gelation of the dispersion. Because of this, regenerated SF dispersion should be stored at 4 °C and for no longer than 1 month. Unlimited time storage can be achieved by lyophilizing

the obtained dispersion. Lyophilized product can further be dissolved in formic acid or 1,1,1,3,3,3-hexafluoro-2-propanol (HFIP)<sup>13</sup> at the desired concentration.

## 1.2. Silk-based materials

Silk is traditionally known by its wide use in the textile industry given its lightweight, soft touch and luster properties. *Bombyx mori*'s silk has become a great material for environmental science and biomedical applications among others because of its biodegradability and biocompatibility.

The  $\beta$ -sheet structure found in silk II polymorph is responsible of silk mechanical properties, which are above most known biopolymers (Table I.1). Because of its unique properties and its versatility, many different materials can be obtained from a SF dispersion or its lyophilized powder (Figure I.3).

Most of the techniques used to construct SF materials are based on the controlled formation of  $\beta$ -sheet structures. Controlling the percentage of  $\beta$ -sheet structure enables tailoring the mechanical, biodegradation and solvent dissolution of silk materials.

**Table I.1.** Comparison of the mechanical properties of biological and synthetic materials <sup>21–25</sup>.

Material	Strength (MPa)	Stiffness (GPa)	Young's Modulus (GPa)	Breaking Strain (%)
<b>B.mori silk</b>	500	5-12	10-17	4-26
<b><i>B.mori</i> degummed silk</b>	610-690	15-17	16-18	4-16
<b>N. Clavipes silk</b>	875-972	11-13	10.9	17-18
<b>Collagen</b>	0.9-7.4	0.0018-0.0460	3.7-11.5	24-68
<b>Elastin</b>	2	0.001	0.001	150
<b>Bone</b>	160	20	8-24	3
<b>Nylon</b>	430-950	5	1.8-5	18
<b>Polylactic acid</b>	28-50	1.2-3	-	2-6
<b>Polypropylene</b>	490	-	4.6	23
<b>Kevlar 49 fiber</b>	3600	130	130	2.7



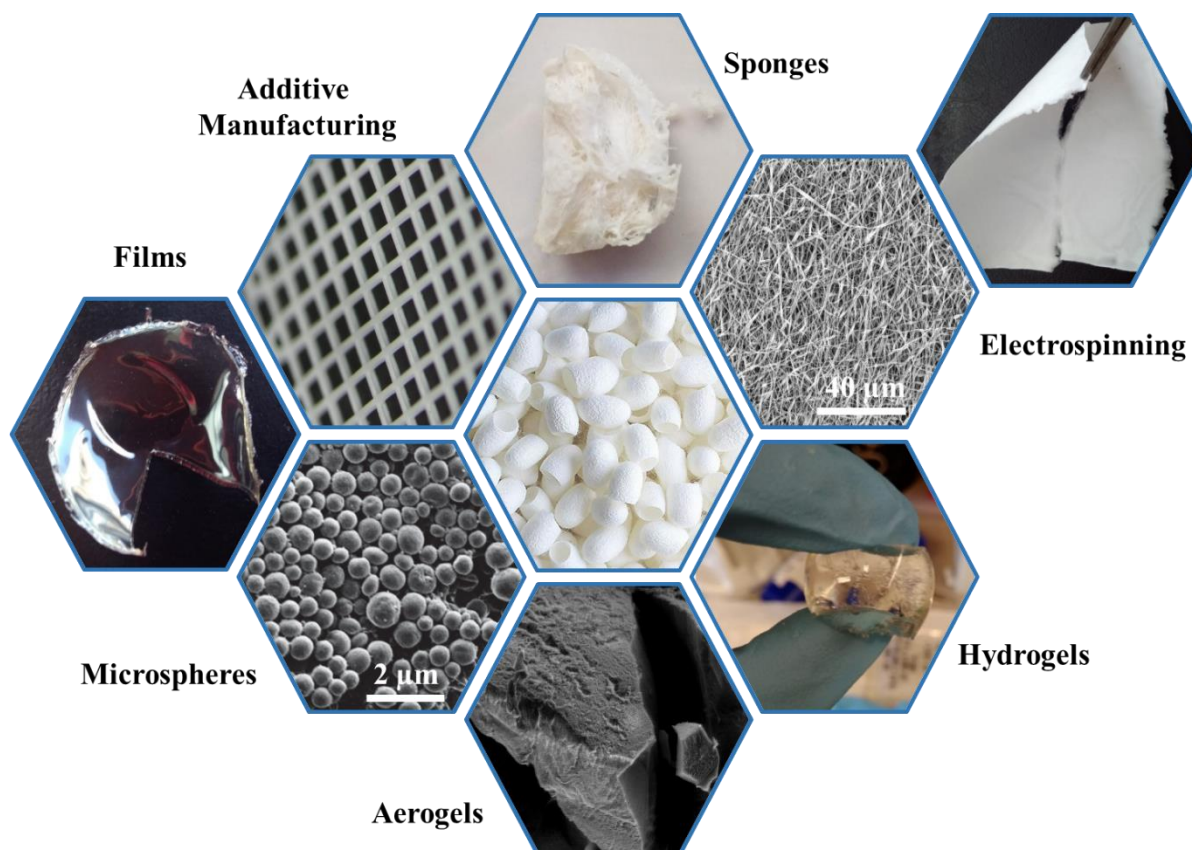


**Figure I.3.** Representation of some of the different silk fibroin-based materials that can be obtained from *Bombyx mori* silk cocoons.

### 1.2.1. Sponges

Silk fibroin sponges are 3D porous materials for which pore size and interconnectivity can be controlled depending on the production method. Silk fibroin sponges are easily produced by mixing the silk dispersion with a porogen (e.g. salt or sugar crystals, polymer or mineral beads) and subsequently inducing silk gelation. Many different procedures have been described, such as the use of sodium chloride (salt leaching), freeze casting<sup>26</sup> or HFIP solvent<sup>13</sup>.

Silk fibroin sponges can be used as scaffolds for bone tissue regeneration due to their macroporous structure that can be tailored to promote the enhanced formation of new and vascularized bone tissue<sup>27</sup>. Several *in vitro* and *in vivo* studies have demonstrated the potential of cellularized scaffolds or acellular materials for bone regeneration<sup>28–32</sup>.

### 1.2.2. Electrospun mats

Electrospinning is a simple technique that consists in the use of an electric field to spin a polymer dispersion into a non-woven mat composed of nanometer diameter fibers. During electrospinning, the polymer dispersion is placed in a syringe with a conductive needle connected to a high voltage electric field (5 - 40 kV). A grounded conductive collector is placed



in front of the needle at a given distance. While the polymer dispersion is extruded through the needle, the high voltage electric field induces its stretching, allowing the formation of nanometer fibers. At this moment, the solvent evaporates and the fibers are deposited on the collector due to the voltage difference <sup>13,33</sup>. Figure I.4 shows a schema of the electrospinning set up.

The nature of the collector used has a great implication on the fiber alignment. If a flat static collector is used, fibers are deposited randomly and the structure of the obtained material is similar to the collagen fiber arrangement found in the extracellular matrix <sup>34</sup>. A rotating mandrel used as collector will result in the alignment of the deposited fibers <sup>13</sup>, which may be interesting for neural regeneration materials <sup>35</sup>.

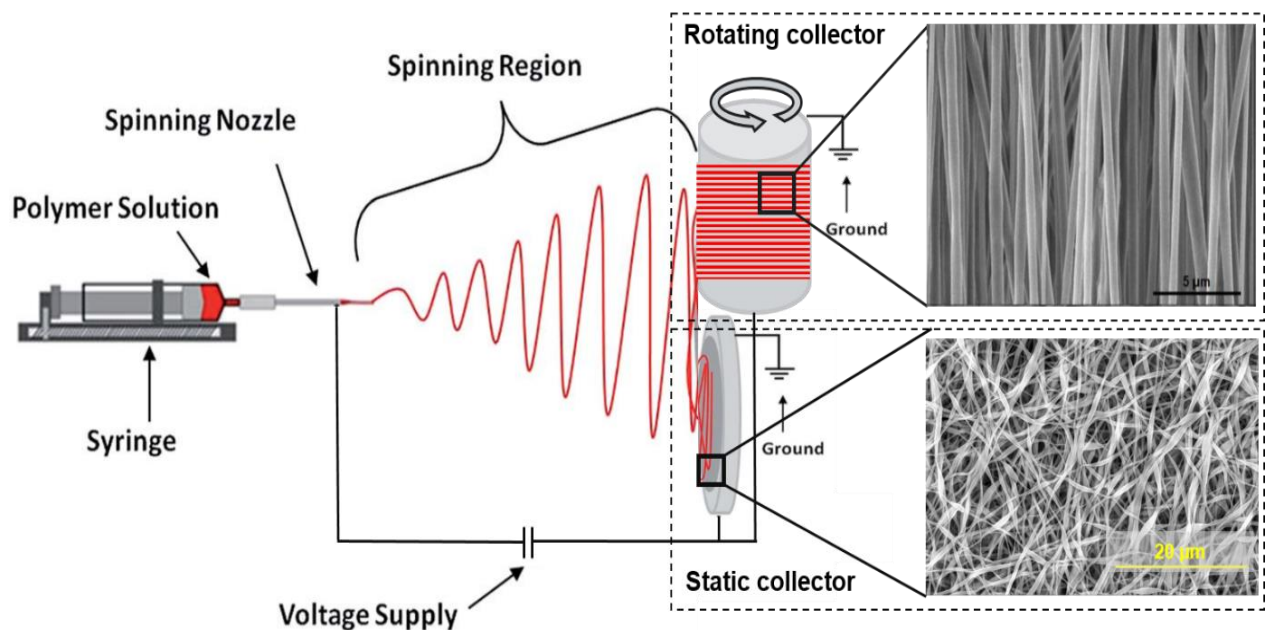


**Figure I.4.** Electrospinning set up. The choice of the collector used has an implication over resultant material. Rotating (right top) and static collectors (right bottom) are shown resulting in aligned or randomly deposited fibers respectively shown by SEM images. Adapted from Lee et al 2014 <sup>36</sup>.

The fiber diameter obtained by electrospinning can be modulated by adjusting the following parameters: polymer concentration, polymer extrusion flow rate, needle to collector distance and applied voltage. The electrospinning procedure may also be sensible to other parameters depending on the polymer used. Silk fibroin electrospinning is highly dependent on humidity and temperature. A variation in one of these parameters will alter the final material obtained.

Electrospun mats can be used in the field of wound dressing, textile <sup>34,37,38</sup>, wearable electrodes, nerve guides <sup>35</sup> and other biomaterials <sup>39</sup>.

### 1.2.3. Microspheres

Silk microspheres can be produced by several methods. Silk can be encapsulated in fatty acid lipids, creating an emulsion of silk microspheres <sup>13</sup>. Another possible procedure consists on a phase separation of silk from another polymer such as poly(vinyl alcohol) (PVA) <sup>13</sup> or by adding potassium phosphate to the aqueous silk dispersion <sup>40</sup>.

Silk has been extensively used for drug delivery, both as a vehicle and due to its stabilizing effect on bioactive molecules and enzymes <sup>41–46</sup>. Silk microspheres are of great interest as encapsulating material in this field, because modulating their degradation rate results in a controlled release of their content <sup>47,48</sup>.

### 1.2.4. Hydrogels

Hydrogels are of increasing interest nowadays given their mechanical properties, which are closer to those of soft tissues in the body than conventional materials such as metals or ceramics. In addition their capacity to swell and retain a high liquid volume renders them very interesting for depollution as environmental hazard removal <sup>49</sup>.

Hydrogels can be used to replace damaged soft tissues such as cartilage, intervertebral disc, cornea and skin among others. SF hydrogels are used as biomolecule protectors (by encapsulation) and they can be found in applications such as drug delivery <sup>50,51</sup>, tissue engineering <sup>52,53</sup>, regenerative medicine <sup>54–58</sup> and catalysis <sup>59</sup>.

The formation of hydrogels consists in the rearrangement of SF molecules to form a greater crystalline structure than the one present in the bulk dispersion. For this purpose, many protocols have been described in the literature to control their formation and tune their characteristics. The main procedures include physical- and chemical-induced gelation.

*Physical gelation* occurs due to the formation of non-covalent bonds such as electrostatic or hydrophobic interactions or hydrogen bonding. This method is based on the creation of non-covalent bonding between the SF chains. Physical gelation protocols include dispersion sonication <sup>58</sup>, vortexing, electrical current application or pH decrease <sup>13</sup>.

*Chemical gelation* is due to the formation of new covalent bonds in presence of an enzyme, a chemical catalyzer or other chemical species. Chemically crosslinked gelation protocols include most of the times the use of enzymes such as oxidases, phosphatases, transglutaminases or peroxidases <sup>60</sup>. A focus is made below on enzymatic assisted crosslinking.

Enzyme crosslinking is the preferred technique for biomedical applications due to its low toxicity, capacity of *in situ* crosslinking and crosslinking to the surrounding extracellular matrix<sup>60</sup>. Moreover, enzymatic catalyzed reactions are highly specific allowing a good control over the reaction product. Although many enzymes have been used in the literature to form hydrogels<sup>60</sup>, horseradish peroxidase is the most extensively used. In this work we will focus on the use of horse-radish peroxidase (HRP).

HRP is an oxydoreductase that catalyzes the conjugation of phenol and aniline derivatives in presence of hydrogen peroxide ( $H_2O_2$ ). Phenol groups being present in tyrosine, the HRP action in proteins results in the formation of dityrosine bonds. In addition, the incorporation of tyramine to desired molecule enables its crosslinking by HRP as well<sup>61,62</sup>.

The use of this enzyme to crosslink peptides, polysaccharides and polymers has been extensively described in the literature<sup>61–67</sup>. In particular HRP crosslinked SF hydrogels have been well described by Partlow *et al.*<sup>68</sup>. They have well characterized the structure, crosslinking kinetics, rheological and mechanical properties as well as the cytotoxicity and biocompatibility of the obtained hydrogels. The authors proved that the properties of this SF hydrogel are highly tunable depending on several parameters such as silk fibroin molecular weight and concentration. In addition, the all-aqueous procedure together with its biocompatibility and *in vivo* tolerance makes this hydrogel a good candidate for biomedical applications and encapsulation of biological factors (growth factors, hormones, cytokines...) preserving their activity.

### 1.2.5. Aerogels

Aerogels are open porous materials of very low density that derive from replacing the liquid component of a gel by a gas. Silk aerogels are generally produced by freeze drying of a silk dispersion or a hydrogel and are then called cryogels. Similarly to sponge materials, a 3D porous scaffold is obtained.<sup>1</sup> Again, porous size and distribution can be tuned by controlling the freezing procedure. One example is the ice template technique that consists in controlling the ice crystal growth through the silk sample to obtain a desired structure<sup>69</sup>. Microchannel containing silk scaffolds can be obtained by this technique<sup>1,70</sup>. Aerogels are used as fire retardant materials, thermal insulators<sup>71,72</sup>, depollution and biomaterials<sup>73</sup> among others.

### 1.2.6. 3D printed structures

The increased development of 3D printing technologies in the last years has made possible to print from polymer dispersions. Silk structures can be printed by using an extrusion like 3D

printer. This approach opens many possibilities to better control the shape and dimensions of the structures. Therefore, the material can be easily adapted for each application <sup>74</sup>.

Many silk-containing bio-inks or 3D printing techniques are being developed. Some approaches have focused on the properties of silk to obtain a construct, for example, by printing in a saline bath to induce a hierarchical assembly of the silk proteins <sup>74</sup>, or by using freeform printing in a bath of synthetic nanoclay and polyethylene glycol (PEG) for a one-step process of printing and *in situ* physical gelation <sup>75</sup>. Other strategies have focused on mixing SF with other polymers and thickening agents, such as PEG <sup>76</sup>, polyols <sup>77</sup> or the polysaccharide Konjac glucomannan <sup>78</sup>. 3D printed structures are of great interest in the tissue engineering field, as they allow the manufacturing of complex and patient-tailored shapes with controlled macroporosity.

### 1.2.7. Foams

Silk memory foams offer a promising and minimally invasive solution for soft tissue regeneration. These materials can be compressed prior to implantation, and then have the ability to recover their volume <sup>79</sup>. *In vivo*, these materials have shown promise as soft tissue fillers, being rapidly colonized by cells and integrating with the surrounding native tissue <sup>80</sup>. These foams can be used as a drug delivery vehicle for bioactive molecules <sup>81</sup> and soft tissue regeneration <sup>82</sup>. Overall, these materials are extremely well suited for soft tissue regeneration and localized drug-delivery at the injury site.

### 1.2.8. Microneedles

The excellent mechanical properties, biocompatibility, biodegradability, benign processing conditions, and stabilizing effect of silk on biological compounds has made it an ideal candidate for the fabrication of microneedle systems for drug delivery. The degradation rate of SF and the diffusion rate of the entrained molecules can be controlled simply by adjusting post-processing conditions <sup>83,84</sup>. These microneedles can further be combined with other materials to make composite microneedles and further tune the release profile. These microneedles have been also associated with insulin <sup>85</sup>, antibiotics <sup>83</sup>, and vaccines <sup>86,87</sup>. Products based on this technology are currently being developed and commercialized for therapeutic applications, in particular by the company Vaxess.

### 1.2.9. Hard silk materials

The mechanical properties of regenerated silk materials can be tuned for orthopedic applications requiring hard materials by controlling the fabrication process. Li et al. <sup>88</sup> have obtained bulk

regenerated silk-based materials with excellent mechanical properties through a biomimetic, all-aqueous process. These materials replicated the nano-scale structure of natural silk fibers and demonstrated excellent machinability, allowing the fabrication of resorbable bone screws, intermedullary nails and fixation plates.

### 1.2.10. Films

Silk can be processed into a thin film by drying, methanol- or water-annealing, or even electrogelation<sup>89,90</sup>. Glycerol can be added to the formulation to obtain a flexible silk film<sup>91</sup>. While silk films are promising in the field of drug delivery<sup>92</sup>, or for the long-term stabilization of vaccines<sup>89</sup>, they also have direct applications in tissue engineering. Their interesting optical transparency and thin format make them ideal candidate for corneal models. They sustain cell adhesion and growth; they can also be patterned to better mimic the cellular organization of the cornea<sup>93</sup>. Pores can also be added to enhance trans-lamellar nutrient diffusion and cell-cell interaction. These films can be further stacked into multi-lamellar structures, and functionalized with RGD-peptide, allowing a biomimetic 3D corneal model<sup>94</sup>.

## 1.3. Applications

The versatility of silk materials and their tunable properties make them of great interest for many applications such as tissue engineering<sup>21,95</sup>, wearable electronics<sup>96</sup> and depollution<sup>97–99</sup>.

### 1.3.1. Biomedical applications

Silk materials are able to overcome most of the challenges found in the biomedical field thanks to their mechanical robustness, biocompatibility and biodegradability. The various materials obtained from silk, as described above, can be used in numerous applications.

Among all the silk materials that are currently used for biomedical applications, the gold standard is silk sutures. Although they have been used in the medical field for much longer, silk sutures were patented in 1966, thus establishing the possibility to use silk in medicine. Silk sutures were first developed to overcome the mechanical problems encountered with traditional sutures. Surgical sutures require a great tensile strength to keep both ends of the wound tight together even under physiological movements such as the heartbeat, stomach or intestinal peristalsis, or muscle contraction and relaxation. In addition, surgeons should be able to do tight knots with sutures. Silk was a great candidate, as it met all these requirements.

Since then, silk materials have continuously been developed for many applications in the biomedical field, such as wound dressing materials<sup>100,101</sup>, skin<sup>53,102</sup>, bone<sup>103</sup>, cartilage<sup>104</sup>,

ocular<sup>50</sup>, vascular<sup>105–107</sup>, neuronal<sup>35,108</sup> and tissue regeneration<sup>95</sup>. Some examples are detailed here after.

#### 1.3.1.1 Wound dressing

After sutures, wound dressings are probably the most common application of silk materials in the biomedical field. Several studies have found that silk materials induce a faster reepithelization than conventional materials in skin burn wounds (Figure I.5)<sup>100</sup>.

Functionalization of electrospun silk materials seems an interesting approach as many active molecules and drugs exist to improve for example cell differentiation and cell proliferation. Silk materials have been functionalized in the literature with epidermal growth factor (EGF) and silver sulfadiazine increasing the overall wound healing process.

Functionalization can also be done by using silk microparticle<sup>101</sup>. In this case the authors chose to functionalize their material with insulin for chronic wound healing applications. Insulin was chosen because of its contribution to wound healing and its acceleration of reepithelization. The overall wound healing effect was studied *in vivo* in diabetic rats. The authors found that SF insulin loaded materials resulted in an increased wound closure rate in comparison with a non-insulin loaded SF material and a conventional gauze.

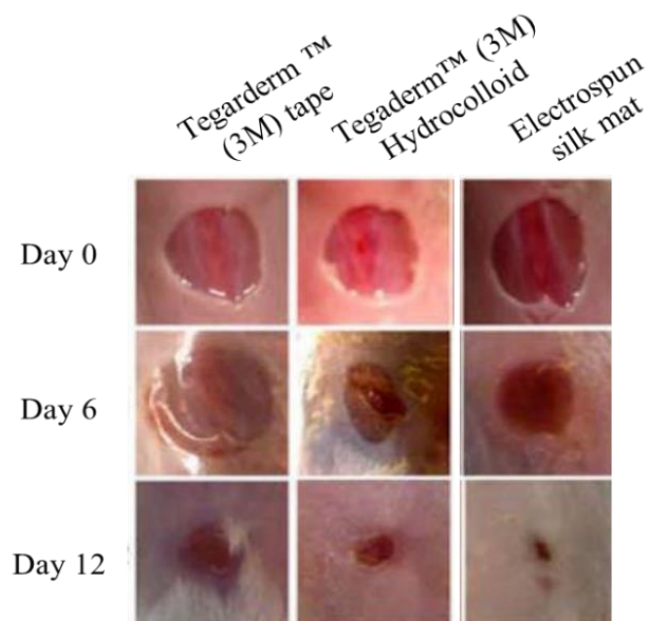


**Figure I.5.** Monitoring wound healing over 0, 6 and 12 days. Comparison of commercial (Tagaderm™ (3M) hydrocolloid) and silk electrospun materials. Tagaderm™ (3M) tape was used as negative control. Adapted from Gil *et al* 2013<sup>100</sup>.



### 1.3.1.2 Skin equivalents

Skin wounds being a great issue in medicine, due to the high incidence of burn wounds, research has further been developed to create skin substitutes. Silk materials are recently entering this field due to the discovery of its improvement in wound closure and its biocompatibility and biodegradability properties.

An artificial skin has been produced by silk electrospinning<sup>102</sup>. Three different electrospinning techniques have been compared: (i) traditional electrospinning (TE), (ii) salt leaching electrospinning (SLE) and (iii) cold plate electrospinning (CPE). CPE materials proved the possibility of having a thicker final material as ice crystals kept the conductivity of the deposited material enhancing the deposition of new polymer over already deposited fibers (Figure I.6).

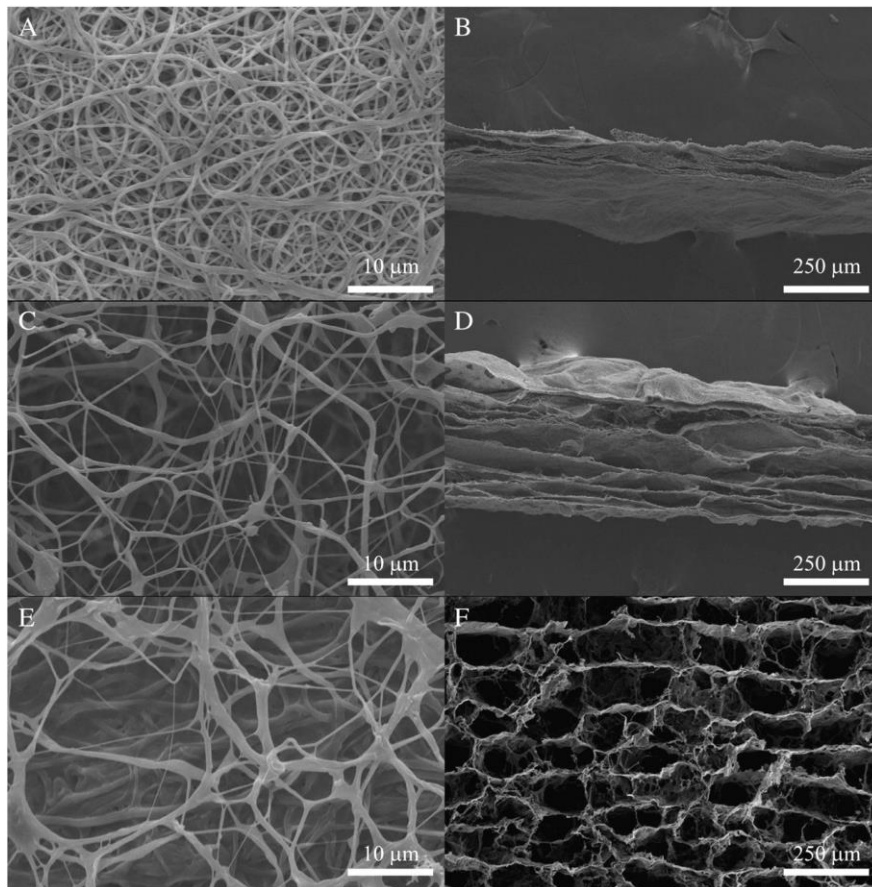


**Figure I.6.** SEM images of surface (left) and section (right) of TE (A, B), SLE (C,D) and CPE (E, F) materials constructed by Sheikh *et al* 2015<sup>102</sup>.

In addition, CPE obtained materials showed an increased cell infiltration and the possibility to create an artificial skin substitute when culturing keratinocytes in the air-liquid interface. This is not possible with the materials obtained by TE and SLE due to lack or poor 3D structure and cell infiltration. Finally, CPE is the only technique than can be used over curved surfaces. This

possibility makes easier the production of personalized systems by using a 3D shaped mold; for instance, mimicking and ear.

Going one step forward Vidal *et al*<sup>53</sup> included cells into their silk skin equivalent. They constructed a very complex skin equivalent including adipose tissue, endothelial cells, keratinocytes, neural, immune and vascularization systems. The hypodermis was constructed on a silk sponge material constructed by salt leaching procedure. Dermis and epidermis layers were shaped into a hydrogel containing complete cell culture media, silk, collagen and fibroblast. Both materials were then placed together to form a full thickness skin equivalent.

The presence of silk in the material is crucial to overcome the main concern about collagen skin equivalents, which is construct contraction. In addition, mechanical properties of silk containing hydrogels are closer to skin than collagen alone materials. Moreover, silk containing materials are useful for up to 6 weeks giving the possibility to study patient specific immune and neuronal responses for a longer period of time *in vivo* and *in vitro*.

#### 1.3.1.3 Bone regeneration

Ideal properties for bone tissue engineering material have been described by several authors in the literature<sup>103,109,110</sup>. These crucial characteristics are: comparable mechanical properties to the bone, biocompatibility, bioresorption and the capacity to deliver osteoprogenitor cells and growth factors. In addition, scaffolds should be able to provide mechanical integrity until the bone is completely regenerated, as they have to support high loads and mechanical stimuli.

When possible, resorbable materials are preferred as they avoid the need for a second surgery to remove the implant. Collagen is the preferred material in this case. However, because of the difficulty to produce it with reasonable costs, and the complexity to control its hierarchical structure that provides the mechanical requirements to the materials, synthetic polymers are used as alternatives.

An extended review on silk-based materials for bone tissue engineering has been recently published by Bhattacharjee *et al.*<sup>103</sup>. Their work shows the possibility of exploiting the great versatility of silk materials for cellularized scaffolds or acellular materials for bone tissue engineering applications. For example, guided bone regeneration was successfully achieved with silk membranes<sup>26</sup>. The main objective was to create a material able to avoid connective tissue invasion into a bone defect, such as after a surgery. Invasion of the defect by soft tissue makes bone regeneration impossible, resulting in a local loss of function. In their *in vivo*



experiment, the authors proved that their material was as performant as the commercially available products. However, it is only useful for small bone defects.

#### 1.3.1.4 Vascular tissue engineering

Cardiovascular diseases are an important health concern. Although the gold standard in this case are autologous transplantation (autografts), this solution is not always possible. Therefore, other materials have to be developed.

Some synthetic materials are already used to construct vascular grafts namely expanded polytetrafluoroethylene (ePTFE, Teflon<sup>®</sup>) and polyethylene terephthalate (PET, Dacron<sup>®</sup>). These materials are largely used in the medical field when large diameter vessels or arteries need to be replaced. However, their performance when replacing small diameter vessels (less than 6 mm) is reduced and far from the ones achieved by autografts. Moreover, they may cause clinical complications such as aneurysm, intimal hyperplasia and thrombosis among others. Due to their characteristic mechanical properties and biocompatibility, silk materials can also be used in the vascular tissue engineering field.

To overcome these issues, Lovett and its group<sup>105</sup> developed a small vessel graft. The resultant tube with tailored diameter is rich in  $\beta$ -sheet structured silk conferring interesting mechanical properties. The incorporation of polyethylene oxide into the silk dispersion resulted in an optimal porosity once PEO removed. This porosity enables small protein diffusion but limits endothelial cell migration.

Vessel grafts have also been produced by combining two electrospun layers and an intermediate textile layer.<sup>106</sup> Authors proved their material to have similar mechanical properties to native arteries, good biocompatibility, cell adhesion and blood hemocompatibility (no complement activation). However further optimization needs to be done as *in vivo* tests in a sheep and a minipig showed a foreign body response.

#### 1.3.1.5 Nerve regeneration

Neural guidance is a key factor for efficient nerve regeneration as the two nerve ends should find each other. A good guidance enhances nerve functional recovery. With this objective, Belanger *et al*<sup>35</sup> managed to produce a three layered silk electrospun material (aligned-random-aligned fibers) (Figure I.7) The aligned nature of the electrospun silk material was able to induce an alignment in Schwann cells in contrast to the randomly growth found when cultured over glass coverslips. Finally, the *in vivo* experiments showed a successful nerve regeneration after 4 months. Moreover, their material had good mechanical properties matching the same tensile

stress that the rat's sciatic nerve (2.6 MPa). In addition to the mechanical properties, the design of the material made surgery easier. Nevertheless, the insulating character of silk materials impairs the electrical potential actions that are essential for neural action and communication.

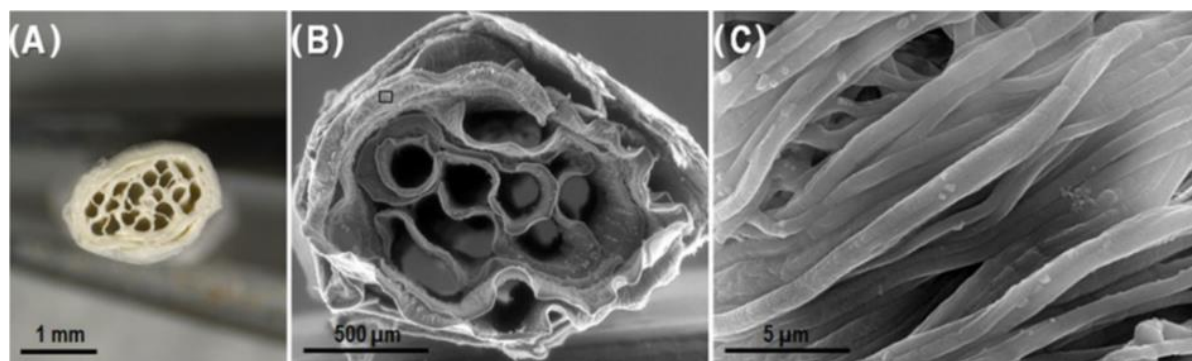


**Figure I.7.** Silk nerve graft produced by rolling electrospun mats to produce conduits. Macroscopic (A) and SEM (B) images showing the conduits. (C) SEM image of the inner layers showing and aligned structure of the electrospun fibers. From Belanger *et al* 2018 <sup>35</sup>.

#### 1.3.1.6 Drug delivery

The controllable degradation rate of silk fibroin materials in the body enables their use as drug delivery devices. Lan and their collaborators<sup>48</sup> produced gentamicin sulfate (GS) impregnated gelatin microspheres (GM) that were embedded into a silk scaffold obtained by freeze drying. The resulting material showed a reduced inflammatory response and accelerated reepithelization *in vivo* while having antibacterial properties.

Similarly, a dual drug loaded silk material was developed <sup>47</sup>. Silk microspheres containing curcumin were prepared and blended into a silk dispersion with doxorubicin hydrochloride (DOX HCl). By electrospinning, the authors obtained a nanofiber silk material containing and hydrophilic drug (DOX HCl) in the shell and a hydrophobic one (curcumin) in the core.

Silk hydrogels can be used for drug delivery as well. Silk hydrogels loaded with bevacizumab, an anti-vascular endothelial growth factor (anti-VEGF), have been created <sup>50</sup>. Bevacizumab is a therapeutic agent against age-related macular degeneration (AMD), an eye disease characterized by the progressive loss of vision. The intravitreal injection of hydrogels in rabbits' eyes showed a sustained drug release for up to 90 days.

#### 1.3.2. Other applications

Although silk is widely being developed for the medical field, interesting applications have been found in further areas such as depollution <sup>97–99</sup>, electronics <sup>96</sup> and material science <sup>72</sup>.

For example, silk has been demonstrated to be a great adsorbent of several components, which renders it interesting for water and air depollution. With this objective, electrospinning has been

used to develop silk air filters<sup>97</sup>. The resultant filters showed a high efficiency air filtration (up to 99,99%) for particles from 0.3 to 10  $\mu\text{m}$  and a decreased pressure drop in comparison with the state-of-the-art materials. In addition, silk filters are biodegradable making easy their recycling process.

Another study has proved the combination of SF with hydroxyapatite to be efficient for water filtration and purification<sup>99</sup>. The described material was able to remove dyes and heavy metal ions from solutions. This result is not achieved with conventional nanofiltration membranes (Figure I.8).

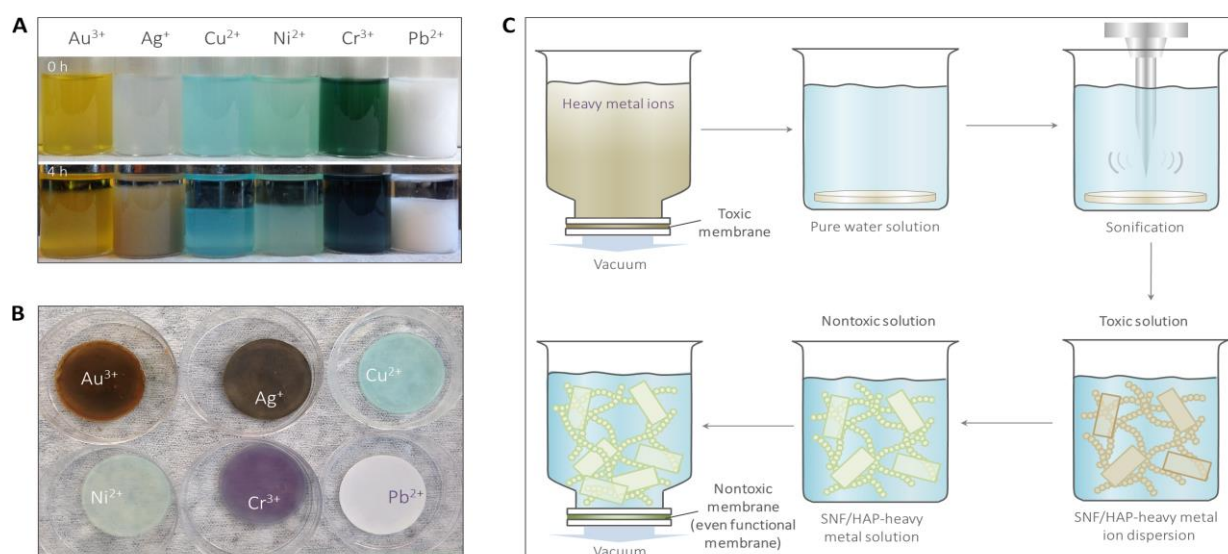


**Figure I.8.** Heavy metal depollution by silk HAP materials. (A) Heavy metal solutions mixed with silk/HAP dispersion at 0 (top) and 24h (bottom). (B) Images of silk/HAP membranes after the filtration of several heavy metal solutions. (C) Possible route of heavy metal recycling by redispersion of a heavy metal adsorbed silk/HAP filter. Adapted from Ling *et al* 2017<sup>99</sup>.

Silk can as well be mixed with silica to form insulating and fire retardant materials.<sup>72</sup> These materials can be easily obtained by a one-step acid catalyzed sol-gel reaction. The resulting silk/silica aerogel shows excellent properties as low density (0.11-0.19  $\text{g}/\text{cm}^3$ ), high surface area (311-798  $\text{m}^2/\text{g}$ ), flexibility in compression and fire retardancy

## 2. Nano objects

Nano-objects have been described by convention as objects with at least one of their three dimensions found at the nanoscale (smaller than 100 nm). Nano-objects are classified into three groups: nanoplates, nanofibers and nanoparticles.

Nanoplates include all ultrathin coatings no matter their area. Even if the coating material is not found in the nanoscale, the surface characteristics can be crucial for their use. Nanofibers can be subdivided into nanorods (rigid filled-in nanofiber), nanowires (electrically conductive

nanofiber) and nanotubes (hollow nanofibers). The materials most widely known in this category are carbon nanotubes. Finally, nanoparticles (NPs) are the most studied group and in the following sections we are going to focus essentially on inorganic NPs.

Many different NPs are currently being developed in the world. NPs can be classified by their composition, shape and structure, such as porous NPs, janus NPs (composed of two distinct areas), irregular and regular NPs. However, the most commonly used classification is based on the constituent material. This classification includes polymer NPs, lipid-based NPs, carbon-based NPs, ceramic NPs, semiconductor NPs and metal/oxide NPs. Some NPs are shown in Figure I.9.

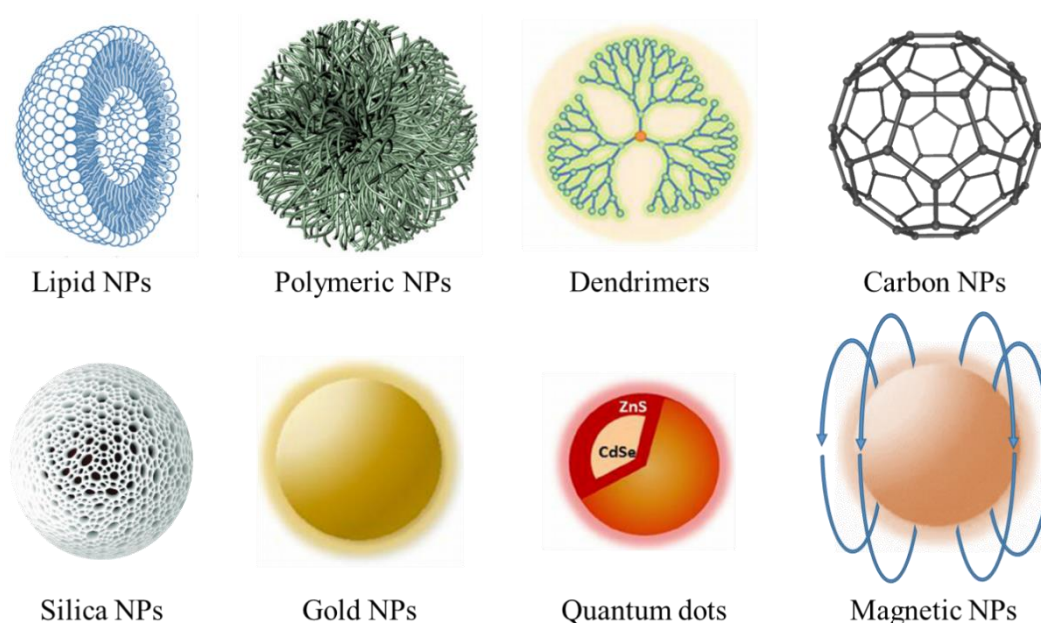


**Figure I.9.** Schematic representation of several nanoparticles types. Adapted from <sup>111,112</sup>.

NPs have a high surface to volume ratio. This characteristic allows the user to have a greater surface with less material, which is crucial for several applications such as catalysis and sensing. Moreover, achieving an enhanced surface with less material therefore also represents an economic interest. In addition, unexpected and tunable properties appear at the nanoscale, which differs from those of the bulk material. In fact, because of their small size, NPs can behave at the atomic level as a single domain. This is called the quantum effect. This characteristic results in specific properties such as surface plasmon resonance or superparamagnetism. However, these properties are dependent on the material composition, and the nanoparticle size and shape. Controlling these parameters is, thus, crucial, for tuning the characteristics of NPs and their properties for the target applications.

Finally, NPs size (<100 nm in one dimension) is close to the regular world of biology and is also comparable to that of biological molecules such as nucleic acids or antibodies, and so they can easily interact with them and with cells. Therefore, another important asset is tailoring the surface properties of NPs, by for example conjugating them with biomolecules and producing hybrid materials that can interact specifically with biological systems <sup>113</sup>.

Despite these advantages, the use of NPs raises a main concern due to their unknown toxicity. Now, it is well-established that NPs are rapidly covered by biomolecules, mostly proteins, when injected in biological fluids, leading to the formation of the so-called “biomolecular corona” <sup>114,115</sup>. Moreover, it is important to consider that the stability of NPs in suspension depends on the equilibrium of attractive and repulsive forces between NPs. This equilibrium is influenced by physicochemical conditions of the surrounding medium, including ionic strength, nature of ions, pH, temperature, and the presence of bio-organic compounds (e.g. steric effect). Destabilization of the NPs suspension may result in their aggregation and precipitation. Given these two main considerations (protein corona formation and stability of the NPs suspension) it is unlikely that NPs preserve their initial size over time in the body. Large-sized NPs can be easily eliminated from the body through conventional routes. Remaining NPs, if any, can be uptaken, stored and even degraded by cells to limit their bioavailability <sup>116–118</sup>.

Although many NPs exist providing interesting applications in different fields from medicine to catalysis, herein we have chosen to focus on gold, silver and iron oxide NPs. These NPs are chosen as model NPs given their extensive use, especially in biomedical applications; and the great knowledge concerning their synthesis and properties.

## 2.1. Nanoparticle synthesis

NPs can be synthesized by top-down or bottom-up methods. Top-down synthesis consists of breaking down the bulk material until the obtention of nanosized particles, such as ball-milling, laser ablation and lithography.

Bottom-up synthesis is performed by building up the nanomaterial atom by atom or molecule by molecule. Bottom-up methods include chemical precipitation, sol-gel processes and micellar and inverse micellar synthesis, hydro/solvo-thermal methods, etc <sup>119</sup>.

A standard and consistent synthesis method for all metal NPs has not yet been found to our knowledge. However, the most described procedures focus on a bottom-up approach: the reduction of metal ions to their neutral stage. The main components needed to synthesize metal



NPs in this way are: (i) a metal salt, acting as an ion source; (ii) a reducing agent; (iii) a solvent and (iv) a stabilizing agent to avoid NPs aggregation. Both the reducing and stabilizing agents play a key role for the control of the size and shape of the obtained NPs, which, as stated earlier, has an important effect on their final properties. Different methods and a variety of molecules have been used as reducing agents for metal NPs synthesis. The Turkevich reaction for gold NPs synthesis is probably the most well-known reaction in the field <sup>120</sup>. This simple reaction is done at room temperature and uses citrate as both a reducing and stabilizing agent. The result is spherical NPs with a tunable diameter of 10 to 100 nm.

Other methods are employed in the case of metal-oxide NPs such as alkaline co-precipitation. For example, iron oxide NPs can be synthesized by adding a mix of  $\text{Fe}^{3+}$  and  $\text{Fe}^{2+}$  ion salts into a basic solution with a controlled flow, which allows control of particle size and shape <sup>121</sup>.

## 2.2. Noble metal nanoparticles

Noble metal NPs are of particular interest in materials because the reduction of material needed allows decreasing costs and lower its environmental impact. Many noble metal NPs are currently used in several applications such as catalysis, biomedicine, environment depollution or electronics.

### 2.2.1. Gold nanoparticles

Gold NPs (Au NPs) are probably the most well-known type of NPs since the preparation of the colloidal “ruby” gold by Michael Faraday in the 19<sup>th</sup> century. Their synthesis is well described in the literature, and is mainly based on the Turkevich reaction, described above. Several variations of the Turkevich reaction or other protocols have been described since then, the main interest being that gold NPs size and shape can be easily tuned by tuning the reaction conditions and the stabilizers. These NPs are used in many fields, from medicine (imaging, diagnostics, therapeutics) to electronics, essentially due to their unique reactivity and optical properties emerging only at the nanoscale. The main property that drives the interest for gold NPs is the Localized Surface Plasmon Resonance (LSPR) effect.

#### 2.2.1.1 Surface Plasmon Resonance effect (SPR)

SPR effect occurs when NPs are small enough to behave as a single domain. In this case, when an electromagnetic field is applied the NPs free electrons oscillate in the same manner than the electrons of the electrical field (Figure I.10 A). This phenomenon is called localized surface enhanced resonance (LSPR). LSPR results in two main effects: (i) and extremely enhancement

of the electromagnetic field in the surface of the NPs; and (ii) an optical extinction at the plasmon resonance frequency. The latter effect occurring in the visible wavelength for noble metals. LSPR being greatly influenced by size and shape (Figure I.10 B), many studies have been based on the ability to control these two parameters for gold NPs <sup>122</sup>.

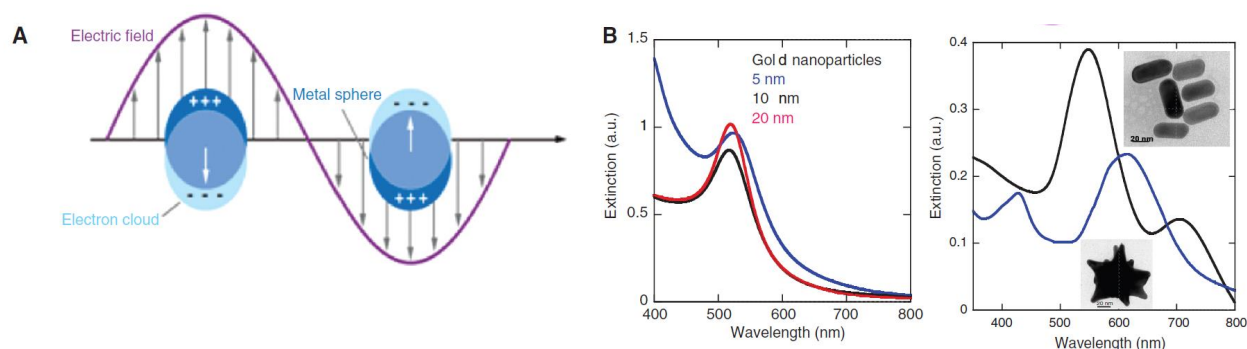


**Figure I.10.** Gold Nanoparticles LSPR effect. (A) Schematic representation of LSPR effect on NPs surface. (B) Influence of NPs size and shape over the LSPR effect. From Szunerits *et al* 2014<sup>123</sup>.

### 2.2.1.2 Applications

Although not as efficient as other NPs, antibacterial properties have been attributed to gold NPs. The mode of action of gold NPs has been elucidated through transcriptomic and proteomics <sup>124</sup>. The authors found that antibacterial action of gold NPs mainly relies on two different mechanisms: (i) changing the cell membrane potential and (ii) inhibiting the ribosomal subunit necessary for tRNA binding. The first mechanism results in an inhibition of ATP synthase, and therefore a general reduction of cell metabolism. The second leads to the stopping of all biological processes within the cell.

The antibacterial mechanisms of many antibiotics and metals include reactive oxygen species (ROS) formation, leading to cell death. Interestingly, no ROS-related process appears in the antibacterial action of gold NPs. This may be the reason why gold NPs are not as toxic for mammalian cells as other metal NPs.

Photothermal therapies can also be achieved by gold NPs as they can be easily excited and locally increase their temperature, inducing surrounding cell death <sup>116</sup>. This therapy relies on the increased sensitivity of tumoral cells to high temperatures. Therefore, at a given temperature, healthy cells can resist while tumoral cells die. For example recently, raspberry-like gold NPs have been synthesized <sup>125</sup> and their heating efficiency under 680 nm, 808 nm and 1064 nm laser irradiation (with higher tissue penetration) was demonstrated.

On the other side, due to its low toxicity <sup>116</sup> and X-ray attenuation capacity, gold NPs have been largely used as a contrast agent for computed tomography (CT). CT is a non-invasive

bioimaging technique broadly used in the biomedical field. However, only bones are enough dense to be clearly visible by this technique.

Gold NPs can easily be functionalized with biological molecules due to their efficient interaction with thiol groups. This provides to gold NPs specific features that may be explored when NPs are used for targeting tumor cells, or for diagnostics. For instance, the functionalization enables the realization of colorimetric assays based on a controlled NP aggregation in the presence of the molecule to be detected. If gold NPs are functionalized with antibodies, they can specifically aggregate in the presence of the antigen, resulting in a visible color change from red to blue or purple <sup>126,127</sup>.

Gold has also been used for sensing through a signal amplification, owing to their unique electrochemical and optical properties. They can simply be applied on the surface of the sensor to increase its sensitivity (by increasing sensor conductivity), or used as signaling probe. The best example of the utilization of Gold NPs in sensing is their use as effective surface-enhanced Raman spectroscopy (SERS) substrates. SERS is a highly sensitive technique that can enhance Raman scattering of molecules adsorbed at the surface due to NP LSPR properties. Therefore, Gold NPs (as well as silver NPs) are attractive candidates for the development of biosensors <sup>128</sup>.

Finally, gold NPs can be used as a catalyst. <sup>129,130</sup> It is worth reminding that nanosized catalysts are of special interest given their high surface area. The higher the surface-to-volume ratio, the lower the amount of catalyst needed to achieve the same catalytic activity. Today gold nanocatalysts are considered as catalysts of choice in fine chemical synthesis for many reactions such as oxidation, reduction, epoxidation, or hydrochlorination <sup>131,132</sup>. Gold NPs are therefore also extensively used for environmental applications such as dye removal in wastewater <sup>133</sup>.

### 2.2.2. Silver nanoparticles

Like gold NPs, silver NPs show a characteristic SPR effect. However, there is no standard way to synthesize these NPs yet. Most synthesis protocols are based on the reduction of silver salts to successfully form silver NPs. Although all the knowledge from gold NP synthesis has been applied to the synthesis of silver NPs, two main challenges remain unsolved.

The first issue that needs to be addressed is the high polydispersity of most silver NP dispersions. Indeed, many syntheses are still unable to control NP size and shape, resulting in a high polydispersity. In addition, the presence of different NP shapes is observed in many situations.



The second drawback relies on the higher reactivity of silver compared to gold. This phenomenon has a direct effect over NP colloidal stabilization over time. This problem can be solved with a better understanding of the interactions of the silver NPs with the environment, as well as an in deep study of the stabilization agents used.

### 2.2.2.1 Applications

Silver has long been known by its antibacterial action. In the past, silver cutlery and water vessels were used to avoid microbial infections, preserving beverages and food <sup>134</sup>. Hippocrates was the first to document the use of silver in medicine. The use of silver as an antibacterial agent has decreased drastically with the arrival of antibiotics. However, the widespread use of these powerful molecules has led to the apparition of antibiotic-resistant bacterial strains. Therefore, the use of silver for antibacterial applications has experienced a gradual revival in recent years. Now, silver is becoming the main alternative to antibiotics. Silver NPs have been proven to have a broad spectrum action against gram positive and gram negative bacteria <sup>135,136</sup>, biofilms <sup>137</sup>, multidrug resistant bacteria <sup>138</sup>, fungi <sup>139,140</sup> and even some virus <sup>141</sup>.

Although some metal ion transporters have been found in bacteria <sup>142</sup>, the apparition of complete microbial resistance to silver has not yet been reported, and seems to be difficult to develop due to the interactions of silver with many different cell components <sup>143</sup>.

The mechanisms of antibacterial activity of silver NPs are not yet clearly elucidated. However, two main hypotheses are reported. The first hypothesis states that the main antibiotic activity is achieved by  $\text{Ag}^+$  ions that are released from silver NPs <sup>134,144</sup>. These released ions either adhere to the cell wall or are taken up by the microorganism. Once in contact with proteins and DNA, silver ions seem to interact with sulfur-containing amino acids and base pairs, respectively. The second hypothesis involves a direct interaction between NPs and microorganisms. Some studies have proven that some silver NPs can *anchor* in the bacteria cell wall, disrupting its organization. This adhesion can be tuned by modifying the  $\zeta$ -potential of NPs <sup>145</sup>.

Both, silver ions and given NPs, can interact with the cell membrane, proteins and DNA. These interactions result in cell leakage and loss of the proton gradient (due to cell wall break); protein dysfunction; DNA damage, ROS production and finally cell death. A schema resuming all these interactions is found in Figure I.11.

However as previously stated, the properties of NPs highly depend on size, shape and surface chemistry; therefore, these results are not transposable to all silver NPs but only to the ones tested within these studies. As an example, Morones *et al* <sup>135</sup> found that NPs 1-10 nm attached

to the cell wall with higher affinity than larger NPs and suggested that this was due to the higher surface to volume ratio. In another study NPs from 5-21 nm were tested and similarly found that smaller NPs had a stronger bactericidal effect.<sup>146</sup> In addition, they compared the NPs action to AgCl clusters and Ag<sup>+</sup> ions and found NPs to be the most effective antibacterial form of silver.

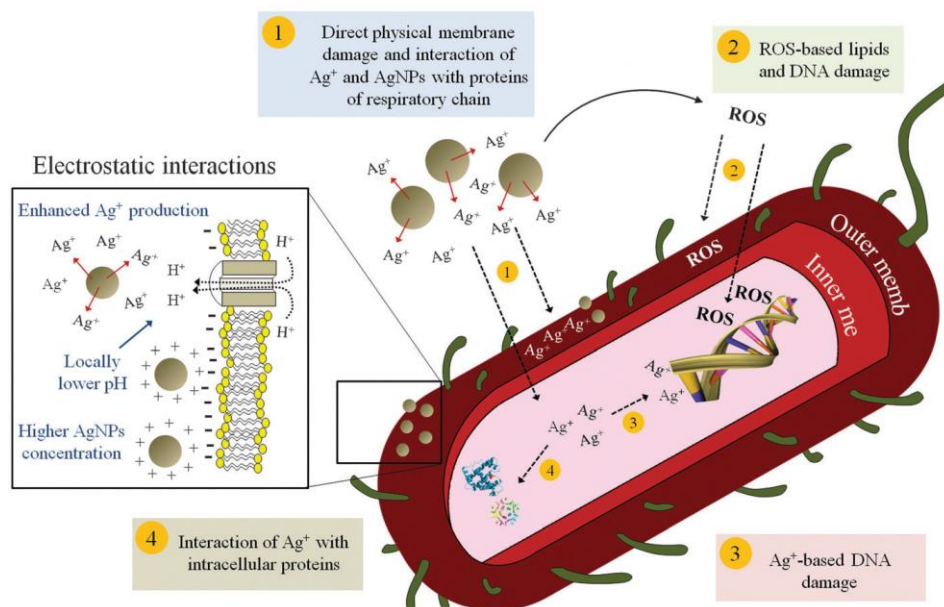


**Figure I.11.** Ag NPs antibacterial mode of action. From Rizello *et al* 2014<sup>142</sup>.

Silver has been initially used in its ion form for biomedical applications. For example surgery cloths and wound dressings, such as, Tegaderm Ag®, Aquacel Ag®; containing silver are commercially available and greatly used<sup>7</sup>. However silver ions can be toxic at high concentrations, therefore the national institute for occupational safety and health (USA) recommended a permissive exposure limit of 0.01 mg/m<sup>3</sup> to all forms of silver<sup>147</sup>. However, great controversies exist regarding the toxicity of silver NPs, as this property depends on their size, shape and surface functionalization. To our knowledge, no silver NP toxicity has been proven except the one resulting from the release of Ag<sup>+</sup> ions. It is important to note that, when studying silver NPs, it is very hard (if not impossible) to differentiate Ag<sup>+</sup> from silver NPs. For example, when silver concentration is verified by Inductively Coupled Plasma (ICP) techniques all types of silver are quantified.

For this reason, and thanks to the progresses gained in nanosciences and nanotechnologies, silver NPs are substituting silver ions in biomedical applications. Acticoat® is, for instance, a commercially available wound dressing containing nanocrystalline silver<sup>144</sup>. Nevertheless,

when using silver NPs as antibacterial agents in the human body, silver ion release should be tailored and reduced to avoid cytotoxicity.

As with gold NPs, the presence of the SPR effect for silver NPs renders them interesting for electronics, sensing and optical applications. In the electronic field, the conductive nature of bulk silver is enhanced in the nanoparticulate form. This property results in the possibility of miniaturizing electronic circuits as well as increasing their performance. In addition, silver NP inks and silver nanowires are used as conductive elements in flexible electronic devices<sup>148</sup>. In the sensing field, the aggregation or destruction of silver NPs in the presence of  $\text{Mn}^{2+}$  and  $\text{Hg}^+$  ions, respectively, can be used to detect these metals in water<sup>149</sup>. In another study, silver NPs were used as DNA protective agent against irradiation damage<sup>150</sup>. Nevertheless, gold NPs are usually preferred for these applications due to their higher stability, easy and controlled synthesis and similar results.

Finally, silver NPs are also used in environmental remediation applications as they possessed also catalytical properties allowing the degradation of several pollutants in water<sup>151</sup>.

### 2.3. Iron oxide nanoparticles

Iron oxide NPs are of special interest because of their magnetic properties that differ from the bulk material. Similar to the LSPR effect for gold or silver NPs, iron oxide NPs present superparamagnetic behaviors in the nanoscale range (NPs of diameter below 20-30 nm). Because of their small size, these NPs act as single domain particles. They are magnetized in a uniform manner, with all the spins aligned in the same direction when a magnetic field is applied<sup>152–154</sup>. Again, the magnetic properties of iron oxide NPs strongly depend on their size and shape, as well as their crystalline state<sup>154,155</sup>.

NPs stabilization plays an important role in magnetic NPs since aggregation is enhanced by the magnetic attraction. Paramagnetic materials are preferred in many applications as their magnetic behavior limits NPs aggregation when no magnetic field is applied. Superparamagnetic properties appear when NPs are small enough. In fact, their magnetic behavior goes from ferromagnetic to superparamagnetic as the NPs diameter decreases.

The use of iron oxide NPs in the biomedical field is possible due to their low toxicity and biocompatibility. NPs toxicity and biocompatibility is strongly dependent on the surface functionalization. Iron oxide NPs can be produced by some bacteria and are used as a geomagnetic orientation system.<sup>156</sup> They have also been found in human cells although their

origin is not known.<sup>157</sup> These findings suggest no toxicity of these NPs. Furthermore, it has been proven that iron oxide NPs are internalized by cells and stored in endosomes suggesting a detoxification mechanism. Surprisingly Van de Walle *et al*<sup>118</sup> found that mesenchymal stem cells (MSCs) were able to internalize magnetite NPs into endosomes, degrade them to soluble iron forms and further resynthesize magnetite NPs. This process is dependent of MSCs differentiation state as it depends on the expression of several genes implicated on iron metabolism procedures.

### 2.3.1. Applications

Because of their magnetic properties and their relaxation times, iron oxide NPs are very good candidates for magnetic resonance imaging (MRI) contrast agents. Iron oxide NPs are a type T2 contrast agent resulting in a black contrast.

Iron oxide NPs are also used for protein, molecule or cell separation thanks to their magnetic properties<sup>152,158</sup>. The right functionalization on iron oxide NPs can enable the specific interaction with the desired molecule. This method is cheap and simplifies all the purification process avoiding chromatography steps. For example, a polymer conjugated with magnetic NPs has been successfully used to specifically purify IgG from a complex biological media<sup>159</sup>.

The possibility to induce iron oxide NPs accumulation in a located region by applying an external magnetic field in the desired area makes them also a very good candidate for targeted drug release applications<sup>160</sup>. This accumulation enables a reduction of the drug dose and reduces its side effects due to none or little systemic concentration.

The application of an external magnetic field to iron oxide NPs can be used as well for hyperthermia therapy. Iron oxide NPs are able to transform the magnetic field energy into heat. This therapy has been successfully used in treating glioblastoma tumors in animal models, resulting in a decrease in cell viability of 52% in the tumor region<sup>161</sup>.

Both gold and iron oxide NPs can be used as theragnosis agents enabling a diagnostic by imaging and therapy by hyperthermia. Interestingly, Liang *et al*<sup>162</sup> combined both targeted accumulation and hyperthermia capacities. They created a magnet into a tumor and magnetized it by applying an external magnetic field. Because of the intrinsic magnetic field induced by the magnet, magnetic NPs injected intravenously were specifically accumulated in the treated tumor. The presence of the local magnetic field combined with the presence of NPs resulted in a thermal ablation of the tumor.

Further applications have been proven in the literature for iron oxide NPs such as tissue adhesion by nanobridging<sup>163</sup>. Iron oxide NPs were simply placed into a skin and a liver wound and strong tissue adhesion was found in both cases. The resultant scars are aesthetic leaving no mark, which is of high interest for facial surgeries among others. These results suggest that nanobridging is a promising technique not only for iron oxide and silica NPs but it could also be applicable for silver NPs in skin wounds for example.

Iron oxide NPs have been used as well to induce mechanical stimulation in cells for tissue engineering applications. Mechanical stimuli being crucial for cell differentiation, the ability to control these stimuli is of great interest. In this field, the internalization of iron oxide NPs into cells has been used to direct cells deeper into engineered scaffolds<sup>164</sup>.

Finally, iron oxide NPs are broadly studied as sorbents of organic and inorganic (heavy metals) pollutants in water and wastewater. In addition to their interesting recycling properties owing to their magnetic properties their molecular oxygen activation performance is also brought forward to explain their interest<sup>165</sup>.

### 3. Silk-based bionanocomposites

The detailed description, given above, regarding silk-based materials, on one hand, and inorganic NPs, on the other hand, demonstrates the promising potential of combining silk and NPs for the design of bionanocomposites with tailored properties and functions. Composite materials enable the properties' combination of several materials as well as the apparition of new properties. These acquired properties render composites very interesting in the materials field. Composites can reach and outperform bulk materials properties with a lesser quantity of the initial material. This reduction results in a production cost reduction in many cases. However, conventional composites consisting on the reinforcement of the properties of a given material, by the combination with others, may results in the loss of important properties<sup>166</sup>.

Nanocomposites consist in the combination of several materials from which at least one is nanosized (<100nm). In contrast to classical composites, nanocomposites reduce the loss of desirable properties found in the original material. Nanocomposites are of great interest as the nanosized material can be added in very little proportions due to its high surface to volume ratio. Nanocomposites can present new properties that are not achieved in classical composites with the same materials. Bionanocomposites are nanocomposites containing a biological material such as collagen, cellulose, alginate or silk. They are developed to replace many tissues, such as tendon<sup>167</sup>, corneal stroma<sup>168</sup>, bone<sup>169</sup> and dermis<sup>170</sup>.

However, the resultant properties brought by NPs are only effective if they are homogeneously distributed within the resultant material. Therefore, when developing any type of nanocomposite, it is crucial to take into account the NPs surface chemistry, stabilization within the bulk material and homogeneous distribution. As previously explained (*see section 2*) NPs stabilization can be easily altered by changing their environment such as ion concentration. Mixing NPs with another material results in a new environment so it is not surprising to observe NPs aggregation and precipitation within the material. These considerations are very important for silk bionanocomposites as in this case silk gelation can easily occur as well due to NPs addition to the dispersion.

Generally, the design of bionanocomposites may be achieved by mechanical mixing or *in situ* synthesis of NPs without or with crosslinking agents<sup>171</sup>. Regarding, silk materials, three different methods were found in the literature. *In situ* synthesis has been largely studied using many different reducing agents. Some studies even proved the ability of silk to reduce metal ions by itself<sup>172–174</sup>. Although this approach reduces the number of steps needed to produce the bionanocomposite, the resultant NPs can be very polydisperse in size and shape. Moreover, the surface chemistry of these NPs is unknown. Altogether, the impossibility to control these parameters could result in unpredictable properties and toxicity, which are highly dependent on the characteristics of the NPs.

A better control of the NPs characteristics can theoretically be achieved by synthesizing them upstream and incorporating them posteriorly into silk materials. However, in these cases it is very important to stabilize NPs in suspension by controlling their surface chemistry. In many situations, the direct incorporation of NPs into the silk regenerated dispersion can induce silk gelation.

Finally, some studies have focused on feeding the desired NPs directly to silkworms expecting them to be found later in the silk cocoons. Despite the proven feasibility of this methodology, its low efficiency (due to NP biodistribution within the silk worm) and the requirement to spread NPs into the worm's environment limits their use<sup>175</sup>.

Silk bionanocomposites is a new technology in constant development. In the following sections, an overview of the silk-based nanocomposites obtained by embedding nanomaterials (mainly inorganic NPs) is presented. We choose here to classify the silk nanocomposites by their potential applications.

### 3.1. Antibacterial activity

The protein nature of silk materials makes them an easy target for bacterial and fungus colonization. The incorporation of antibacterial NPs into silk tissues is, thus required as it allows a better conservation of such luxury cloths, and reduces the apparition of bad odors. In the biomedical field, the presence of such NPs avoids, or at least delay, the apparition of infections.

Among the existing NPs, silver NPs are largely the most used for antibacterial applications, as described above. Although most of the efforts have been dedicated for silk textiles, other silk materials have been functionalized with silver NPs. Several authors have developed *in situ* synthesis of silver NPs into silk materials. For this purpose, UV irradiation was used to synthesize silver NPs directly in silk dispersions<sup>176</sup>, films<sup>177</sup>, sponges<sup>178</sup>, fibers, textiles and electrospun mats<sup>16,176–182</sup>. *In situ* synthesis of NPs into silk textiles was not uniform over the silk fibers. This may be due to a different silver ion adsorption, depending on silk chemical groups available. Silver ion release was studied for electrospun mats and was found to be dependent on the  $\beta$ -sheet content. While both materials acquired antibacterial activities, only the electrospun materials with low  $\beta$ -sheet content resulted in a cytotoxic effect. This result agrees with the known toxicity of silver ions discussed in *section 2.2.2*.

In another study, light was used as a reducing agent for the *in situ* synthesis of silver NPs into a silk dispersion<sup>183</sup>. The resultant dispersion was mixed with Carbopol 934, which acted as a gelling agent. However, although the antibacterial activity of the silver NPs/silk dispersion was proven, no tests were performed for the gel nanocomposite. The topical application of this gel in animal skin wound models resulted in a faster wound closure rate in comparison with silk, silver NPs and Carbopol gels and Soframycin gel, a commercially available product. These results support the idea that silk enhances wound closure. In addition, a difference was observed between silk and silver NPs/silk gels, suggesting a synergistic effect of both components in wound healing.

Silver NP-loaded silk hydrogels have been also used for bone regeneration<sup>181</sup>. Silver NPs were *in situ* synthesized using light as a reducing agent as well. A strong antibacterial activity was obtained for hydrogels containing more than 0.5% silver NPs. Biocompatibility was assessed by seeding osteoblast cells on the hydrogels. A silver NPs concentration-dependent decrease in cell viability was observed.

*In situ* NP synthesis in silk materials has also been developed using natural molecules such as caffeic acid, flavonoids, vitamin C, citrate, *R. apiculata* leaves extract, *Streptomyces* cell extract

or honeysuckle extract as reducing agents<sup>184–190</sup>. Once again, the resultant materials had acquired antibacterial activities and no cytotoxic effects were detected. Interestingly, the materials synthesized using caffeic acid had a UV irradiation protection role. This result suggests a new application in sun protective cloths of silver containing textiles.

Silk sponges and films containing silver NPs have been developed as well<sup>191,192</sup>. In this case NPs were synthesized in the SF dispersion used to prepare such materials. Interestingly they proved that silk alone was able to reduce  $\text{Ag}^+$  into  $\text{Ag}^0$  efficiently to form silver NPs. The reduction ability of SF, sericin and peptides has been used as well by many authors<sup>172–174</sup>. However, all these *in situ* synthesis procedures resulted in NPs with uncontrolled sizes and shapes. These two parameters are crucial to evaluate NPs properties. In addition, no information about NP surface chemistry and the presence of remaining toxic silver ions were given in these cases. Altogether, materials obtained by this methodology may not possess the desired property (antibacterial in this case), because of a low reproducibility, and may even present undesired properties or effects (such as toxicity) for the final application.

As alternative, other studies have focused on mixing already synthesized NPs with silk<sup>193,194</sup>. For example, Gulrajani *et al*<sup>194</sup> studied a two-step silk fabrics functionalization with silver NPs. The latter were synthesized and then silk fabric was soaked into silver NPs suspension. The authors studied the effect of pH on the NP uptake, revealing that NPs are more effectively adsorbed into silk in acidic media. Furthermore, the authors reported that the silk uptake with NPs is temperature dependent as well. Silver NPs were better adsorbed into silk fabrics at the lowest temperature (40 °C) and that adsorption decreases as temperature increases (up to 80 °C).

In a more recent study, a two-step method was developed to functionalize silk fabrics with silver NPs<sup>186</sup>. Interestingly the resulting materials were able to inhibit the growth of both *E.coli* and *S.aureus* even after 30 washes, suggesting a strong bond between silk and silver NPs. However further tests are required to evaluate the release of silver ions and NPs.

Other studies have focused on the antibacterial activity of gold<sup>174,181,195</sup>, platinum<sup>196</sup>, copper oxide<sup>197</sup>, zinc oxide<sup>198</sup>, cerium oxide<sup>199</sup>, selenium oxide NPs<sup>200</sup>. An *in situ* synthesis of gold NPs into a HAP containing silk hydrogel was carried out by Ribeiro *et al*.<sup>181</sup>. Once the hydrogel formed, gold NPs were synthesized by heating the solution up to 60 °C. Interestingly, a significant antibacterial activity was observed against *S. aureus* (MSSA and MRSA), *E. coli* and *P. aeruginosa* but not against *S. epidermidis*. Similarly, Tang *et al*<sup>195</sup> obtained silk fabrics with *in situ* synthesized gold NPs by heating to 85 °C. The result was an antibacterial, UV



irradiation blocking and thermal conducting tissue very interesting for textile applications. However, as for silver NPs, *in situ* synthesis does not allow a control of the NP size.

### 3.2. Tissue engineering

In the biomedical field, different NPs containing silk materials have been developed for tissue engineering. Gold NPs can be incorporated into the silk electrospinning dispersion to obtain silk nanofibers with well dispersed NPs by traditional<sup>201</sup> and wet<sup>202</sup> electrospinning techniques. In both cases, incorporation of gold NPs into electrospun silk materials results in an increase of mechanical properties. *In vitro* tests showed no cytotoxicity and a good cell attachment to the scaffolds. In addition, cell attachment can be enhanced by functionalizing gold NPs with the integrin binding peptides RGD<sup>201</sup>. The resultant materials were tested *in vivo* by Akturk et al<sup>202</sup> for wound closure. Although no significant difference was seen between silk with or without gold NPs further tests are planned to be carried out with higher NPs content.

The incorporation of gold NPs into silk scaffolds has been also used to increase material conductivity. Electrical stimuli being crucial for nerve and cardiac tissues, this modification greatly impacts these tissue regeneration processes. For example, electrospun silk containing gold NPs materials have been rolled into a conduit to replace sciatic nerve *in vivo*<sup>203</sup>. As a result, gold-containing silk materials outperformed pure silk materials in term of nerve regeneration. In another study, the presence of gold NPs in silk materials allowed a better mesenchymal stem cell differentiation towards cardiac lineage<sup>204</sup>.

Most of the silk-based bionanocomposites developed for biomedical applications have focused on bone tissue regeneration. Because of its osteoconductive properties, silk materials containing hydroxyapatite (HAP) have been extensively studied. Nanocomposite scaffolds made of silk and HAP are particularly interesting due to the ability of silk to “regulate” the mineralization of calcium phosphate compounds, presumably through chemical interactions involving silk chemical groups<sup>205,206</sup>.

A true bone replacement was developed by Ribeiro *et al.*<sup>52</sup>. They created a silk hydrogel functionalized with HAP NPs. HAP is a calcium phosphate widely used in bone tissue engineering as its composition is very close to the mineral phase constituting bone tissues. *In vitro* experiments proved that the nano-HAP-containing materials enhanced the expression level of the osteoblastic phenotype of an osteoblast-like cell line and cell metabolic activity. Their main challenge was to avoid nano-HAP aggregation during silk gelation. The material containing 15 % HAP showed a homogeneous dispersion of nano-HAP over the silk hydrogel

with no visible aggregation. The aggregation state of nano-HAP remains, however, the main constraint for the design of a silk-based material with a higher nano-HAP content.

Adequately matching the morphology of the implant and the surrounding bone is crucial for the proper integration of the implant in the surrounding bone. Recent work has focused on using or tuning the rheological properties of silk/HAP-based pastes for 3D printing applications. These approaches allow the formation of biomimetic and macroporous silk/HAP nanocomposite scaffolds. Using sodium alginate (SA) as a binder, Huang et al. were able to 3D print scaffolds with large, interconnected pores and a relatively high compressive strength. Human bone marrow-derived mesenchymal stem cells (hMSCs) seeded on the scaffolds adhered, proliferated and differentiated toward an osteogenic lineage<sup>207</sup>. In addition to scaffold-based applications for bone regeneration, Heimbach et al. successfully developed a silk/HAP/polylactic acid composite for the fabrication of high strength bioresorbable fixation devices, presenting promising properties for clinical applications in orthopedics<sup>208</sup>.

Although to a much lesser extent, other NPs have been incorporated into silk materials for bone tissue engineering. For example TiO<sub>2</sub> NPs or GO have been used to increase the mechanical resistance of silk sponges and hydrogels<sup>209–211</sup>. Magnetic NPs have interesting properties that can be used to apply a magnetic stimuli to cells and tissues<sup>212–215</sup>. Recently Aliramaji *et al*<sup>212</sup> developed a silk chitosan magnetite bionanocomposite scaffold by freeze casting. They found that the addition of magnetite NPs to the silk/chitosan scaffold did not change its porous structure. Interestingly, no magnetite release was detected in a PBS solution after 48h proving the stability of NPs into the scaffold. The combination of magnetite NPs within the scaffold together with the static magnetic field applied resulted in no osteosarcoma cell cytotoxicity and increased cell attachment (Figure I.12 A).

Overall, the results described above demonstrate the potential of NPs incorporation as a tool for material functionalization (by improving mechanical properties for example), but also to serve as biochemical cues for the surrounding cells, as evidenced here in the context of bone tissue engineering. As our understanding of mechanisms and signaling pathways progresses, the regeneration of complex tissues may benefit from combinations of NPs, or spatial patterning to better induce regeneration.

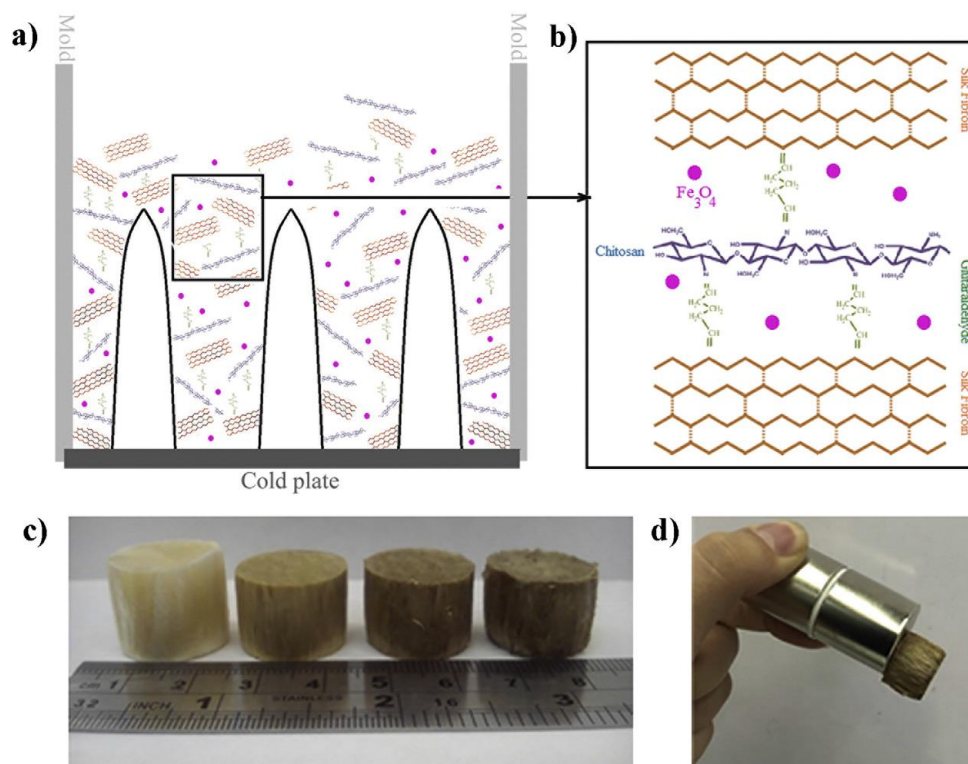


**Figure I.12.** (a) The schematic illustrates the freeze-casting technique showing the sublimation of the solidified solvent, and then densification of the walls, which result in a porous structure with unidirectional channels where pores are the ice crystals. (b) Magnified illustration of the chemical structures occurs in the scaffold solution. (c) The fabricated scaffolds; as can be seen a color variation is clearly shown, due to the different amounts of nanoparticles used in the scaffolds. (d) Attraction of the magnetic scaffold to a permanent magnet. From Alirajami *et al* 2017 <sup>212</sup>.

### 3.3. Hyperthermia

Hyperthermia is an adjuvant therapy for cancer stirring great interest as it theoretically allows for a localized treatment. Hyperthermia uses various external energies, such as magnetic field, microwave, ultrasound, infrared radiations, to locally increase the body temperature and therefore destroy tumor cells. The heaters can be plasmonic or superparamagnetic NPs <sup>216,217</sup>.

Among hyperthermia modality, phototherapy is a very interesting noninvasive therapy, in which light is used to induce local cell death. Due to the intrinsic light absorption of biological tissues, photothermal therapies can be only achieved in the near infrared region (NIR). State-of-the-art photothermal agents, namely gold nanorods and nanostars, are not efficient in the NRI II transparency window.

In a recent study, Wang *et al* have developed silk nanofibers containing gold NPs <sup>218</sup>. The assembly of NPs into a specifically manner results in a broader absorption of light at the NIR and a red shift of the maximum. As a result, gold NPs containing silk nanofibers reached a higher temperature than gold NPs alone under the same conditions. Therefore, the ability to

pattern how and where NPs adhere silk materials may result in an increased efficiency as it was shown than confinement of gold NPs as an impact on their photothermal ability <sup>117</sup>.

Differently, injectable silk hydrogels containing gold NPs have been developed for photothermia treatments of infections <sup>219</sup>. Silk hydrogel was obtained by vortexing a silk dispersion in which gold NPs can be incorporated. The obtained hydrogel was injected in the infected site and heating production was promoted by laser exposition. Interestingly heat was produced locally and was able to reduce bacterial population, reducing infection. The silk hydrogel assured the spatial stabilization of the gold NPs at the injection site (Figure I.13).

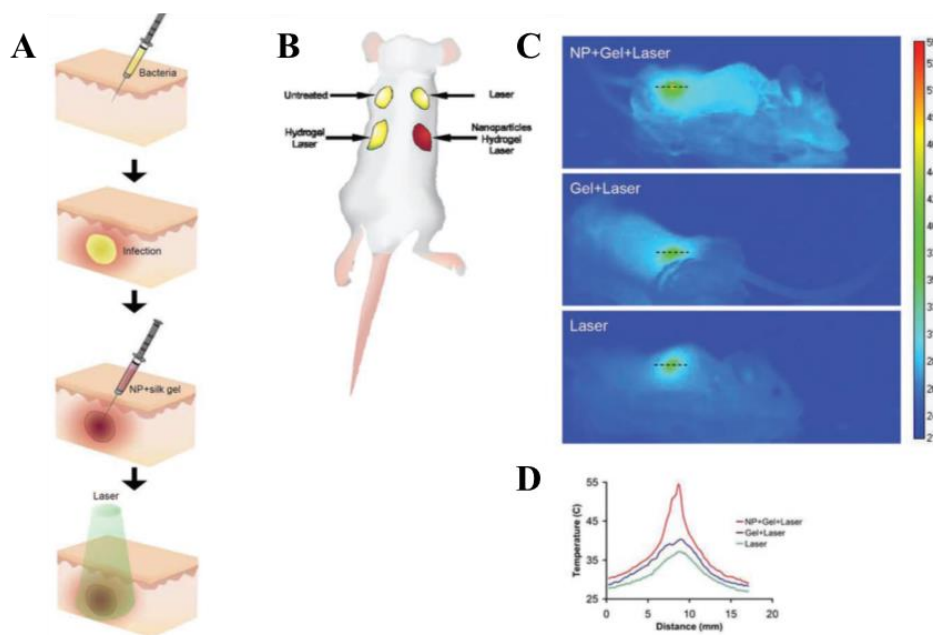


**Figure I.13.** *In vivo* experimental schematic and temperature mapping. (A) Schematic of subcutaneous injection procedure. Infection was allowed to fester for 24 h after bacterial injection. (B) Layout of the four infection sites (red represents color of gel + NP composite). (C) Temperature map of the three infection sites receiving laser treatment (power 150 mw, exposure time 10 min). NP concentration was 40 ×. Graph: temperature profile les corresponding to dashed black lines. Scale bar in ° C. From Kojic *et al.* 2012 <sup>219</sup>.

Light penetration limitations into biological structures can be overcome by using a magnetic field for hyperthermia treatments. In this case magnetic nanoparticles are usually placed in the treatment zone and produce heat under an external magnetic field <sup>220</sup>. Injectable silk hydrogels have been formulated for intratumoral injection <sup>221</sup>. The application of a magnetic field successfully enabled deep tumor ablation while no damage was observed in surrounding tissue. Furthermore, the magnetic field can be used to direct the material to the target spot, reducing systemic distribution of the magnetic NPs.

### 3.4. Imaging

The possibility to follow up silk implants by non-invasive imaging can be achieved by introducing fluorescent or contrast agents. As an example, the introduction of iron oxide NPs into silk materials allows the use of MRI to visualize them *in vivo* <sup>221</sup>. Another approaches used NIR emitting NaYF<sub>4</sub>@SiO<sub>2</sub> NPs that were synthesized and then directly feed to silk worms <sup>222</sup>. The resultant silk materials obtained from the silk cocoon were clearly visible by NIR II imaging once implanted into mouse. Similarly Fan *et al* fed silk worms with fluorescent carbon nanodots resulting in the obtaining of fluorescent silk fibers <sup>223</sup>. Although the materials showed no cytotoxicity, their fluorescent capacity was not evaluated *in vivo*. These results are encouraging for the *in vivo* monitoring of silk implants. Interestingly this ability will allow the follow up of the degradation or possible breaking of such implant without the need of extra surgery.

### 3.5. Electronics and sensing

The transparency, flexibility but resistant, biodegradable and biocompatible properties of silk have been used in many cases to develop wearable electrodes and sensors. In many cases, NPs are incorporated into a support to increase detection sensibility.

As for hyperthermia, gold NPs-containing silk materials have been coupled to thermoelectric chips. By doing so and incorporating the chip into an implantable device, light can be used as an energy source. However, optimization is still needed to see these devices in our daily life <sup>224</sup>.

Silk sensors have been developed to detect ammonia <sup>225</sup> and immunoglobulin G <sup>226</sup>. For example the detection of ammonia has been done with *in situ*-synthesized gold NPs into a silk dispersion with UV-B light as reducing agent <sup>225</sup>. Interestingly the authors found that the UV absorption of gold NPs decreased as the ammonia concentration increased. However, no control of the size and shape NPs was observed, as evidenced by the presence of different shaped NPs. NPs absorbance being dependent on this parameter, absorption differences can be observed from NPs batch to batch. Silk materials have also been used to protect enzyme-mediated biosensors of hydrogen peroxide <sup>227</sup> and methyl paraoxon, carbofuran and phoxim <sup>228</sup>.

Due to their surface plasmon, gold NPs-embedded silk films have been developed to enhance Surface-Enhanced Raman Spectroscopy (SERS) signal <sup>229</sup>. They found that the signal enhancement factor by the produced silk/gold NP films was around 150-fold. However, the authors found that the light absorption of gold NPs was influenced by the presence of the silk,

and red shifted by 20 nm. This result indicates a silk-induced change in the optical properties of gold NPs. They suggested that this effect was due to the different refractive index of silk and aqueous solution and showed a better fit with experimental data when silk's refractive index was used. Their results suggest a strong capability of these films to be used as biosensors. These results are in agreement with the ones found by Liu *et al* on their *in situ*-synthesized gold NPs silk fabrics <sup>230</sup>.

Silk hydrogels containing carbon nanotubes have also been successfully developed to respond to mechanical stimuli <sup>231</sup>. The resultant composite was able to sense pressure variations, bending and compression forces. These abilities are interesting for medical applications such as arterial pressure monitoring and intracranial pressure. The authors successfully integrated gold NPs into the system, resulting in a laser-mediated degradation system due to heat production. Altogether the silk hydrogel was able to trigger a laser exposition-mediated degradation when detecting epileptic episodes (mechanical stimuli). The incorporation of drugs into the hydrogel allows then a controlled therapy in the required moment.

Differently, Ma *et al* were able to print microcircuits in a silk/GO-based paper in a large-scale manner <sup>232</sup>. The possibility to have a well-designed circuit structure allows the fine-tuning of the electrode response to external stimuli such as relative humidity changes or proximity sensing. In another study, silk materials were used to prevent fluorescence quenching due to quantum dot (QD) aggregation. The immobilization of CdTe QDs increased its fluorescence lifetime and the IgG sensing capability. Silk fibers have also been used to direct the arrangement and *in situ* synthesis of CdS QDs for photoluminescence applications <sup>233</sup>.

Surprisingly Schmucker and his team developed physical and chemical nanotags for anti-counterfeiting applications <sup>234</sup>. They successfully embedded nickel nanodisc structures with or without chromophores, into silk textiles by electrospinning. The unlimited combinations of structure and chromophores enable the creation of multiple tags identifying different products.

### 3.6. Catalysis

Currently, nanocatalysts are largely used for industrial applications due to the increased surface-to-volume ratio, allowing the same catalytic activity than bulk materials but requiring less catalysts. However, because of their nanometric dimensions, their collection for reutilization is particularly difficult. Therefore, there is an increasing interest in immobilizing these nanomaterials into supports. Silk has been used for specific reactions due to its biodegradation

and biocompatible features. The catalysis activities of platinum <sup>196</sup>, gold <sup>191</sup>, palladium <sup>235,236</sup> and iron oxide NPs <sup>59</sup> have been studied into silk materials.

Silk sponges and films containing gold NPs were developed by Das *et al.* for catalysis purpose using the same preparation methodology used for silk materials containing silver NPs (previously explained) <sup>191</sup>. The reduction of 4-nitrophenol catalyzed by gold NPs containing silk materials was proven and characterized in their study.

On the other side, iron oxide NPs were synthesized *in situ* into silk materials by Luo *et al.* who prepared silk hydrogels containing magnetite NPs <sup>59</sup>. A co-precipitation methodology was used to prepare the NPs-embedded silk hydrogel by dipping the hydrogel into a solution containing FeCl<sub>2</sub> and FeCl<sub>3</sub>, and adding ammonium hydroxide to trigger the NPs synthesis. The magnetic and catalytic activities of magnetite were preserved in the obtained silk materials. Such materials could be used in environmental chemistry applications and be easily separated by their magnetic properties; however, their use in biological applications is compromised by the presence of ammonium hydroxide.

Interestingly, the immobilization of palladium nanoparticles into silk materials not only conserved its catalytic activity but also enhanced the chemoselectivity of the hydrogenation catalyzed reaction <sup>235,236</sup>.

### 3.7. Depollution

In addition to the mechanical strength, biocompatibility and biodegradability of silk, this material is also a good absorbent for aromatic dyes. Therefore, the combination of silk's absorbent properties, which are dependent on the pH and dye concentration, with the catalytical activity of several NPs has been explored.

Aziz *et al.* evaluated the combination of silk electrospun nanofilters with TiO<sub>2</sub> NPs for anionic dye removal <sup>237</sup>. Interestingly they found that the absorption capacities of the materials increased as the NPs content increased. When studying the effect of pH they found that a better absorption was achieved at acidic pH. Similarly, silk iron oxide NPs materials were developed for anionic dye removal <sup>238</sup>. The photocatalytic activity of CuO<sub>2</sub> NPs embedded in silk for dye removal has also been explored <sup>239</sup>. Altogether, these results give promising insights into wastewater treatment with a biodegradable material.

Another study has proved the combination of SF with hydroxyapatite to be efficient for water filtration and purification <sup>99</sup>. The obtained material was able to remove dyes and heavy metal ions from solutions, a result that is not achieved with conventional nanofiltration membranes.

Silk can also be mixed with silica to form insulating and fire retardant material <sup>72</sup>. These materials can be easily obtained by a one-step acid catalyzed sol-gel reaction. The resulting silk/silica aerogel shows excellent properties as low density (0.11-0.19 g/cm<sup>3</sup>), high surface area (311-798 m<sup>2</sup>/g), flexibility in compression and fire retardancy.



## 4. Conclusion

Our walkthrough the state of the art left us with no doubt of the versatility of silk fibroin. As proven by many authors, it can be shaped up in many different materials in a tunable manner that allows an easy adaptation to each application. In addition, the possibility to functionalize these materials with NPs raises a world of new properties. Such silk nanocomposites have been largely developed in the literature, for example for antibacterial and tissue engineering applications because of their biocompatibility and biodegradability. Moreover, the great adaptability given by different silk materials and the infinite combinations with nanocomponents have proven to be well-adapted to these applications with encouraging results. On the other side, emerging applications of silk nanocomposites have also been described in many other fields such as catalysis, electronics, imaging and sensing devices. In the future, different combinations of silk/NPs materials may evolve and be developed for other applications. In addition, the increasing concern on climate change and plastic pollution place biodegradable materials such as silk in the spotlight.

However, silk-based nanocomposites still have some drawbacks to overcome and notably in their production. Two main strategies for silk nanocomposite preparation are largely studied in the literature: *in situ* synthesis and the addition of previously synthesized NPs (upstream) to the silk material. *In situ* synthesis methods are promising as they reduce the number of reaction steps needed to obtain the final functionalized material. Although great advances have been done in NP synthesis, no straightforward method exists yet. The synthesis of NPs needs to: (i) have perfect control over size and shape which influence their properties; (ii) control the surface chemistry of NPs to control their interaction with the surrounding media; (iii) stabilize the NPs, avoiding NP aggregation or precipitation and allow for perfect dispersion in their environment. Nevertheless, silk-based nanocomposites obtained by *in situ* methodology often fail to control efficiently NP size, shape and dispersion, which are crucial for a given application. On the other side, the synthesis of NPs prior to the addition to silk materials permit to have a perfect control on these aspects but the addition of as synthesized NPs to SF dispersion may result in silk gelation and could intervene in the formation of silk scaffolds and modify its properties.

Overall, the resultant nanocomposite should have NPs of controlled size, shape and surface chemistry. These NPs should be homogeneously distributed within the material without disturbing the desired properties found in the bulk material. Although many different silk-based nanocomposites have been successfully produced in the literature relatively few data could be

found on the influence of NPs over silk structure and an in deep characterization of these structure is often missing.

Therefore, this project aims to develop a straightforward method to prepare silk-based nanocomposites that is transposable for at least several of the existing silk materials and that allows the use of different NPs. Gold, silver and iron oxide NPs have been chosen as model NPs given their well-known properties and their extensive use in biomedical applications among others. Given the inherent drawbacks of the *in situ* synthesis methods and the knowledge of the TIMR laboratory on NPs synthesis into aqueous solutions, NPs will be synthesized upstream and incorporated into the silk materials / dispersion. Moreover, this work aims to provide strong guidelines for the design and fabrication of silk-based nanocomposites by performing an in-deep characterization of the dispersion of these NPs within silk dispersion.

Thus, the main objectives are:

1. To develop a reproducible NPs synthesis method that allows a good control over their shape, size, surface chemistry and results in a stable NPs suspension over time.
2. To develop a transposable methodology to produce several silk-based nanocomposites.
3. To provide consistent knowledge on the effect of NPs presence over the structure of silk and their changes when mixed into the same dispersion.
4. To explore a proof of concept application for some of the silk-based nanocomposites showing the apparition of new properties and the interest of incorporating such NPs.

The final goal is not to develop a specific material for a given application but to create a transposable methodology that can be applied for many silk materials containing different NPs. This project aims to increase silk materials functionality by providing the possibility to acquire new properties that depend on the chosen NPs.

## References

1. Xiong, R., Grant, A. M., Ma, R., Zhang, S. & Tsukruk, V. V. Naturally-derived biopolymer nanocomposites: Interfacial design, properties and emerging applications. *Mater. Sci. Eng. R Reports* **125**, 1–41 (2018).
2. Hakimi, O., Knight, D. P., Vollrath, F. & Vadgama, P. Spider and mulberry silkworm silks as compatible biomaterials. *Compos. Part B Eng.* **38**, 324–337 (2007).
3. Koh, L. D. *et al.* Structures, mechanical properties and applications of silk fibroin materials. *Prog. Polym. Sci.* **46**, 86–110 (2015).
4. Vepari, C. & Kaplan, D. L. Silk as a biomaterial. *Prog. Polym. Sci.* **32**, 991–1007 (2007).
5. Hu, X. *et al.* Regulation of silk material structure by temperature-controlled water vapor annealing. *Biomacromolecules* **12**, 1686–1696 (2011).
6. Poza, P., Pérez-Rigueiro, J., Elices, M. & LLorca, J. Fractographic analysis of silkworm and spider silk. *Eng. Fract. Mech.* **69**, 1035–1048 (2002).
7. Uttayarat, P. *et al.* Antimicrobial electrospun silk fibroin mats with silver nanoparticles for wound dressing application. *Fibers Polym.* **13**, 999–1006 (2012).
8. Mori, K. *et al.* Production of a chimeric fibroin light-chain polypeptide in a fibroin secretion-deficient naked pupa mutant of the silkworm *Bombyx mori*. *J. Mol. Biol.* **251**, 217–228 (1995).
9. Marsh, R. E., Corbey, R. B. & Pauling, L. An Investigation of the Structure silk fibroin. *Biochim. Biophys. Acta* **16**, (1955).
10. Kambe, Y. *et al.* Beta-sheet content significantly correlates with the biodegradation time of silk fibroin hydrogels showing a wide range of compressive modulus. *Polym. Degrad. Stab.* **179**, 109240 (2020).
11. Cao, Y. & Wang, B. Biodegradation of silk biomaterials. *Int. J. Mol. Sci.* **10**, 1514–1524 (2009).
12. Li, M. & Li, J. Biodegradation behavior of silk biomaterials. *Silk Biomater. Tissue Eng. Regen. Med.* 330–348 (2014) doi:10.1533/9780857097064.2.330.
13. Rockwood, D. N. *et al.* Materials fabrication from *Bombyx mori* silk fibroin. *Nat. Protoc.* **6**, 1612–1631 (2011).
14. Zhang, W. *et al.* Silk Fibroin Biomaterial Shows Safe and Effective Wound Healing in Animal Models and a Randomized Controlled Clinical Trial. *Adv. Healthc. Mater.* **6**, 1–16 (2017).
15. Altman, G. H. *et al.* Silk-based biomaterials. *Biomaterials* **24**, 401–416 (2003).

16. Calamak, S. *et al.* Ag/silk fibroin nanofibers: Effect of fibroin morphology on Ag<sup>+</sup> release and antibacterial activity. *Eur. Polym. J.* **67**, 99–112 (2015).
17. Shi, C. *et al.* An antibacterial and absorbable silk-based fixation material with impressive mechanical properties and biocompatibility. *Sci. Rep.* **6**, 2–13 (2016).
18. Song, W. *et al.* Magnetic-Silk Core–Shell Nanoparticles as Potential Carriers for Targeted Delivery of Curcumin into Human Breast Cancer Cells. *ACS Biomater. Sci. Eng.* **3**, 1027–1038 (2017).
19. Zhou, J., Cao, C., Ma, X. & Lin, J. Electrospinning of silk fibroin and collagen for vascular tissue engineering. *Int. J. Biol. Macromol.* **47**, 514–519 (2010).
20. Phillips, D. M. *et al.* Dissolution and regeneration of Bombyx mori silk fibroin using ionic liquids. *J. Am. Chem. Soc.* **126**, 14350–14351 (2004).
21. Li, G. *et al.* Silk-Based Biomaterials in Biomedical Textiles and Fiber-Based Implants. *Adv. Healthc. Mater.* **4**, 1134–1151 (2015).
22. Huang, W., Ling, S., Li, C., Omenetto, F. G. & Kaplan, D. L. Silkworm silk-based materials and devices generated using bio-nanotechnology. *Chem. Soc. Rev.* **47**, 6486–6504 (2018).
23. Meyers, M. A., Chen, P. Y., Lin, A. Y. M. & Seki, Y. Biological materials: Structure and mechanical properties. *Prog. Mater. Sci.* **53**, 1–206 (2008).
24. Wenger, M. P. E., Bozec, L., Horton, M. A. & Mesquidaz, P. Mechanical properties of collagen fibrils. *Biophys. J.* **93**, 1255–1263 (2007).
25. Guthold, M. *et al.* A comparison of the mechanical and structural properties of fibrin fibers with other protein fibers. *Cell Biochem. Biophys.* **49**, 165–181 (2007).
26. Cai, Y. *et al.* Silk fibroin membrane used for guided bone tissue regeneration. *Mater. Sci. Eng. C* **70**, 148–154 (2017).
27. Karageorgiou, V. & Kaplan, D. Porosity of 3D biomaterial scaffolds and osteogenesis. *Biomaterials* **26**, 5474–5491 (2005).
28. Correia, C. *et al.* Development of silk-based scaffolds for tissue engineering of bone from human adipose-derived stem cells. *Acta Biomater.* **8**, 2483–2492 (2012).
29. Mandal, B. B., Grinberg, A., Gil, E. S., Panilaitis, B. & Kaplan, D. L. High-strength silk protein scaffolds for bone repair. *Proc. Natl. Acad. Sci. U. S. A.* **109**, 7699–7704 (2012).
30. Hofmann, S. *et al.* Remodeling of tissue-engineered bone structures in vivo. *Eur. J. Pharm. Biopharm.* **85**, 119–129 (2013).
31. Kim, H. J. *et al.* Bone tissue engineering with premineralized silk scaffolds. *Bone* **42**, 1226–1234 (2008).

32. Zhang, W. *et al.* Porous silk scaffolds for delivery of growth factors and stem cells to enhance bone regeneration. *PLoS One* **9**, 1–9 (2014).
33. Sheikh, F. A. *et al.* Facile and highly efficient approach for the fabrication of multifunctional silk nanofibers containing hydroxyapatite and silver nanoparticles. *J. Biomed. Mater. Res. - Part A* **102**, 3459–3469 (2014).
34. Hodgkinson, T., Yuan, X. F. & Bayat, A. Electrospun silk fibroin fiber diameter influences in vitro dermal fibroblast behavior and promotes healing of ex vivo wound models. *J. Tissue Eng.* **5**, (2014).
35. Belanger, K. *et al.* A multi-layered nerve guidance conduit design adapted to facilitate surgical implantation. *Heal. Sci. Reports* **1**, e86 (2018).
36. Lee, H., Yanilmaz, M., Toprakci, O., Fu, K. & Zhang, X. A review of recent developments in membrane separators for rechargeable lithium-ion batteries. *Energy and Environmental Science* vol. 7 3857–3886 (2014).
37. Wharram, S. E., Zhang, X., Kaplan, D. L. & McCarthy, S. P. Electrospun silk material systems for wound healing. *Macromol. Biosci.* **10**, 246–257 (2010).
38. Çalamak, S., Erdoğan, C., Özalp, M. & Ulubayram, K. Silk fibroin based antibacterial bionanotextiles as wound dressing materials. *Mater. Sci. Eng. C* **43**, 11–20 (2014).
39. Yukseloglu, S. M., Sokmen, N. & Canoglu, S. Biomaterial applications of silk fibroin electrospun nanofibres. *Microelectron. Eng.* **146**, 43–47 (2015).
40. Lammel, A. S., Hu, X., Park, S. H., Kaplan, D. L. & Scheibel, T. R. Controlling silk fibroin particle features for drug delivery. *Biomaterials* **31**, 4583–4591 (2010).
41. Li, A. B. *et al.* Enhanced Stabilization in Dried Silk Fibroin Matrices. *Biomacromolecules* **18**, 2900–2905 (2017).
42. Pritchard, E. M., Dennis, P. B., Omenetto, F., Naik, R. R. & Kaplan, D. L. Review: Physical and chemical aspects of stabilization of compounds in silk. *Biopolymers* vol. 97 479–498 (2012).
43. Li, A. B., Kluge, J. A., Guzewicz, N. A., Omenetto, F. G. & Kaplan, D. L. Silk-based stabilization of biomacromolecules. *J. Control. Release* **219**, 416–430 (2015).
44. Wenk, E., Merkle, H. P. & Meinel, L. Silk fibroin as a vehicle for drug delivery applications. *Journal of Controlled Release* vol. 150 128–141 (2011).
45. Pritchard, E. M., Szybala, C., Boison, D. & Kaplan, D. L. Silk fibroin encapsulated powder reservoirs for sustained release of adenosine. *J. Control. Release* **144**, 159–167 (2010).
46. Lu, Q. *et al.* Stabilization and release of enzymes from silk films. *Macromol. Biosci.* **10**, 359–368 (2010).

47. Li, H., Zhu, J., Chen, S., Jia, L. & Ma, Y. Fabrication of aqueous-based dual drug loaded silk fibroin electrospun nanofibers embedded with curcumin-loaded RSF nanospheres for drugs controlled release. *RSC Adv.* **7**, 56550–56558 (2017).
48. Lan, Y. *et al.* Therapeutic efficacy of antibiotic-loaded gelatin microsphere/silk fibroin scaffolds in infected full-thickness burns. *Acta Biomater.* **10**, 3167–3176 (2014).
49. Hou, X., Mu, L., Chen, F. & Hu, X. Emerging investigator series: Design of hydrogel nanocomposites for the detection and removal of pollutants: From nanosheets, network structures, and biocompatibility to machine-learning-assisted design. *Environ. Sci. Nano* **5**, 2216–2240 (2018).
50. Lovett, M. L. *et al.* Silk hydrogels for sustained ocular delivery of anti-vascular endothelial growth factor (anti-VEGF) therapeutics. *Eur. J. Pharm. Biopharm.* **95**, 271–278 (2015).
51. Niu, C. *et al.* Design and performance of a poly(vinyl alcohol)/silk fibroin enzymatically crosslinked semi-interpenetrating hydrogel for a potential hydrophobic drug delivery. *RSC Adv.* **9**, 41074–41082 (2019).
52. Ribeiro, M. *et al.* Development of silk fibroin/nanohydroxyapatite composite hydrogels for bone tissue engineering. *Eur. Polym. J.* **67**, 66–77 (2015).
53. Vidal, S. E. L. *et al.* 3D biomaterial matrix to support long term, full thickness, immuno-competent human skin equivalents with nervous system components. *Biomaterials* **198**, 194–203 (2019).
54. Chao, P. G. *et al.* Silk hydrogel for cartilage tissue engineering. *J. Biomed. Mater. Res. - Part B Appl. Biomater.* **95**, 84–90 (2010).
55. Yodmuang, S. *et al.* Silk microfiber-reinforced silk hydrogel composites for functional cartilage tissue repair. *Acta Biomater.* **11**, 27–36 (2015).
56. Frauchiger, D. A. *et al.* A review of the application of reinforced hydrogels and silk as biomaterials for intervertebral disc repair. *Eur. Cells Mater.* **34**, 271–290 (2017).
57. Li, Z. *et al.* Topical application of silk fibroin-based hydrogel in preventing hypertrophic scars. *Colloids Surfaces B Biointerfaces* **186**, 110735 (2020).
58. Fernández-García, L. *et al.* Safety and tolerability of silk fibroin hydrogels implanted into the mouse brain. *Acta Biomater.* **45**, 262–275 (2016).
59. Luo, K. yuan & Shao, Z. zhong. A novel regenerated silk fibroin-based hydrogels with magnetic and catalytic activities. *Chinese J. Polym. Sci. (English Ed.)* **35**, 515–523 (2017).
60. Nezhad-Mokhtari, P., Ghorbani, M., Roshangar, L. & Soleimani Rad, J. Chemical gelling of hydrogels-based biological macromolecules for tissue engineering: Photo- and enzymatic-crosslinking methods. *Int. J. Biol. Macromol.* **139**, 760–772 (2019).

61. Bang, S. *et al.* Preventing postoperative tissue adhesion using injectable carboxymethyl cellulose-pullulan hydrogels. *Int. J. Biol. Macromol.* **105**, 886–893 (2017).
62. Bi, B., Liu, H., Kang, W., Zhuo, R. & Jiang, X. An injectable enzymatically crosslinked tyramine-modified carboxymethyl chitin hydrogel for biomedical applications. *Colloids Surfaces B Biointerfaces* **175**, 614–624 (2019).
63. Jin, R. *et al.* Enzymatically-crosslinked injectable hydrogels based on biomimetic dextran-hyaluronic acid conjugates for cartilage tissue engineering. *Biomaterials* **31**, 3103–3113 (2010).
64. Hoang Thi, T. T., Lee, Y., Le Thi, P. & Park, K. D. Engineered horseradish peroxidase-catalyzed hydrogels with high tissue adhesiveness for biomedical applications. *J. Ind. Eng. Chem.* **78**, 34–52 (2019).
65. Wang, L. S. *et al.* Modulation of chondrocyte functions and stiffness-dependent cartilage repair using an injectable enzymatically crosslinked hydrogel with tunable mechanical properties. *Biomaterials* **35**, 2207–2217 (2014).
66. Chen, F. *et al.* An Injectable Enzymatically Crosslinked Carboxymethylated Pullulan/Chondroitin Sulfate Hydrogel for Cartilage Tissue Engineering. *Sci. Rep.* **6**, 1–12 (2016).
67. van Loo, B. *et al.* Enzymatic Outside-In Crosslinking Enables Single-step Microcapsule Production for High-throughput 3D Cell Microaggregate Formation. *Mater. Today Bio* **6**, 100047 (2020).
68. Partlow, B. P. *et al.* Highly tunable elastomeric silk biomaterials. *Adv. Funct. Mater.* **24**, 4615–4624 (2014).
69. Grenier, J. *et al.* Mechanisms of pore formation in hydrogel scaffolds textured by freeze-drying. *Acta Biomater.* **94**, 195–203 (2019).
70. Qian, L. & Zhang, H. Controlled freezing and freeze drying: A versatile route for porous and micro-/nano-structured materials. *J. Chem. Technol. Biotechnol.* **86**, 172–184 (2011).
71. Maleki, H. & Huesing, N. Silica-silk fibroin hybrid (bio)aerogels: two-step versus one-step hybridization. *J. Sol-Gel Sci. Technol.* (2019) doi:10.1007/s10971-019-04933-4.
72. Maleki, H., Montes, S., Hayati-Roodbari, N., Putz, F. & Huesing, N. Compressible, Thermally Insulating, and Fire Retardant Aerogels through Self-Assembling Silk Fibroin Biopolymers Inside a Silica Structure - An Approach towards 3D Printing of Aerogels. *ACS Appl. Mater. Interfaces* **10**, 22718–22730 (2018).
73. Mandal, B. B. & Kundu, S. C. Cell proliferation and migration in silk fibroin 3D scaffolds. *Biomaterials* **30**, 2956–2965 (2009).

74. Mu, X. *et al.* 3D Printing of Silk Protein Structures by Aqueous Solvent-Directed Molecular Assembly. *Macromol. Biosci.* **20**, 1900191 (2020).
75. Rodriguez, M. J. *et al.* 3D freeform printing of silk fibroin. *Acta Biomater.* **71**, 379–387 (2018).
76. Zheng, Z. *et al.* 3D Bioprinting of Self-Standing Silk-Based Bioink. *Adv. Healthc. Mater.* **7**, 1–12 (2018).
77. Jose, R. R., Brown, J. E., Polido, K. E., Omenetto, F. G. & Kaplan, D. L. Polyol-Silk Bioink Formulations as Two-Part Room-Temperature Curable Materials for 3D Printing. *ACS Biomater. Sci. Eng.* **1**, 780–788 (2015).
78. Sommer, M. R., Schaffner, M., Carnelli, D. & Studart, A. R. 3D Printing of Hierarchical Silk Fibroin Structures. *ACS Appl. Mater. Interfaces* **8**, 34677–34685 (2016).
79. Brown, J. E. *et al.* Shape Memory Silk Protein Sponges for Minimally Invasive Tissue Regeneration. *Adv. Healthc. Mater.* **6**, (2017).
80. Bellas, E. *et al.* Injectable Silk Foams for Soft Tissue Regeneration. *Adv. Healthc. Mater.* **4**, 452–459 (2015).
81. Chambre, L. *et al.* Tunable Biodegradable Silk-Based Memory Foams with Controlled Release of Antibiotics. *ACS Appl. Bio Mater.* **3**, 2466–2472 (2020).
82. Ornell, K. J. *et al.* Local delivery of dinutuximab from lyophilized silk fibroin foams for treatment of an orthotopic neuroblastoma model. *Cancer Med.* **9**, 2891–2903 (2020).
83. Tsioris, K. *et al.* Fabrication of silk microneedles for controlled-release drug delivery. *Adv. Funct. Mater.* **22**, 330–335 (2012).
84. Yin, Z. *et al.* Swellable silk fibroin microneedles for transdermal drug delivery. *Int. J. Biol. Macromol.* **106**, 48–56 (2018).
85. Wang, S. *et al.* Insulin-Loaded Silk Fibroin Microneedles as Sustained Release System. *ACS Biomater. Sci. Eng.* **5**, 1887–1894 (2019).
86. Demuth, P. C., Min, Y., Irvine, D. J. & Hammond, P. T. Implantable silk composite microneedles for programmable vaccine release kinetics and enhanced immunogenicity in transcutaneous immunization. *Adv. Healthc. Mater.* **3**, 47–58 (2014).
87. Boopathy, A. V. *et al.* Enhancing humoral immunity via sustained-release implantable microneedle patch vaccination. *Proc. Natl. Acad. Sci. U. S. A.* **116**, 16473–16478 (2019).
88. Li, C. *et al.* Regenerated silk materials for functionalized silk orthopedic devices by mimicking natural processing. *Biomaterials* **110**, 24–33 (2016).
89. Stinson, J. A. *et al.* Thin silk fibroin films as a dried format for temperature stabilization of inactivated polio vaccine. *Vaccine* **38**, 1652–1660 (2020).



90. Bressner, J. E. *et al.* Rapid fabrication of silk films with controlled architectures via electrogelation. *J. Mater. Chem. B* **2**, 4983–4987 (2014).
91. Lu, S. *et al.* Insoluble and flexible silk films containing glycerol. *Biomacromolecules* **11**, 143–150 (2010).
92. Zhou, J. *et al.* Regenerated silk fibroin films with controllable nanostructure size and secondary structure for drug delivery. *ACS Applied Materials and Interfaces* vol. 6 21813–21821 (2014).
93. Lawrence, B. D., Marchant, J. K., Pindrus, M. A., Omenetto, F. G. & Kaplan, D. L. Silk film biomaterials for cornea tissue engineering. *Biomaterials* **30**, 1299–1308 (2009).
94. Gil, E. S. *et al.* Helicoidal multi-lamellar features of RGD-functionalized silk biomaterials for corneal tissue engineering. *Biomaterials* **31**, 8953–8963 (2010).
95. Kundu, B., Rajkhowa, R., Kundu, S. C. & Wang, X. Silk fibroin biomaterials for tissue regenerations. *Adv. Drug Deliv. Rev.* **65**, 457–470 (2013).
96. Kim, D. H. *et al.* Dissolvable films of silk fibroin for ultrathin conformal bio-integrated electronics. *Nat. Mater.* **9**, 1–7 (2010).
97. Gao, X., Gou, J., Zhang, L., Duan, S. & Li, C. A silk fibroin based green nano-filter for air filtration. *RSC Adv.* **8**, 8181–8189 (2018).
98. Ling, S., Jin, K., Kaplan, D. L. & Buehler, M. J. Ultrathin free-standing bombyx mori silk nanofibril membranes. *Nano Lett.* **16**, 3795–3800 (2016).
99. Ling, S. *et al.* Design and function of biomimetic multilayer water purification membranes. *Sci. Adv.* **3**, 1–12 (2017).
100. Gil, E. S., Panilaitis, B., Bellas, E. & Kaplan, D. L. Functionalized Silk Biomaterials for Wound Healing. *Adv. Healthc. Mater.* **2**, 206–217 (2013).
101. Li, X. *et al.* Functionalized silk fibroin dressing with topical bioactive insulin release for accelerated chronic wound healing. *Mater. Sci. Eng. C* **72**, 394–404 (2017).
102. Sheikh, F. A. *et al.* 3D electrospun silk fibroin nanofibers for fabrication of artificial skin. *Nanomedicine Nanotechnology, Biol. Med.* **11**, 681–691 (2015).
103. Bhattacharjee, P. *et al.* Silk scaffolds in bone tissue engineering: An overview. *Acta Biomater.* **63**, 1–17 (2017).
104. Zhou, F. *et al.* Silk fibroin-chondroitin sulfate scaffold with immuno-inhibition property for articular cartilage repair. *Acta Biomater.* **63**, 64–75 (2017).
105. Lovett, M. *et al.* Silk fibroin microtubes for blood vessel engineering. *Biomaterials* **28**, 5271–5279 (2007).

106. Alessandrino, A. *et al.* Three-Layered Silk Fibroin Tubular Scaffold for the Repair and Regeneration of Small Caliber Blood Vessels: From Design to in vivo Pilot Tests. *Front. Bioeng. Biotechnol.* **7**, 1–17 (2019).
107. Enomoto, S. *et al.* Long-term patency of small-diameter vascular graft made from fibroin, a silk-based biodegradable material. *J. Vasc. Surg.* **51**, 155–164 (2010).
108. Varone, A. *et al.* The potential of *Antheraea pernyi* silk for spinal cord repair. *Sci. Rep.* **7**, 1–10 (2017).
109. Swetha, M. *et al.* Biocomposites containing natural polymers and hydroxyapatite for bone tissue engineering. *International Journal of Biological Macromolecules* vol. 47 1–4 (2010).
110. Holzwarth, J. M. & Ma, P. X. Biomimetic nanofibrous scaffolds for bone tissue engineering. *Biomaterials* vol. 32 9622–9629 (2011).
111. Hasany, M. *et al.* Silica nanoparticle surface chemistry: An important trait affecting cellular biocompatibility in two and three dimensional culture systems. *Colloids Surfaces B Biointerfaces* **182**, 110353 (2019).
112. Mc Carthy, D. J., Malhotra, M., O’Mahony, A. M., Cryan, J. F. & O’Driscoll, C. M. Nanoparticles and the blood-brain barrier: Advancing from in-vitro models towards therapeutic significance. *Pharm. Res.* **32**, 1161–1185 (2015).
113. Sperling, R. A. & Parak, W. J. Surface modification, functionalization and bioconjugation of colloidal Inorganic nanoparticles. *Philos. Trans. R. Soc. A Math. Phys. Eng. Sci.* **368**, 1333–1383 (2010).
114. Monopoli, M. P., Åberg, C., Salvati, A. & Dawson, K. A. Biomolecular coronas provide the biological identity of nanosized materials. *Nat. Nanotechnol.* **7**, 779–786 (2012).
115. Lynch, I. *et al.* NANOINTERACT: A rational approach to the interaction between nanoscale materials and living matter? *J. Phys. Conf. Ser.* **170**, 012040 (2009).
116. Balfourier, A. *et al.* Unexpected intracellular biodegradation and recrystallization of gold nanoparticles. *Proc. Natl. Acad. Sci. U. S. A.* **117**, 103–113 (2020).
117. Plan Sangnier, A. *et al.* Endosomal Confinement of Gold Nanospheres, Nanorods, and Nanoraspberries Governs Their Photothermal Identity and Is Beneficial for Cancer Cell Therapy. *Adv. Biosyst.* **4**, 1900284 (2020).
118. Van de Walle, A. *et al.* Biosynthesis of magnetic nanoparticles from nanodegradation products revealed in human stem cells. *Proc. Natl. Acad. Sci. U. S. A.* **116**, 4044–4053 (2019).

119. Su, S. S. & Chang, I. Review of production routes of nanomaterials. in *Commercialization of Nanotechnologies-A Case Study Approach* (eds. Brabazon, D. et al.) 15–29 (Springer International Publishing, 2017). doi:10.1007/978-3-319-56979-6\_2.
120. Turkevich, J., Stevenson, P. C. & Hillier, J. A study of the nucleation and growth processes in the synthesis of colloidal gold. *Discuss. Faraday Soc.* **11**, 55–75 (1951).
121. Mascolo, M. C., Pei, Y. & Ring, T. A. Room Temperature Co-Precipitation Synthesis of Magnetite Nanoparticles in a Large pH Window with Different Bases. *Materials (Basel)*. **6**, 5549–5567 (2013).
122. Aufaure, R. *et al.* One pot microwave assisted synthesis of bisphosphonate alkene capped gold nanoparticles. *RSC Adv.* **4**, 59315–59322 (2014).
123. Szunerits, S., Spadavecchia, J. & Boukherroub, R. Surface plasmon resonance: Signal amplification using colloidal gold nanoparticles for enhanced sensitivity. *Rev. Anal. Chem.* **33**, 153–164 (2014).
124. Cui, Y. *et al.* The molecular mechanism of action of bactericidal gold nanoparticles on *Escherichia coli*. *Biomaterials* **33**, 2327–2333 (2012).
125. Plan Sangnier, A. *et al.* Raspberry-like small multicore gold nanostructures for efficient photothermal conversion in the first and second near-infrared windows. *Chem. Commun.* **55**, 4055–4058 (2019).
126. De Crozals, G., Bonnet, R., Farre, C. & Chaix, C. Nanoparticles with multiple properties for biomedical applications: A strategic guide. *Nano Today* **11**, 435–463 (2016).
127. Zhou, W., Gao, X., Liu, D. & Chen, X. Gold Nanoparticles for In Vitro Diagnostics. *Chem. Rev.* **115**, 10575–10636 (2015).
128. Szekeres, G. P. & Kneipp, J. SERS probing of proteins in gold nanoparticle agglomerates. *Front. Chem.* **7**, 1–10 (2019).
129. León, E. R., Rodríguez, E. L., Beas, C. R., Plascencia-Villa, G. & Palomares, R. A. I. Study of Methylene Blue Degradation by Gold Nanoparticles Synthesized within Natural Zeolites. *J. Nanomater.* **2016**, (2016).
130. Zhang, Y., Cui, X., Shi, F. & Deng, Y. Nano-gold catalysis in fine chemical synthesis. *Chemical Reviews* vol. 112 2467–2505 (2012).
131. Carabineiro, S. A. C. Supported Gold Nanoparticles as Catalysts for the Oxidation of Alcohols and Alkanes. *Frontiers in Chemistry* vol. 7 702 (2019).
132. Alshammari, A. S. Heterogeneous gold catalysis: From discovery to applications. *Catalysts* vol. 9 402 (2019).

133. Begum, R. *et al.* Chemical reduction of methylene blue in the presence of nanocatalysts: a critical review. *Rev. Chem. Eng.* **0**, 749–770 (2019).
134. Yang, K. *et al.* Antimicrobial hydrogels: Promising materials for medical application. *Int. J. Nanomedicine* **13**, 2217–2263 (2018).
135. Morones, J. R. *et al.* The bactericidal effect of silver nanoparticles. *Nanotechnology* **16**, 2346–2353 (2005).
136. Agnihotri, S., Mukherji, S. & Mukherji, S. Size-controlled silver nanoparticles synthesized over the range 5–100 nm using the same protocol and their antibacterial efficacy. *RSC Adv.* **4**, 3974–3983 (2014).
137. Guo, J. *et al.* Silver nanoparticles exert concentration-dependent influences on biofilm development and architecture. *Cell Prolif.* **52**, 1–8 (2019).
138. Lara, H. H., Ayala-Núñez, N. V., del Turrent, L. C. I. & Padilla, C. R. Bactericidal effect of silver nanoparticles against multidrug-resistant bacteria. *World J. Microbiol. Biotechnol.* **26**, 615–621 (2010).
139. Kim, K. J. *et al.* Antifungal activity and mode of action of silver nano-particles on *Candida albicans*. *BioMetals* **22**, 235–242 (2009).
140. Chudasama, B., Vala, A. K., Andhariya, N., Upadhyay, R. V. & Mehta, R. V. Antifungal activity of multifunctional Fe<sub>3</sub>O<sub>4</sub>-Ag nanocolloids. *J. Magn. Magn. Mater.* **323**, 1233–1237 (2011).
141. Lara, H. H., Ayala-Núñez, N. V., Ixtapan-Turrent, L. & Rodriguez-Padilla, C. Mode of antiviral action of silver nanoparticles against HIV-1. *J. Nanobiotechnology* **8**, 1–10 (2010).
142. Rizzello, L. & Pompa, P. P. Nanosilver-based antibacterial drugs and devices: Mechanisms, methodological drawbacks, and guidelines. *Chem. Soc. Rev.* **43**, 1501–1518 (2014).
143. Chudasama, B., Vala, A. K., Andhariya, N., Upadhyay, R. V. & Mehta, R. V. Enhanced antibacterial activity of bifunctional Fe<sub>3</sub>O<sub>4</sub>-Ag core-shell nanostructures. *Nano Res.* **2**, 955–965 (2009).
144. Reidy, B., Haase, A., Luch, A., Dawson, K. A. & Lynch, I. Mechanisms of silver nanoparticle release, transformation and toxicity: A critical review of current knowledge and recommendations for future studies and applications. *Materials (Basel)*. **6**, 2295–2350 (2013).

145. Cao, H., Liu, X., Meng, F. & Chu, P. K. Biological actions of silver nanoparticles embedded in titanium controlled by micro-galvanic effects. *Biomaterials* **32**, 693–705 (2011).
146. Choi, O. & Hu, Z. Size dependent and reactive oxygen species related nanosilver toxicity to nitrifying bacteria. *Environ. Sci. Technol.* **42**, 4583–4588 (2008).
147. U.S. Department of Health, Education, and Welfare: Report and Memoranda. NIOSH 1992, publication no. 92-100 . (1992).
148. Cai, Y. *et al.* Large-scale and facile synthesis of silver nanoparticles: Via a microwave method for a conductive pen. *RSC Adv.* **7**, 34041–34048 (2017).
149. Annadhasan, M., Muthukumarasamyvel, T., Sankar Babu, V. R. & Rajendiran, N. Green synthesized silver and gold nanoparticles for colorimetric detection of  $\text{Hg}^{2+}$ ,  $\text{Pb}^{2+}$ , and  $\text{Mn}^{2+}$  in aqueous medium. *ACS Sustain. Chem. Eng.* **2**, 887–896 (2014).
150. Chandrasekharan, D. K., Khanna, P. K., Kagiya, T. V. & Nair, C. K. K. Synthesis of nanosilver using a vitamin C derivative and studies on radiation protection. *Cancer Biother. Radiopharm.* **26**, 249–257 (2011).
151. Guerra, F. D., Attia, M. F., Whitehead, D. C. & Alexis, F. Nanotechnology for environmental remediation: Materials and applications. *Molecules* **23**, 1–23 (2018).
152. Cardoso, V. F. *et al.* Advances in Magnetic Nanoparticles for Biomedical Applications. *Adv. Healthc. Mater.* **7**, 1–35 (2018).
153. Laurent, S. *et al.* Magnetic iron oxide nanoparticles: Synthesis, stabilization, vectorization, physicochemical characterizations and biological applications. *Chem. Rev.* **108**, 2064–2110 (2008).
154. Wu, W., Jiang, C. Z. & Roy, V. A. L. Designed synthesis and surface engineering strategies of magnetic iron oxide nanoparticles for biomedical applications. *Nanoscale* **8**, 19421–19474 (2016).
155. Demortière, A. *et al.* Size-dependent properties of magnetic iron oxide nanocrystals. *Nanoscale* **3**, 225–232 (2011).
156. Baumgartner, J. *et al.* Magnetotactic bacteria form magnetite from a phosphate-rich ferric hydroxide via nanometric ferric (oxyhydr)oxide intermediates. *Proc. Natl. Acad. Sci. U. S. A.* **110**, 14883–14888 (2013).
157. Gieré, R. Magnetite in the human body: Biogenic vs. anthropogenic. *Proc. Natl. Acad. Sci. U. S. A.* **113**, 11986–11987 (2016).
158. Wu, A., Ou, P. & Zeng, L. Biomedical applications of magnetic nanoparticles. *Nano* **5**, 245–270 (2010).

159. Cheng, F., Zhu, C., He, W., Zhao, J. & Qu, J. PSBMA-Conjugated Magnetic Nanoparticles for Selective IgG Separation. *Langmuir* **35**, 1111–1118 (2019).
160. Benyettou, F. *et al.* Potent and selective in vitro and in vivo antiproliferative effects of metal-organic trefoil knots. *Chem. Sci.* **10**, 5884–5892 (2019).
161. Pires, F. *et al.* Consenso Brasileiro de Nutrição em Transplante de Células-Tronco Hematopoiéticas : Idosos Stem Cell Transplantation : Elderly. **17**, 1–16 (2019).
162. Liang, B. *et al.* An artificially engineered ‘tumor bio-magnet’ for collecting blood-circulating nanoparticles and magnetic hyperthermia. *Biomater. Sci.* **7**, 1815–1824 (2019).
163. Meddahi-Pellé, A. *et al.* Organ repair, hemostasis, and in vivo bonding of medical devices by aqueous solutions of nanoparticles. *Angew. Chemie - Int. Ed.* **53**, 6369–6373 (2014).
164. Santos, L. J., Reis, R. L. & Gomes, M. E. Harnessing magnetic-mechano actuation in regenerative medicine and tissue engineering. *Trends Biotechnol.* **33**, 471–479 (2015).
165. Gutierrez, A. M., Dziubla, T. D. & Hilt, J. Z. Recent advances on iron oxide magnetic nanoparticles as sorbents of organic pollutants in water and wastewater treatment. *Rev. Environ. Health* **32**, 111–117 (2017).
166. Mishra, R. & Militky, J. Nanocomposites. in *Nanotechnology in Textiles* (ed. The Textile Institute Book Series) 263–310 (Elsevier, 2019). doi:10.1016/B978-0-08-102609-0.00006-7.
167. Yang, G., Lin, H., Rothrauff, B. B., Yu, S. & Tuan, R. S. Multilayered polycaprolactone/gelatin fiber-hydrogel composite for tendon tissue engineering. *Acta Biomater.* **35**, 68–76 (2016).
168. Watanabe, K. *et al.* Highly Transparent and Tough Filler Composite Elastomer Inspired by the Cornea. *ACS Mater. Lett.* **2**, 325–330 (2020).
169. Raja, N. & Yun, H. S. A simultaneous 3D printing process for the fabrication of bioceramic and cell-laden hydrogel core/shell scaffolds with potential application in bone tissue regeneration. *J. Mater. Chem. B* **4**, 4707–4716 (2016).
170. Song, J. *et al.* Nano-silver in situ hybridized collagen scaffolds for regeneration of infected full-thickness burn skin. *J. Mater. Chem. B* **3**, 4231–4241 (2015).
171. Aimé, C. & Coradin, T. Nanocomposites from biopolymer hydrogels: Blueprints for white biotechnology and green materials chemistry. *Journal of Polymer Science, Part B: Polymer Physics* vol. 50 669–680 (2012).
172. Zhang, G., Liu, Y., Gao, X. & Chen, Y. Synthesis of silver nanoparticles and antibacterial property of silk fabrics treated by silver nanoparticles. *Nanoscale Res. Lett.* **9**, 1–8 (2014).

173. Yu, K. *et al.* In situ assembly of Ag nanoparticles (AgNPs) on porous silkworm cocoon-based wound film: Enhanced antimicrobial and wound healing activity. *Sci. Rep.* **7**, 1–13 (2017).
174. Zhou, L. *et al.* Minimizing antibiotic dosage through in situ formation of gold nanoparticles across antibacterial wound dressings: A facile approach using silk fabric as the base substrate. *J. Clean. Prod.* **243**, 118604 (2020).
175. Xu, Z., Shi, L., Yang, M. & Zhu, L. Preparation and biomedical applications of silk fibroin-nanoparticles composites with enhanced properties - A review. *Materials Science and Engineering C* vol. 95 302–311 (2019).
176. Jia, M., Chen, Z., Guo, Y., Chen, X. & Zhao, X. Efficacy of silk fibroin–nano silver against staphylococcus aureus biofilms in a rabbit model of sinusitis. *Int. J. Nanomedicine* **12**, 2933–2939 (2017).
177. Zhou, H. *et al.* In situ decoration of Ag@AgCl nanoparticles on polyurethane/silk fibroin composite porous films for photocatalytic and antibacterial applications. *Eur. Polym. J.* **118**, 153–162 (2019).
178. Hu, C. *et al.* Berberine / Ag nanoparticle embedded biomimetic calcium phosphate scaffolds for enhancing antibacterial function. 568–579 (2020).
179. Raho, R. *et al.* Photo-assisted green synthesis of silver doped silk fibroin/carboxymethyl cellulose nanocomposite hydrogels for biomedical applications. *Mater. Sci. Eng. C* **107**, 110219 (2020).
180. Lu, Z., Meng, M., Jiang, Y. & Xie, J. UV-assisted in situ synthesis of silver nanoparticles on silk fibers for antibacterial applications. *Colloids Surfaces A Physicochem. Eng. Asp.* **447**, 1–7 (2014).
181. Ribeiro, M. *et al.* Antibacterial silk fibroin/nanohydroxyapatite hydrogels with silver and gold nanoparticles for bone regeneration. *Nanomedicine Nanotechnology, Biol. Med.* **13**, 231–239 (2017).
182. Fei, X. *et al.* Green synthesis of silk fibroin-silver nanoparticle composites with effective antibacterial and biofilm-disrupting properties. *Biomacromolecules* **14**, 4483–4488 (2013).
183. Patil, S., George, T. & Mahadik, K. Green synthesized nanosilver loaded silk fibroin gel for enhanced wound healing. *J. Drug Deliv. Sci. Technol.* **30**, 30–36 (2015).
184. Shahid, M., Cheng, X. W., Tang, R. C. & Chen, G. Silk functionalization by caffeic acid assisted in-situ generation of silver nanoparticles. *Dye. Pigment.* **137**, 277–283 (2017).

185. Dhas, S. P., Anbarasan, S., Mukherjee, A. & Chandrasekaran, N. Biobased silver nanocolloid coating on silk fibers for prevention of post-surgical wound infections. *Int. J. Nanomedicine* **10**, 159–170 (2015).
186. Zhou, Y. & Tang, R. C. Facile and eco-friendly fabrication of AgNPs coated silk for antibacterial and antioxidant textiles using honeysuckle extract. *J. Photochem. Photobiol. B Biol.* **178**, 463–471 (2018).
187. Zhou, Y. & Tang, R. C. Facile and eco-friendly fabrication of colored and bioactive silk materials using silver nanoparticles synthesized by two flavonoids. *Polymers (Basel)*. **10**, (2018).
188. Baygar, T., Sarac, N., Ugur, A. & Karaca, I. R. Antimicrobial characteristics and biocompatibility of the surgical sutures coated with biosynthesized silver nanoparticles. *Bioorg. Chem.* **86**, 254–258 (2019).
189. Meng, M. *et al.* Controllable in situ synthesis of silver nanoparticles on multilayered film-coated silk fibers for antibacterial application. *J. Colloid Interface Sci.* **461**, 369–375 (2016).
190. Gao, A., Chen, H., Hou, A. & Xie, K. Efficient antimicrobial silk composites using synergistic effects of violacein and silver nanoparticles. *Mater. Sci. Eng. C* **103**, (2019).
191. Das, S. & Dhar, B. B. Green synthesis of noble metal nanoparticles using cysteine-modified silk fibroin: Catalysis and antibacterial activity. *RSC Adv.* **4**, 46285–46292 (2014).
192. Yu, W. *et al.* Preparation of Ag nanoparticle dispersed silk fibroin compact. *Appl. Surf. Sci.* **262**, 212–217 (2012).
193. Karthikeyan, K. *et al.* Fabrication of novel biofibers by coating silk fibroin with chitosan impregnated with silver nanoparticles. *J. Mater. Sci. Mater. Med.* **22**, 2721–2726 (2011).
194. Gulrajani, M. L., Gupta, D., Periyasamy, S. & Muthu, S. G. Preparation and application of silver nanoparticles on silk for imparting antimicrobial properties. *J. Appl. Polym. Sci.* **108**, 614–623 (2008).
195. Tang, B., Sun, L., Kaur, J., Yu, Y. & Wang, X. In-situ synthesis of gold nanoparticles for multifunctionalization of silk fabrics. *Dye. Pigment.* **103**, 183–190 (2014).
196. Zou, F. *et al.* Functionalization of silk with in-situ synthesized platinum nanoparticles. *Materials (Basel)*. **11**, 1–13 (2018).
197. Abbasi, A. R., Noori, N., Azadbakht, A. & Bafarani, M. Dense coating of surface mounted Cu<sub>2</sub>O nanoparticles upon silk fibers under ultrasound irradiation with antibacterial activity. *J. Iran. Chem. Soc.* **13**, 1273–1281 (2016).



198. Patil, P. P., Meshram, J. V, Bohara, R. A., Nanaware, S. G. & Pawar, S. H. ZnO nanoparticle-embedded silk fibroin-polyvinyl alcohol composite film: A potential dressing material for infected wounds. *New J. Chem.* **42**, 14620–14629 (2018).
199. Lu, Z. *et al.* Fabrication of CeO<sub>2</sub> nanoparticle-modified silk for UV protection and antibacterial applications. *J. Colloid Interface Sci.* **435**, 8–14 (2014).
200. Chung, S., Ercan, B., Roy, A. K. & Webster, T. J. Addition of selenium nanoparticles to electrospun silk scaffold improves the mammalian cell activity while reducing bacterial growth. *Front. Physiol.* **7**, 1–6 (2016).
201. Cohen-karni, T. *et al.* Nanocomposite Gold-Silk Nano fi bers. *Nano Lett.* **12**, 5403–5406 (2012).
202. Akturk, O. *et al.* Wet electrospun silk fibroin/gold nanoparticle 3D matrices for wound healing applications. *RSC Adv.* **6**, 13234–13250 (2016).
203. Das, S. *et al.* In vivo studies of silk based gold nano-composite conduits for functional peripheral nerve regeneration. *Biomaterials* **62**, 66–75 (2015).
204. Sridhar, S., Venugopal, J. R., Sridhar, R. & Ramakrishna, S. Cardiogenic differentiation of mesenchymal stem cells with gold nanoparticle loaded functionalized nanofibers. *Colloids Surfaces B Biointerfaces* **134**, 346–354 (2015).
205. Kong, X. D., Cui, F. Z., Wang, X. M., Zhang, M. & Zhang, W. Silk fibroin regulated mineralization of hydroxyapatite nanocrystals. *J. Cryst. Growth* **270**, 197–202 (2004).
206. Zakharov, N. A. *et al.* Synthesis and properties of calcium hydroxyapatite/silk fibroin organomineral composites. *Inorg. Mater.* **53**, 333–342 (2017).
207. Huang, T. *et al.* 3D-printed scaffolds of biomineralized hydroxyapatite nanocomposite on silk fibroin for improving bone regeneration. *Appl. Surf. Sci.* **467–468**, 345–353 (2019).
208. Heimbach, B., Tonyali, B., Zhang, D. & Wei, M. High performance resorbable composites for load-bearing bone fixation devices. *J. Mech. Behav. Biomed. Mater.* **81**, 1–9 (2018).
209. Kim, J. H. *et al.* 3D silk fibroin scaffold incorporating titanium dioxide (TiO<sub>2</sub>) nanoparticle (NPs) for tissue engineering. *Int. J. Biol. Macromol.* **68**, 158–168 (2014).
210. Kim, J. *et al.* International Journal of Biological Macromolecules Osteoinductive silk fibroin / titanium dioxide / hydroxyapatite hybrid scaffold for bone tissue engineering. *Int. J. Biol. Macromol.* **82**, 160–167 (2016).
211. Wang, L. *et al.* Application of injectable silk fibroin/graphene oxide hydrogel combined with bone marrow mesenchymal stem cells in bone tissue engineering. *Colloids Surfaces A Physicochem. Eng. Asp.* **604**, 125318 (2020).

212. Aliramaji, S., Zamanian, A. & Mozafari, M. Super-paramagnetic responsive silk fibroin/chitosan/magnetite scaffolds with tunable pore structures for bone tissue engineering applications. *Mater. Sci. Eng. C* **70**, 736–744 (2017).
213. Brito-Pereira, R. *et al.* Silk fibroin-magnetic hybrid composite electrospun fibers for tissue engineering applications. *Compos. Part B Eng.* **141**, 70–75 (2018).
214. Karahaliloğlu, Z., Yalçın, E., Demirbilek, M. & Denkbaş, E. B. Magnetic silk fibroin e-gel scaffolds for bone tissue engineering applications. *J. Bioact. Compat. Polym.* **32**, 596–614 (2017).
215. Tanasa, E. *et al.* Impact of the magnetic field on 3T3-E1 preosteoblasts inside SMART silk fibroin-based scaffolds decorated with magnetic nanoparticles. *Mater. Sci. Eng. C* **110**, 1–13 (2020).
216. Chicheł, A., Skowronek, J., Kubaszewska, M. & Kanikowski, M. Hyperthermia - Description of a method and a review of clinical applications. *Reports Pract. Oncol. Radiother.* **12**, 267–275 (2007).
217. Kolosnjaj-Tabi, J., Marangon, I., Nicolas-Boluda, A., Silva, A. K. A. & Gazeau, F. Nanoparticle-based hyperthermia, a local treatment modulating the tumor extracellular matrix. *Pharmacol. Res.* **126**, 123–137 (2017).
218. Wang, J., Zhang, Y., Jin, N., Mao, C. & Yang, M. Protein-Induced Gold Nanoparticle Assembly for Improving the Photothermal Effect in Cancer Therapy. *ACS Appl. Mater. Interfaces* **11**, 11136–11143 (2019).
219. Kojic, N. *et al.* Focal infection treatment using laser-mediated heating of injectable silk hydrogels with gold nanoparticles. *Adv. Funct. Mater.* **22**, 3793–3798 (2012).
220. Sohail, A., Ahmad, Z., Bég, O. A., Arshad, S. & Sherin, L. Revue sur le traitement par hyperthermie médiée par nanoparticules. *Bull. Cancer* **104**, 452–461 (2017).
221. Qian, K.-Y. *et al.* Injectable ferrimagnetic silk fibroin hydrogel for magnetic hyperthermia ablation of deep tumor. *Biomaterials* **259**, 120299 (2020).
222. Deng, Z. *et al.* A general strategy for designing NIR-II emissive silk for their in vivo monitoring of an implanted stent model beyond 1500 nm. *J. Mater. Chem. B* **8**, 4587–4592 (2020).
223. Fan, S. *et al.* Super-strong and Intrinsically Fluorescent Silkworm Silk from Carbon Nanodots Feeding. *Nano-Micro Lett.* **11**, 1–11 (2019).
224. Tao, H. *et al.* Gold nanoparticle-doped biocompatible silk films as a path to implantable thermo-electrically wireless powering devices. *Appl. Phys. Lett.* **97**, (2010).

225. Ranjana, R., Parushuram, N., Harisha, K. S., Asha, S. & Sangappa, Y. Silk fibroin a bio-template for synthesis of different shaped gold nanoparticles: Characterization and ammonia detection application. *Mater. Today Proc.* (2019) doi:10.1016/j.matpr.2019.11.259.
226. Sohail Haroone, M. *et al.* Luminous composite ultrathin films of CdTe quantum dots/silk fibroin co-assembled with layered doubled hydroxide: Enhanced photoluminescence and biosensor application. *J. Mater.* **4**, 165–171 (2018).
227. Yin, H., Ai, S., Shi, W. & Zhu, L. A novel hydrogen peroxide biosensor based on horseradish peroxidase immobilized on gold nanoparticles-silk fibroin modified glassy carbon electrode and direct electrochemistry of horseradish peroxidase. *Sensors Actuators, B Chem.* **137**, 747–753 (2009).
228. Yin, H., Ai, S., Xu, J., Shi, W. & Zhu, L. Amperometric biosensor based on immobilized acetylcholinesterase on gold nanoparticles and silk fibroin modified platinum electrode for detection of methyl paraoxon, carbofuran and phoxim. *J. Electroanal. Chem.* **637**, 21–27 (2009).
229. Guo, C., Hall, G. N., Addison, J. B. & Yarger, J. L. Gold nanoparticle-doped silk film as biocompatible SERS substrate. *RSC Adv.* **5**, 1937–1942 (2015).
230. Liu, J. *et al.* Surface enhanced Raman scattering (SERS) fabrics for trace analysis. *Appl. Surf. Sci.* **386**, 296–302 (2016).
231. Zhang, S. *et al.* Body-Integrated, Enzyme-Triggered Degradable, Silk-Based Mechanical Sensors for Customized Health/Fitness Monitoring and In Situ Treatment. *Adv. Sci.* **7**, 1–10 (2020).
232. Ma, R. & Tsukruk, V. V. Serigraphy-Guided Reduction of Graphene Oxide Biopapers for Wearable Sensory Electronics. *Adv. Funct. Mater.* **27**, (2017).
233. Han, J. *et al.* Patterning and photoluminescence of CdS nanocrystallites on silk fibroin fiber. *J. Nanoparticle Res.* **12**, 347–356 (2010).
234. Schmucker, A. L. *et al.* Combined chemical and physical encoding with silk fibroin-embedded nanostructures. *Small* **10**, 1485–1489 (2014).
235. Ikawa, T., Sajiki, H. & Hirota, K. Highly chemoselective hydrogenation method using novel finely dispersed palladium catalyst on silk-fibroin: Its preparation and activity. *Tetrahedron* **61**, 2217–2231 (2005).
236. Sajiki, H., Ikawa, T., Yamada, H., Tsubouchi, K. & Hirota, K. Preparation of silk fibroin-supported Pd(0) catalyst for chemoselective hydrogenation: Reduction of palladium(II) acetate by methanol on the protein. *Tetrahedron Lett.* **44**, 171–174 (2003).

237. Aziz, S., Sabzi, M., Fattahi, A. & Arkan, E. Electrospun silk fibroin/PAN double-layer nanofibrous membranes containing polyaniline/TiO<sub>2</sub> nanoparticles for anionic dye removal. *J. Polym. Res.* **24**, 0–6 (2017).
238. Liu, H., Wang, Z., Li, H., Wang, H. & Yu, R. Controlled synthesis of silkworm cocoon-like  $\alpha$ -Fe<sub>2</sub>O<sub>3</sub> and its adsorptive properties for organic dyes and Cr(VI). *Mater. Res. Bull.* **100**, 302–307 (2018).
239. Kim, J. W., Ki, C. S., Um, I. C. & Park, Y. H. A facile fabrication method and the boosted adsorption and photodegradation activity of CuO nanoparticles synthesized using a silk fibroin template. *J. Ind. Eng. Chem.* **56**, 335–341 (2017).
240. Osman, A. M., Wong, K. K. Y. & Fernyhough, A. ABTS radical-driven oxidation of polyphenols: Isolation and structural elucidation of covalent adducts. *Biochem. Biophys. Res. Commun.* **346**, 321–329 (2006).

## Chapter II: Design and characterization of gold, silver and iron oxide silk-NPs bionanocomposites

---



## 1. Introduction

This chapter presents the synthesis and characterization of NPs, silk fibroin-NPs (silk-NPs) dispersion preparation and the synthesis and characterization of silk-based materials and bionanocomposites. Although different techniques exist to produce silk-NPs bionanocomposites, as described in chapter I, *in situ* synthesis strategies often result in uncontrolled NP size/shape and state of aggregation, and therefore NPs properties. Hence, the characterization of these parameters is crucial and that is why we proposed to produce well defined NPs, their introduction in SF dispersion prior to formation of the given silk scaffold.

The first part of this chapter focuses on the synthesis and characterization of NPs based on studies previously realized in the laboratory. Accordingly, our approach consists in the synthesis of several controlled NPs upstream with the same functionalization for further incorporation into SF dispersion.

In a second part, the mixture of NPs with SF dispersion and its use to prepare silk-NPs bionanocomposites are studied. We present the possibility of using the same NPs/SF mixture to prepare silk-NPs electrospun materials, hydrogels, cryogels, sponges and additive manufactured bionanocomposites. Moreover, material properties can be adapted to each application and designed on demand.

Furthermore, although many SF bionanocomposites have been developed, the impact of NP incorporation on the silk structure and properties remains poorly documented. Most of the studies reported in the literature focus on the key acquired property due to NP incorporation, such as for example antibacterial activity for silver NPs (Ag NPs). Yet, an in-depth characterization of silk-NPs bionanocomposites is a pivotal step for guiding the design of functional materials with biologically relevant applications. This section ends with an in deep characterization of the physicochemical and biological properties of silk-NPs hydrogel bionanocomposites.

## 2. Materials and methods

### 2.1. Materials

Hydrogen tetrachloroaurate (III) ( $\text{HAuCl}_4 \cdot 3\text{H}_2\text{O}$ ,  $\geq 99.9\%$ ), silver nitrate ( $\text{AgNO}_3$ ,  $\geq 99.9\%$  alfa aesar), sodium ascorbate, iron (II) chloride tetrahydrate ( $\text{FeCl}_2 \cdot 4\text{H}_2\text{O}$ ,  $\geq 99.9\%$ ), iron (III) chloride hexahydrate ( $\text{FeCl}_3 \cdot 6\text{H}_2\text{O}$ ,  $\geq 99.9\%$ ), sodium carbonate ( $\text{Na}_2\text{CO}_3$ , 99.8%, anhydrous), hydrogen peroxide ( $\text{H}_2\text{O}_2$ , 35 wt.%) and Nunc Thermanox plastic coverslips (174934) were purchased from Fisher Scientific. HMBP- $\text{C}\equiv\text{CH}$  (1-hydroxy-1-phosphonohept-6-ynyl) phosphonic acid was synthesized as previously reported <sup>1</sup>. *Bombyx mori* silk cocoons were obtained from Stef Francis (Newton Abbot, GB).

Lithium bromide (LiBr, reagent plus  $\geq 99.9\%$ ); horseradish peroxidase type VI (HRP, P8375); PDMS (Sylgard 184); gelatin from porcine skin (G1890); 2,2'-Azino-bis (3-Ethylbenzthiazoline-6-Sulfonic Acid) (ABTS); Acridine Orange (A6014); phosphate buffered saline solution (PBS); DAPI (28718-90-3); phalloidin Sulfo-Rhodamine SR101 (FP-033991) and 3-(4,5-dimethylthiazol-2-yl)-5-(3-carboxymethoxyphenyl)-2-(4-sulfophenyl)-2H-tetrazolium (MTS) reagent (CellTiter 96® AQueous One Solution Cell Proliferation Assay (MTS), Promega) were purchased from Sigma Aldrich.

Trypsin 0.25% - EDTA, Dulbecco's Modified Eagle's Medium (DMEM), L-glutamine (200 mM), fetal bovine serum (A3160801) and penicillin (10,000 U/mL) - streptomycin (10,000  $\mu\text{g/mL}$ ) were purchased from GIBCO, Life technologies. Laponite XLG was purchased from BYK additives, Southern Clay Products.

### 2.2. Nanoparticle synthesis

#### 2.2.1. Gold nanoparticles

Gold nanoparticles (Au NPs) were synthesized by adapting a protocol previously described for Pd NPs <sup>2</sup>. 19 mL of demineralized water were mixed with 250  $\mu\text{L}$  of  $\text{HAuCl}_4$  (20 mM) and 500  $\mu\text{L}$  of HMBP- $\text{C}\equiv\text{CH}$  ( $\text{pK}_a$  values are 1.9, 2.8, 6.8 and 10.2 <sup>3</sup>) dispersed in water solution (40 mM) previously adjusted at  $\text{pH} = 10$ . The solution was placed under vigorous stirring at room temperature (RT) and 55  $\mu\text{L}$  of sodium ascorbate (17.6  $\text{mg L}^{-1}$ ) were added. The reaction was considered finished after 30 min. Suspensions were dialyzed to remove potential traces of unreacted materials (MWCO 100 kDa) and then stocked at 4 °C.



### 2.2.2. Silver nanoparticles

Silver nanoparticles (Ag NPs) synthesis follow a similar protocol to that of Au NPs. 19 mL demineralized water was mixed with 11.76  $\mu\text{L}$  of  $\text{AgNO}_3$  (850 mM) and 1 mL of HMBP- $\text{C}\equiv\text{CH}$  water solution (40 mM) previously adjusted at  $\text{pH} = 10$ . 110  $\mu\text{L}$  of sodium ascorbate (17.6  $\text{mg L}^{-1}$ ) were added just before heating the mixture under microwave. Microwave synthesis reactor (Monovawe 300, Anton Paar GmbH) was programed to follow three steps: (i) quick heating step to reach 100  $^{\circ}\text{C}$ ; (ii) temperature hold during 15 minutes and (iii) temperature decrease to 55  $^{\circ}\text{C}$ . Stirring was carried out with a magnetic stirrer at 1200 rpm during all the reaction time. Suspensions were dialyzed to remove potential traces of unreacted materials (MWCO 100 kDa) and then stocked at 4  $^{\circ}\text{C}$ .

### 2.2.3. Iron oxide nanoparticles

Iron oxide nanoparticles (IONPs) were synthesized by an alkaline co-precipitation method. 0.01 mol of  $\text{FeCl}_2 \cdot 4\text{H}_2\text{O}$  were dissolved in 7.5 mL of HCl 1 M to prevent premature oxidation of  $\text{Fe}^{2+}$  to  $\text{Fe}^{3+}$  in aqueous solutions. 0.02 mol of  $\text{FeCl}_3 \cdot 6\text{H}_2\text{O}$  were dissolved in 160 mL of water, and mixed with the ferrous solution in an ultrasound bath. The obtained  $\text{Fe}^{2+} / \text{Fe}^{3+}$  solution was added, with a peristaltic pump set at 400  $\text{mL min}^{-1}$ , into a reactor with a controlled temperature ( $T = 30^{\circ}\text{C}$ ) containing 84 mL of 2 M NaOH solution. Reaction was carried under constant stirring at 2000 rpm during 2 h. At this point a 2,5 M HCl solution was used to neutralize the remaining NaOH. The dispersion was then placed at neutral pH as NPs are not charged and can easily be separated by magnetic force. Neodymium magnets were used to induce NPs precipitation. Water was added to the precipitated NPs to wash them. The procedure was repeated three times. Then, pH was set to 2 by adding 1M HCl to stabilize the obtained IONPs. The IONPs suspension was stored at 4 $^{\circ}\text{C}$ .

The resultant NPs were coated posteriorly with HMBP- $\text{C}\equiv\text{CH}$ . A solution of  $0.34 \times 10^{-6}$  M HMBP- $\text{C}\equiv\text{CH}$  was prepared in water and adjusted at pH 2 by adding 1M HCl. This solution was mixed with IONPs ( $\sim 0.2$  M) in a 1:1 volume ratio and stirred for 2 hours. The resultant suspension was sonicated for 30 minutes. Ligand excess was removed by washing the NPs at a  $\text{pH} = 2$ , by allowing NP precipitation in presence of a magnetic field, removing supernatant and suspending the precipitated NPs in HCl  $10^{-2}$  M. The procedure was repeated three times. NPs were then suspended in water at pH 7 as a stable colloidal suspension. Suspension was stored at 4 $^{\circ}\text{C}$ .

## 2.3. Nanoparticle characterization

### 2.3.1. IONPs concentration determination

The iron concentration of IONPs dispersions were calculated by a direct and indirect method. For direct method UV-vis spectrometry was used to measure absorbance at 480 nm of a diluted IONPs dispersion. The Beer-Lambert Law gives the correlation between the obtained absorbance and the dispersion concentration. Herein we used  $\varepsilon = 420 \text{ L mol}^{-1} \text{ cm}^{-1}$ .

$$[Fe] = \frac{Abs \times Dilution\ factor}{\varepsilon \times L} \quad (II.1)$$

However, this is only and approximate concentration given that  $\varepsilon$  is highly dependent on the size of the obtained NPs. The exact iron concentration can be calculated by an indirect method using KSCN. Herein a complete oxidation is required to convert all iron ions into  $Fe^{3+}$ , which is able to form the  $FeSCN^{2+}$  complex (as described in equation (II.2)) whose maximum absorbance is found at 475 nm.



By using the approximate concentration determined by direct method, 15 mM IONPs dispersions were prepared and 10  $\mu\text{L}$  were added into a 15 mL falcon. The iron oxidation was carried out by adding 100  $\mu\text{L}$  of 20 %  $H_2O_2$  and 100  $\mu\text{L}$  of 7 M  $HNO_3$ . Mixtures were heated at 80°C between 2-3 h. Cooled samples were then mixed with 1 mL  $H_2O$  and 100  $\mu\text{L}$  of 2 M KSCN. The addition of KSCN results in a reddish color apparition with a specific UV-vis maximum absorbance at 475 nm. UV-vis absorbance at 475 nm was measured immediately after KSCN addition using a Perkin Elmer Lambda 12 UV-vis spectrophotometer in 1 cm path length quartz cuvette at room temperature. Calibration curve was obtained by preparing solutions with known iron concentrations, processing them in the same manner and plotting the absorbance as function of the iron concentrations. Experimental  $\varepsilon$  was determined from the calibration curve and used to determine sample iron concentration (Equation (II.1)).

### 2.3.2. UV-vis spectrophotometry

Absorbance scans of all NPs suspensions (Au NPs ~ 0.25 mM, Ag NPs ~ 0.5 mM and IONPs ~ 0.5 mM) were performed between 200 and 800 nm using a Perkin Elmer Lambda 12 UV-vis spectrophotometer in 1 cm path length quartz cuvette at room temperature.

### 2.3.3. Dynamic light scattering (DLS)

The hydrodynamic diameter and  $\zeta$  potential of NPs in aqueous media was analyzed by means of DLS at 25 °C using a Zetasizer ULTRA (Malvern) equipped with a monochromatic He-Ne laser beam at a wavelength of 632.8 nm. The experiments were performed on demineralized aqueous suspensions of NPs (pH 7), which were sonicated for 10 minutes before measurements. Results correspond to the Z average of five replicates and the polydispersity index (PDI, in brackets).

### 2.3.4. Transmission Electron Microscopy (TEM)

TEM micrographs were recorded using a JEOL JEM-2100F instrument (Japan) at an acceleration voltage of 200 kV and visualized with a CCD camera. Samples were diluted in deionized water, a drop was added onto a copper mesh grid coated with an amorphous carbon film and allowed to air-dry. The crystallinity and cartography of the NPs was analyzed using selected area electron diffraction (SAED) and high-resolution transmission electron microscopy (HRTEM).

#### 2.3.4.1 Image analysis by Image J

TEM micrographs were analyzed with Image J software to determine NPs crystalline diameter. A script (Figure A.1) was created in which images were converted into 8-bit, contrast was enhanced with a fixed saturation value of 4 and normalized. A band pass filter and a color threshold were applied to the image. Scale bar was set from a previous measurement to convert pixels into nm and the scale bar from the image was removed to avoid its measurement as a particle. Particles parameter were analyzed using the Analyze particle option by setting size from 100-900 (in pixels) and circularity from 0 to 1. An overlay image was created in each case containing the counted NPs with their assigned number (Figure A.2), the calculated values were saved in an excel file.

#### 2.3.4.2 Calculation of the number of NPs $L^{-1}$ for each synthesis

The concentration in terms of number of NPs  $L^{-1}$  was calculated for each system. To do so, NPs were assimilated to spheres and NPs crystalline diameters (previously calculated from TEM image analysis) were used to calculate the volume of a sphere with the corresponding diameter ( $V_{sph}$ ). The number of Au, Ag and Fe atoms in each suspension was calculated from the solutions concentrations by using the Avogadro's number. The number of NPs  $L^{-1}$  was calculated by using the following equation:

$$NPs\ L^{-1} = \frac{[NPs\ solution] \times N_A}{\left(\frac{V_{sph}}{V_{unit\ cell}} \times A_{unit\ cell}\right)} \quad (II.3)$$

Where [NPs solution] is the concentration on Au, Ag or Fe within the suspension;  $N_A$  is Avogadro's number;  $V_{sph}$  is the volume of the sphere previously calculated;  $V_{unit\ cell}$  is the corresponding volume of the crystalline unit cell ( $6.74 \times 10^{-2} \text{ nm}^3$  for Fcc Au,  $6.82 \times 10^{-2} \text{ nm}^3$  for Fcc Ag and  $5.92 \times 10^{-1} \text{ nm}^3$  for Fcc  $\text{Fe}_3\text{O}_4$ ) and  $A_{unit\ cell}$  is the number of atoms per unit cell.

### 2.3.5. Determination of the number of HMBP-C $\equiv$ CH molecules / surface

The number of HMBP-C $\equiv$ CH molecules per  $\text{nm}^2$  into the surface of NPs were evaluated by Energy dispersive X-ray (EDX). NPs suspensions were deposited over a carbon support for SEM / EDX analysis allowing the obtention of the phosphor (contained within HMBP-C $\equiv$ CH) to metal (Au, Ag or Fe) ratio ( $R_{P:M}$ ).

NPs were assimilated to spheres and NPs crystalline diameters (previously calculated from TEM image analysis) were used to calculate the volume of a sphere with the corresponding diameter ( $V_{sph}$ ). Then the number of metal (Au, Ag or Fe) atoms per NP was calculated by using the following formula:

$$N^{\circ}\ metal\ atoms \cdot NP^{-1} = \frac{V_{sph}}{(V_{unit\ cell} \times A_{unit\ cell})} \quad (II.4)$$

The number of P atoms per NP was then calculated from the  $N^{\circ}$  of metal atoms calculated with equation (II.4) and the P to metal ratio obtained from EDX ( $R_{P:M}$ ) as described in the following equation:

$$N^{\circ}\ P\ atoms \cdot NP^{-1} = \frac{N^{\circ}\ metal\ atoms \cdot NP^{-1}}{R_{P:M}} \quad (II.5)$$

Each HMBP-C $\equiv$ CH molecule composed of two P atoms, the number of HMBP-C $\equiv$ CH molecules per NP is obtained by dividing the  $n^{\circ}$  of P atoms  $\cdot NP^{-1}$  by two. The division of the obtained number of HMBP-C $\equiv$ CH molecules by the NP surface area allows the estimation of the surface occupied by each HMBP-C $\equiv$ CH molecule.

## 2.4. Silk fibroin dispersion preparation

SF dispersion was obtained as described elsewhere <sup>4</sup>. Briefly *Bombyx mori* silk cocoons were cut into small pieces and boiled for 30 min in a 0.02 M sodium carbonate (Na<sub>2</sub>CO<sub>3</sub>) solution to remove sericin. The resultant fibers were rinsed three times with abundant demineralized water and dried under a chemical hood overnight. Dried fibers can be stocked at room temperature indefinitely.

SF fibers were dispersed by placing them in a 9.3 M lithium bromide (LiBr) solution and ensuring that they are all in contact with the solution. The suspension was incubated at 60 °C during maximum 4h. The resultant honey-like dispersion was dialyzed for 48 h against 2 L of distilled water in a dialysis cassette (3,500 MWCO, Thermo Fisher Scientific). Insoluble residues were removed by centrifuging twice at 9,000 rpm for 20 min. SF dispersion was stored at 4 °C. Storage time is limited at this stage as dispersion gels after approximately 1 month.

The SF concentration of the obtained dispersion was calculated by weighting a small volume of the dispersion, letting it dry and weighting the dry SF. equation (II.6) was used to calculate SF concentration (w/w). In general, 6 % SF dispersions are used.

$$SF \% = \frac{W_{dried\ SF} - W_{empty\ weight\ boat}}{W_{wet\ SF} - W_{empty\ weight\ boat}} \times 100 \quad (II.6)$$

## 2.5. Silk bionanocomposites synthesis

### 2.5.1. Electrospinning

SF dispersion was placed in dialysis cassette at RT to allow water evaporation until a 10 – 20% SF concentration was obtained. Even after SF concentration the surface tension of SF is not high enough for electrospinning and has to be increased by mixing with other polymers such as polyethylene oxide (PEO MM=900 kDa, M<sub>v</sub> ~900,000, Sigma-Aldrich). The electrospinning dispersion was prepared by mixing 10 % SF with 5 % PEO in a 1:4 volume ratio.

The prepared electrospinning dispersion was placed into a 5 mL plastic syringe with a 19 G stainless steel needle connected to a high voltage generator (Gamma High Voltage Research ES-30P Ormond Beach, FL, USA). A grounded flat Plexiglas collector, covered with an aluminum foil to allow electric conductivity, was placed in front of the needle tip at a distance of 20 cm. Electrospinning dispersion was dispensed with a syringe pump (Thermo Scientific, Waltham, MA) at a flow rate of 0.015 mL·min<sup>-1</sup> while a voltage between 9-10 kV was applied

to the needle tip. Sample was collected during 50-120 minutes for mat formation. Relative humidity ranged between 30-50%.

At this stage, sample is soluble in water. This can be avoided by the formation of  $\beta$  sheet structures through water annealing. To do so, collected samples were placed under vacuum in presence of water for at least 4h. Samples were then immersed in water at 37°C during 48 h to remove PEO. Samples were then dried and stored at RT. The functionalization of silk electrospun materials was carried out using two methods: the addition of NPs to the SF electrospinning dispersion or posterior functionalization of the electrospun silk material.

#### 2.5.1.1 Addition of NPs to electrospinning dispersion

NPs can be incorporated to SF dispersion before or after its concentration for electrospinning. Silk-Au NPs, silk-Ag NPs or silk-IONPs electrospinning dispersions were prepared by mixing 1005  $\mu\text{L}$  of 15.92 % SF dispersion with 595  $\mu\text{L}$  NPs ( $\sim 0.25$  mM Au NPs,  $\sim 0.5$  mM Ag NPs or 160 mM IONPs) and 400  $\mu\text{L}$  5 % PEO.

#### 2.5.1.2 Electrospun material functionalization with NPs

Posterior functionalization has been carried by two different methods: *ex situ* and *in situ*. *Ex situ* functionalization was done by adding 500  $\mu\text{L}$  of  $\sim 0.25$  mM Au NPs or 0.21 M IONPs (non HMBP-C $\equiv$ CH coated) over 1  $\text{cm}^2$  electrospun silk mat and allowing it to air dry. IONPs embedded sample was then washed with water and 400  $\mu\text{L}$  of HMBP-C $\equiv$ CH (44 mM pH 10) were placed on top for 30 minutes. Au NPs and IONPs embedded materials were rinsed with abundant water to remove excess NPs and let to air dry. Samples were stored at RT. This procedure can be repeated to obtain a material containing a higher concentration of NPs.

*In situ* synthesis can be achieved for Au NPs and Ag NPs. Au NPs are synthesized at RT their synthesis over a material is easier. Herein a 4  $\text{cm}^2$  electrospun silk mat was placed in a concave glass support. The *in situ* reaction was carried at RT by adding 250  $\mu\text{L}$  of  $\text{HAuCl}_4$  (20 mM), 500  $\mu\text{L}$  of HMBP-C $\equiv$ CH (44 mM pH 10) and 55  $\mu\text{L}$  sodium ascorbate (17.6  $\text{mg mL}^{-1}$ ) in a first step. Solution was mixed and then 500  $\mu\text{L}$  of demineralized water and 55  $\mu\text{L}$  sodium ascorbate (17.6  $\text{mg mL}^{-1}$ ) were added. Finally, 1 mL of demineralized water and 25  $\mu\text{L}$  of  $\text{HAuCl}_4$  (20 mM) were added to induce reaction.

Ag NPs were *in situ* synthesized over a 4  $\text{cm}^2$  electrospun silk mat by placing it in a concave surface and adding 1 mL demineralized water, 5  $\mu\text{L}$   $\text{AgNO}_3$  (0.2125 M), 100  $\mu\text{L}$  HMBP-C $\equiv$ CH (44 mM pH 10) and 10  $\mu\text{L}$  sodium ascorbate (17.6  $\text{mg mL}^{-1}$ ). Sample was placed in a water

bath and heated at 80°C for 30 minutes. Sample was removed washed with abundant water and left to air dry and stored at RT.

### 2.5.2. Hydrogels

SF hydrogels were synthesized by following the protocol originally described by Partlow et al<sup>5</sup>. For SF hydrogels 6% SF dispersion was mixed either with water or NPs suspension (final concentration of ~0.155 mM, ~0.153 mM and 0.2 mM for Au NPs, Ag NPs and IONPs respectively) in a 1:1.6 ratio. Gelation was induced by adding 10 units of horseradish peroxidase (1 U·μL<sup>-1</sup>, HRP type VI, Sigma Aldrich) and 10 μL of 1 % hydrogen peroxide (H<sub>2</sub>O<sub>2</sub>, Sigma Aldrich) per mL of silk dispersion. Table II.1 recapitulates the volume ratios.

**Table II.1.** Volume ratios in SF hydrogel. NPs dispersion used were Au NPs ~ 0.25 mM, Ag NPs ~ 0.5 mM and IONPs up to ~ 150 mM.

Dispersions	Volume ratio
SF / H <sub>2</sub> O or NPs dispersion	1:1.6
HRP / SF	1:100
H <sub>2</sub> O <sub>2</sub> / SF	1:100

Gelation was carried out in PDMS molds (Figure A.3) for easy post manipulation and in a glass desiccator in presence of two water-containing beakers to increase humidity and avoid gel evaporation. Gelation time was dependent on the gel final volume (4-72 h).

### 2.5.3. Cryogels

SF cryogels were prepared by freeze drying swelled hydrogels previously frozen either with liquid N<sub>2</sub>, or by placing them at -20 or -80 °C freezer.

### 2.5.4. Sponges

SF sponges were prepared using a salt leaching method as described by Rockwood et al<sup>4</sup>. 1 mL of SF (6%) dispersion was mixed with 2 g of sodium chloride crystals with a controlled diameter between 200-400 μm. The mixing process is very important to ensure a homogeneous material as SF gelation occurs almost instantaneously. The two components were mixed by pouring them at the same time into the final recipient while slowly turning it. Remaining air bubbles were removed by gently tapping the recipient against the bench top. Once mixed, samples were left at room temperature O/N to gel.

Salt from gelled samples was removed by immersing the recipient in demineralized water and stirring. Water was renewed at least 6 times during 48 h. At this point silk sponges were



removed from their recipient and placed in demineralized water for 24 h and water changes were performed regularly. Samples can be stored in water at 4 °C or dried at RT.

Silk-NPs sponge bionanocomposites were prepared by mixing a concentrated SF dispersion (13.65 %) with Au NPs (~ 0.5 mM) or IONPs (~ 74.5 mM) aqueous dispersion in a 1:1 volume ratio. 1 mL of the blended dispersion was then used to obtain sponges by mixing with 2 g of sodium chloride crystals (200 – 400 µm) and following the procedure previously explained.

### 2.5.5. 3D printing

Silk 3D printed structures were prepared by using two different methodologies. The first one enables the printing a silk / NPs bioink into a salt bath <sup>6</sup>. The second uses a blended dispersion of silk, gelatin, glycerol and NPs to be printed into a laponite suspension.

#### 2.5.5.1 SF bioink into salt bath

SF dispersion or SF/NP blended dispersions were placed in dialysis cassette at 4 °C to allow water evaporation until a 25 – 30 % SF concentration was reached. Specifically, 74 mL of 7 % SF dispersion were mixed with 2 mL of 160 mM IONPs and 75 mL 7 % SF were mixed with 3 mL ~ 0.5 mM Au NPs dispersion prior to concentration. Concentrated dispersion was placed into a 3 mL syringe. Multilayered (up to 10 layers) square simple mesh structures were designed with side length of 6 mm. G code commands were manually written to control the print path. Samples were printed using an Inkredible 3D printer (Cellink, Sweden) using compressed air to extrude silk ink through a 33G chamfered dispensing nozzle. Silk ink was extruded to the bottom of a salt bath (4 M NaCl and 0.5 M K<sub>2</sub>PO<sub>3</sub>). Air pressure and printing speed were 210 kPa and 1 mm·s<sup>-1</sup> respectively. Once printed samples were rinsed with deionized water and freeze dried for long time conservation.

#### 2.5.5.2 Blended SF/gelatin/glycerol bioink into laponite bath

SF dispersion was placed in dialysis cassette at RT to allow water evaporation until a 20 - 40% SF concentration was reached. Bioink formulation was prepared by mixing SF/gelatin/glycerol (70%) at a 3:3:1 ratio. 400 µL of Au NPs (~ 0.25 mM), Ag NPs (~ 0.25 mM) or IONPs (160 mM) were incorporated to the formulation while silk and gelatin final concentrations were set to 10% (w/w). A laponite nanoclay suspension was prepared by dissolving Laponite XLG (BYK additives, Southern Clay Products) in deionized water. The suspension was stirred at room temperature and left stirring at 60 RPM for 8 hours. The suspension was then allowed to settle for an additional 8 hours.



The printing process was carried out using a homemade 3D printer. Briefly, a cylindrical design was developed in Solidworks and sliced using Repetier software. The bioink was placed in a 5 mL syringe (Becton-Dickinson), extruded through a 23G needle into a 6-well cell culture plate containing a laponite suspension as previously described in the literature <sup>7</sup>. Extrusion rate and printing speed were tuned for optimal deposition of the filament in the laponite suspension. The printed constructs were placed at -20°C overnight and lyophilized. After freeze-drying, the constructs were removed from the dried laponite and placed in a methanol solution, to ensure water-insolubility. Samples were stored at RT.

## 2.6. Hydrogel characterization

### 2.6.1. Enzyme activity assay

The catalytic activity of HRP was evaluated by monitoring the oxidation of ABTS<sup>2-</sup> (also referred as ABTS) by H<sub>2</sub>O<sub>2</sub> by UV-Vis spectrophotometry. Reaction was done in quartz cuvette containing 315 µL of demineralized water; 615 µL of ~ 0.25 mM Au NPs or 0.325 mM IONPs suspension or water; 10 µL of H<sub>2</sub>O<sub>2</sub> 1% and 10 µL of HRP (~ 2 U mL<sup>-1</sup>) and 50 µL ABTS<sup>2-</sup> (20 mM). The production of ABTS<sup>•+</sup> (also referred as ABTS<sup>++</sup> by some authors <sup>8</sup>) was evaluated by UV-vis spectrophotometry by measuring the absorbance of a given solution at 420 nm during the first 2 minutes of reaction at room temperature. The possibility of ABTS<sup>2-</sup> oxidation in presence of NPs but without HRP was also evaluated.

### 2.6.2. Hydrogel thickness to volume correlation

Hydrogels of different volumes (Table II.2) were prepared in 24 well plate to evaluate whether the thickness to volume correlation is linear. Hydrogels were prepared in triplicate for each condition. Hydrogel thickness was measured with a caliper after a gelation time of 72 h.

**Table II.2.** Solution volumes used to prepare silk hydrogels with different final volume

Solutions	Volume ( $\mu\text{L}$ )			
	1	2	3	4
SF 6 %	200	300	400	600
H <sub>2</sub> O or NPs	320	480	640	960
HRP	2	3	4	6
H <sub>2</sub> O <sub>2</sub>	2	3	4	6

### 2.6.3. Scanning Electron Microscopy

Scanning electron microscopy (SEM) images were taken using FEI Quanta FEG 250 instrument. In some cases, SF samples were metalized with a 5 nm gold layer using a Quorum Q150R S sputter for higher image resolution.

### 2.6.4. Confocal fluorescence microscopy

Swollen hydrogels were stained by immersion in an acridine orange solution for 5 minutes. Samples were abundantly rinsed with demineralized water three times to remove excess acridine orange. Samples were visualized with a Zeiss (LSM 710, 40x/1.40 Oil DIC) microscope.

### 2.6.5. UV-visible spectrophotometry

Samples were analyzed with Perkin Elmer Lambda 12 UV-vis spectrophotometer. Silk and silk-NPs hydrogels were prepared in quartz cuvettes and absorption scan between 300-800 nm were recorded 24h later.

### 2.6.6. Hydrogel gelation kinetics (fluorescence spectrometry)

Fluorescence spectra were obtained with Cary Eclipse Fluorescence spectrometer (Agilent Technologies) and 1 cm path length quartz cuvettes. Measures were carried out at 25 °C. Excitation and emission slits were set at 5 nm and the photomultiplier was set at -500V. Spectrometer scan was set to analyze samples' emission (300-600 nm) every 10 minutes when excited at 290 and 340 nm. Gelation kinetics were monitored for 240 minutes.

### 2.6.7. Swelling behavior

Swelling percentage ( $S_w\%$ ) was evaluated by weight gain. 400  $\mu\text{L}$  samples were prepared in a PDMS mold ( $\varnothing$  10 mm  $h$  = 5 mm) and let gel for 24 h. Once gelled sample weight was measured ( $W_0$ ) and samples were individually immersed in deionized water. Weight was measured over the time ( $W_{xh}$ , where  $xh$  represents the time in hours at which sample has been measured) by taking the sample out from water and carefully removing excess water before weighting. Swelling percentage was calculated as follows:

$$S_w\% = \frac{W_0 - W_{xh}}{W_0} \times 100 \quad (\text{II.7})$$

Due to possible damage during gel manipulation different samples were used for each time point. Three different gels were measured at each time point to evaluate sample variability.

### 2.6.8. Compression tests

Unconfined compression tests were evaluated with Shimadzu Autograph AGS-X over cylindrical probes using a 100 N captor. Cylindrical probes were prepared in 24 well plate with a final volume of 2.6 mL and let gel for 72 h. Gelled probes were immersed in demineralized water for 48 h to ensure that they were all at the same hydration state when tested. Height and diameter of the probes were measured with a digital caliper before tests. Measurements were done 6 times to minimize measurement error. Probe was placed between two stainless steel parallel plates. Upper plate was then lowered towards the sample without contact and the test was performed.

Unconfined compression tests were done in texture mode, compression tests. Tests methodology was set into three steps: (i) pretest (ii) test and (iii) end of experiment. In pretest step, the upper plate lowering speed was set to 1 mm  $\text{min}^{-1}$  until a 0.005 N force is detected. For test step lowering speed was set to 0.5 mm  $\text{min}^{-1}$  until probe breaking (force drops under 50 % of the maximum measured value) or 75 % strain was reached. Force measurements were recorded every 0.5% strain variation.

Given the elastomeric behavior of silk hydrogels, compression modulus is dependent on the strain. Therefore compression modulus was calculated at 20 and 40 % strain points as in Partlow et al.<sup>4</sup>. Reproducibility was assured by testing at least four different samples for each condition ( $n \geq 4$ ). Results are given as mean  $\pm$  standard deviation. Two-way ANOVA (analysis of variance) with Tukey's post hoc multiple comparison tests were performed using R software to determine statistical significance within all different conditions. As a result, different conditions

are classified within different letter groups if a significant difference is found ( $p$  adj value  $\leq 0.05$ ).

### 2.6.9. Attenuated Total Reflectance Fourier Transformation Infrared Spectroscopy

Infrared spectra were recorded with an Agilent Technologies Cary 600 series FTIR with an attenuated total reflectance (ATR) with germanium crystal. The data resulted from averaging 16 scans at a resolution of  $4\text{ cm}^{-1}$ . To be able to do FTIR the samples were dried at  $4^{\circ}\text{C}$  previous to ATR-FTIR analysis.

### 2.6.10. Biocompatibility evaluation

#### 2.6.10.1 Cytotoxicity

Indirect cytotoxicity of hydrogels with and without NPs were evaluated as described by ISO 10993-5. Hydrogels were prepared in cylindrical PDMS mold (base diameter was 16.6 mm). Sample final volume was  $500\text{ }\mu\text{L}$ . Hydrogels were left to gel for 72 h in a desiccator in presence of water to limit hydrogels evaporation. Samples were sterilized by 30-minute immersion in ethanol 70 %. Samples were immersed either in water or in DMEM culture media for 48 h to achieve complete hydration. Samples were transferred to a falcon tube and extraction media ((DMEM, supplemented by 10% fetal bovine serum, 1% L-glutamine and 1% antibiotics (Penicillin/Streptomycin)) was added. Latex ( $1\text{ cm}^2$ ) was used as positive control. Extraction was performed for 24 h at  $37^{\circ}\text{C}$  under constant agitation.

In parallel, a 96 well plate was seeded with L929 cells at a  $1 \times 10^4$  cell / well concentration. Plate was incubated at  $37^{\circ}\text{C}$ , 5%  $\text{CO}_2$  for 24 h to allow cell adhesion. Cell adhesion and homogeneous distribution was evaluated by optical microscopy. Culture media was removed and  $100\text{ }\mu\text{L}$  of extracted media were added to each well. DMEM culture media (extraction vehicle) and latex extractions were used as positive and negative controls respectively. Samples were incubated at  $37^{\circ}\text{C}$ , 5%  $\text{CO}_2$  for 24 h. At this point cell morphology was evaluated by optical microscopy to assess cell damage and contrast MTS results. MTS reactant (CellTiter 96® AQueous One Solution Cell Proliferation Assay (MTS), Promega) was thaw at  $37^{\circ}\text{C}$  and  $20\text{ }\mu\text{L}$  were added to each well. Cells were incubated for 2 h and absorbance was read at 490 nm with iMark microplate reader (Bio-Rad Laboratories). Samples were tested in triplicate for all conditions.

#### 2.6.10.2 Cell adhesion and immunostaining

20  $\mu\text{L}$  of hydrogel mixture were placed over 10 mm diameter coverslips and let gel O/N. Formed hydrogels were sterilized by immersion in 70 % ethanol during 30 minutes. Samples were washed with sterile distilled water three times. Human dermal fibroblast (HDF) were cultured over silk hydrogels at a density of 5,000 cells  $\text{cm}^{-2}$  in DMEM media. Samples were incubated at 37°C, 5%  $\text{CO}_2$  for 48 h. After incubation, DMEM media was removed and cells were fixed with 4% formaldehyde during 15 minutes and immuno-stained with DAPI (2  $\mu\text{g mL}^{-1}$ ) and phalloidin Sulfo-Rhodamine SR101 (0.099  $\text{nmol mL}^{-1}$ ) for visualization of nuclei and actin cytoskeleton respectively.

### 3. Results and discussion

#### 3.1. Use of bisphosphonates as NPs stabilizing agents

Bisphosphonates are analogue molecules of the endogenous pyrophosphate (P-O-P). Pyrophosphates result from the metabolism of adenosine triphosphate (ATP) molecules, which are the key energy drivers of all cells. In the body, pyrophosphates play an important role in the control of bone mineralization <sup>9</sup>.

In bisphosphonates, a carbon (P-C-P) replaces the central oxygen atom found in pyrophosphates. As a result, bisphosphonates cannot be degraded in the body and, if not absorbed, are eliminated unaltered by renal filtration. Although absorption is very low, even when administered intravenously, bisphosphonates accumulate mainly in crystalline calcium regions such as bone.

Bisphosphonates inhibit the activity of bone resorption cells called osteoclast. Because of this, bisphosphonates are used to treat diseases where bone resorption occurs such as osteoporosis, Paget's disease and osteogenesis imperfecta <sup>10</sup>. The bisphosphonate most commonly used for osteoporosis treatment is alendronate (Figure II.1). Under the name FOSAMAX® its dosage is of 70 mg once a week <sup>11</sup>.

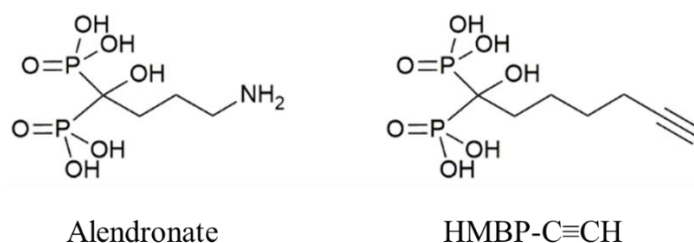


**Figure II.1.** Alendronate (left) and HMBP-C≡CH (right) chemical structures.

Given their use in medicine and their chelating ability for metal ions, bisphosphonates have been coupled to NPs in many occasions <sup>12</sup>. For example bisphosphonates have been used to stabilize superparamagnetic iron oxide NPs used as contrast agents <sup>13</sup>; to synthesize and stabilize gold NPs <sup>1,14</sup>.

In this work, we have chosen (1-hydroxy-1-phosphonohept-6-ynyl) phosphonic acid (HMBP-C≡CH) as stabilizing agent because of the possibility of using simple click chemistry to further functionalize our NPs <sup>1</sup>.

### 3.2. Nanoparticle synthesis

Nanoparticle synthesis procedures are crucial for the NP final properties. As stated before, NP properties strongly depend on their size and shape. Therefore, any synthesis method should be capable of controlling these two parameters. The synthesis of NPs was performed following a bottom up approach that enables a better control and homogeneity over size and shape. Gold and Silver NPs were synthesized by adapting a previously described synthesis of Pd NPs<sup>2</sup>. Gold NPs (Au NPs) were synthesized in aqueous media at RT using a one-pot reaction, which consists in the reduction of  $\text{HAuCl}_4$  salt, by sodium ascorbate in presence of HMBP- $\text{C}\equiv\text{CH}$  as stabilizing agent. This method allows the synthesis of phosphonate-decorated NPs in water with a biocompatible ligand, without a ligand-exchange procedure.

Typical TEM micrograph of the obtained Au NPs showed spherical NPs with a narrow size distribution (mean diameter of  $4.7 \pm 1.2$  nm) (Figure II.2). HRTEM micrographs revealed that NPs are mostly monodomain. Inter-reticular distances were measured using intensity line profiles, revealing the lattice planes distancing by  $d_{200} = 2.1$  Å (Figure II.2 B). SAED patterns clearly showed the diffraction spots corresponding to (111), (200) and (220) crystal planes corresponding to the face centered cubic lattice of gold (Figure II.2 C). This crystalline structure contains 4 Au atoms per unit cell allowing the determination of Au atoms per NP. This information together with EDX analysis (Table II.3) allows the estimation of the surface area occupied by one HMBP- $\text{C}\equiv\text{CH}$  molecule (as previously detailed in chapter II section 2.3.5) to  $0.53 \text{ nm}^2$ . The determination of hydrodynamic diameter by means of DLS suggest a slight aggregation of these NPs, however, no NPs precipitation occurs in suspension for several months suggesting that this effect is limited.

Silver NPs (Ag NPs) were synthesized using a similar methodology. In this case, the reaction was carried out in a monowave reactor at  $100^\circ\text{C}$ . This results in the formation of spherical (mean diameter of  $23.3 \pm 5.4$  nm) and crystalline NPs, as shown by TEM and HR-TEM micrographs (Figure II.2 D-F). HRTEM revealed lattice planes distancing by  $d_{200} = 2.1$  Å corresponding to face centered cubic structure of crystalline silver. This crystalline structure contains 4 Ag atoms per unit cell allowing the determination of Ag atoms per NP. Together with EDX analysis (Table II.3) the surface area occupied by one HMBP- $\text{C}\equiv\text{CH}$  molecule was estimated to  $0.51 \text{ nm}^2$ . The hydrodynamic Z average diameter of Ag NPs was 34 nm and PDI was 0.22 nm determined by DLS (Table II.3). The difference within TEM and DLS diameters can be explained by different factors such as the presence of a solvation layer and other molecules in

the NPs surface when they are found in suspension, which are not visible by TEM. Such results prove a good stability of such NPs in suspension without NPs aggregation.

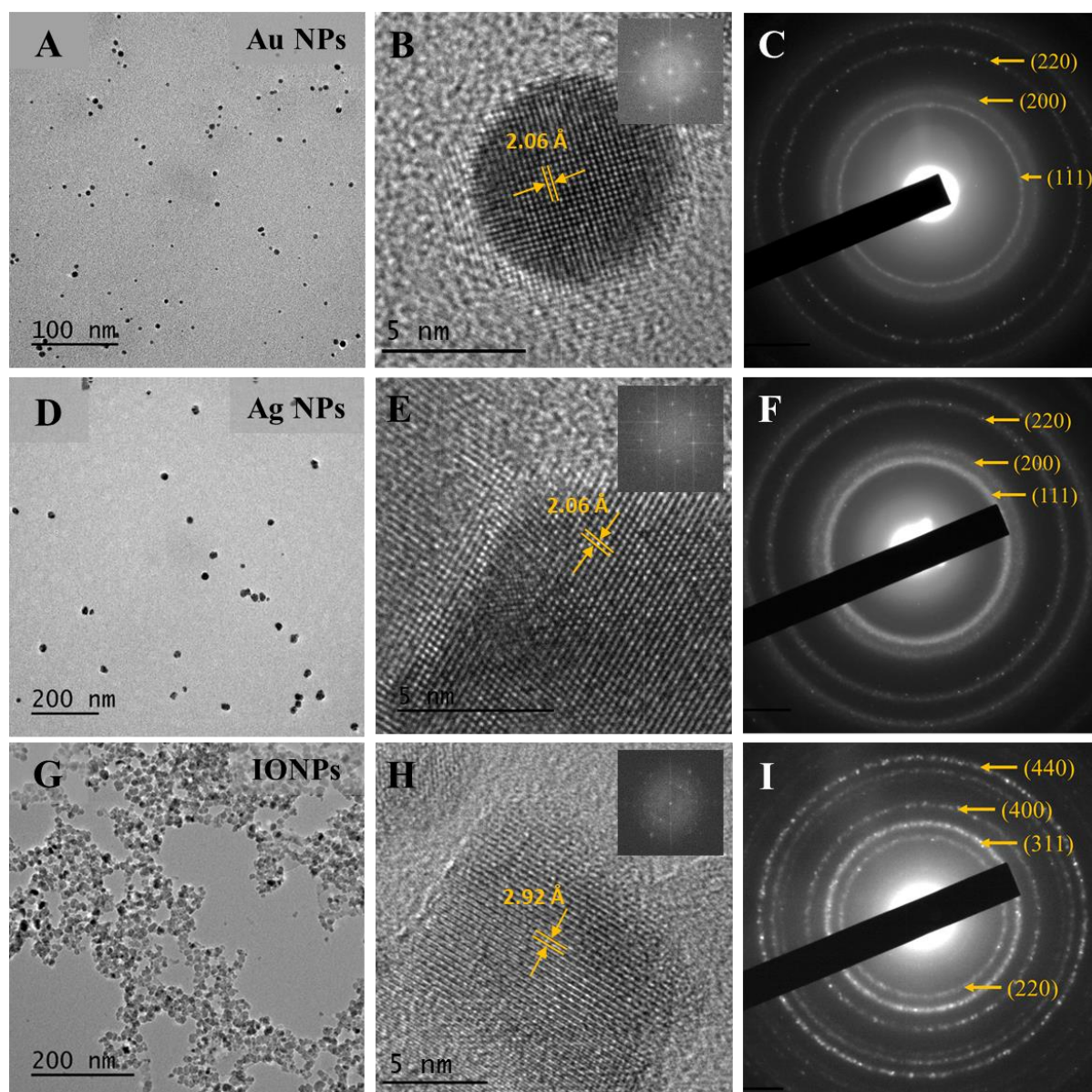
Iron oxide NPs (IONPs) were synthesized by the classical co-precipitation method using a mixture of  $\text{FeCl}_3$  and  $\text{FeCl}_2$ . The obtained NPs were posteriorly coated with HMBP- $\text{C}\equiv\text{CH}$ . TEM and HR-TEM images showed a spherical and homogeneous size distribution of  $7 \pm 1.8$  nm. SAED patterns clearly show the diffraction spots corresponding to (220), (311), (400) and (440) crystal planes (Figure II.2 I) with lattice planes distancing by  $d_{220} = 2.9 \text{ \AA}$  characteristic of planes of cubic spinel structure from magnetite ( $\text{Fe}_3\text{O}_4$ ) or maghemite ( $\gamma\text{-Fe}_2\text{O}_3$ ) (Figure II.2 H). This crystalline structure contains 24 Fe atoms per unit cell allowing the determination of Fe atoms per NP. Together with EDX analysis (Table II.3) the surface area occupied by one HMBP- $\text{C}\equiv\text{CH}$  molecule was estimated to  $0.47 \text{ nm}^2$ . DLS analysis resulted in hydrodynamic diameter of 55 nm PDI 0.19 nm (Table II.3). A significant difference between TEM and DLS determined diameters is seen in the case of IONPs. Such an increase in the NPs diameter in suspension can be explained by the aggregation of NPs, which is probably due to magnetic interactions <sup>15</sup>. Nevertheless, this aggregation is limited as no NPs precipitation occurs in suspension for several months.

Table II.3 summarizes all the NPs size and  $\zeta$  potential. The NPs stability in suspension is also driven, in all cases, by their surface coating with HMBP- $\text{C}\equiv\text{CH}$ , which results in an overall negative  $\zeta$  potential, due to the phosphonate functions. Charge repulsion forces avoid NPs aggregation in suspension.

**Table II.3.** Characteristics of the nanoparticles used in this study, TEM diameters are presented as mean  $\pm$  SD, DLS diameters correspond to the Z-average and PDI within brackets. Metal to P ratios are expressed in atom % and were determined by EDX.

Nanoparticle type	Mean diameter (nm)		$\zeta$ -potential (mV)	Metal to P ratio (atom %)	SA ( $\text{nm}^2$ ) / HMBP- $\text{C}\equiv\text{CH}$
	TEM	DLS			
Au NPs	$4.7 \pm 1.2$	21.98 (0.26)	$-47.7 \pm 1.4$	89.93 : 10.07	0.53
Ag NPs	$23.3 \pm 5.4$	34 (0.22)	$-43.4 \pm 1.4$	97.88 : 2.12	0.51
IONPs	$7.0 \pm 1.8$	55 (0.19)	$-48.5 \pm 1.5$	91.69 : 8.31	0.47





**Figure II.2.** TEM, HRTEM and SAED micrographs of Au NPs (A-C), Ag NPs (D-F) and IONPs (G-I). HRTEM images show the interplanar distance and the crystallographic planes are presented in SAED micrographs.

### 3.3. SF extraction

SF dispersion was successfully obtained by following the protocol described by Rockwood *et al.*<sup>4</sup>. Boiling time is a crucial aspect, as it will have a great impact on the SF molecular weight, therefore samples should be boiled during the same time. Previous studies have shown that boiling for 30 minutes results in 100 kDa SF approximatively<sup>4</sup>. Boiling for longer times will result in SF fragments with lower molecular weight. Herein we have chosen to boil samples during 30 minutes. Resultant fibers were successfully dispersed in a LiBr solution due to its capacity to disrupt hydrogen bonds found within SF  $\beta$  sheet. The disruption of H bonds allows the obtaining of an unstructured SF that can be easily dispersed in water. However, the formation of such bonds is thermodynamically favorable and occurs approximatively after one

month (when the dispersion is stored at 4°C) resulting in the gelation of the SF dispersion. The SF concentration of the resultant solution varied from 5 to 6 % and can be posteriorly concentrated. Figure II.3 shows a schematic overview of the SF extraction protocol.

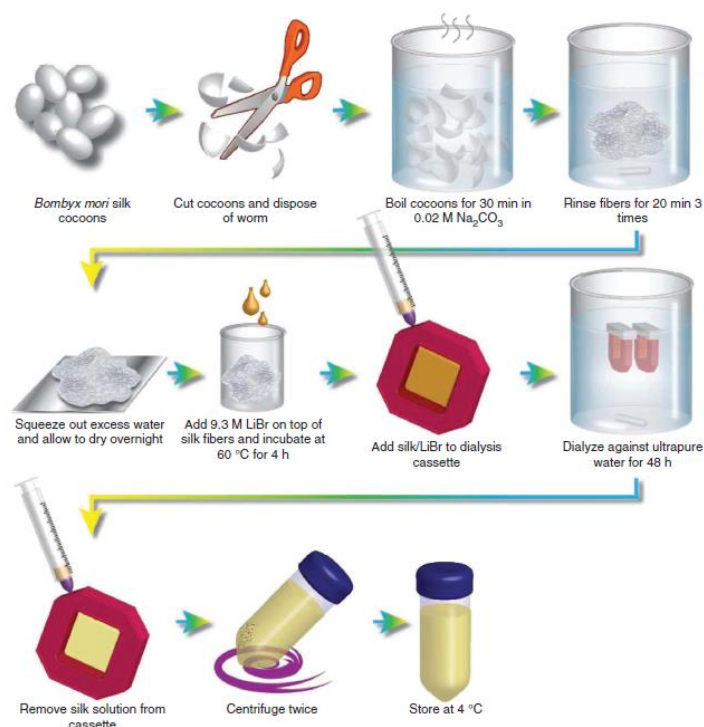


**Figure II.3.** Silk fibroin extraction protocol. Reproduced with permission from Rockwood *et al*<sup>4</sup>.

### 3.4. SF/NPs dispersion

The possibility of SF extracted dispersion gelation due to pH variations, changes in the ionic force or high NPs concentration has previously been stated in chapter I. The different HMBP- $\text{C}\equiv\text{CH}$  coated NPs were mixed with SF without inducing SF gelation, even with highly concentrated NPs suspensions (as tested for IONPs with up to 20% in mass of iron oxide). Thus, the possibility of mixing SF dispersion with NPs aqueous suspensions can enable the formation of well-dispersed NPs embedded silk-based bio-nanocomposites. These results can be explained by the surface characteristics of the synthesized NPs that present a fairly negative zeta potential at pH 7 (Table II.3). We can hypothesize that the presence of negatively charged SF (isoelectric point  $< 7$ <sup>16</sup>) may prevent NP aggregation through electrostatic interaction and/or steric effect.

The possibility of mixing SF and NPs dispersions allow the preparation of several silk-NPs bionanocomposites. We therefore first evaluated the preparation of electrospun mats containing NPs as previous work were successfully conducted on these silk materials at UTC for nerve regeneration<sup>17,18</sup>.

### 3.5. SF and SF / NPs electrospun mats

Several methods have been described in the literature to incorporate NPs into electrospun materials as previously reported in Chapter I:3. Herein two methods were evaluated: addition of NPs to the SF electrospinning dispersion and functionalization of the electrospun material.

#### 3.5.1. Addition of NPs to electrospinning dispersion

Silk-NPs electrospun bionanocomposites resulting from the mixture of NPs into the electrospinning dispersion showed the presence of Au NPs, Ag NPs and IONPs within the silk fibers as shown in Figure II.4 B-F. The electrospinning procedure was not significantly impacted by the presence of NPs into the electrospinning dispersion. However, the presence of a high concentration of IONPs required the application of a higher voltage to obtain an electrospun material. This behavior may be due to the higher NPs concentration and the nature of IONPs. Further research must be done to have a better understanding of this behavior. SEM / EDX analysis did not detect the NPs within silk-NPs electrospun bionanocomposites. Nevertheless, the presence of all NPs within the fibers was proven by TEM and STEM analysis of single fibers. Despite the overall dispersion of Au NPs and Ag NPs observed within the fibers slight aggregation was seen for IONPs probably due to their aggregated state in suspension as previously depicted by DLS. Moreover, NPs concentration is limited when using this procedure as a given percentage of silk and PEO dispersions has to be respected in the electrospinning dispersions. Therefore, we evaluated an *ex situ* methodology as well.

Finally, although electrospun materials were successfully obtained in all cases, the great impact of humidity over the silk electrospinning process together with the impossibility of the system to control this parameter resulted in no reproducibility. For example, the diameter and fiber shape were dependent on these two parameters. Therefore, different materials were evaluated for the rest of this work. A focus was made first on silk hydrogels that can also lead to cryogels by simple lyophilization.



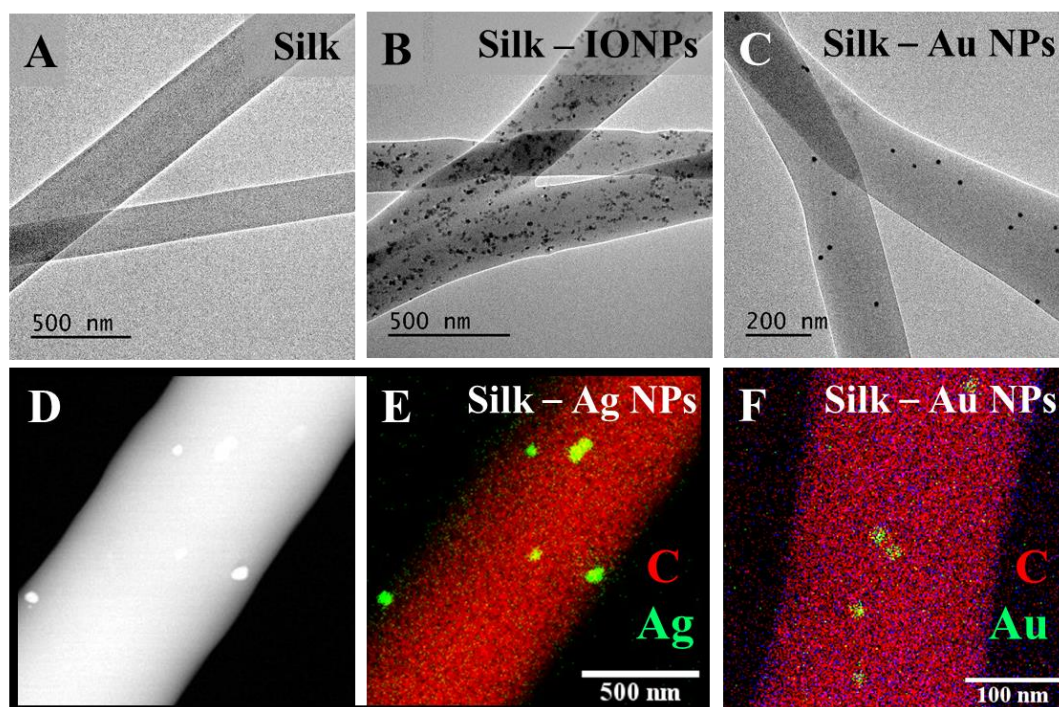


**Figure II.4.** Silk electrospun fibers (A) and silk-NPs electrospun bionanocomposites fibers (B-F). TEM (B, C) and STEM (D-F) images show the presence of IONPs, Au NPs and Ag NPs within silk fibers.

### 3.5.2. Electrospun material functionalization with NPs

The NPs concentration limit encountered when adding NPs into the electrospinning dispersion can be overcome by posterior functionalization of silk electrospun materials. Herein two different approaches were evaluated. Au NPs and Ag NPs were *in situ* synthesized into electrospun mats given their one pot reaction synthesis. Au NPs were homogeneously distributed within the material surface (Figure II.5 C) resulting in a macroscopic homogeneous colored tissue (Figure II.5 A bottom). However, Ag NPs were produced in a heterogeneous manner resulting in big NPs formation at several spots (Figure II.5 D). Visually Ag NPs containing electrospun mats had acquired a yellowish color in which grey stains were visible. *Ex situ* functionalization was carried with IONPs by letting dry a small volume of NPs suspension on top of the silk electrospun mat. This procedure resulted in a complete SF fiber coating by IONPs as shown by MEB imaging (Figure II.5 E).

*In situ* and *ex situ* functionalization showed promising results although homogeneity needs to be optimized. Nevertheless this procedures may result in an easier NPs release into the environment, therefore this factor should be further characterized in the future before using the as synthesized materials.

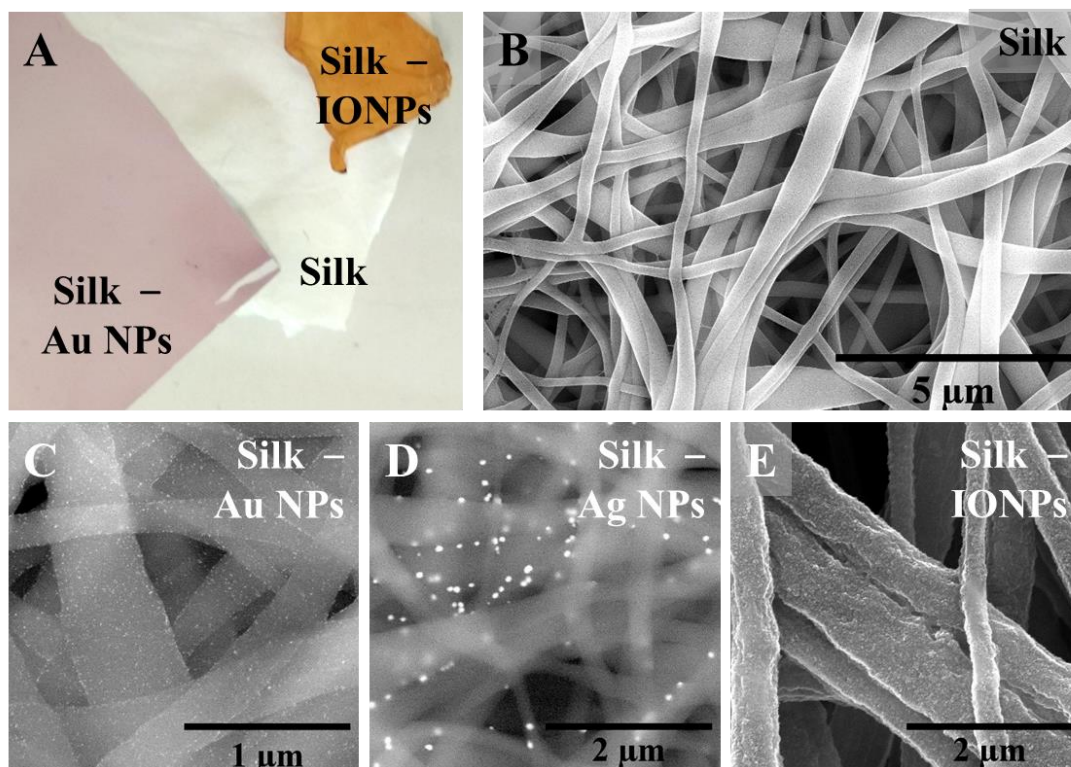
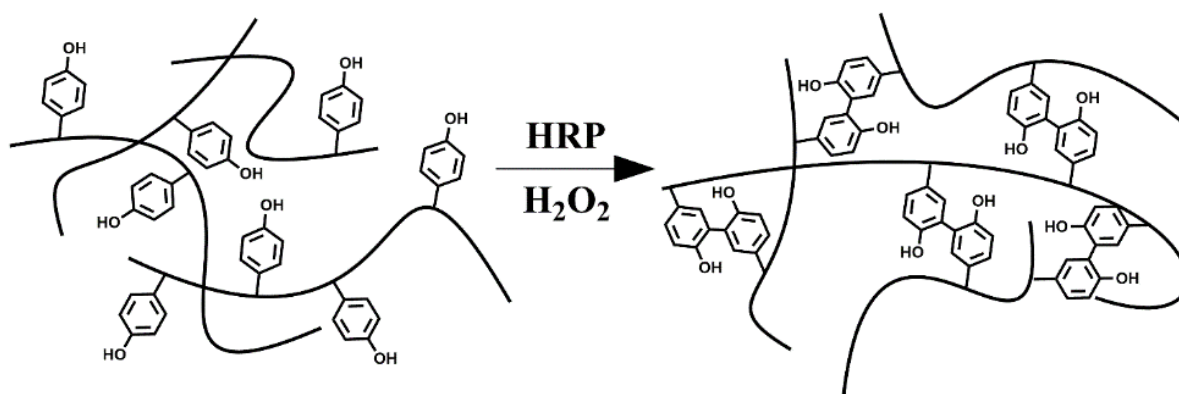


**Figure II.5.** Silk electrospun mats (A, B). MEB images show silk-Au NPs (C), silk-Ag NPs (D) electrospun mats synthesized by the *in situ* methodology and silk-IONPs (E) mats synthesized by the *ex situ* methodology.

### 3.6. Hydrogels

Silk hydrogels find applications in different fields from biomedicine to pollution control as previously reported in this work (Chapter I:1.2.4). Moreover, in comparison to electrospun mats, hydrogel synthesis is much easier to set up as it does not require any special equipment. In addition, the ability to fine-tune the mechanical, swelling and degradation properties of silk hydrogels permits to tackle a broad field of unmet material characteristics. Therefore, because of their versatility and the ability to fine-tune their properties, the rest of this work focuses on enzymatically crosslinked silk hydrogels.

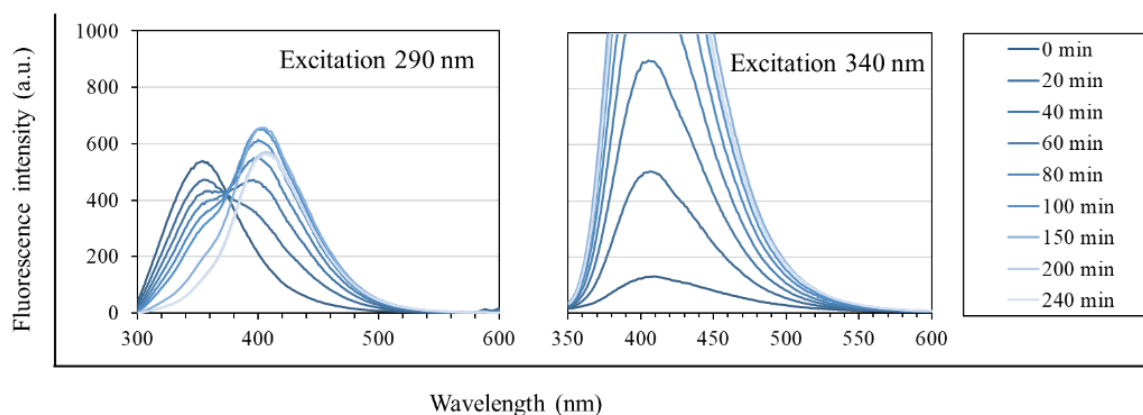
Enzyme assisted gelation method was used to produce silk-NPs hydrogel bionanocomposites. This procedure consists on the enzymatic crosslinking of tyrosines found within SF by the enzyme horseradish peroxidase (HRP). The reaction gives rise to the formation of dytyrosines as shown in Figure II.6. Silk hydrogels were successfully formed from SF-NPs mixture dispersion by simply adding HRP and H<sub>2</sub>O<sub>2</sub> adapting the protocol described by Partlow et al.<sup>5</sup>. The dispersions were maintained at room temperature for at least 4 hours (gelation time depends on the hydrogel final volume) until the gelation process was completed.



**Figure II.6.** SF enzymatic crosslinking reaction.

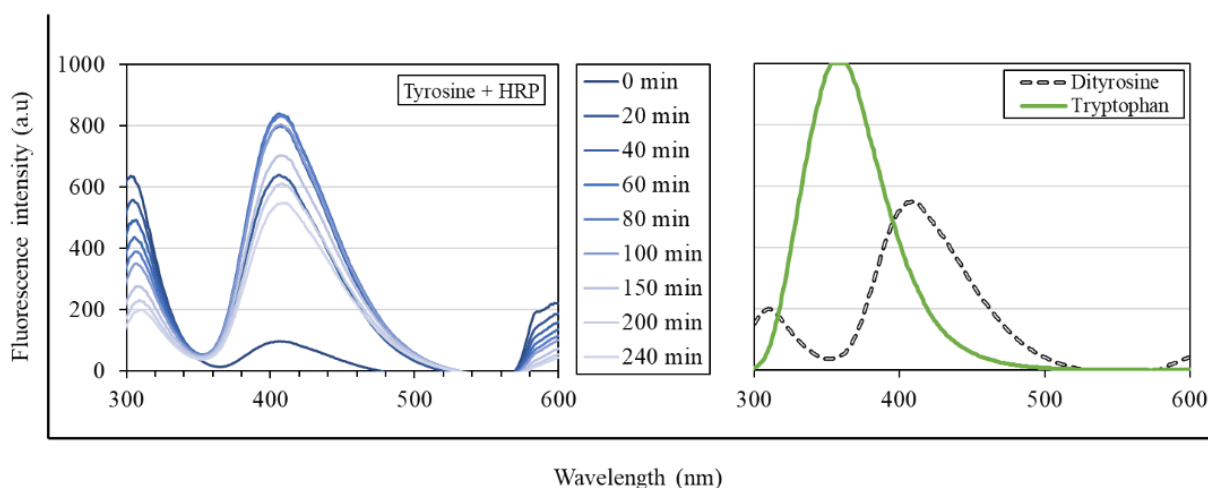
Fluorescence emission of the aromatic group in tyrosine and tryptophan<sup>19</sup> have been proposed as an efficient way to characterize silk materials<sup>20–23</sup>. Tyrosine fluorescence is described to be constant among different conditions of the surrounding environment. However this is not the case for tryptophan whose fluorescence is strongly dependent on the environment and so on the protein conformational state<sup>24</sup>. Both amino acids being present in SF it is reasonable to expect SF to emit fluorescence in a similar manner. In addition, SF hydrogels were formed by the enzymatic crosslinking of two tyrosines giving rise to a dityrosine complex that emits fluorescence allowing a monitoring of the hydrogel formation through fluorescence spectrometry<sup>25–27</sup>.

Figure II.7 shows the spectra evolution during hydrogel formation when excited at 290 nm (up) and 340 nm (bottom). For excitation at 290 nm, an initial peak found at 354 nm disappears as a peak at 408 nm appears over time. We speculate that the initial fluorescence found in SF dispersion is due to the combination of both tyrosine and tryptophan emission resulting in an emission peak at 354 nm. This peak is found between tyrosine and tryptophan emissions in pure state in water, 303 nm and 358 nm respectively, when excited at the same wavelength (Figure II.7). The apparition of the second peak, at emission wavelength of 408 nm, can be explained by the formation of dityrosine bonds which emission is of 411 nm at the same excitation wavelength.



**Figure II.7.** Silk hydrogel gelation kinetics. Emission fluorescence spectra during hydrogel formation of silk hydrogels when excited at 290 nm (left) and 340 nm (right).

Interestingly, when excited at 340 nm, an emission peak appears at 408 nm during hydrogel formation. However, no fluorescence is seen in these conditions neither for tyrosine, dityrosine or tryptophan amino acids in water (Figure II.8). This result could be explained by the protein conformational changes taking place during hydrogel formation. This phenomenon could result in a change in the environment of tryptophan amino acid, which may induce a different fluorescence emission. However further analysis should be performed for a better understanding of these results.



**Figure II.8.** Fluorescence spectra of tyrosine in presence of HRP over time (left), dityrosine and tryptophan (right) when excited at 290 nm.

### 3.6.1. Cryogels

The structure characterization of silk hydrogels was not possible in a wet state. To do so cryogels were prepared by freeze-drying the previously formed hydrogels. As a result, porous materials were obtained, however the light and elastic nature of silk materials made impossible the porosity characterization by Brunauer–Emmett–Teller (BET) technique. Interestingly it was



found that the pore size can be tuned by controlling the freezing temperature of the hydrogel. Samples frozen using liquid nitrogen ( $N_2$ ) presented the smallest pore size when compared to  $-80^\circ C$  and  $-20^\circ C$  freezing temperatures (Figure II.9). The biggest pore size was observed in samples frozen at  $-20^\circ C$ . These results can be explained by the freezing speed. When using  $N_2$  water molecules are rapidly frozen resulting in small crystal formation. When higher temperatures are used, the freezing speed is decreased allowing the formation of bigger water crystals and therefore resulting in a bigger pore diameter after lyophilization. Because of their smaller and more homogeneous pore size distribution, cryogels obtained by using  $N_2$  as freezing agent were used for sample characterization in the following sections.

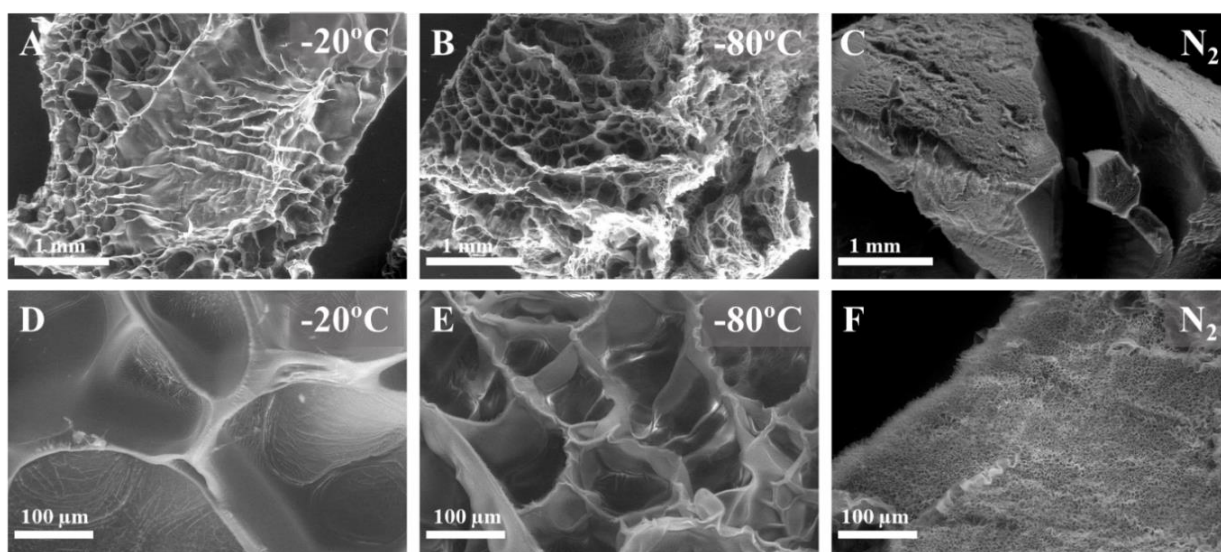


**Figure II.9.** MEB images of silk cryogels frozen at  $-20^\circ C$  (A, D),  $-80^\circ C$  (B,E) and with  $N_2$  (C, F) and freeze-dried. The freezing temperature has great influence over the silk cryogel porous structure. Lower temperatures result is smaller and more homogeneous pores.

### 3.6.2. Silk-NPs hydrogel bionanocomposites

Silk hydrogels being formed by an enzymatic crosslinking it is crucial to evaluate the effect of NPs presence over the enzyme catalytic activity. The activity of HRP was evaluated in presence of Au NPs and IONPs. 2,2'-Azino-bis (3-Ethylbenzthiazoline-6-Sulfonic Acid) ( $ABTS^{2-}$ , also referred as ABTS) was used as enzyme substrate. HRP can catalyze the oxidation of  $ABTS^{2-}$  to  $ABTS^{\bullet}$  (also called  $ABTS^{+}$ ) by  $H_2O_2$  described in the following reaction:



While  $ABTS^{2-}$  has no color,  $ABTS^{\bullet}$  is green and has a maximum absorbance at  $420\text{ nm}$ <sup>28</sup>. The reaction was monitored for 3 minutes under UV-Vis spectrometry at  $420\text{ nm}$ . The  $ABTS^{\bullet}$  absorbance being almost the same as the one for Ag NPs, the activity evaluation in presence of this NPs was not possible. Results showed that the presence of Au NPs or IONPs did not induce



any noticeable decrease the enzymatic activity (Figure II.10). Furthermore, the activity found in presence of IONPs was increased probably due to the well-known Fenton reaction occurring in presence of these NPs<sup>29,30</sup>. Nevertheless, one must note that without the presence of the enzyme this activity is not sufficient to promote SF gelation in these conditions.

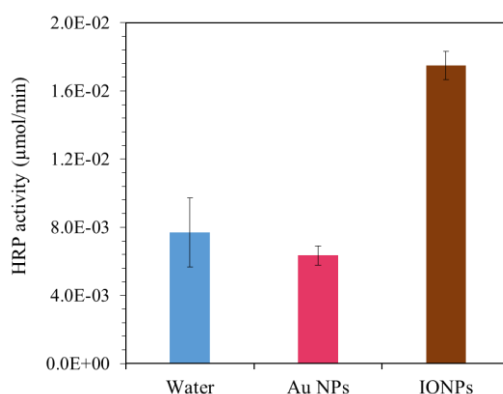


**Figure II.10.** Enzymatic activity of HRP in presence of Au NPs and IONPs. No significant difference is seen within the activity of HRP in water and in Au NPs aqueous suspension. However, the activity seems to be enhanced in presence of IONPs. This result is explained by the Fenton reaction by which IONPs can catalyze the oxidation of ABTS<sup>2-</sup> by H<sub>2</sub>O<sub>2</sub> by themselves.

### 3.6.2.1 *In situ* characterization

Similarly, to silk hydrogels, the formation of silk-NPs hydrogel bionanocomposites was monitored *in situ* using fluorescence spectrophotometry. Figure II.11 shows the comparison of the spectra evolution during hydrogel formation when excited at 290 nm (up) and 340 nm (bottom). The same behavior was observed for all hydrogels with and without NPs although fluorescence emission intensity was decreased in presence of NPs. This behavior has previously been described and discussed in section Chapter I:3.6.

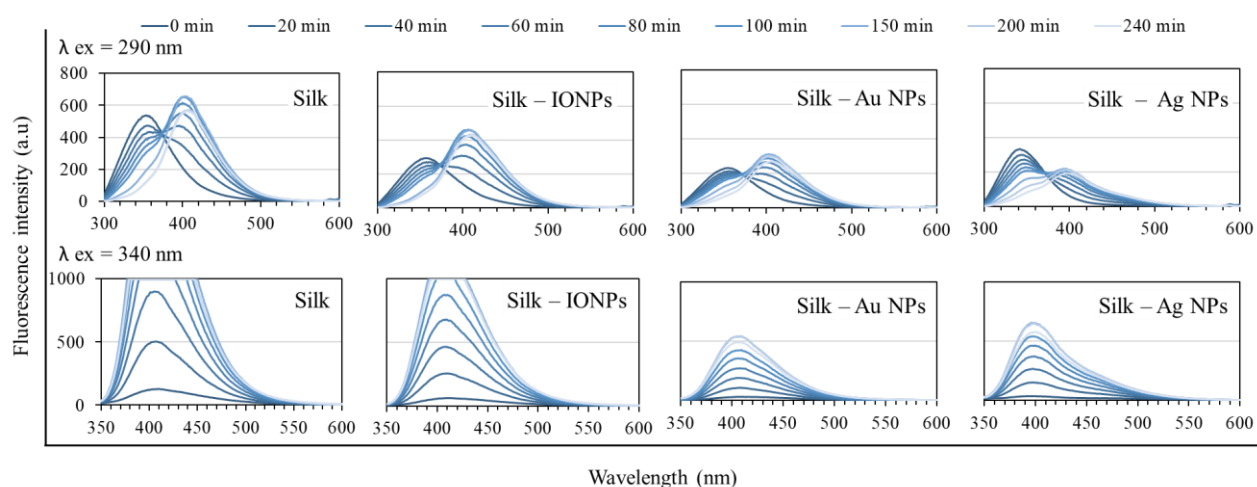


**Figure II.11.** Silk hydrogel gelation kinetics. Emission fluorescence spectra during the formation of silk, silk-Au NPs, silk-Ag NPs and silk-IONPs hydrogels when excited at 290 nm (up) and 340 nm (bottom). Fluorescence emission is quenched in presence of NPs but the same type of curves are obtained.

Overall, gelation monitoring can be done by following the fluorescence emission intensity of the peaks appearing at 408 nm over time when exciting at 290 and 340 nm. When comparing the maximum fluorescence emission intensity at 408 nm of silk-NPs hydrogels bionanocomposites with uncharged silk hydrogels, a clear decrease was observed. This phenomenon is depicted on Figure II.12. It appears that compared to silk hydrogels the intensity difference is constant over time for each sample. The intensity difference value is only dependent on the type of NPs contained in the material. In fact, when exciting at 290 nm, the fluorescence emission at 408 nm is less impacted by IONPs than by Au NPs and then Ag NPs (Figure II.12 A). However, for excitation at 340 nm Au NPs induced a slightly greater intensity decrease than Ag NPs (Figure II.12 B). As we did not observe any structural difference between hydrogels (see results of *ex situ* characterization of SF-NPs hydrogels below), this phenomenon can be explained by the NPs light absorption inducing a quenching of fluorescence. Dityrosine formation in SF gives rise to a fluorescence emission at 408 nm that is very close from the maximum absorbance wavelength of Ag NPs used in this study. Therefore, Ag NPs highly quenched dityrosine fluorescence emission. The same phenomenon takes place in presence of Au NPs and IONPs to a lesser extent; their maximum absorption wavelength being further from 408 nm, the intensity decrease is smaller.

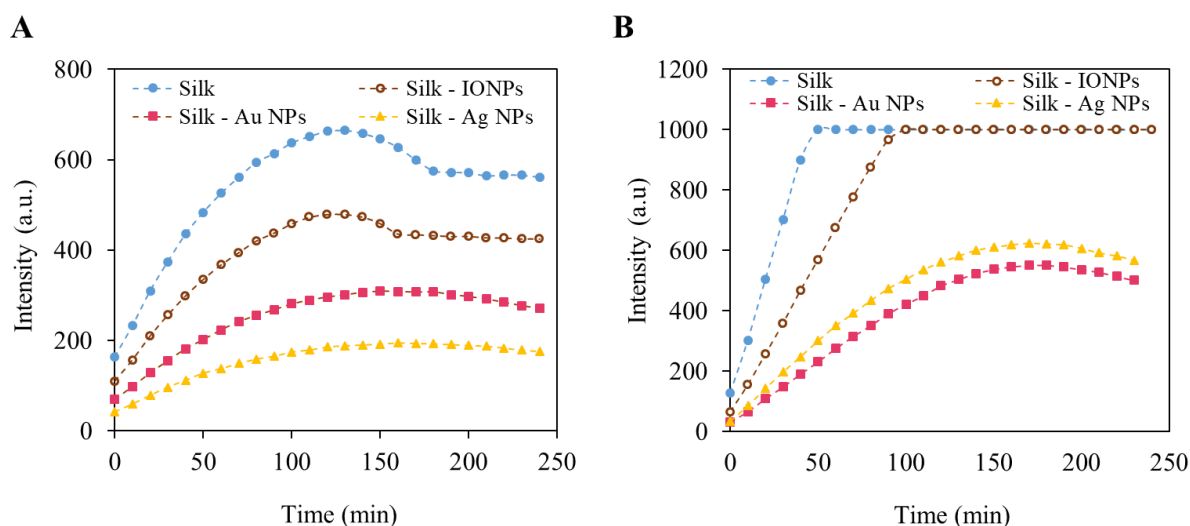


**Figure II.12.** Comparison of maximum fluorescence emission at 408 nm of silk, silk-Au NPs, silk-Ag NPs and silk-IONPs hydrogels over gelation time when excited at 290 nm (A) or 340 nm (B). Fluorescence emission is quenched by the presence of NPs within the hydrogel.

Silk-NPs hydrogel bionanocomposites were successfully formed in all cases from SF-NPs mixture dispersion by simply adding HRP and  $\text{H}_2\text{O}_2$  adapting the protocol described by Partlow *et al.*<sup>5</sup> (Figure II.13 A); even in the presence of high NPs concentration such as 50 mM IONPs. Suspensions of each NPs were added to SF dispersion in the same concentration ( $\sim 1.5 \times 10^{-4}$

mol.L<sup>-1</sup>) except for IONPs (obtainable in more concentrated suspension) for which concentration was increased up to 20% in mass (Fe vs SF). It moreover appeared that when the volume of SF-NPs dispersions was increased, the thickness of the formed hydrogel (prepared in the same mold) is linearly correlated (Figure II.13 B). This relation remains the same for silk and silk-NPs hydrogels and whatever the constitution of the NPs.

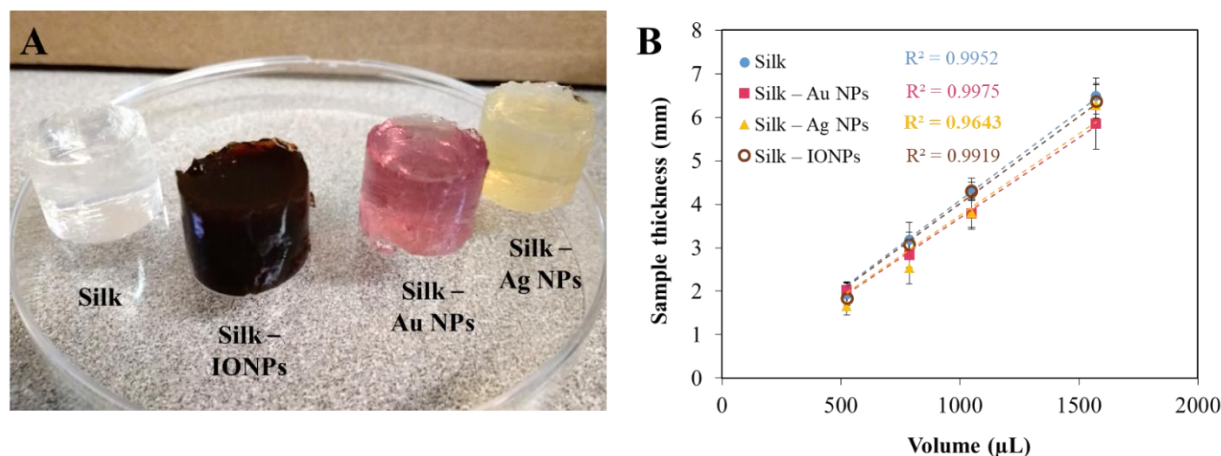


**Figure II.13.** From left to right silk hydrogel and silk-IONPs, silk-Au NPs and silk-Ag NPs hydrogel bionanocomposites (A). Hydrogel thickness to liquid volume correlation is linear and similar for all silk and silk-NPs hydrogels (B).

### 3.6.2.2 *Ex situ* characterization

#### **Macroscopic features**

An *ex situ* characterization was conducted over the formed hydrogels. The presence of Au NPs, Ag NPs and IONPs into silk-NPs hydrogel bionanocomposites was clearly visible to the naked eye and was further assessed by UV-vis absorption spectra (Figure II.14). NPs seem to be homogeneously distributed into SF hydrogels from a qualitative visual analysis. Silk-Au NPs and silk-Ag NPs hydrogel bionanocomposites showed a maximum absorbance at 520 and 430 nm respectively. These results match the absorption spectra of NPs suspensions alone while no absorbance was observed in these regions for silk hydrogel. These values agree with the results found in the literature for spherical Au NPs and Ag NPs<sup>31,32</sup>. In addition, the absence of an important shift of the maximum absorbance peak depicts a good NPs dispersion within the hydrogel bionanocomposite with no NPs aggregation.

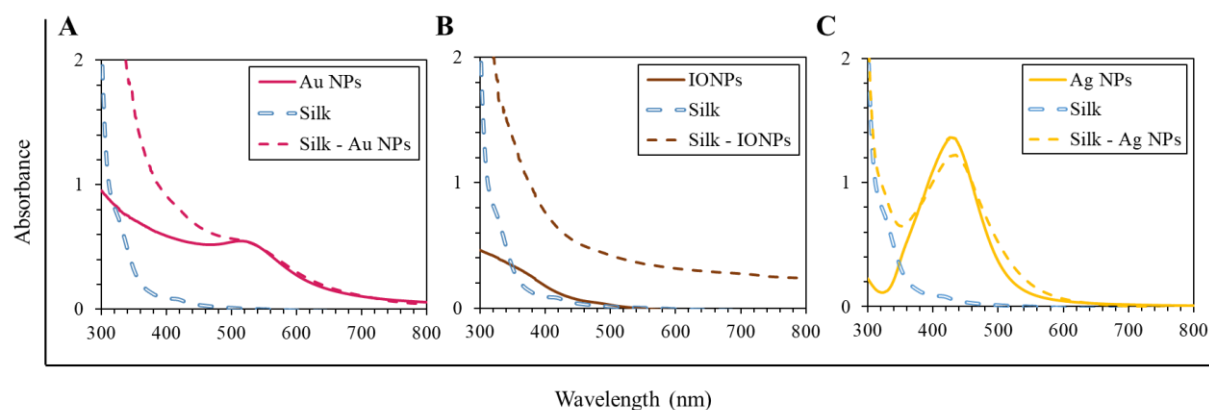


**Figure II.14.** UV-vis spectra of NPs suspensions, silk and silk-NPs hydrogels (B Au NPs, C IONPs, D Ag NPs). For silk-Au NPs and silk-Ag NPs an identical maximum absorption is seen when compared with the NPs suspensions.

NPs release in water was studied by measuring the UV-vis absorbance of water containing the hydrogels. After 14 days, no UV absorption was detected in the solution indicating that none or very few NPs were released from the silk-NPs hydrogel bionanocomposite. These results are very interesting for further biological applications as NPs will not easily be released into the body.

### *Structural properties*

The structure of all hydrogels was evaluated by SEM (after freeze-drying) and by confocal microscopy (in their wet state). Figure II.15 shows the morphology of all samples. SEM images show that highly macroporous structures were obtained with no significant morphological change when any of the NPs were added (Figure II.15 A-D). This macroporous morphology appears in an aligned manner. These morphological characteristics are confirmed with the confocal microscopy images (on hydrogels) that are also relatively similar whatever the NPs added (Figure II.15 E-H). These results agree with the previous findings on maintaining of the HRP activity in presence of NPs and concurred to prove that the same reaction takes place with or without NPs. As previously observed for SF electrospun mats containing NPs we were not able to visualize NPs by SEM and surprisingly EDX analysis were not able to detect the presence of any of the NPs constituting metals though we already proved that they are clearly present. These results could be explained by the low concentration of NPs in the silk-NPs hydrogel bionanocomposites and may result from a very good dispersion within the material.

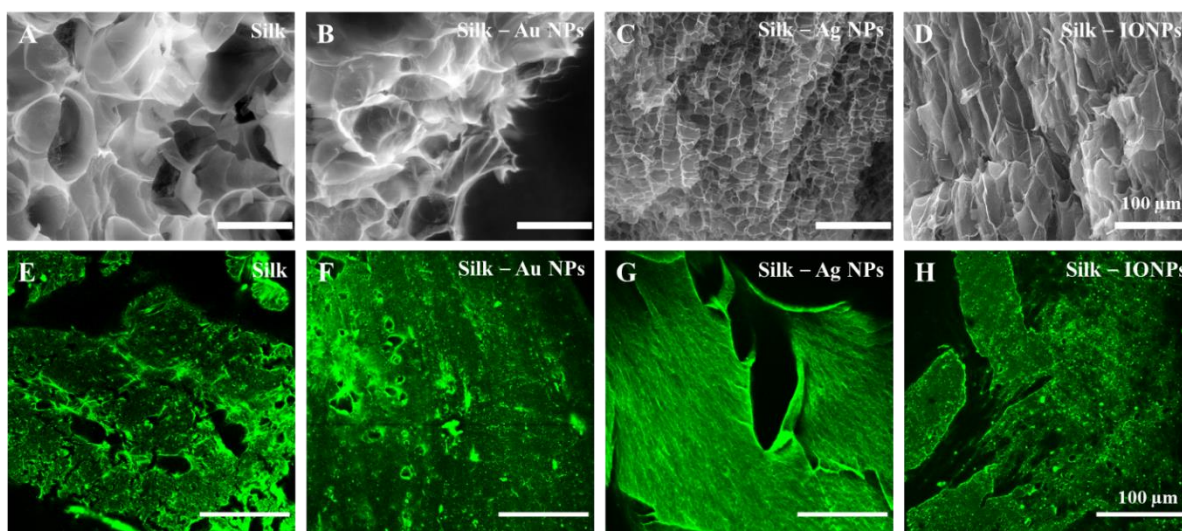


**Figure II.15.** SEM micrographs of cryogels and confocal microscopy micrographs of hydrogels. Silk (A, E); silk-Au NPs (B, F); silk-Ag NPs (C, G) and silk-IONPs (D, H) bionanocomposites. Scale bars correspond to 100 μm.

In order to prove indubitably the presence of the NPs into the silk-NPs hydrogel bionanocomposite we performed TEM on the cryogels. Figure II.16 shows that all kinds of NPs are well embedded into the hydrogel silk-NPs hydrogel bionanocomposites. Moreover, NPs are specifically attached to silk fibers with a homogeneous dispersion. Moderate NPs aggregation is seen in the case of silk-IONPs. These results agree with the aggregated state of these NPs previously depicted by DLS.

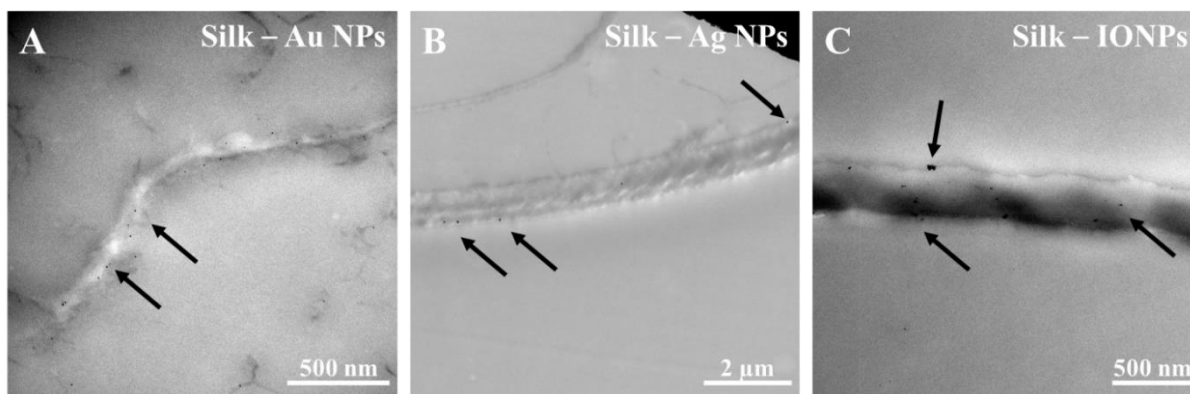


**Figure II.16.** TEM images of silk cryogels slices embedded with Au NPs (A), Ag NPs (B) and IONPs (C). Black arrows point some of the NPs seen.

Attenuated total reflectance Fourier Transformation Infrared spectra (ATR-FTIR) can be used to evaluate silk secondary structure by their amide bands. This technique allows the differentiation of two silk polymorphs silk I and silk II. Silk I polymorph has coiled secondary structure while silk II contains  $\beta$ -sheets. Previous studies state that infrared absorption at 1648-1654 and 1535-1542  $\text{cm}^{-1}$  correspond to silk I structure. Peaks in the regions 1610-1630, 1695-1700 and 1510-1520  $\text{cm}^{-1}$  correspond to silk II structure<sup>33</sup>. Figure II.17 shows the FTIR spectra for silk and silk-NPs hydrogels. All four hydrogels show a silk II structure with no significant



differences seen between SF and any of the SF hydrogels containing NPs. These results also agree with the similar structure seen by SEM and confocal microscopy.

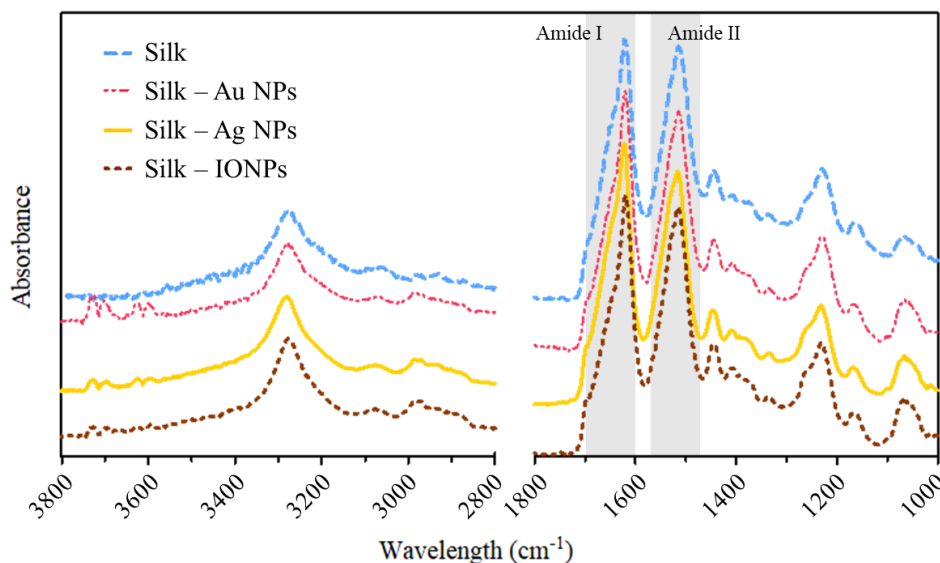


**Figure II.17.** ATR-FTIR spectra of silk and silk-NPs hydrogels. Grey band depict amide regions that allow the identification of a silk II structure given that peaks are found in the regions 1610-1630, 1695-1700 and 1510-1520  $\text{cm}^{-1}$ .

### Swelling behavior

Figure II.18 shows the swelling behaviors for all silk and silk-NPs. Incorporation of NPs into silk hydrogels tends to decrease in an important manner their swelling behaviors. These results agree with previous studies in which the incorporation of IONPs into silk-based scaffolds reduced its PBS uptake<sup>34</sup>. While the maximum swelling percentage is reduced to a half for silk-Ag NPs hydrogel bionanocomposites, a further reduction to a third and a quarter is seen for silk-Au NPs and silk-IONPs hydrogel bionanocomposites respectively. To elucidate the origin of this effect, the number of NPs  $\text{L}^{-1}$  for each silk-NPs hydrogel bionanocomposite was calculated from the concentration of the NPs ( $\sim 0.15 \text{ mM Au}$ ,  $\sim 0.15 \text{ mM Ag}$ ,  $\sim 0.2 \text{ mM Fe}$ ), the crystalline diameter (calculated by TEM image analysis) and the crystalline structure of each NPs type. Herein we found that the overall number of NPs  $\text{L}^{-1}$  was significantly smaller for silk-Ag NPs hydrogel bionanocomposites ( $2.33 \times 10^{14} \text{ NPs L}^{-1}$ ) when compared with silk-Au NPs ( $7.40 \times 10^{16} \text{ NPs L}^{-1}$ ) and silk-IONPs ( $1.65 \times 10^{16} \text{ NPs L}^{-1}$ ). Therefore, the increased number of NPs in silk-Au NPs and silk-IONPs hydrogel bionanocomposites may explain the cause of the greater reduction of the swelling percentage seen within these materials. These results suggest that for NPs with the same  $\zeta$ -potential the swelling behavior of silk-NPs hydrogels is impacted by the number of NPs rather than by their nature. However further experiments should be conducted to validate this hypothesis.

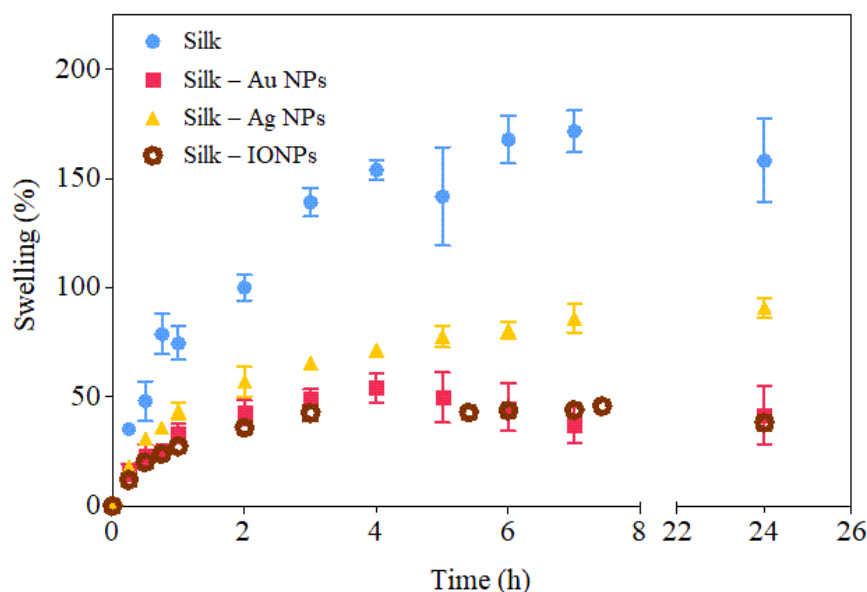


**Figure II.18.** Silk, silk-Au NPs, silk-Ag NPs and silk-IONPs hydrogel swelling behavior. Swelling capacity of silk hydrogels bionanocomposites is impaired. Further studies should be done to elucidate why some NPs have a higher influence on this behavior.

### *Mechanical properties*

Mechanical properties were evaluated by unconfined compression tests. SF behaves as an elastomer material and therefore the tangent modulus is dependent on the strain. All SF hydrogels showed an increase in the tangent modulus when the strain percentage was increased in agreement with the mechanical elastomer behavior (Figure A.4). For this reason, 20 and 40 % strain points were set to compare the tangent modulus between different samples <sup>5</sup>. Figure II.19 shows the tangent modulus obtained for silk and silk-NPs hydrogels. Tukey's multiple comparison tests allowed grouping conditions into significant groups (letters a to c). No significant difference is found within samples corresponding to the same letter group. No major differences were observed between the different samples containing NPs tested. Only a slight difference was detected at 40 % strain between silk and silk-Au NPs and silk-Ag NPs hydrogels. Once again, these results appear to point out that, at this concentration, there is no difference in terms of structure and properties of silk-NPs hydrogel bionanocomposites.

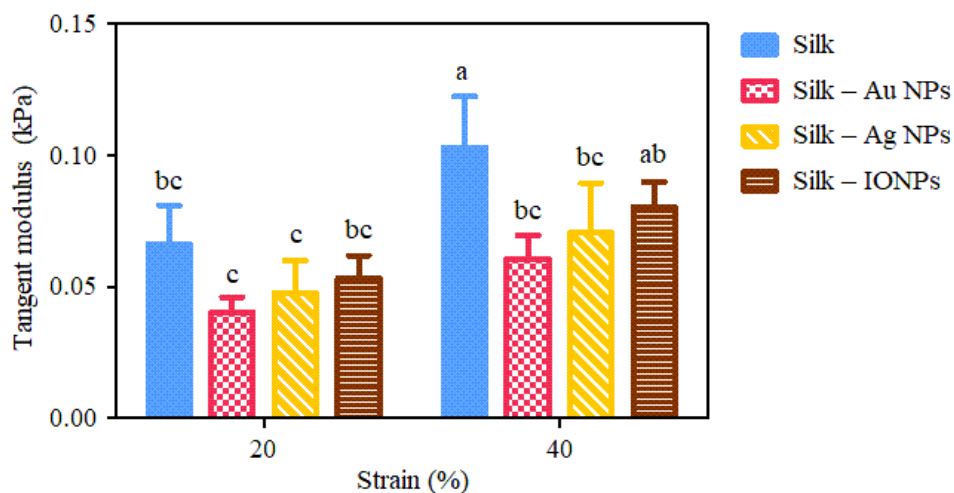


**Figure II.19.** Tangent modulus of silk, silk – NPs hydrogel. Letters represent the group classification after Tukey's multiple comparisons statistical analysis. Samples are classified within different letter groups if a significant difference is found ( $p$  adj value  $\leq 0.05$ ).

### 3.6.2.3 Biocompatibility evaluation

The lack of cytotoxicity effects induced by the material is crucial when used for biomedical applications. Cytotoxicity was evaluated using material extracts over L929 murine fibroblasts by a MTS test as described in ISO10993-5. Results shown in Figure II.20 show no cytotoxicity for any of the conditions tested whether hydrogels were hydrated in DMEM media or sterile demineralized water. Interestingly the silver concentration in our hydrogels ( $\sim 0.15$  mM) was almost 9-fold higher than the silver concentration of  $16.78 \mu\text{M}$  found to reduce L929 cell viability by a 50% in the same culture conditions by Souter *et al*<sup>35</sup>. These results suggest that there is no silver release occurring from our silk hydrogels and therefore they do not cause any cell cytotoxicity.

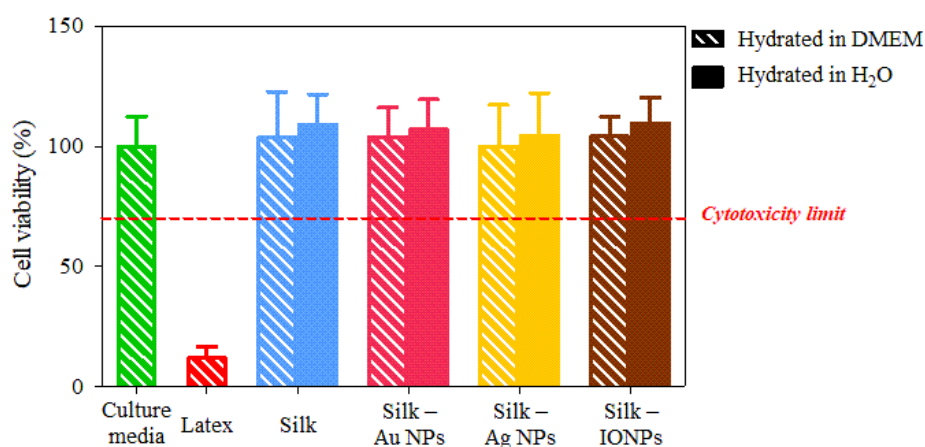


**Figure II.20.** MTS results for silk and silk-NPs hydrogels showed no cytotoxicity for any of the conditions. Two different hydrogel swelling solutions were evaluated: water and culture media. Culture media and latex were used as negative and positive control respectively.



The evaluation of the biocompatibility of these silk bionanocomposites is crucial for their use in biomedical applications. Herein, Human Dermal Fibroblasts (HDF) were seeded over silk hydrogels to evaluate the cellular adhesion on this material *in vitro*. Thermanox plastic coverslips were used as control surface. Immunostaining with DAPI and phalloidin against F-actin enabled the visualization of nuclei (blue) and actin cytoskeleton (red) respectively by confocal fluorescence microscopy. Moreover, the autofluorescence of silk hydrogels (green) enabled the visualization of their structure. Figure II.21 shows that HDF cells are able to adhere in all conditions showing cytoskeletal extensions to form focal adhesions and interact with neighboring cells. This morphology shows that human dermal fibroblasts are able to adhere and survive in the surface of a silk hydrogel with (whatever their nature) or without NPs *in vitro*, supporting the biocompatibility of the material.

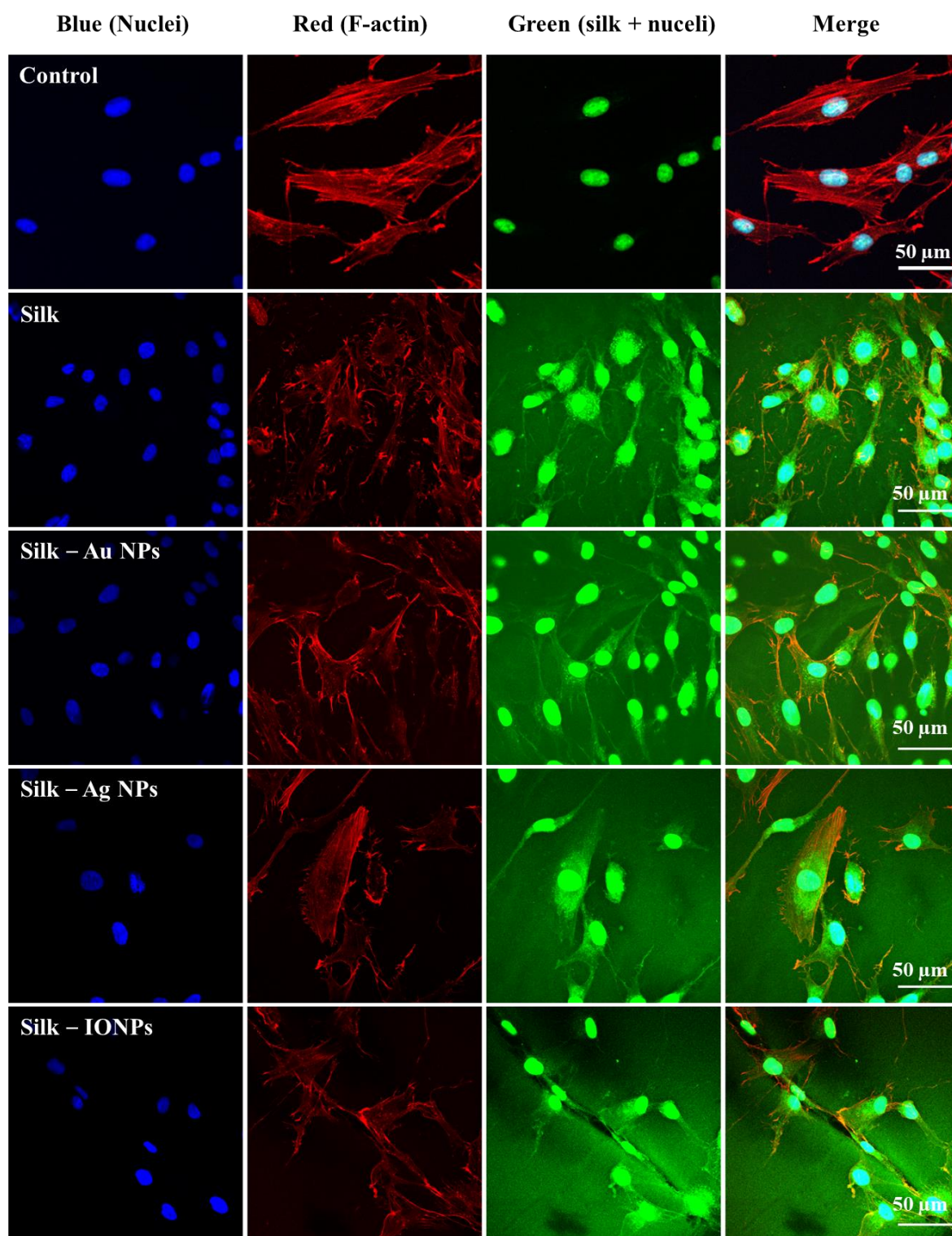


**Figure II.21.** HDF cells after 48h culture over a control surface, silk and silk-NPs hydrogels visualized with confocal fluorescence microscopy at x40 magnification. From left to right; cell nuclei in blue (DAPI), actine cytoskeleton in red (phalloidin Sulfo-Rhodamine SR101), silk autofluorescence and cell nucleus in green and composite image.

### 3.7. Other silk-NPs bionanocomposites

The possibility of producing both silk-NPs silk electrospun mats and hydrogel bionanocomposites from a SF / NPs mixture suggested that this dispersion could be further used to produce different silk-NPs bionanocomposites. In the following sections, this possibility is explored for the design of silk-NPs sponge bionanocomposites and structures produced by additive manufacturing.

#### 3.7.1. Sponges

The applications and interest of silk sponges have been largely discussed in Chapter I:1.2.1. Herein SF and silk-NPs sponges were successfully formed by following the protocol described by Rockwood *et al*<sup>4</sup> and adapting it to start from a SF / NPs dispersion. Although sponges were formed, the control over the top surface morphology was difficult if not impossible. Moreover, the heterogeneous pore size distribution is visible at naked eye. MEB imaging further revealed the expected macroporous structure formed by a fibrous structure characteristic from silk materials (Figure II.22 A). The incorporation of Au NPs and IONPs into the silk dispersion resulted in homogeneously colored silk sponges as shown in Figure II.22 B. As for silk hydrogels, the presence of NPs into SF sponges did not change the macroporous structure significantly even at high IONPs concentrations. Moreover, no NPs clusters were visible in the surface of the material. Despite the visible color difference, Au and Fe elements were not detected by EDX analysis suggesting a very homogeneous distribution and incorporation of NPs within the bionanocomposite as it has already been observed for hydrogels and cryogels.

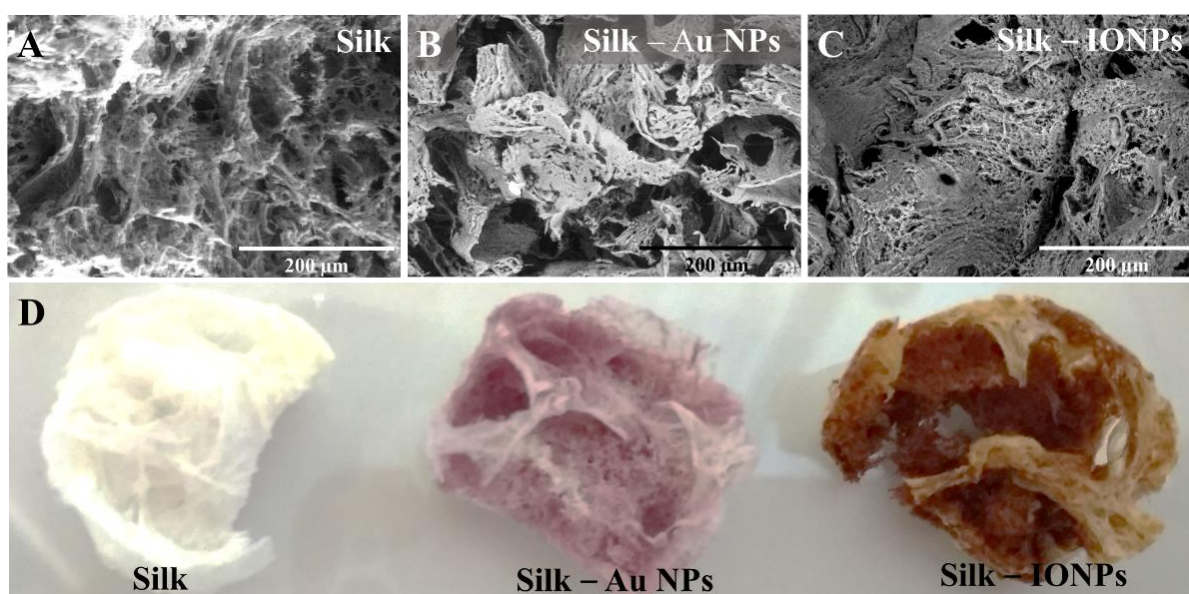


**Figure II.22.** SEM image of silk (A), silk-Au NPs (B) and silk-IONPs (C) sponges. (D) Macroscopic images of (from left to right) silk, silk-Au NPs, and silk-IONPs sponges.

The acquisition of magnetic properties of silk-IONPs sponge bionanocomposites were evaluated by simply approaching a neodymium magnet. Although a stronger attraction was found when the material was immersed in water, dry silk-IONPs sponge bionanocomposites were magnetic as well. It is important to consider that these are only proof of concept results and further investigations should be conducted to provide an in-depth characterization.

### 3.7.2. 3D printing

The increasing interest on additive manufacturing techniques, especially in biomedical applications, has driven us to evaluate whether the incorporation of NPs into a SF based bioink was feasible. 3D printing of SF structures was possible with two different techniques as shown in Figure II.23. The two techniques used herein resulted in homogeneously colored materials when NPs were integrated within the 3D printing ink, suggesting that NPs are present throughout the entire material.

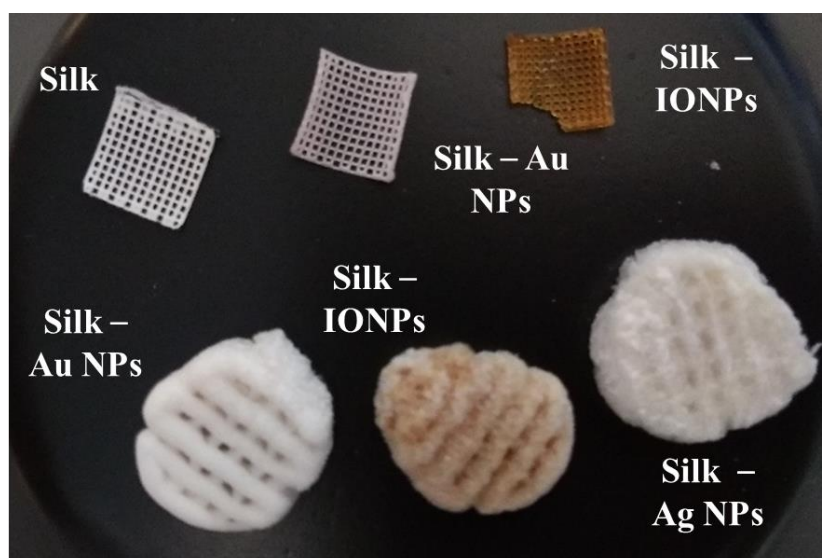


**Figure II.23.** Macroscopic view of 3D printed silk and silk-NPs structures obtained by printing into a salt (top) or laponite bath (bottom).

The use of inks containing NPs was possible and again no structural changes were found in the final material. The first technique consists on inducing silk gelation when in contact to a saline solution and results in smooth surface filaments (Figure II.24 A) <sup>6</sup>. The second technique printing over a laponite bath and posterior SF crosslinking by immersion in methanol results in a macroporous structure much more interesting for biomedical applications (Figure II.24 B). However further investigations need to be conducted to improve the printing resolution of this technique. Nevertheless, the possibility of using two different techniques increases the possible uses of such materials allowing a better adaptation to the specific requirements of each application.



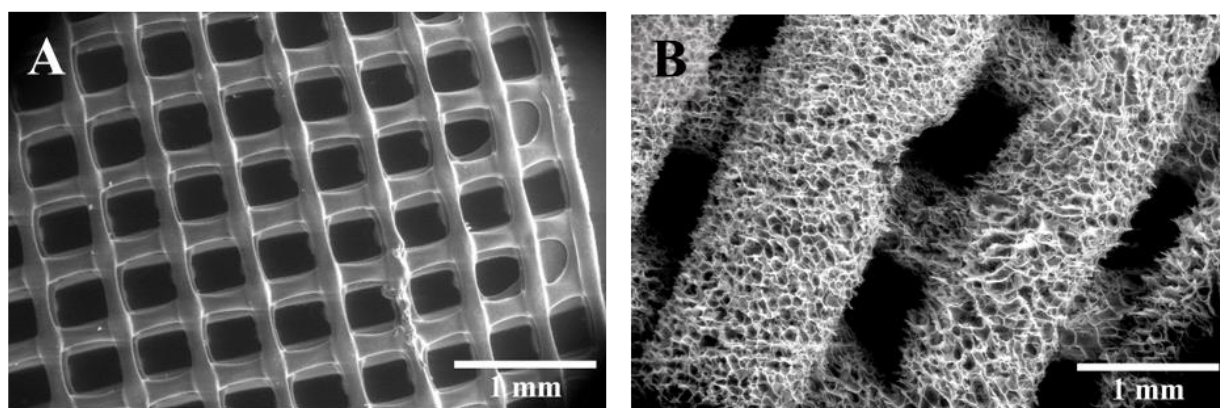


**Figure II.24.** SEM images show the surface difference of silk structures printed into a salt (A) or a laponite bath (B). Structures printed within a salt bath result in smoother surface while the roughness of the structures printed within a laponite bath is much more interesting for cell adhesion and therefore biomedical applications.

## 4. Conclusion

Herein a methodology to produce silk-NPs bionanocomposite scaffolds was developed. The present approach based on the use of a biocompatible ligand, allow NPs synthesis and stabilization in water while avoiding spontaneous gelation upon their addition to the SF dispersion. This mixture allowed the production of silk-NPs electrospun mats bionanocomposites despite some trouble to control and replicate. Posterior introduction of NPs on the electrospun mats is also possible by dipping them into NPs suspension or by performing the NPs synthesis *in situ*. Nevertheless, the use of materials produced by these approaches could be compromised for several applications as concern can be raised onto the potential leaching of NPs. Similarly the SF / NPs mixture obtained allowed the formation of silk-NPs hydrogel bionanocomposites. These structures were successfully obtained with all NPs. The in deep characterization of silk hydrogels *in situ*, by studying their formation, and *ex situ* by diverse methodologies provides strong guidelines for the design and fabrication of SF based bionanocomposites. These results show that the presence of NPs does not modify the formation and morphology characteristics of the obtained materials. However, the swelling capacity is impaired. The as obtained hydrogels proved a good biocompatibility showing no effect over cell proliferation and adhesion. In addition, the presence of HMBP-C≡CH in the NPs surface could be easily used for further functionalization of the resultant materials for example by coupling fluorophores, catalysts, drugs and peptides<sup>1,36–39</sup>.

Finally, we demonstrate the feasibility of our approach to produce other silk-NPs bionanocomposites such as sponges and 3D printed structures. The two materials were obtained successfully, but will need to be further characterized. Altogether, these results suggest that the same protocol could be applied to many other existing SF materials.

Next chapter focuses on the silk-NPs hydrogel bionanocomposites acquisition of NPs derived properties, specifically in antibacterial, magnetic and catalytic activity for Ag NPs, IONPs and Au NPs respectively.

## References

1. Aufaure, R. *et al.* Versatile ‘click’ synthesis of 1-hydroxy-1,1-methylenebisphosphonic acids with thioalkoxy substituents for the preparation of stable gold nanoparticles. *New J. Chem.* **41**, 12153–12158 (2017).
2. Iben Ayad, A. *et al.* ‘water soluble’ palladium nanoparticle engineering for C-C coupling, reduction and cyclization catalysis. *Green Chem.* **21**, 6646–6657 (2019).
3. Niemi, R., Turhanen, P., Vepsäläinen, J., Taipale, H. & Järvinen, T. Bisphosphonate prodrugs: Synthesis and in vitro evaluation of alkyl and acyloxymethyl esters of etidronic acid as bioreversible prodrugs of etidronate. *Eur. J. Pharm. Sci.* **11**, 173–180 (2000).
4. Rockwood, D. N. *et al.* Materials fabrication from Bombyx mori silk fibroin. *Nat. Protoc.* **6**, 1612–1631 (2011).
5. Partlow, B. P. *et al.* Highly tunable elastomeric silk biomaterials. *Adv. Funct. Mater.* **24**, 4615–4624 (2014).
6. Mu, X. *et al.* 3D Printing of Silk Protein Structures by Aqueous Solvent-Directed Molecular Assembly. *Macromol. Biosci.* **20**, 1900191 (2020).
7. Rodriguez, M. J. *et al.* 3D freeform printing of silk fibroin. *Acta Biomater.* **71**, 379–387 (2018).
8. Koleva, I. I., Niederländer, H. A. G. & Van Beek, T. A. Application of ABTS radical cation for selective on-line detection of radical scavengers in HPLC eluates. *Anal. Chem.* **73**, 3373–3381 (2001).
9. Ziegler, S. G., Gahl, W. A. & Ferreira, C. R. Disorders and Mechanisms of Ectopic Calcification. in *Genetics of Bone Biology and Skeletal Disease: Second Edition* 571–595 (Elsevier Inc., 2018). doi:10.1016/B978-0-12-804182-6.00032-0.
10. Bishop, N. J. & Russell, G. Bisphosphonates. *Osteogenes. Imperfecta A Transl. Approach to Brittle Bone Dis.* 495–500 (2013) doi:10.1016/B978-0-12-397165-4.00053-8.
11. Agence Nationale de sécurité du médicament et des produits de santé. Notice patient. <http://agence-prd.ansm.sante.fr/php/ecodex/notice/N0197570.htm> (2011).
12. Turhanen, P. A., Vepsäläinen, J. J. & Peräniemi, S. Advanced material and approach for metal ions removal from aqueous solutions. *Sci. Rep.* **5**, 1–8 (2015).
13. Karageorgou, M. A. *et al.* Gallium-68 labeled iron oxide nanoparticles coated with 2,3-dicarboxypropane-1,1-diphosphonic acid as a potential PET/MR imaging agent: A proof-of-concept study. *Contrast Media Mol. Imaging* **2017**, (2017).

14. Aufaure, R. *et al.* One pot microwave assisted synthesis of bisphosphonate alkene capped gold nanoparticles. *RSC Adv.* **4**, 59315–59322 (2014).
15. Hotze, E. M., Phenrat, T. & Lowry, G. V. Nanoparticle Aggregation: Challenges to Understanding Transport and Reactivity in the Environment. *J. Environ. Qual.* **39**, 1909–1924 (2010).
16. Foo, C. W. P. *et al.* Role of pH and charge on silk protein assembly in insects and spiders. *Appl. Phys. A Mater. Sci. Process.* **82**, 223–233 (2006).
17. Belanger, K. *et al.* A multi-layered nerve guidance conduit design adapted to facilitate surgical implantation. *Heal. Sci. Reports* **1**, e86 (2018).
18. Belanger, K. A. A functionalizable nerve graft design based on an organized electrospun silk fibroin nanofiber biomaterial for peripheral nerve regeneration. (Université de Technologie de Compiègne, 2017).
19. TEALE, F. W. & WEBER, G. Ultraviolet fluorescence of the aromatic amino acids. *Biochem. J.* **65**, 476–482 (1957).
20. Georgakoudi, I. *et al.* Intrinsic fluorescence changes associated with the conformational state of silk fibroin in biomaterial matrices. *Opt. Express* **15**, 1043 (2007).
21. Amirikia, M., Shariatzadeh, S. M. A., Jorsaraei, S. G. A. & Mehranjani, M. S. Auto-fluorescence of a silk fibroin-based scaffold and its interference with fluorophores in labeled cells. *Eur. Biophys. J.* **47**, 573–581 (2018).
22. Rice, W. L. *et al.* Non-invasive characterization of structure and morphology of silk fibroin biomaterials using non-linear microscopy. *Biomaterials* **29**, 2015–2024 (2008).
23. Wray, L. S. *et al.* Effect of processing on silk-based biomaterials: Reproducibility and biocompatibility. *J. Biomed. Mater. Res. - Part B Appl. Biomater.* **99 B**, 89–101 (2011).
24. Ghisaidoobe, A. B. T. & Chung, S. J. Intrinsic tryptophan fluorescence in the detection and analysis of proteins: A focus on förster resonance energy transfer techniques. *International Journal of Molecular Sciences* vol. 15 22518–22538 (2014).
25. Malencik, D. A., Sprouse, J. F., Swanson, C. A. & Anderson, S. R. Dityrosine : Preparation , Isolation , and Analysis 1. *Anal. Biochem.* **213**, 202–213 (1996).
26. Tsikrika, K., Lemos, M. A., Chu, B. S., Bremner, D. H. & Hungerford, G. Time-resolved fluorescence observation of di-tyrosine formation in horseradish peroxidase upon ultrasound treatment leading to enzyme inactivation. *Spectrochim. Acta - Part A Mol. Biomol. Spectrosc.* **173**, 324–327 (2017).



27. Huang, Y. F., Lu, S. C., Huang, Y. C. & Jan, J. S. Cross-linked, self-fluorescent gold nanoparticle/polypeptide nanocapsules comprising dityrosine for protein encapsulation and label-free imaging. *Small* **10**, 1939–1944 (2014).
28. Osman, A. M., Wong, K. K. Y. & Fernyhough, A. ABTS radical-driven oxidation of polyphenols: Isolation and structural elucidation of covalent adducts. *Biochem. Biophys. Res. Commun.* **346**, 321–329 (2006).
29. Lyngsie, G., Krumina, L., Tunlid, A. & Persson, P. Generation of hydroxyl radicals from reactions between a dimethoxyhydroquinone and iron oxide nanoparticles. *Sci. Rep.* **8**, 1–9 (2018).
30. Lin, Z. R., Zhao, L. & Dong, Y. H. Quantitative characterization of hydroxyl radical generation in a goethite-catalyzed Fenton-like reaction. *Chemosphere* **141**, 7–12 (2015).
31. Szunerits, S., Spadavecchia, J. & Boukherroub, R. Surface plasmon resonance: Signal amplification using colloidal gold nanoparticles for enhanced sensitivity. *Rev. Anal. Chem.* **33**, 153–164 (2014).
32. Agnihotri, S., Mukherji, S. & Mukherji, S. Size-controlled silver nanoparticles synthesized over the range 5–100 nm using the same protocol and their antibacterial efficacy. *RSC Adv.* **4**, 3974–3983 (2014).
33. Calamak, S. *et al.* Ag/silk fibroin nanofibers: Effect of fibroin morphology on Ag<sup>+</sup> release and antibacterial activity. *Eur. Polym. J.* **67**, 99–112 (2015).
34. Aliramaji, S., Zamanian, A. & Mozafari, M. Super-paramagnetic responsive silk fibroin/chitosan/magnetite scaffolds with tunable pore structures for bone tissue engineering applications. *Mater. Sci. Eng. C* **70**, 736–744 (2017).
35. Souter, P., Cunningham, J. C., Horner, A. & Genever, P. G. The variable toxicity of silver ions in cell culture media. *Toxicol. Vitro.* **60**, 154–159 (2019).
36. Nehlig, E., Motte, L. & Guénin, E. Magnetic nano-organocatalysts: Impact of surface functionalization on catalytic activity. *RSC Adv.* **5**, 104688–104694 (2015).
37. Belkahla, H. *et al.* USPIO-PEG nanoparticles functionalized with a highly specific collagen-binding peptide: A step towards MRI diagnosis of fibrosis. *J. Mater. Chem. B* **8**, 5515–5528 (2020).
38. Bolley, J. *et al.* Carbodiimide versus click chemistry for nanoparticle surface functionalization: A comparative study for the elaboration of multimodal superparamagnetic nanoparticles targeting  $\alpha\beta 3$  integrins. *Langmuir* **29**, 14639–14647 (2013).

39. Barosi, A. *et al.* Synthesis and activation of an iron oxide immobilized drug-mimicking reporter under conventional and pulsed X-ray irradiation conditions. *RSC Adv.* **10**, 3366–3370 (2020).

## Chapter III: Potential applications of silver, gold and iron oxide silk-NPs hydrogel bionanocomposites

---



## 1. Introduction

Although four different silk-NPs bionanocomposite materials were successfully synthesized in chapter II, we have chosen silk hydrogels for the rest of this work due to their easier synthesis method and their increasing interest for soft tissue replacement among other applications. In addition, the ability to fine-tune the mechanical, swelling and degradation properties of silk hydrogels permits to tackle a broad field of unmet material characteristics. Silk hydrogels have been extensively characterized in Chapter I:2.6 providing the required knowledge to allow the optimization and adjustment of the material properties to match specific application requirements. The present chapter presents three possible applications of silk-NPs hydrogel bionanocomposites:

- i. Antibacterial application for silk-Ag NPs and silk-Au NPs hydrogel bionanocomposites;
- ii. Brain injection and MRI monitoring for silk-IONPs hydrogel bionanocomposites;
- iii. Depollution application for silk-Au NPs hydrogel bionanocomposites

Each section of this chapter focuses on one application and contains a brief introduction providing to the reader the background and importance of each application.

## 2. Antibacterial applications

### 2.1. Introduction

SF properties have extensively been discussed in Chapter I:1. SF biodegradability, biocompatibility and enhanced mechanical properties make it an interesting material for biomedical applications. SF hydrogels have already been developed for tissue engineering <sup>1,2</sup>, skin substitutes <sup>3</sup>, drug delivery <sup>4</sup> and wound healing gels <sup>5</sup> among many others. However, the proteic nature of SF together with the high-water content of hydrogels makes them a great substrate for bacteria development.

Bacterial infections can occur during medical device implantation or other surgeries. These infections are an increasing concern due to the existence of multidrug resistant bacteria. In these cases, the use of antibiotics is not sufficient and another solution must be found. Silver is known by its broad-spectrum antibacterial properties. However silver ions are toxic for the human body and their use is not appropriate for biomedical devices <sup>6</sup>. Instead, the use of silver nanoparticles (Ag NPs) as antibacterial agent has given promising results <sup>7–12</sup>.

Although much less effective, antibacterial properties have also been attributed to Au NPs as reported earlier in Chapter I:2.2.1.2. Gold being the inherent material for excellence for biomedical applications due to its low toxicity its use as antibacterial agent has been explored in the literature.

This section focuses on the antibacterial activity of silk-Au NPs and silk-Ag NPs hydrogel bionanocomposites that have been extensively characterized in Chapter I:2.6. Their antibacterial activity is evaluated against gram-negative and gram-positive bacteria.

## 2.2. Materials and methods

### 2.2.1. Materials

Muller-Hilton and Luria-Broth culture media, and AC Agar for microbiology, phosphate buffered saline tablets (PBS, P4417) were purchased from Sigma-Aldrich.

Bacterial strains *Escherichia coli* (*E.coli*) ATCC 25922, *Staphylococcus epidermidis* (*S. epidermidis*) CIP 6821 and CIP 105777 were purchased from American Type Culture Collection (ATCC) and the collection of bacteria of the Institut Pasteur (CIP) respectively.

### 2.2.2. Antibacterial activity

500  $\mu$ L hydrogels were prepared in PDMS molds of diameter ( $\varnothing$ ) 16.6 mm and h = 3 mm. Gelation was done in a desiccator in presence of water to avoid gel evaporation. Gelation time was set to 24 h. Gelled samples were removed from the mold and sterilized by a 30 minutes immersion in 70 % ethanol. Samples were posteriorly washed with abundant sterile water three times. Sterilized samples were left to hydrate in water for 5h.

#### 2.2.2.1 Bacteria culture

All bacteria strains were kept in glycerolized aliquots at  $-20^{\circ}\text{C}$ . All *E. coli* cultures and tests were done in Luria-Broth culture media (agar and liquid). Both *S. epidermidis* strains were cultured in Muller-Hilton culture media (agar and liquid). Liquid cultures were prepared one day before the tests; 5 mL of culture media were placed in a 15 mL falcon tube and a 100  $\mu$ L inoculum from thawed bacterial aliquots was added. Tubes were incubated slightly open overnight (O/N) at  $36^{\circ}\text{C}$  in a horizontal rocking machine. Bacterial growth was evaluated by measuring the optical density (OD) at 620 nm.

#### 2.2.2.2 Zones of inhibition / Agar diffusion test

SF hydrogels without NPs were used as negative control. The test zones of inhibition was used to assess antibacterial activity by release against two strains of gram-positive *S. epidermidis* (CIP 6821 and CIP 105.777) and gram-negative *E. coli* (ATTC 25922) bacteria. Muller-Hilton ( $25\text{ g}\cdot\text{L}^{-1}$ ) and Luria-Broth ( $20\text{ g}\cdot\text{L}^{-1}$ ) culture media were used for *S. epidermidis* and *E. coli*, respectively. Bacterial cultures turbidity was measured by absorbance at 620 nm. Bacterial cultures with an  $A_{620\text{nm}} = 1$  were diluted 1:100 in PBS. Agar plates (culture media + agar  $15\text{ g}\cdot\text{L}^{-1}$ ) were inoculated with 20  $\mu$ L bacteria that were homogeneously distributed with a microbiological spreader. Each hydrogel was placed in the center of an inoculated agar Petri dish. Petri dishes were then incubated upside down at  $37^{\circ}\text{C}$  O/N to allow bacteria growth. All

Petri dishes were imaged with Scan 500 (Interscience) and zones of inhibition surrounding the samples were evaluated. To evaluate whether bacteria could grow where the hydrogels were placed, the latter were removed from all samples and Petri dishes were incubated again at 37 °C O/N. Samples were imaged the day after. All conditions were tested in triplicate.

#### 2.2.2.3 Indirect contact agar diffusion test

Indirect contact agar diffusion tests were performed to evaluate whether the hydrogel was able to release any antibacterial agent (namely  $\text{Ag}^+$  or Ag NPs themselves) in a sufficient concentration to inhibit bacterial growth. Sterile hydrogels were placed over sterile agar Petri dish and those were incubated upside down at 37 °C O/N to allow substance release. Hydrogels were removed from agar Petri dishes and an *E. coli* bacterial solution of  $A_{620\text{nm}} = 0.01$  was sprayed over agar. Samples were incubated upside down at 37 °C O/N to allow bacterial growth. Petri dishes were imaged using Scan 500 (Interscience). All tests were performed in triplicate.



## 2.3. Results and discussion

### 2.3.1. Antibacterial activity

The use of Ag NPs as an antibacterial agent is largely extended nowadays. However Ag<sup>+</sup> ions are known to be toxic to humans and several diseases have been related to silver ion exposure<sup>13,14</sup>. Therefore, the use of Ag NPs instead of silver ions is preferred as no toxicity has yet been found to our knowledge. Furthermore, the possibility to use Au NPs instead has been explored in the literature due to the lower toxicity of gold ions. Moreover the results previously presented in this work (Chapter I:2.6.10) proved the lack of cytotoxicity of all the silk-NPs hydrogel bionanocomposites.

#### 2.3.1.1 Bacteria strain selection

When evaluating the antibacterial activity, it is important to consider the nature of the microorganism used as well as the application of the final material. Therefore, the selected bacterial strains must at least cover the gram-positive and gram-negative families and be in accordance with the application of the material. In this study, three bacterial strains were chosen for antibacterial activity evaluation: *E. coli* ATCC 25922 (G<sup>-</sup>) and *S. epidermidis* CIP 6821 and CIP 105.777 (G<sup>+</sup>) (called ATCC 35984 or RP62A as well). *E. coli* being one of the most prevalent microorganisms in the ecosystem and the cause of several common diseases it is the gold standard from the gram-negative family. On the other hand, as silk-NPs bionanocomposites are mainly used at the interface between wound and external environment, *S. epidermidis* has been chosen because of its implication in skin infections. Moreover, this strain is a good representative from the gram-positive family. The formation of biofilms by several bacteria allow a higher resistance towards antibacterial agents due to the formation of a *fortified* structure. This ability is here taken into account by the selection of *S. epidermidis* CIP 105.777<sup>15,16</sup>.

#### 2.3.1.2 Antibacterial activity evaluation

The test zones of inhibition has been largely used by many authors to evaluate the antibacterial activity of Ag NPs embedded materials<sup>17–21</sup>. Herein, the antibacterial activity has been evaluated using this method that consists on placing the sample onto an inoculated agar Petri dish and observing if there is any bacterial growth inhibition effect in the zone surrounding the sample. The protocol is depicted in Figure III.1.

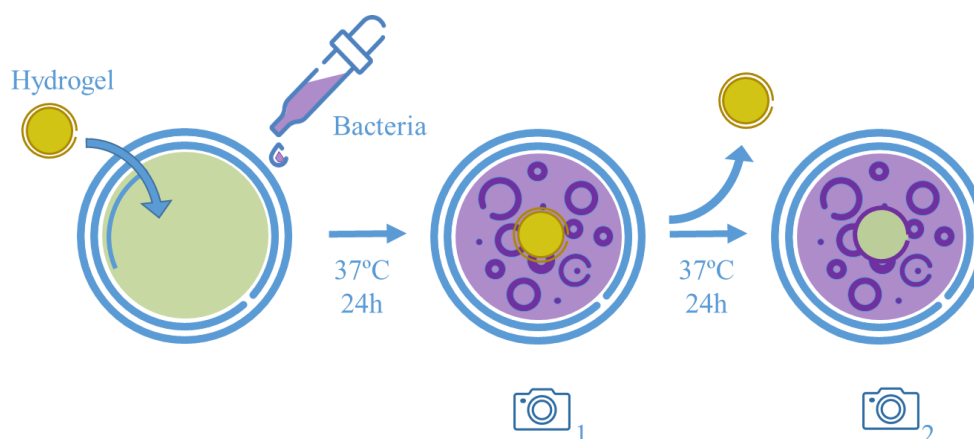


**Figure III.1.** Schema of zones of inhibition protocol. Briefly, the hydrogel is placed over a bacteria inoculated Petri dish and incubated for 24 h at 37°C. After taking a picture, hydrogel was removed and the Petri dish was again incubated at 37°C for additional 24h. The camera icons indicate the time point at which images were taken. The bacterial growth inhibition was evaluated at this stage.

As shown in Figure III.2 A and C a small halo of inhibition was found for almost all samples. The presence of this halo even in silk samples suggests that it is due to the dehydration of hydrogel. The water release of all samples occurring when incubated at 37 °C may push bacteria away from the surrounding areas of the hydrogel. However, a closer look to the hydrogels reveals that bacteria were able to grow on silk hydrogel but not on silk-Au NPs and silk-Ag NPs hydrogel bionanocomposites. Accordingly, two main hypothesis can be considered. The bacterial growth inhibition is caused either (i) by direct contact between bacteria and hydrogels, or (ii) by a release of Au or Ag in the form of NPs or ions in the medium surrounding the hydrogel.

Further experiments were conducted to assess whether bacteria could grow after being in direct contact with silk-Au NPs and silk-Ag NPs hydrogel bionanocomposites. This evaluation was carried out by removing the hydrogels from the agar plate after the test and incubating the Petri dish overnight at 37 °C. Bacteria growth was only observed in the zones where the silk and silk-Au NPs hydrogels were initially placed (Figure III.2 B and D). These results suggests that silk-Au NPs hydrogel bionanocomposites do not show an antibacterial activity in the studied conditions. However, bacteria were unable to grow where silk-Ag NPs hydrogel bionanocomposites had been (Figure III.2 F). The antibacterial effect of these materials seems to be slightly more efficient on Gram positive, *S. epidermidis*, strains compared to Gram negative, *E. coli*, strain. Nevertheless, further evaluations should be conducted to elucidate the antibacterial mechanism. These results, together with the lack of Ag NPs release from the hydrogel in water, suggest that the antibacterial activity of our hydrogel takes place by direct contact rather than by release.

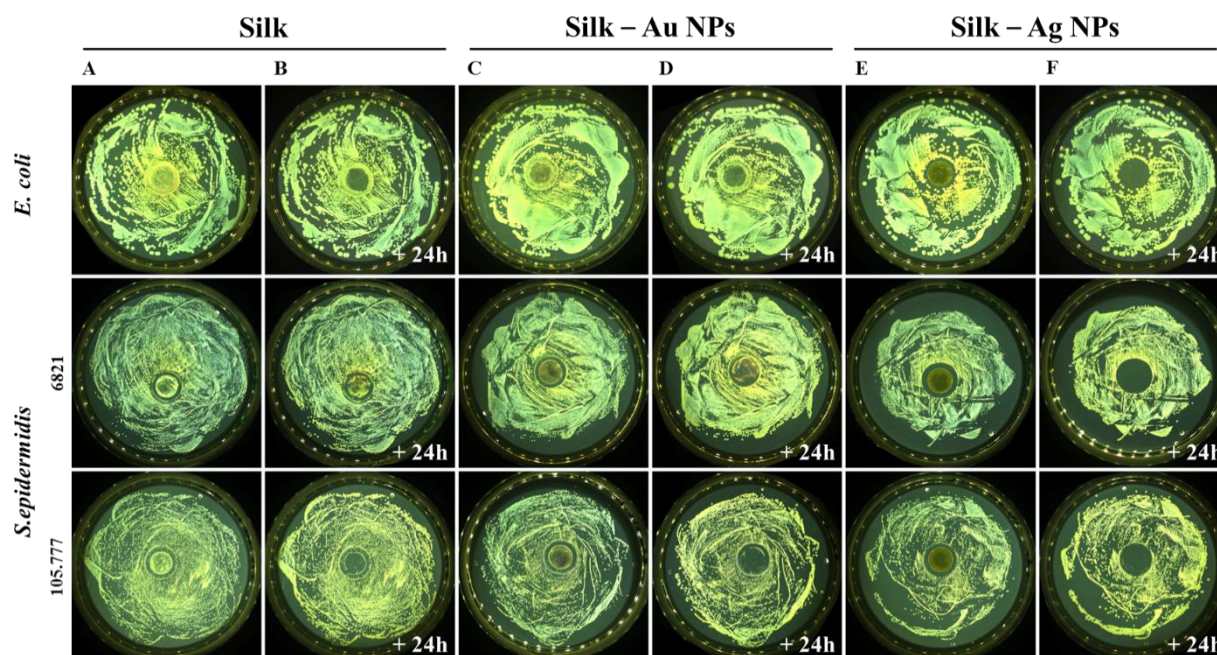


**Figure III.2.** *E. coli* and *S. epidermidis* bacteria growth in presence of silk or silk-NPs hydrogels ((A) silk, (C) silk-Au NPs and (E) silk-Ag NPs). Hydrogel was then removed and bacteria were incubated O/N ((B) silk, (D) silk-Au NPs and (F) silk-Ag NPs) showing that bacteria were not able to grow were the silk-Ag NPs hydrogel bionanocomposite had been.

To validate this hypothesis we placed silk-Au NPs and silk-Ag NPs hydrogel bionanocomposites on a sterile agar Petri dish and incubated it upside down O/N at 37 °C to allow the presumable release to occur. Then, we removed the hydrogel from the agar and inoculated *E. coli*. A spray was used to avoid any possible removal of Ag<sup>+</sup> ions or Ag NPs presumably released from the hydrogel bionanocomposites. Samples were then incubated again O/N at 37 °C. The detailed protocol used for this experiment is depicted in Figure III.3. Figure III.4 shows that no growth inhibition can be observed in any situation, indicating that the antibacterial activity of silk-Ag NPs hydrogel bionanocomposites is not due to a something (ions or NPs) released from the hydrogel.

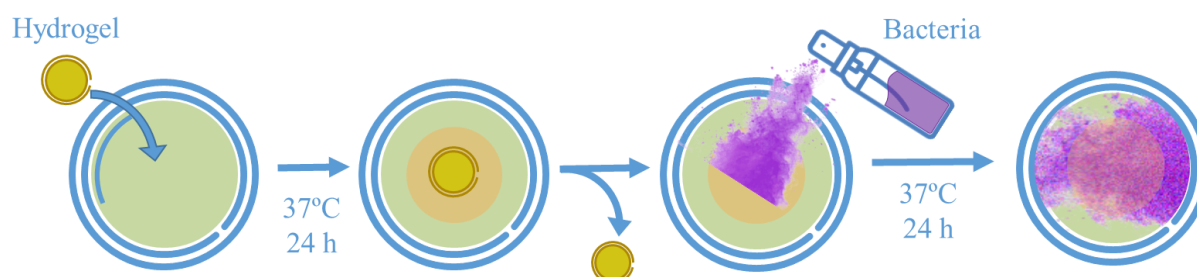


**Figure III.3.** Schema of the protocol used for antibacterial evaluation through indirect contact agar diffusion test. Hydrogel is placed in a sterile Petri dish and incubated at 37°C for 24h to allow release, then hydrogel is removed and bacteria are sprayed over the plate. Growth inhibition is evaluated after 24h incubation at 37°C.

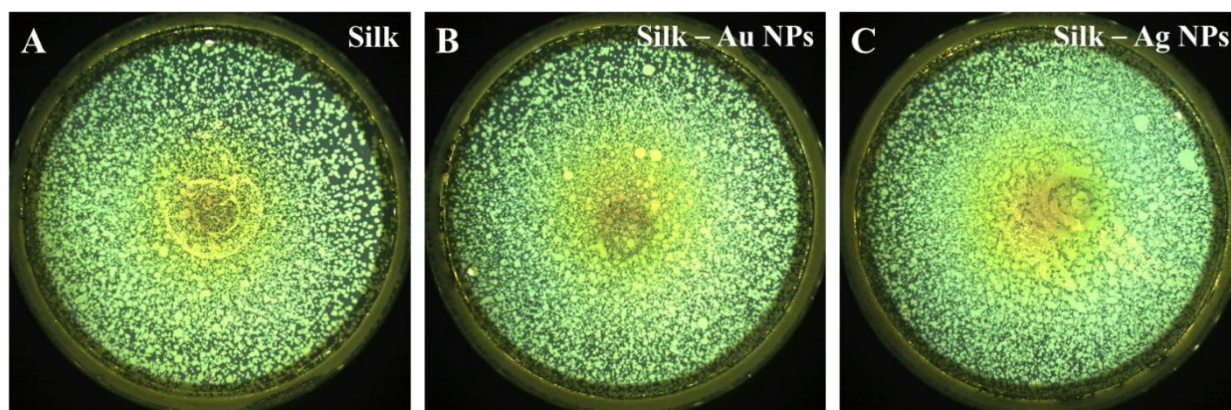


**Figure III.4.** Antibacterial activity by indirect contact with silk (A), silk-Au NPs (B) and silk-Ag NPs hydrogels (C). Hydrogels were kept over the agar media at 37°C O/N and then removed. Agar was sprayed with *E.coli* bacteria and left to grow O/N.

## 2.5. Conclusion

This section proves the antibacterial activity of silk-Ag NPs hydrogel bionanocomposites against gram-negative and gram-positive bacteria, although no antibacterial activity was found for silk-Au NPs hydrogel bionanocomposites. Strong evidence suggest that this antibacterial activity is achieved by direct contact and not by silver ion release as previously suggested in many cases within the literature to explain NPs antibacterial mechanism. These results together with the biocompatibility of silk-Ag NPs hydrogel bionanocomposites reported in Chapter I:2.6.10 render these materials very interesting for biomedical applications. As an example, they could be used as antibacterial implantable scaffolds to reduce bacterial infections derived from surgery. However, many others applications may be addressed with such material. In addition, the possibility to functionalize, in an easy manner, the embedded NPs allow to best match the properties of the materials to the patient needs or desired application.





### 3. Magnetic properties and MRI applications

#### 3.1. Introduction

Several diseases such as Alzheimer, cerebral stroke or glioblastoma, can cause brain damage resulting in dramatic impact in human life. In these cases, damaged tissue undergoes necrosis (degradation) leaving a cavity that cannot be easily filled by cells due to the lack of supporting material. Moreover, the necrotic process results in the formation of a barrier in order to protect healthy tissue from damaged area. Both processes avoid neurogenesis (formation of new neurons) and neural tissue regeneration<sup>22,23</sup>. Up to date treatments focus on two main points of action. In first place, the main aim is to stop the disease development. Long monitoring, prevention of further brain damage and disease recurrence follow this step<sup>24</sup>. However, these approaches fail to recover the tissue function and therefore are only useful in a minority of all cases, when disease is diagnosed at early stages. To overcome this issue research has focused in the replacement of lost tissue or the induction of existing tissue regeneration. Although successful advances have been made in the field of tissue regeneration in different organs such as heart or liver, many challenges remain in the regeneration of neural tissue due to its low regeneration capacity.

As stated before, the existence of a supporting material is crucial to enhance neural tissue regeneration. The increasing use of silk hydrogels to replace soft tissue in regenerative medicine has been already described in the previous section. The development of these materials are of special interest for brain implants and regenerative therapies due to their adaptable mechanical properties and have been already studied<sup>23</sup>. In addition, hydrogels can be implanted into a damaged brain through a minimal invasive surgery such as injection. On the other side, IONPs are widely known by their use as contrast agents for MRI providing a non-invasive imaging possibility.

The combination of silk regenerative properties together with the imaging possibility of the implant through MRI thanks to IONPs is promising for brain regeneration. This section focuses on the use of silk-IONPs hydrogel bionanocomposites as cavity filler after neural damage. Firstly, the IONPs magnetic properties are evaluated in suspension and within the silk-IONPs hydrogel. Then the evaluation of several implant surgeries is presented together with the study of their impact and presence of the hydrogel in the brain. Monitoring of implanted hydrogel is done *in vivo* by MRI. Post-mortem analysis are carried by histology and immunostaining. *In vivo* studies have been carried for up to 3 months to evaluate long-term response.

## 3.2. Materials and methods

### 3.2.1. Magnetic properties

A vibrating sample magnetometer (VSM Quantum Design, Versalab) was used for magnetic characterization. VSM measures the magnetization by cycling the applied field from -30 to +30 kOe with a step rate of  $25 \text{ Oe s}^{-1}$ . Magnetization measurements were performed on IONPs suspensions and cryogels at 300 K. The zero field cooled (ZFC) curve was obtained by first cooling the system in zero field from 260 to 50 K. Next, an external magnetic field of 100 Oe was applied, and subsequently the magnetization was recorded with a gradual increase in temperature from 50 to 260 K. The field cooled (FC) curve was measured by decreasing the temperature from 260 to 50 K in the same applied field of 100 Oe.

### 3.2.2. *In vivo* implants

All *in vivo* experiments were conducted in strict accordance with the recommendations of the European Community (2010/63/EU) and the French legislation (decree no 2013-118) for use and care of laboratory animals. Experiments were conducted on Fisher F344 adult rats raised at NeuroSpin. Prior to surgery rats were weighted, anesthetized with a mixture of ketamine / xylazine and placed into a stereotaxic frame. Under aseptic conditions a skin incision was made, the skull was exposed, the bregma was identified (Figure III.5) and a burr hole was drilled (at 3.2 mm lateral). At this point, the protocol was adapted to each implanted material as explained in the following sections. Once sample was implanted, drilled hole was filled in with bone wax, wound was disinfected with iodate water and sutured. Animals were monitored until wake up.

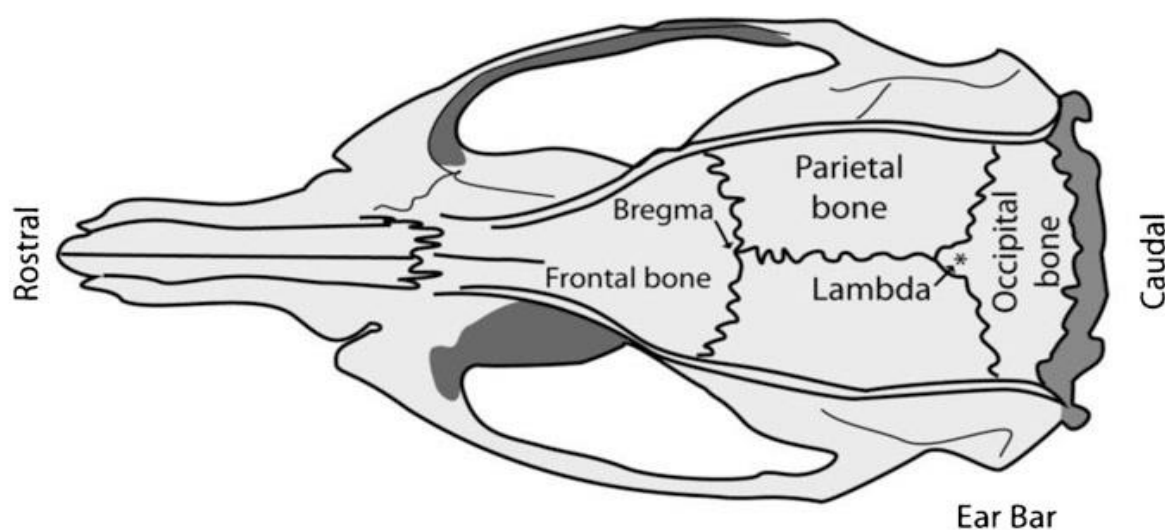


**Figure III.5.** Schematic of a rat skull depicting the position of bregma relative to the frontal and parietal skull bones and the position for placing of the ear bars. From Assi *et al* 2012<sup>25</sup>.



### 3.2.2.1 Brain implantation of cross-linked hydrogel

#### *In-syringe hydrogel*

Silk-IONPs hydrogels bionanocomposites (0.2 mM IONPs) were prepared into 1 mL syringes. Briefly, dispersions were mixed in the same proportions than previously explained (Chapter I:2.5.2) and 200  $\mu$ L were placed into a syringe. Samples were incubated at RT O/N for gelation. Once gelled, samples were sterilized by a 30 minutes immersion in 70 % ethanol and washed with abundant sterile demineralized water. Samples were left to hydrate in water and stored at 4°C for at least 24 h. Approximately 5  $\mu$ L of hydrogel prepared directly into the syringe were extruded with the help of a catheter with needle (Surflo® IV catheter 24G, Terumo) into the left brain hemisphere. Injection was done in two rats over bregma at coordinates: 3.2 mm lateral (left) and 5 mm depth.

#### *Beads*

Silk-IONPs hydrogels bionanocomposites (0.2 mM IONPs) were prepared into small beads. Briefly, dispersions were mixed in the same proportions than previously explained (Chapter I:2.5.2.); beads were produced by depositing 10  $\mu$ L drops over and hydrophobic flat surface (PDMS). Samples were incubated at RT O/N for gelation. Once gelled, samples were sterilized by a 30 minutes immersion in 70 % ethanol, washed with abundant sterile demineralized water, left to hydrate in water and stored at 4°C for at least 24 h. Beads were placed into the right brain hemisphere with surgical clamps through the drilled hole produced following the previously explained procedure. Implantation was done in two rats over bregma at coordinates: 3.2 mm lateral (right) and 5 mm depth.

### 3.2.2.2 Brain injection of hydrogel dispersion

The injection of hydrogel dispersion for *in situ* gelation was evaluated. Four adult Fisher F344 rats (aged around 6 months, 3 female 1 male) were used. Hydrogel mixture was prepared immediately before injection and 5  $\mu$ L were injected using a Hamilton syringe at a flow rate of 2  $\mu$ L min<sup>-1</sup>. Injection was done within the bregma at coordinates of 3.2 mm lateral and 5 mm depth.

## 3.2.3. Magnetic resonance imaging

### 3.2.3.1 *In vitro* MRI

Silk-IONPs hydrogels bionanocomposites with various concentrations of IONPs ([Fe] = 0.05 to 0.2 mM) were prepared at 25 °C and included into an agarose gel. In order to generate T2 weighted images and thus calculate T2 maps, a multi-slice-multiecho sequence (TE = 11, 33,

55, 77, 99 ms; 16 echos; echo spacing = 11 ms and TR = 2500 ms) with a 1 mm slice thickness was used to generate high-resolution coronal images (Matrix:  $192 \times 192$ , Pixel size:  $0.234 \times 0.234$  mm). By graphing changes in relaxation rate  $R_2$  ( $R_2 = 1/T_2$ ) at different concentration, the transverse relaxivity  $r_2$  is obtained from the slope.

#### 3.2.3.2 *In vivo MRI*

*In vivo* MRI images were generated with rats alive. Animals were anesthetized with isoflurane during the entire acquisition time. In order to generate T2 weighted images and thus calculate T2 maps, a multi-gradient echo (MGE) sequence (echo time (TE) = from 3 to 27 ms; 8 echos; echo spacing = 3.5 ms and repetition time (TR) = 90 ms) was used to generate high-resolution coronal images (Matrix:  $214 \times 186 \times 104$ , Field-of-View =  $32.1 \times 27.9 \times 15.6$  mm<sup>3</sup>, spatial resolution =  $150 \times 150 \times 150$   $\mu$ m<sup>3</sup>). Acquisition time was set to 29 minutes.

#### 3.2.4. Histology and immunostaining

An exsanguinous perfusion was made prior to brain removal. Brain was fixed with 4% PFA for 2h, placed in a sucrose bath and slowly frozen in isopentane at  $-30$  °C. Once frozen samples were stored at  $-80$  °C. Samples were cut using a cryostat into 30  $\mu$ m thickness slices. Slices were immersed for 2 h in a blocking / permeating solution composed of 5% donkey serum, 1% BSA, triton (different concentration depending on the antibody used) diluted into PBS 0.01M.

Fixed and permeabilized samples were then immunostained at RT with pertinent primary and secondary antibodies. Table III.1 and Table III.2 recapitulate all the antibodies used and specify their concentration, the requirement of triton concentration for cell permeabilization and the required incubation time. All antibodies were diluted into 0.01M PBS containing 5 % donkey serum. Finally, samples were stained with DAPI and mounted into microscopes coverslips with Progold. Microscope slides were observed with AxioObserver Z1 fluorescence microscope (Zeiss) and treated using the Zen2 software (Zeiss).

**Table III.1.** Primary antibodies used. References, supplier, dilution, incubation times and permeabilization solution requirements.

Primary antibodies	Reference	Supplier	Dilution	Incubation time	Permeabilization
Rabbit anti <b>GFAP</b>	ab7260	Abcam	1/500	1 h	1% Triton
Goat anti <b>Iba1</b>	ab5076	Abcam	1/500	1 h	1% Triton
Mouse anti <b>CD8</b>	ab33786	Abcam	1/500	1 h	1% Triton
Chicken anti <b>Nestin</b>	ab134017	Abcam	1/500	1 h	1% Triton
Rabbit anti <b>Caspase 3</b>	ab13847	Abcam	1/500	1 h	1% Triton
Rabbit anti <b>TBR1</b>	ab31940	Abcam	1/100	2 h	1% Triton
Rabbit anti <b>CD133</b>	ab16518	Abcam	1/50	2 h	0.2 % Triton
Rabbit anti $\beta$ -tubuline III	ab18207	Abcam	1/1000	2h	0.2 % Triton
Mouse anti <b>NeuN</b> Alexa 488	MAB377X	Millipore	1/100	1h	1% Triton
Chicken anti <b>TBR2</b>	AB15894	Millipore	1/100	2 h	1% Triton

**Table III.2.** Secondary antibodies used. References, supplier, dilution and incubation times.

Secondary antibodies	Reference	Supplier	Dilution	Incubation time
Donkey anti-rabbit Alexa647	ab150067	Abcam	1/250	1 h
Donkey anti-goat Alexa647	ab150135	Abcam	1/250	1 h
Donkey anti-mouse Alexa647	ab150111	Abcam	1/250	1 h
Donkey anti-chick Cy3	AP194C	Millipore	1/250	1 h

### 3.3. Results and discussion

#### 3.3.1. Magnetic properties

IONPs have been long used as contrast agents for MRI due to their superparamagnetic properties. Magnetization curves (Figure III.6 A) indicate that silk-IONPs cryogel bionanocomposites exhibit a superparamagnetic behavior with a saturate magnetization around 0.08 emu per g of cryogel or 50 emu per g of IONPs in accordance of such sized IONPs <sup>26</sup>. Note that comparing Silk-IONPs cryogel bionanocomposites and water dispersion (Figure A.5), magnetization remained similar while silk-IONPs cryogel bionanocomposites blocking temperature decreased ( $T_b = 90$  K) compared to IONPs water dispersion ( $T_b = 130$  K) as shown in Figure III.6 B. This decrease of  $T_b$  is in accordance with efficient dispersion of IONPs within the cryogel by reducing the particle-particle interactions.

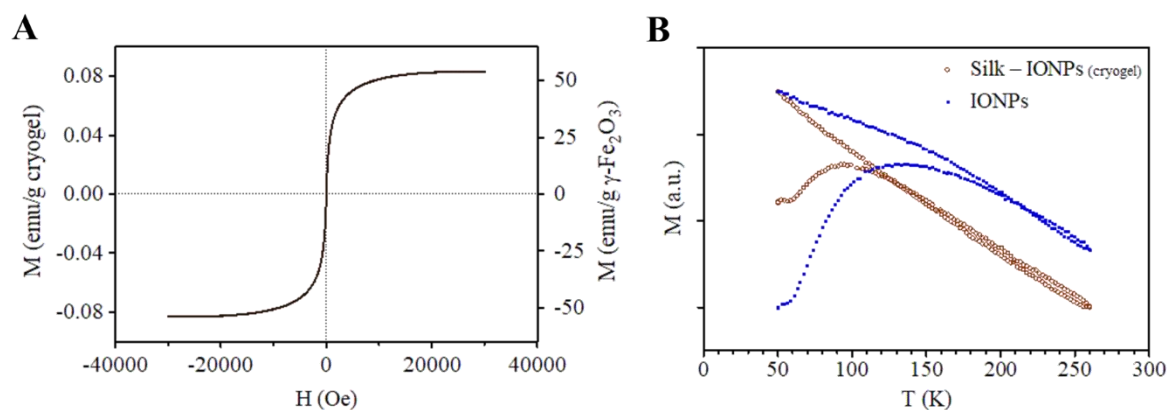


**Figure III.6.** (A) Magnetization curve of IONPs embedded silk cryogel by mass of silk or mass of IONPs showing the superparamagnetic behavior of the material. (B) Sample magnetization as function of temperature comparing IONPs embedded silk cryogels (brown) with IONPs dispersion (blue). Decreased  $T_b$  for IONPs embedded cryogels suggests better IONPs dispersion within the material than in suspension.

Herein we also aimed to explore the potency of using MRI to follow our silk-IONPs hydrogel bionanocomposite. To investigate the MR signal enhancement effects, silk and silk-IONPs (0.05 to 0.2 mM) hydrogels were embedded in a 3% agarose gel and measured on a 7 T MRI scanner at 25°C. As shown in Figure III.7 A, T2 weighted images change drastically in signal intensity with an increasing amount of IONPs within silk-IONPs hydrogel bionanocomposites, indicating that these materials generated MR contrast on transverse ( $T_2$ ) proton relaxation times weighted sequences. The transverse  $r_2$  relaxivity was found to be  $231 \text{ mM}^{-1} \text{ s}^{-1}$ , suggesting high  $T_2$  contrasting effect (Figure III.7 B). These results suggest that the silk-IONPs hydrogel bionanocomposites can be monitored over time by a non-invasive technique as MRI.

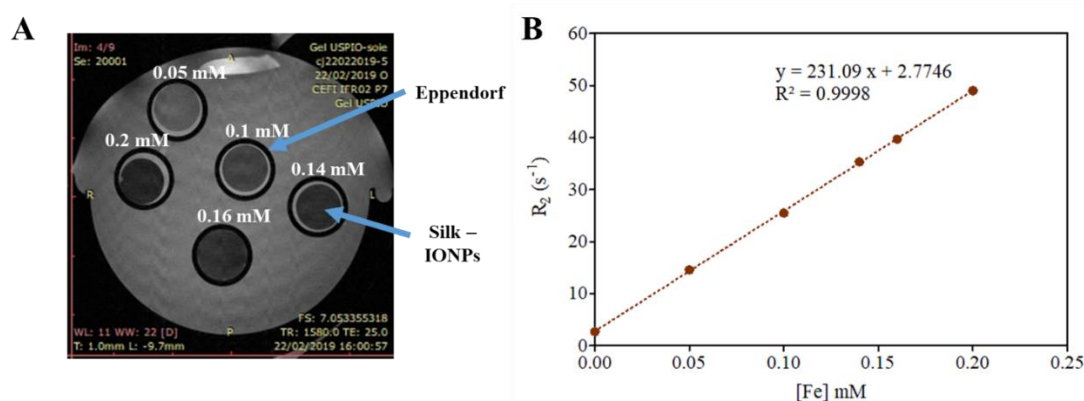


**Figure III.7.** (A) MRI images obtained from several silk-IONPs hydrogel bionanocomposites with different iron concentration. Clear image contrast enhancement is seen as a function of the iron concentration. (B) Proton transverse relaxation rates ( $R_2$ ) measured at 7 T for silk-IONPs hydrogel bionanocomposites.

### 3.3.2. *In vivo* implantations

#### 3.3.2.1 Crosslinked hydrogel

Two fisher F344 rats were injected in the cortical area of the brain at a depth of 5 mm with silk-IONPs in-syringe gelled hydrogels and beads. The first set of injections did not allow a precise control of the injected volume and injection area, reducing the chances, in case it was needed for a precise application, to target a desired zone. In addition, the high viscosity of the formed hydrogel resulted in both cases in the removal of a part of the deposited gel from the injection site when the syringe was pulled out. However, silk-IONPs hydrogel bionanocomposite was still seen in the deeper zone of the brain, in the periventricular area where it had been placed.

The implantation of gelled beads was performed in the opposite brain hemisphere of the same two rats. The surgery demonstrated that solidified materials were not flexible enough to be easily implanted into the brain resulting in an uncontrolled and superficial position of the material in the outer layers of the cortex. This surgery was successfully conducted only in one of the cases, as the bead did not stay in place in the second case. Moreover, this procedure was too invasive and destructive for the brain tissues. Nevertheless, rats survived for 12 days. In one of the cases, a stroke was determined as the cause of the death.

Immunostaining was carried against specific cell types, namely microglia and astrocytes, due to their neuron supporting and protective role in brain tissues. Microglia cells are the brain specific macrophages. They play a key role in brain immunity response by scanning the tissue for abnormalities. During brain tissue damage these cells are activated and able to migrate to the damaged area, proliferate, phagocyte (internalizing something into the cell) and degrade cell debris, unknown, potentially neurotoxic, or abnormal molecules that may be present in the tissue environment<sup>27</sup>. On the other side, astrocytes are key for neuron survival as they nourish

them and control the surrounding areas by playing an important role in the immune response and maintaining the blood brain barrier (BBB). This cell type is also very important for tissue regeneration after brain damage<sup>28</sup>. In addition, although lymphocytes T CD8<sup>+</sup> are part of the peripheral immunity system and should not be present in the brain, they can enter neuronal tissues after brain damage due to blood capillary disruption. This cell type is responsible of targeting foreign body molecules for their elimination from the body.

Post-mortem histology and immunostaining images allowed the confirmation of the presence of silk-IONPs hydrogel bionanocomposite into the brain due to its autofluorescence into the green and orange channels. Such autofluorescence must be taken into account for image interpretation. Immunostaining against glial-fibrillary acidic protein (GFAP) and ionized calcium-binding adaptor molecule 1 (iba-1) allowed the visualization of astrocytes and microglia respectively. At this stage silk-IONPs hydrogel bionanocomposite was largely infiltrated by microglia, astrocytes and lymphocytes T CD8 (peripheral immunity cells) suggesting a foreign body response (Figure III.8). Figure III.8 shows astrocyte activation within the implant area and a general brain apoptosis (induced cell death) response, which was revealed by a caspase immunostaining, probably resulting from a great inflammatory response.

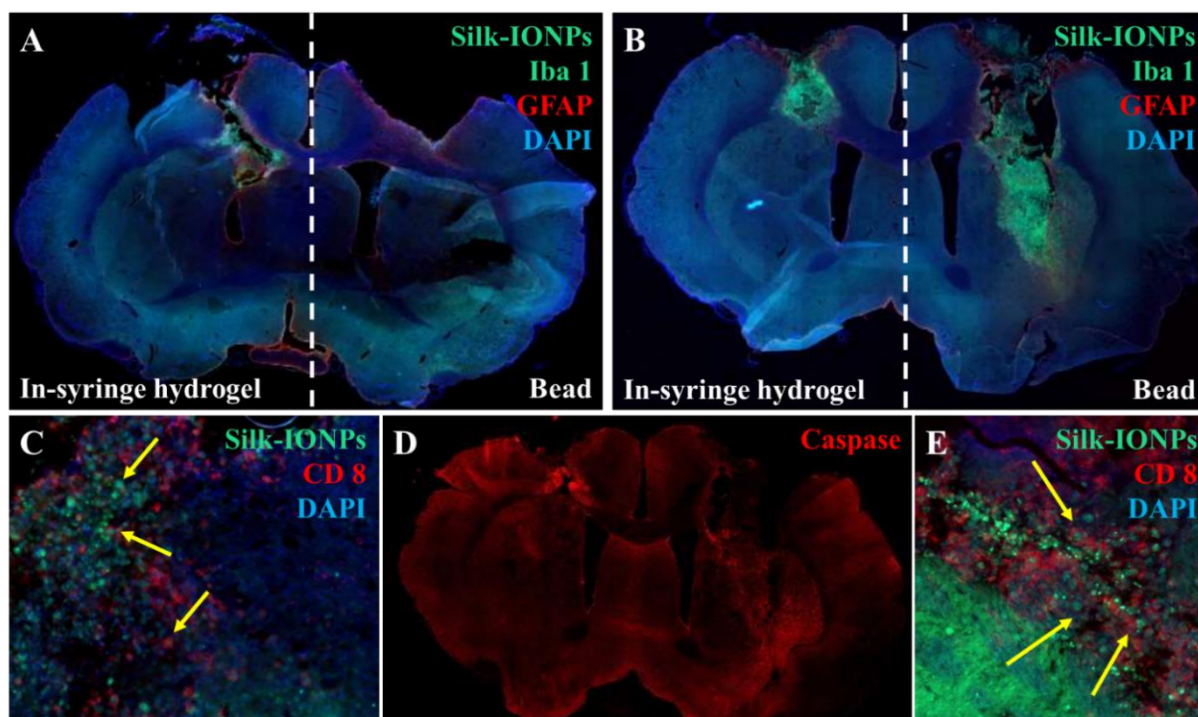


**Figure III.8.** General overview of implanted silk-IONPs hydrogel bionanocomposites within the brain, in-syringe hydrogel (left) and hydrogel beads (right) (A, B, C). Images A and B show staining for Iba 1, GFAP and DAPI corresponding to astrocytes, microglia and cell nucleus respectively. Silk-IONPs hydrogel is as well autofluorescent in green. A closer look and staining against lymphocytes CD8 show that these cells have incorporated silk hydrogel (yellow arrows) (C, E). Caspase staining reveals the overall apoptosis within the brain (D). © CEA-NeuroSpin Courtesy of S.Mériaux and F.Geffroy.



### 3.3.2.2 *In situ* crosslinking

In order to elucidate whether the inflammation was due to the invasiveness of the surgical procedure or because of the implanted material, a new implantation was conducted. In this case the silk-IONPs hydrogel mixture was prepared (Chapter I:2.5.2) and immediately injected into the rat brain for *in situ* crosslinking. Preliminary tests showed that silk and silk-NPs hydrogel crosslinking was efficiently performed *in vitro* in culture media supporting the possibility of *in situ* crosslinking. This procedure was less invasive resulting in less surgical procedure-related brain damage. Four Fisher F344 rats were included in this study in order to evaluate the body response after 7, 15, 30 and 90 days.

Although the injection was done before complete gelation, the viscosity of the dispersion remained high, at the limit accepted for this procedure, resulting in a partial hydrogel removal when pulling the syringe out from the brain after injection. Nevertheless, silk-IONPs hydrogel was still present in the deepest zone of injection as seen in histology slices. The apparition of green autofluorescence in the injection are indicates the good *in situ* crosslinking as no fluorescence is seen for uncross-linked SF dispersion. Although morphologically, the rat brain show less destructed area compared to the first set of experiments this methodology was also invasive and part of the cortex was missing after brain extraction. The rats did not show any sign of distress and no untimely death of the animals was observed.

*In vivo* MRI was conducted at each time point prior to brain extraction for histology. In all cases, silk-IONPs hydrogel bionanocomposite was clearly seen within the injected area filling up the entire gap produced during surgery (Figure III.9). However, the major part of the silk-IONPs hydrogel was found in the cortex area probably due to the viscosity of the material as previously observed during surgery and removal of a part of the injected gel from the injection site when the syringe was pulled out. Importantly, no IONPs diffusion within the surrounding tissues was observed as the MRI contrast remained within the injection zone without fading away. This result is corroborated by the fact that no NPs release was seen *in vitro* as previously discussed in chapter II. In contrast to histology slices, MRI images allow the *in situ* visualization of the entire material. However, the major part of the silk-IONPs hydrogel found at the surface of the brain is removed during histology and immunostaining procedures given the drastic conditions required during sample manipulation. Therefore, histology images should be completed with MRI to better understand whether an empty space seen in histology slices was or not filled up with the hydrogel *in vivo*.

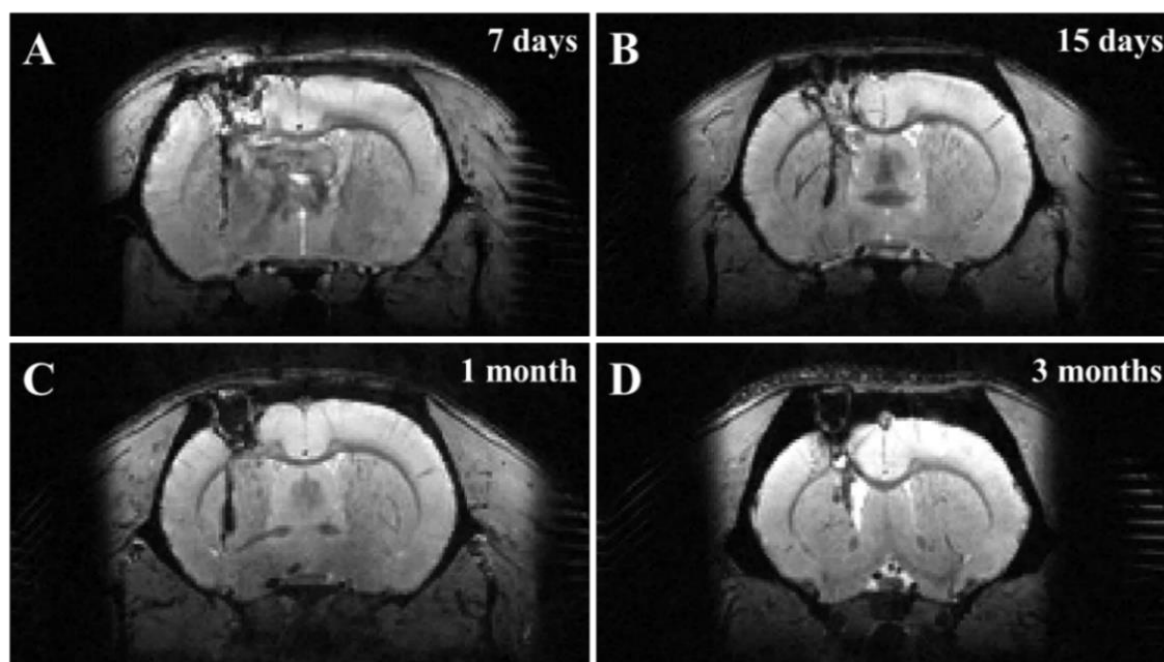


**Figure III.9.** MRI images obtained at 7 (A), 15 days (B), 1 (C) and 3 months (D) after silk-IONPs hydrogel into the rat's brain. Silk-IONPs hydrogel is clearly seen in all stages filling in the whole produced during surgery. © CEA-NeuroSpin Courtesy of S.Mériaux and F.Geffroy.

Immunostaining against glial-fibrillary acidic protein (GFAP) and ionized calcium-binding adaptor molecule 1 (iba-1) allowed the visualization of astrocytes and microglia respectively. Both immunostainings revealed higher cell activation within the injection zone in comparison with the rest of the brain at 7 days. Astrocyte activation was further increased and found within all the brain at 3 months suggesting a prolonged effort for brain tissue regeneration (Figure III.10 A-D). Moreover, astrocyte morphology evolves from rounded and big shapes at early stages (7 days) (Figure III.10 E) to smaller and elongated shapes, similar to the one found at basal state, at 3 months (Figure III.10 H).

Microglia evolution over time showed a great activation peak at 15 days at which the whole brain was impacted depicting a great inflammatory response at this stage (Figure III.11). However, this activation was reduced almost to the basal state at 3 months suggesting an acute inflammation often found in this kind of procedures. Tissue acute inflammation may be beneficial to induce tissue regeneration for example after tumor excision. Chronic inflammation (further than 1 month) could also be beneficial and enhance neurogenesis processes, however it should be closely monitored as it can induce neuronal death and tissue dysfunction as well <sup>28</sup>. Herein, several factors can be at the origin of this inflammation such as the presence of H<sub>2</sub>O<sub>2</sub> into the hydrogel, the difference between brain tissue and hydrogel's mechanical properties or even the surgery itself. Further tests injecting the hydrogel mixture without the H<sub>2</sub>O<sub>2</sub>, a hydrogel



matching the mechanical properties of the brain tissue, or just a standard solution should be performed to elucidate the origin of such inflammatory response.

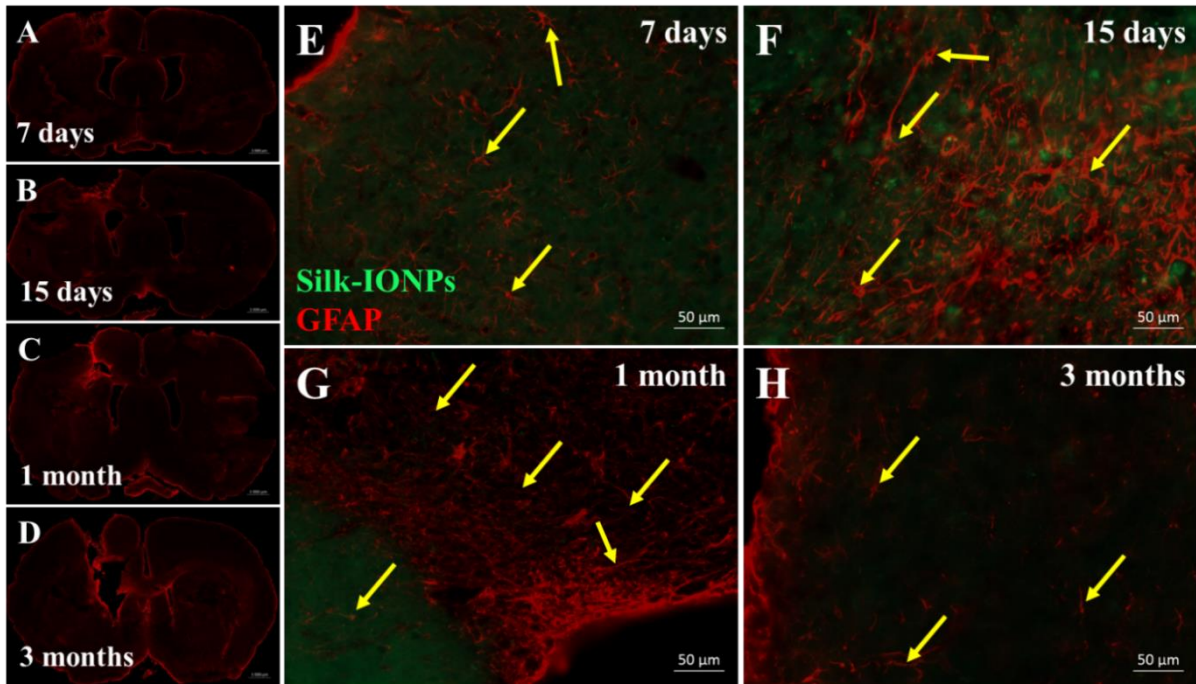


**Figure III.10.** Fluorescence microscopy images showing astrocytes (staining against GFAP, red) and silk-IONPs hydrogel (green autofluorescence). Images A to D show the increasing overall astrocyte activation within the entire brain from 7 days to 3 months. Images E-H allow a closer look into the astrocyte morphology. At early stages big and rounded cells are present while they elongate to their basal state at 3 months. Yellow arrows point some astrocyte cells. Scales bars correspond to 1000 μm for images A-D and 50 μm for images E-H. © CEA-NeuroSpin Courtesy of S.Mériaux and F.Geffroy.

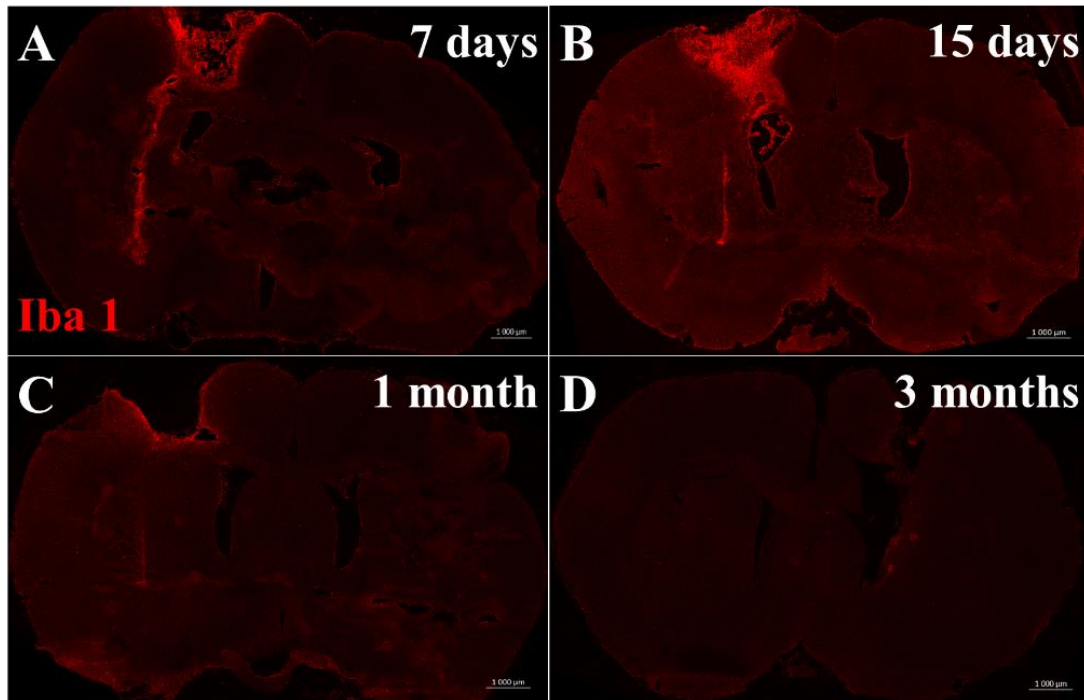


**Figure III.11.** Fluorescence microscopy images showing immunostaining against Iba 1 (red) depicting microglia cells. Maximum activation is found after 15 days (B) and the presence of such cells decrease to a basal state at 3 months. Scale bar corresponds to 1000 μm. © CEA-NeuroSpin Courtesy of S.Mériaux and F.Geffroy.

A closer look into the silk hydrogel revealed a great infiltration of the material by microglial cells and lymphocytes T CD8<sup>+</sup> suggesting an immune response towards the elimination of the implanted material. Moreover, parts of silk hydrogel were visible inside lymphocytes T CD8<sup>+</sup> cells, due to its green autofluorescence, depicting good hydrogel removal by those cells. This process is present at 15 days and 1 month where many cells have internalized silk as seen in Figure III.12 A, and decreases at 3 months probably due to the degradation of the hydrogel and the decrease of the inflammatory response. After 3 months, silk hydrogel degradation is visible as less material is present within the tissue (Figure III.12). It is important to note that lymphocytes T CD8<sup>+</sup> are exclusively present into the injection area suggesting a well-targeted immune response against the foreign material injected (Figure A.6). These results suggest the possible degradation of the material within the brain. This degradation rate could be tuned in the future by changing the hydrogel characteristics and could be adapted for long time functions such as drug release.

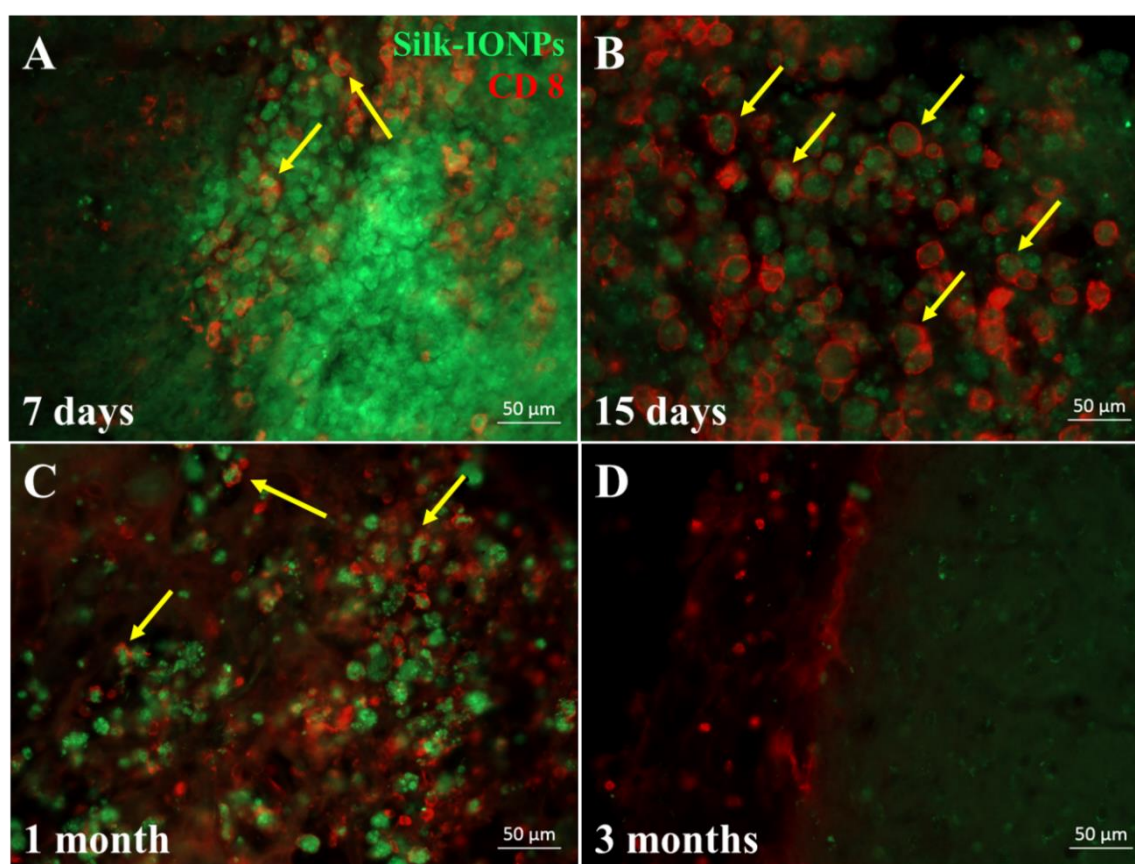


**Figure III.12.** Fluorescence microscopy images showing immunostaining against lymphocytes T CD8. Insert images show the overall image of the brain showing that these cells are only present within the injection area. Images A to C correspond to rats at 7, 15 days, 1 and 3 months. Silk-IONPs is autofluorescent in green. Yellow arrows show lymphocytes T CD8 that have internalized silk-IONPs hydrogel bionanocomposite. Scale bar corresponds to 50 µm. © CEA-NeuroSpin Courtesy of S.Mériaux and F.Geffroy.

On the other side, caspase immunostaining revealed a general apoptosis response over the entire brain. A higher intensity is seen at 7 and 15 days within the top of the injection zone, however this corresponds to the orange autofluorescence of the wax used to close the bone hole (Figure A.7). The merge image between caspase and NeuN (depicting neurons) staining images allows to correlate whether the observed cell death correspond or not to neurons. Figure III.13 shows that at 7 and 15 days both staining do not colocalize indicating that the observed cell death corresponds to other cells; probably damaged cells through surgery and up regulated cells during the inflammatory response. A colocalization of both markers is seen after 1 and 3 months indicating that neuron cell death take place at this time point. It is important to consider that a great number of cells are produced during an inflammatory response and those should be removed together with the damaged cell, once their function is over. Importantly, no further apoptosis is induced because of the hydrogel presence into the brain.

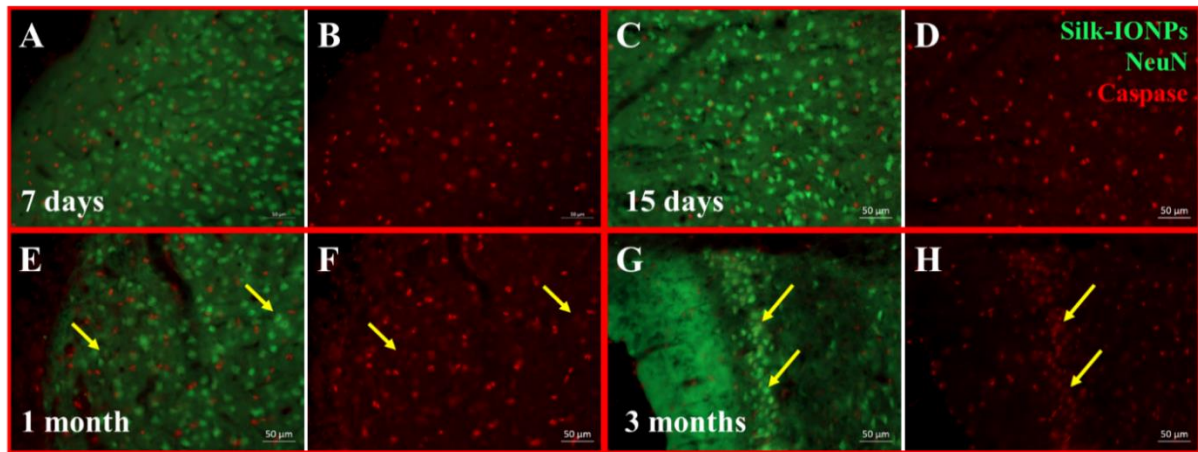


**Figure III.13.** Fluorescence microscopy merged (left) images and red channel (right) showing caspase (red) and NeuN (green). Silk-IONPs hydrogel bionanocomposite is as well fluorescent in green. No colocalization of the markers is seen at 7 and 15 days depicting that apoptose seen at these points do not concern neurons. Colocalization of both markers is seen after 1 and 3 months (yellow arrows) suggesting neuron apoptosis at these stages . Scale bars correspond to 50  $\mu$ m. © CEA-NeuroSpin Courtesy of S.Mériaux and F.Geffroy.

Finally, several immunostainings were performed in order to shown the presence of stem cells, new neuron formation and angiogenesis procedures. The entire stem cell population cannot be marked by a singular receptor due to their inherent capability to differentiate into several cell types. Herein we have chosen to use CD133 staining, as this receptor has been shown to be present in neural stem cells <sup>29</sup>. CD133 staining proved the presence of stem cells within the entire brain up to 3 months (Figure III.14). This receptor is rarely seen in a healthy brain; therefore, herein we successfully induced stem cell proliferation.

In order to elucidate whether part of these stem cells gave rise to new neuron formation, staining against TBR 2 and TBR 1 were performed. These transcription factors appear during



neurogenesis. A CD133<sup>+</sup> cell becomes then TBR2<sup>+</sup> and later TBR1<sup>+</sup> to finally become a newly formed neuron expressing  $\beta$  tubuline III <sup>29</sup>. At early stages a very low signal is present for both transcription factors being stronger around the injection area for TBR1 (Figure III.14 C, G). The presence of these transcription factors evolves with time up to 3 months were the expression of the two can be greatly found within the entire brain and specially in the injection area. Although  $\beta$  tubuline III expression is often present within healthy rat brain, a greater expression was observed in this case over the injection area and the cortex at early stages, and within the entire brain at 3 months. These results suggest an effective tissue reparation process from the injection as depicted by the presence of TBR1<sup>+</sup> cells at early stages. In addition, this procedure is prolonged and extended to the entire brain at 3 months, supporting a good brain regeneration over time. Longer experiments could allow to elucidate whether this regeneration is sufficient to close the wound formed in an efficient manner.

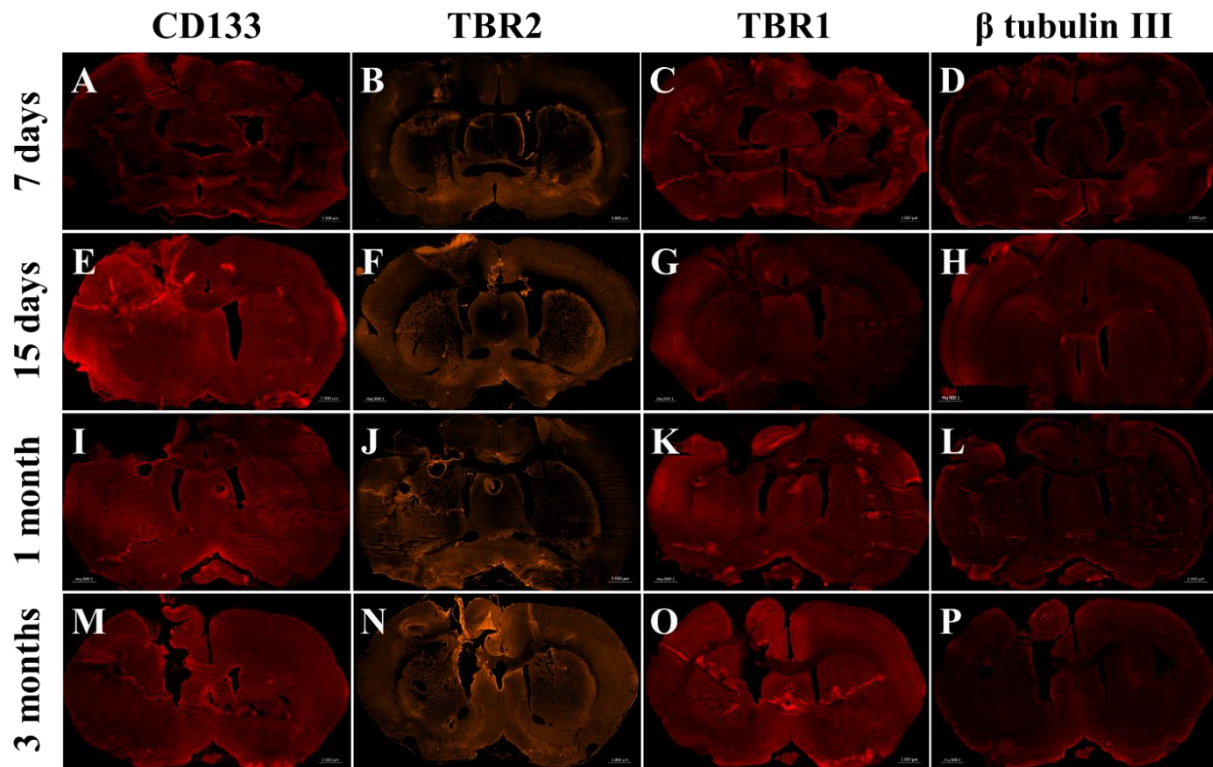


**Figure III.14.** Fluorescence microscopy images showing neuronal stem cell markers CD133, TBR2, TBR1 and  $\beta$  tubulin III at 7, 15 days, 1 and 3 months after injection. The overall expression of all the markers shows a good regeneration process taking part into the brain with the production of new neurons up to 3 months after injection. Scale bars correspond to 1000  $\mu$ m. © CEA-NeuroSpin Courtesy of S.Mériaux and F.Geffroy.

When speaking of new tissue formation is very important to assess if angiogenesis (formation of new blood vessels) takes place. Without this process, the survival of the new formed tissue is compromised. Herein an immunostaining against nestin allowed the visualization of angiogenic stem cells, capable to differentiate into endothelial cells able to form capillaries <sup>29</sup>.

Figure III.15 shows a great presence of nestin<sup>+</sup> cells at 7 and 15 days at the hydrogel's edge following an aligned structure suggesting the formation of new blood vessels. The presence of nestin<sup>+</sup> cells decreases over time and it is hardly visible at 1 and 3 months probably because cells were mature at this stages no longer expressing nestin <sup>29</sup>. A good formation of new capillaries is seen at early stages. Further analysis to prove the existence of such vasculature after 3 months could be shown by using other endothelial cell markers such as CD34 for newly formed vessels or CD31 for mature vasculature.

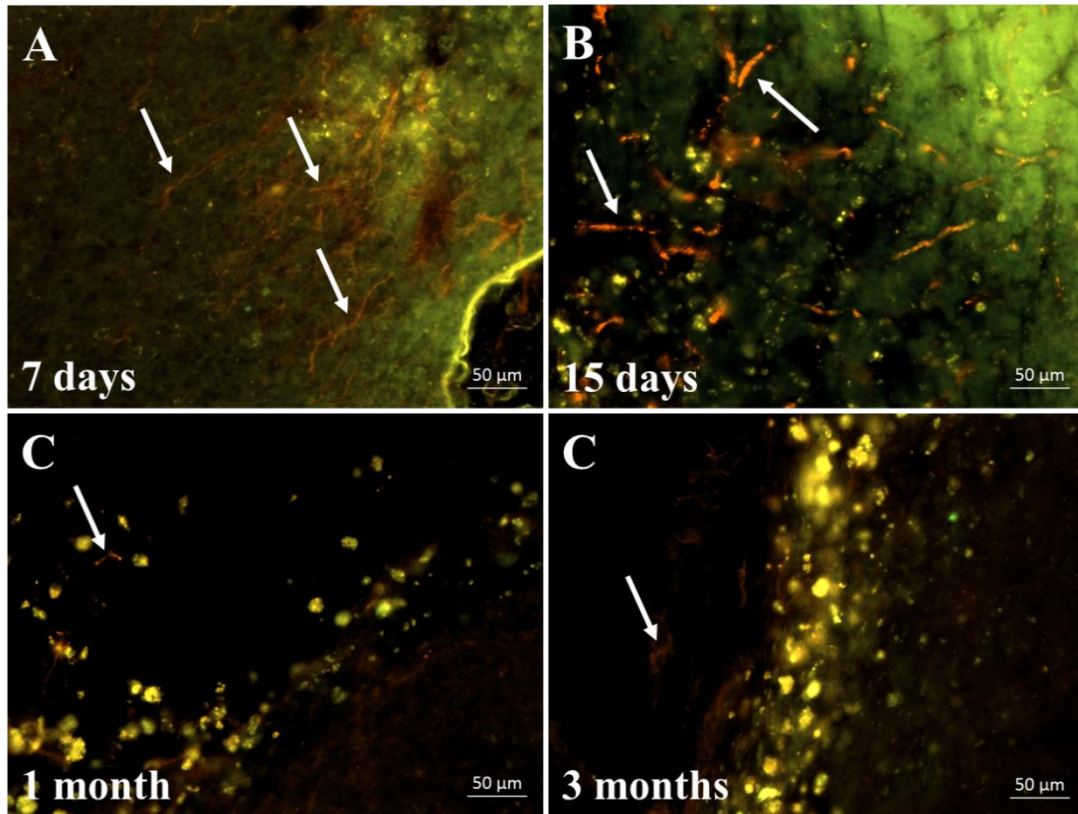


**Figure III.15.** Fluorescence microscopy images showing nestin immunostaining (orange) and silk-IONPs autofluorescence (green) at 7, 15 days, 1 and 3 months. Yellow coloration corresponds to the colocalization of both fluorescence. Nestin expressing cells are highly present at early stages (7 and 15 days (A,B)), white arrows depict nestin<sup>+</sup> cells arranged into what seems new vessels formed. Scale bars correspond to 50 μm. © CEA-NeuroSpin Courtesy of S.Mériaux and F.Geffroy.

### 3.4. Conclusion

Herein we demonstrate the acquisition of magnetic properties when embedding IONPs Nps into silk hydrogels. Moreover, magnetization curves are in agreement with previous results depicting good NPs dispersion within the silk-IONPs hydrogel as the blocking temperature decreased when compared to IONPs dispersion. This section proves the possibility of using MRI techniques to follow the hydrogel position *in vitro* and *in vivo* with low IONPs concentrations required.

*In vivo* experiments revealed the requirement of a minimally invasive surgery for the implantation of silk-IONPs hydrogel within the brain. Therefore, the injection of the hydrogel mixture for an *in situ* crosslinking was the most effective in terms of brain damage induction. Moreover, this methodology allowed a better control of the hydrogel position within the brain. Nevertheless, it is important to take into account that the objective is to use these materials to replace tumors; therefore, an invasive surgery is already required. These preliminary experiments allowed us to evaluate the brain tissue response to silk-IONPs hydrogel bionanocomposite. Moreover the presence of IONPs into the silk hydrogel allowed the monitoring of the material *in vivo* by MRI through the entire duration of the experiment, revealing that NPs stay within the hydrogel without diffusing into the surrounding tissues. Overall, an acute inflammation was observed together with an immune response to remove the silk hydrogel and a great tissue regeneration process from the early stages. These results support the possibility to use silk-IONPs hydrogel bionanocomposites as brain fillers after tumor ablation. However, the material can be adapted for long-term drug delivery applications or the induction of tissue regeneration after other brain diseases such as stroke or Alzheimer.

## 4. Depollution

### 4.1. Introduction

The increasing global industrialization is raising many concerns about environmental pollution. Industrial wastes are poorly treated before disposal. Residual waters arrive into rivers, lakes, underground water and seawaters containing a great amount of pollutants. The presence of pollutants such as heavy metal ions and organic dyes in the environment strongly affects the ecosystem and consecutively human health. Furthermore, water is an essential resource for life and the amount of drinkable water is in constant decrease due to pollution and increasing worldwide population.

Organic dyes are widely used in textile, paper, paint, cosmetics, printing, plastics and pharmaceutical industries among others<sup>30</sup>. Yet, several organic dyes are greatly toxic for living organisms and are potentially carcinogenic and mutagenic. In the environment, these molecules are poorly or no degraded due to their complex aromatic structures. Their recalcitrant structure drives environmental accumulation where small modifications or combinations with other molecules can further increase their toxicity<sup>31</sup>. Methylene blue (MB) is a cationic dye extensively used by industry and it is therefore used as model dye for many depollution applications. When ingested, MB may, indeed, cause nausea, vomiting or gastritis<sup>32</sup>.

Extensive researches have been conducted for the development of efficient water depollution methods. Techniques such as precipitation, flocculation, ion exchange, filtration, adsorption and photodegradation have been successfully used<sup>32</sup>. Depollution through adsorption remains, however, the most widely used method due to its cost effectiveness and simplicity<sup>33</sup>. Ideal adsorbent materials should have high adsorption capacities, biodegradability, ease regeneration and recyclability. In this context, SF materials have been developed in applications dealing with depollution of organic and inorganic compounds<sup>34–40</sup>.

The main issue in the adsorption approaches lies on the fact that pollutants are not eliminated, but only removed from the environment. Activated carbon is the adsorbent material most largely used. When it reaches its maximum adsorbent capacity, this material is either degraded *a posteriori* by pyrolysis, an energy consuming process producing a high amount of CO<sub>2</sub>, or directly discarded into landfills, thus contributing to further pollution<sup>41</sup>. Therefore, an adsorbent-based approach should be accompanied by a non-pollutant dye/material degradation strategy.



To overcome this issue, two main strategies have been developed: material regeneration and dye degradation. The regeneration of the material allows its reutilization increasing its lifetime and performance. Dye degradation can be achieved through catalysis. In particular, the use of NPs, which exhibit high surface-to-volume ratio, has been widely explored in this field as less catalyst is needed. A variety of NPs have been used for dye degradation including silver, platinum, iron, palladium and gold <sup>42–47</sup>. Although palladium NPs are probably the most well-known nanocatalyst, their expensiveness and toxicity reduces their interest in depollution applications. In contrast, Au NPs have a reduced toxicity and better stability over time.

In this section, the MB adsorption capacities of SF sponges and hydrogels are assessed by measuring the MB adsorption in aqueous media. The obtained results are then fitted with the Langmuir and Freundlich isotherm models. Furthermore, the effects of hydrogel pretreatments with ionic solution (salt ions) and pH on the adsorption capacity of the materials are investigated. The regeneration of the studied materials and their further recycling is also studied. A particular attention is given to the association of SF materials and Au NPs to combine adsorbent capacity and dye-degradation catalysis processes.

## 4.2. Materials and methods

### 4.2.1. Materials

Methylene blue (MB, M9140), brilliant blue (BB, erioglaucine disodium salt, 861146), NaCl, NaBH<sub>4</sub> were purchased from Sigma-Aldrich with minimum 98.5% purity. Silk hydrogels and sponge were prepared following the procedure detailed in chapter II.

### 4.2.2. Dye adsorption

SF materials (0.034 and 0.075 g of SF for hydrogel and sponge, respectively) were immersed in 15 mL of MB (10 mg L<sup>-1</sup>) or BB (10 mg L<sup>-1</sup>) solution and placed in a horizontal agitator at RT.

#### 4.2.2.1 Adsorption kinetics analysis

For MB, adsorption kinetics were evaluated by measuring the absorption at 664 nm of the solution over time. A calibration curve was prepared for different MB concentrations (0.5 – 10 mg L<sup>-1</sup>) and the molar extinction coefficient was determined using the Beer-Lambert law. The experimental data was then analyzed by using pseudo-first-order and pseudo-second-order kinetic models as previously described in the literature<sup>33,38,48</sup>. Pseudo-first-order and pseudo-second-order kinetic models are generally given as equations (II.1) and (III.2), respectively:

$$\log(q_e - q_t) = \log(q_e) - \frac{k_1 t}{2.303} \quad (\text{III.1})$$

$$\frac{t}{q_t} = \frac{1}{k_2 q_e^2} + \frac{1}{q_e} t \quad (\text{III.2})$$

Where  $q_e$  and  $q_t$  are adsorption capacity (mg g<sup>-1</sup>) at equilibrium and at time  $t$  (min) respectively.  $k_1$  and  $k_2$  are pseudo-first-order constant (min<sup>-1</sup>) and pseudo-second-order rate constant (g mg<sup>-1</sup> min<sup>-1</sup>), respectively.

#### 4.2.2.2 Adsorption isotherms

The adsorption capacity of silk sponges and swollen hydrogels were evaluated by immersing the samples in 15 mL of MB solution (10 - 200 mg L<sup>-1</sup>) and placing in a horizontal agitator at RT during 48 h to reach the equilibrium concentration ( $C_e$ ; MB concentration in the solution at the equilibrium state). After incubation, the absorbance at 664 nm of the solution was measured.  $C_e$  and the adsorption capacity ( $q_e$ ; mg g<sup>-1</sup>; mass of adsorbed MB (mg) per mass of adsorbent (g)) parameters were calculated for each point. Results were fitted with the Langmuir and Freundlich adsorption models as these models are widely used within the literature<sup>33,38,48,49</sup>. Equation (III.3) describes the Langmuir model.

$$q_e = \frac{q_m K_L C_e}{1 + K_L C_e} \quad (\text{III.3})$$

This equation can be linearized to:

$$\frac{C_e}{q_e} = \frac{1}{q_m K_L} + \frac{1}{q_m} \times C_e \quad (\text{III.4})$$

On the other side, the Freundlich experimental model is described by the following equation:

$$q_e = K_F C_e^{1/n} \quad (\text{III.5})$$

And linearized:

$$\ln(q_e) = \ln(K_F) + \frac{1}{n} \ln(C_e) \quad (\text{III.6})$$

Where  $q_e$  is the adsorption capacity (mg MB g adsorbent<sup>-1</sup>);  $q_m$  the maximum adsorption capacity (mg g<sup>-1</sup>);  $C_e$  the MB concentration at the equilibrium state (mg L<sup>-1</sup>);  $n$  represents the heterogeneity of adsorbent;  $K_L$  and  $K_F$  are the adsorption constants (L mg<sup>-1</sup>) of the Langmuir and Freundlich models respectively.

#### 4.2.3. Materials pretreatment

The effect of pH (3.5, 5 and 8) and ion pretreatments (0.6 M, NaCl, ionic strength (I) = 0.6 M) on the adsorption capacities of silk hydrogels were evaluated given their better adsorption performance. After gelation, samples were immersed in demineralized water for 48 h at RT for complete swelling. Swollen materials were then treated by immersion into a given pretreatment solution for additional 48 h. Pretreatment solution pH were adjusted using 1M HCl / NaOH solutions. Prior to MB adsorption, materials were abundantly rinsed with demineralized water.

#### 4.2.4. MB release

MB saturated materials were prepared by immersing them into MB solutions (10 mg L<sup>-1</sup>) for 6 days. MB release was performed by immersing MB saturated silk materials in aqueous solution (pH 3, 10<sup>-3</sup> M HCl) and monitoring by spectrophotometry at 664 nm.

#### 4.2.5. Catalytic activity

1.5 mL silk-Au NPs hydrogel bionanocomposites (0.034 g SF and ~ 0.15 mM final Au NPs concentration) were placed in water to allow complete swelling during 48 h. Hydrogels were immersed in 5 mL of MB solution (10, 50 or 100 mg L<sup>-1</sup>) and 500 µL of 1 M NaBH<sub>4</sub> were added. Reaction was carried out under constant stirring and a 2 mL aliquot was taken out at a

given time for absorbance measurement ( $\lambda = 664$  nm). Due to the high speed of the reaction, it was not possible to measure the absorbance at several time points for a single reaction. Therefore, four different reactions were carried and a single time point measurement was evaluated for each one of them.

The possibility to further chemically reduce MB using the same silk-Au NPs hydrogel was evaluated by adding 1 mL of MB ( $10 \text{ mg L}^{-1}$ ) and 500  $\mu\text{L}$  of 1 M  $\text{NaBH}_4$  after complete MB reduction. This procedure was repeated up to 15 times. The same procedure was repeated three times using a  $100 \text{ mg L}^{-1}$  solution.

### 4.3. Results and discussion

#### 4.3.1. MB adsorption

The adsorption kinetics of MB by SF materials was evaluated by UV-Vis spectrophotometry. MB adsorption kinetics by g of silk are shown in Figure III.16 showing that silk hydrogels have a greater adsorption capacity than silk sponges. Pseudo-first-order and pseudo-second-order kinetic models were used to analyze the obtained data. The kinetic parameters were obtained from the slope and interception of the plots of these models and are summarized in Table III.3. The maximum mass of MB adsorbed by gram of silk was set as the experimental  $q_e$  ( $q_{e \text{ exp}}$ ). For both materials experimental data was better fit to the pseudo-first-order model as depicted by slightly higher correlation coefficients. Nevertheless  $q_e$  calculated ( $q_{e \text{ calc}}$ ) by this model are lower than the experimentally obtained ( $q_{e \text{ exp}}$ ). Therefore, the pseudo-second-order kinetic model better explains the adsorption kinetics of both materials. These results are in agreement with the ones found for SF graphene oxide hydrogels within the literature<sup>5034</sup>. Nevertheless, measurements for longer times and higher MB concentrations should be done to check whether the maximum adsorption value found here really corresponds to the  $q_e$ .

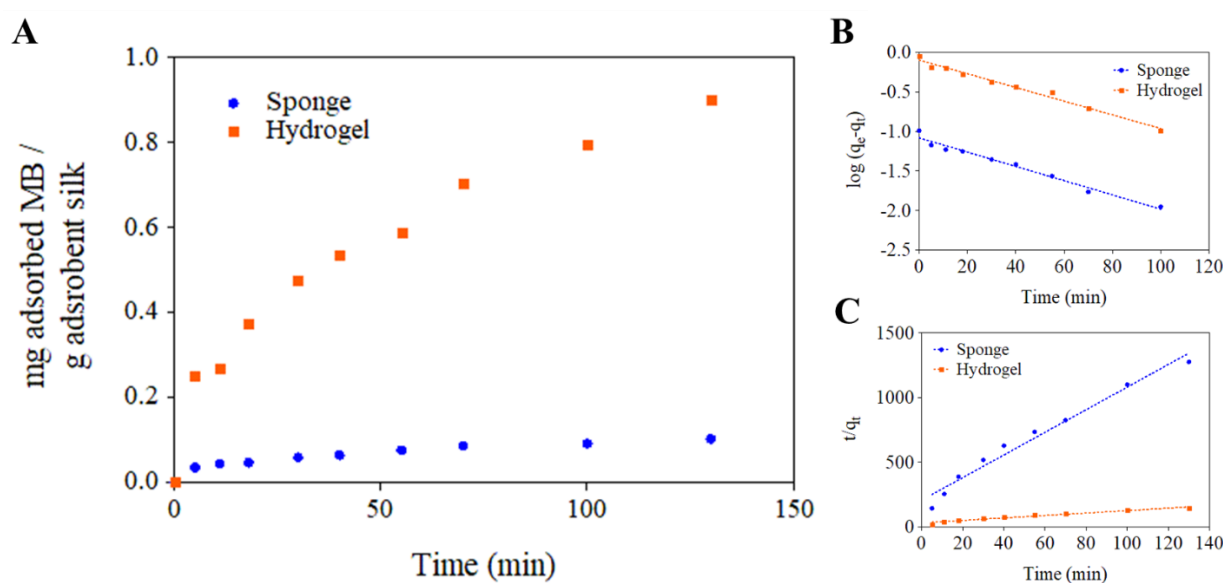


**Figure III.16.** MB adsorption kinetics of silk sponges (blue) and hydrogels (orange) (A). Plots of pseudo-first-order (B) and pseudo-second-order (C) kinetic models for silk sponges and hydrogels.

**Table III.3.** Silk hydrogels and sponges adsorption kinetic parameters for pseudo-first-order and pseudo-second-order kinetic models

Silk material	Kinetic model	Kinetic parameters				$q_{e \text{ exp}}$ ( $\text{mg g}^{-1}$ )
		$K_1$ ( $\text{min}^{-1}$ )	$K_2$ ( $\text{g mg}^{-1} \text{ min}^{-1}$ )	$q_{e \text{ calc}}$ ( $\text{mg g}^{-1}$ )	$R^2$	
Sponge	Pseudo-first-order	0.0207	-	0.0827	0.9766	0.1021
	Pseudo-second-order	-	0.0144	0.1144	0.8466	
Hydrogel	Pseudo-first-order	0.0200	-	0.7976	0.9744	0.8987
	Pseudo-second-order	-	0.0316	1.0601	0.9624	

Adsorption capacities of both materials were evaluated by immersing them in MB solutions ranging from 10 – 200  $\text{mg L}^{-1}$  during 48 h to reach the equilibrium concentration ( $C_e$ ; MB concentration in the solution at the equilibrium state). Two well-known adsorption models were used to describe the adsorption mechanism. Langmuir model is a theoretical model based on the fact that adsorption takes place in the surface, only as a monolayer, and in a reversible manner. In contrast, the Freundlich model is an empirical model in which multilayered adsorption is considered. Table III.4 summarizes the values of each parameter for Langmuir and Freundlich models as well as the correlation coefficient value  $R^2$ . Our results were better fitted with the Langmuir model suggesting that adsorption takes place in a monolayer manner (Figure III.17). These results are in agreement with most of the studies on organic dye adsorption found in the literature<sup>38,51–53</sup>.

**Table III.4.** Value for the parameters in Langmuir and Freundlich adsorption models and the correlation factor with the experimental data.

Silk material	Langmuir			Freundlich		
	$q_m$	$K_L$	$R^2$	$1/n$	$K_F$	$R^2$
Hydrogels	25.77	0.23	0.996	0.34	6.33	0.624
Sponges	15.20	0.25	0.993	0.26	5.14	0.645

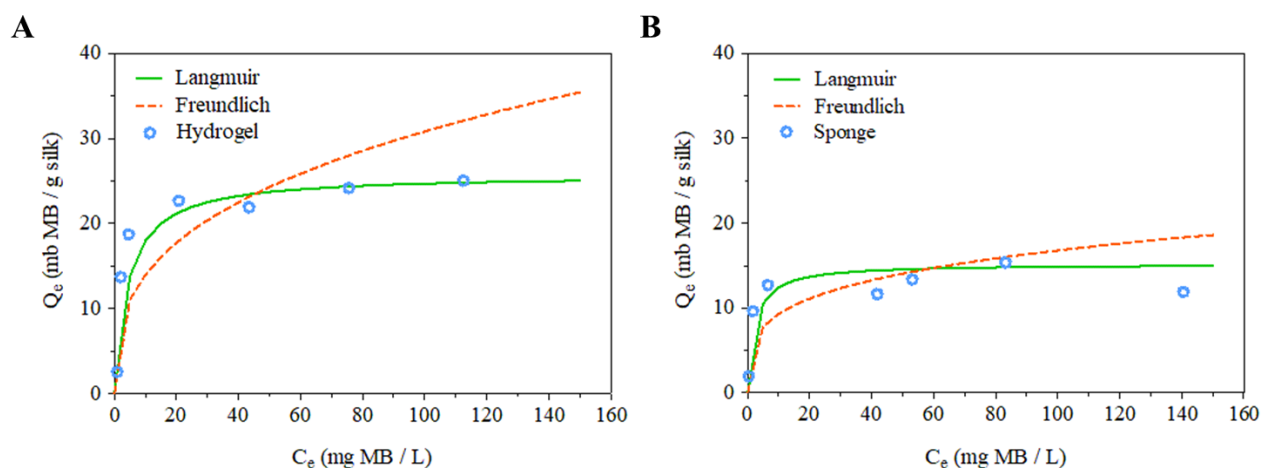


**Figure III.17.** Methylene blue adsorption by silk hydrogels (A) and sponges (B) fitted to the Langmuir and Freundlich adsorption models. Best fit is found with the Langmuir model in both cases.

We hypothesized that the adsorption of MB was mainly due to electrostatic interactions. SF hydrogels were tested under three different conditions to evaluate this hypothesis: (i) the pretreatment of SF materials with different pH solutions or (ii) with sodium chloride and (iii) the use of an anionic dye.

#### 4.3.2. Effect of pH

Silk being a protein, its overall charge is pH dependent and can therefore be modulated by varying this factor. To validate our hypothesis based on an electrostatic interaction, the effect of pH pretreatment was studied. To this end, hydrogel samples were immersed during 48h in solutions at pH of 3.5, 5 and 8. The pH was adjusted with HCl or NaOH. Silk hydrogels were washed with demineralized water and immersed in 10 mg L<sup>-1</sup> MB solutions. UV-vis spectrophotometry showed a pH dependent MB adsorption. MB adsorption capacity increased as pH of the pretreatment solution increased (Figure III.18).

This result can be explained by the isoelectric point (pI) of SF. The pI of the heavy chain of SF has been described in the literature to be 4.39<sup>54</sup>. Under this pH, SF overall charge is positive, while over this pH it is negative. The changes induced within the silk hydrogel during pH pretreatment are still present once the material is placed in aqueous solution. This memory effect may be probably due to the liquid phase composing the hydrogel from which ions (Na<sup>+</sup>, Cl<sup>-</sup>, H<sup>+</sup> and OH<sup>-</sup>) cannot be simply removed by rinsing the material with water. Therefore, for pretreatments at pH below their pI SF materials are positively charged and electrostatic repulsion with MB (also positively charged) occurs. As the pH of the pretreatment solution increases, SF materials become more negatively charged having a better electrostatic attraction



for MB. The optimal pH is 8. However, a shrinking effect was seen in samples incubated within the pretreatment solution at pH 3.

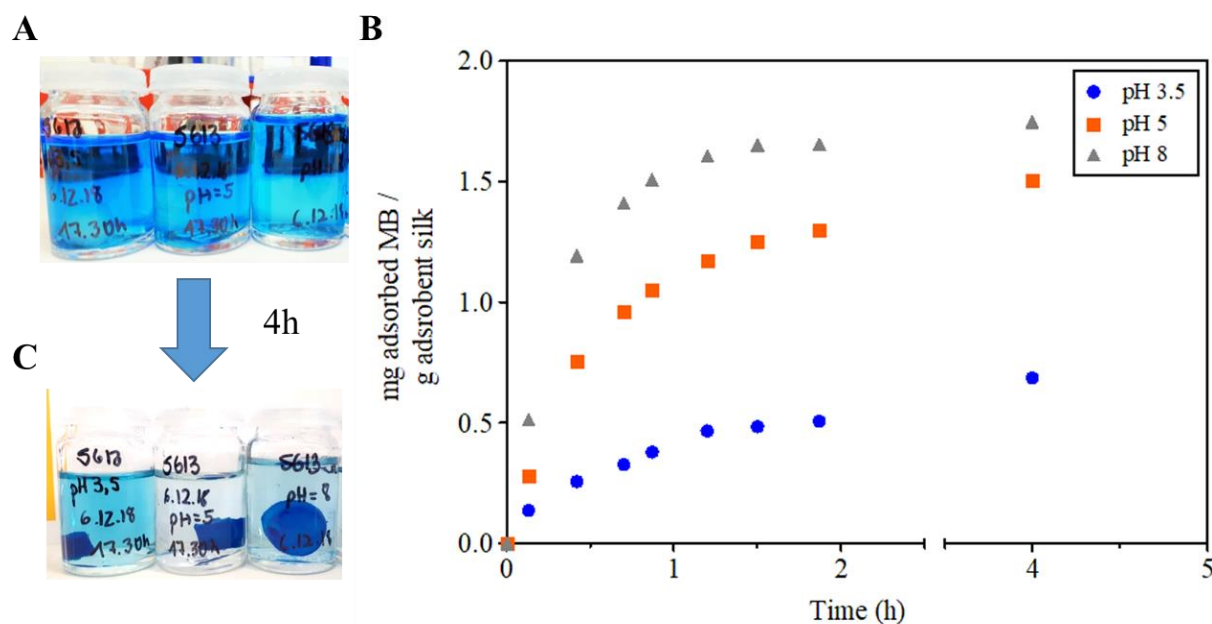


**Figure III.18.** MB adsorption by silk hydrogels after three different pH treatments. Initial (A) and final (C) images of pH treated silk hydrogels submerged in methylene blue solutions. From left to right pH treatments were 3.5, 5 and 8 respectively in both images. Quantitative analysis of the mass of methylene blue adsorbed over time by UV-Vis spectrometry at 664nm (B).

### 4.3.3. Effect of salt concentration

Completely swollen hydrogels were immersed in 0.6 M NaCl ( $I = 0.6$  M) solutions for 48 h. We chose the salt concentration corresponding to seawater salinity in order to validate our hypothesis on electrostatic interactions and investigate the adsorption performance of our materials in such environment.

After salt pretreatment, hydrogels had shrunk considerably and became opaque (Figure III.19 A), interestingly the immersion of this material in aqueous solutions did not restore their original swelling state suggesting an ion induced structure change. Prior to MB adsorption, samples were rinsed with demineralized water, however it is important to note that this step does not result in the complete removal of salt ions from hydrogel. Samples were then immersed in MB  $10 \text{ mg L}^{-1}$  during 3 h. MB adsorption was monitored by UV-Vis spectrophotometry. The pretreatment of hydrogels with salt resulted in a decrease of both, the adsorption rate and the maximum adsorption capacity. These phenomena are depicted in Figure III.19 B by a smaller slope and the apparition of a *plateau* at lower MB adsorbed mass.

These results suggest that the remaining salt ions within the silk hydrogel after the pretreatment interfere with the adsorption of MB suggesting an electrostatic mediated adsorption. Moreover,

the change of the swelling state probably results in a reduced specific surface (accessible for MB adsorption) affecting the MB adsorption. Further experiments need to be done to elucidate how the ion-induced change on the swelling state of the hydrogel influences the MB adsorption capacity.

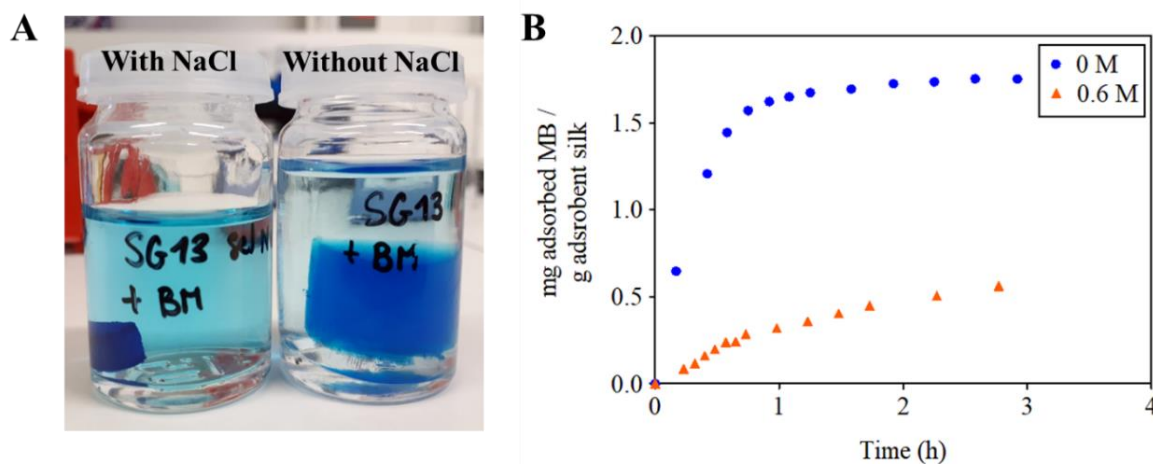


**Figure III.19.** Images of sodium chloride treated (left) or not (right) silk hydrogels after MB adsorption (A). After salt pretreatment silk hydrogel was considerable shrunk. MB adsorption kinetics after sodium chloride pretreatment (B).

#### 4.3.4. Brilliant blue adsorption

Interestingly, the exact opposite adsorption behavior was observed when using brilliant blue (BB), an anionic dye, instead (Figure III.20). In fact, BB was best adsorbed at pH 3 and the materials adsorption capacity decreased as pH increased. These results agree with the ones found in the literature when using silk/GO and silk/TiO<sub>2</sub> composite materials to adsorb different cationic and anionic dyes<sup>34,55</sup>. Overall, these results strongly support our hypothesis consisting of an electrostatic-based interaction adsorption mechanism.

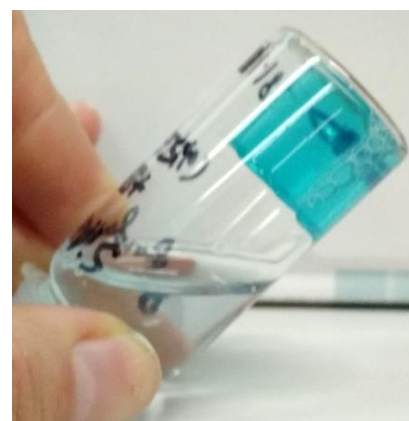


**Figure III.20.** Brilliant Blue adsorption by silk hydrogel at pH 3. In contrast to MB, BB can be completely adsorbed at pH 3.

#### 4.3.5. Comparison with other materials

Many different materials are actually being developed for dye removal. Table III.5 compiles some of these materials and their maximum adsorption capacities for MB: Although the results obtained within this work are largely outcome in some other cases presented in the literature, it is important to consider that these are only proof of concept results and further optimization of the materials should be conducted.

**Table III.5** Summary of MB removal materials and their maximum removal capacities.

Material	Maximum capacity	Reference
Silk Sponge	15.20 mg g <sup>-1</sup>	This work
Silk hydrogel	25.77 mg g <sup>-1</sup>	
Silk-graphene oxide aerogel	1322.71 mg g <sup>-1</sup>	34
Graphene oxide hydrogel	714.29 mg g <sup>-1</sup>	33
Alginate beads-magnetic NPs-activated carbon	18.23 mg g <sup>-1</sup>	56
Polyacrylamide dextran sulfate hydrogels	19.145 mg g <sup>-1</sup>	48
exfoliated montmorillonite nanosheets-chitosan	530 mg g <sup>-1</sup>	53
Activated carbon-sodium lauryl sulfate	195.7 mg g <sup>-1</sup>	

#### 4.3.6. Adsorbent regeneration and recycling

For successful application, adsorbent materials should not further pollute the environment by neither their production nor their degradation (methods and byproducts). Therefore, biodegradable materials are of increasing interest in this field. In addition, the possibility to regenerate and recycle these materials reduces its cost increasing their useful life. The ability to regenerate and reuse SF materials has been evaluated in this section. Regeneration procedures should allow a maximum release of the adsorbed dye while preserving the adsorption capacity of the material. Herein, we investigated the materials release kinetics of adsorbed MB in acid solution (pH 3).

MB saturated materials were prepared by immersing them into MB solutions (10 mg L<sup>-1</sup>) for 6 days. The immersion of MB saturated SF materials into acid aqueous solution (pH = 3) resulted in a dye release into the solution (Figure III.21 A). This behavior agrees with the previously described effect of pH over SF materials. When SF materials are immersed in acid solutions, SF overall charge becomes positive and electrostatic repulsion within SF and MB occurs resulting in a dye release into the solution. By using this methodology, up to ~ 29 % of adsorbed MB by SF hydrogels was released into the solution (Figure III.21 B). The regenerated materials were then reused for MB adsorption conserving a ~ 70 % of its initial adsorption capacity. After 2 cycles, the material was still useful although its dye release capacity was reduced by ~ 30 %. This reduction of the adsorption capacity could be explained by two hypothesis (i) the saturation

of several adsorption sites due to the incapacity of the material to release all the adsorbed MB molecules; and (ii) the hydrogel volume reduction induced by acid solution treatment. A combination of both hypotheses may also be possible, however further analysis should be done to better elucidate the reason of this decrease over the adsorption capacity.

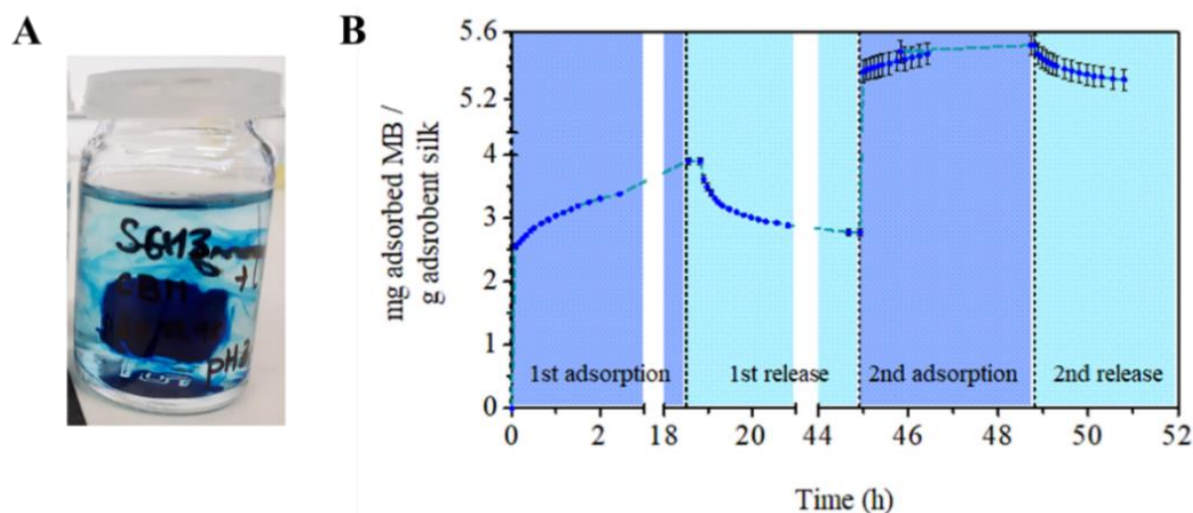


**Figure III.21.** MB saturated hydrogel immersion in pH 3 solution results in MB release (A). MB adsorption (pH 7) and release (pH 3) cycles by silk hydrogels (B).

#### 4.3.7. MB degradation by gold NPs

The use of Au NPs as catalyst has been largely studied in the literature<sup>57–59</sup>. Au NPs have been proved to catalyze the reduction of MB to leuco methylene blue (LMB, colorless) by sodium borohydride ( $\text{NaBH}_4$ )<sup>47,60</sup>. This reaction was chosen as model reaction as it can be easily followed by UV-Vis measurements due to blue color extinction. The combination of the MB adsorbent capacity with the catalytic activity of Au NPs can further be used in a continuous water treatment procedure. Not only Au NPs are able to degrade MB, but the direct contact of both elements is enhanced by the adsorption capacity of the SF material.

Figure III.22 B shows that after only 15 minutes all the MB had been reduced to LMB. Not only the reaction occurs in a fast manner but the hydrogel can be reused by adding more MB and  $\text{NaBH}_4$  at least up to 15 times resulting in the degradation of  $5.9 \mu\text{mol}$  of MB by each  $\mu\text{mol}$  of Au NPs. In addition, no MB degradation was observed when a silk hydrogel was used instead in presence of  $\text{NaBH}_4$ . These results are encouraging for MB adsorption and degradation. In spite of the great reduction of MB observed, the chosen reaction results in the production of hydrogen gas that is entrapped within the hydrogel (Figure III.22 A) resulting in partial break

down of the material. Nevertheless, the NPs were attached to the remaining silk fibers and no release into the solution was observed.

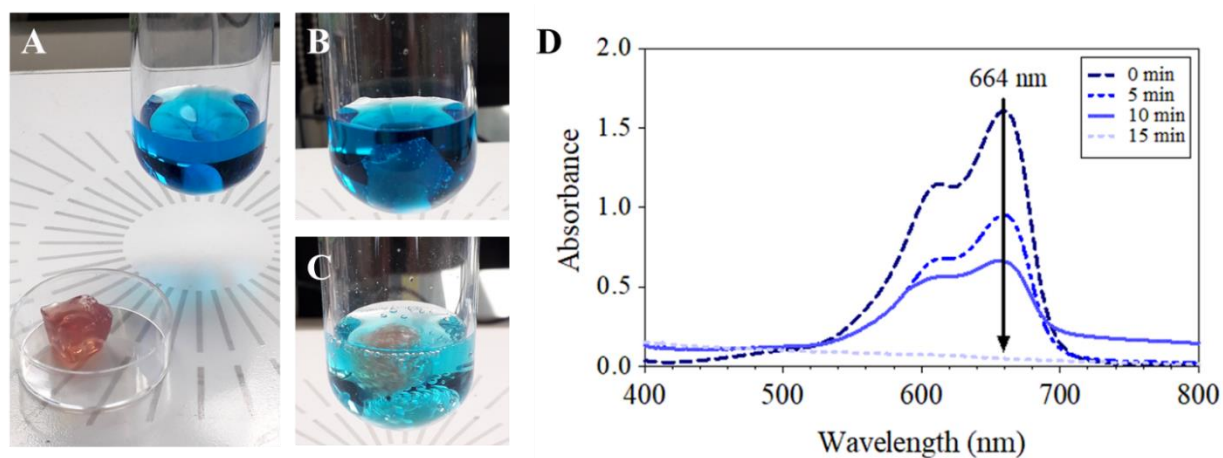


**Figure III.22.** Silk-Au NPs hydrogel bionanocomposite and MB solution (A), image taken at the start (B) and during (C) MB reduction reaction. The formation of H<sub>2</sub> results in gas bubbles entrapped within the silk-Au NPs hydrogel. MB reduction kinetics monitored by UV-vis spectrophotometry (D).

## 4.1. Conclusion

To our knowledge the use of silk materials as adsorbents has rarely been studied up to date. Herein the maximum adsorption capacity of silk hydrogels has been evaluated. The better fit of the experimental data with the Langmuir adsorption model indicates an adsorption in a monolayer manner. Moreover, the results found in this section strongly suggest an electrostatic mediated interaction between MB and silk materials. This interaction is in fact impaired in presence of salt, or within an acid media due to the positive charge of silk materials at this stage. In addition, the use of an anionic dye resulted in an opposite behavior confirming the electrostatic interaction hypothesis. This work also shows the possibility of using pH 3 solutions to restore and reuse silk materials. Finally, the addition of Au NPs allows the coupling of the dye removal capacities of silk with its *in situ* degradation by catalysis.

Herein this section provides a biodegradable material capable of removing and degrading MB from an aqueous solution within a simple procedure. It is important to note that the results presented here are just a proof of concept and that the material can be easily tuned and functionalized to optimize its performance. Future investigations could focus in the use of HRP enzyme (used for hydrogel crosslinking) for pollutant degradation as recently shown in the literature <sup>61</sup>.



## References

1. Frauchiger, D. A. *et al.* A review of the application of reinforced hydrogels and silk as biomaterials for intervertebral disc repair. *Eur. Cells Mater.* **34**, 271–290 (2017).
2. Yodmuang, S. *et al.* Silk microfiber-reinforced silk hydrogel composites for functional cartilage tissue repair. *Acta Biomater.* **11**, 27–36 (2015).
3. Vidal, S. E. L. *et al.* 3D biomaterial matrix to support long term, full thickness, immunocompetent human skin equivalents with nervous system components. *Biomaterials* **198**, 194–203 (2019).
4. Lovett, M. L. *et al.* Silk hydrogels for sustained ocular delivery of anti-vascular endothelial growth factor (anti-VEGF) therapeutics. *Eur. J. Pharm. Biopharm.* **95**, 271–278 (2015).
5. Li, Z. *et al.* Topical application of silk fibroin-based hydrogel in preventing hypertrophic scars. *Colloids Surfaces B Biointerfaces* **186**, 110735 (2020).
6. Kaczmarek, B., Nadolna, K. & Owczarek, A. The physical and chemical properties of hydrogels based on natural polymers. in *Hydrogels Based on Natural Polymers* 151–172 (Elsevier, 2020). doi:10.1016/B978-0-12-816421-1.00006-9.
7. Lara, H. H., Ayala-Núñez, N. V., del Turrent, L. C. I. & Padilla, C. R. Bactericidal effect of silver nanoparticles against multidrug-resistant bacteria. *World J. Microbiol. Biotechnol.* **26**, 615–621 (2010).
8. Lara, H. H., Ayala-Núñez, N. V., Ixtepan-Turrent, L. & Rodriguez-Padilla, C. Mode of antiviral action of silver nanoparticles against HIV-1. *J. Nanobiotechnology* **8**, 1–10 (2010).
9. Guo, J. *et al.* Silver nanoparticles exert concentration-dependent influences on biofilm development and architecture. *Cell Prolif.* **52**, 1–8 (2019).
10. Agnihotri, S., Mukherji, S. & Mukherji, S. Size-controlled silver nanoparticles synthesized over the range 5–100 nm using the same protocol and their antibacterial efficacy. *RSC Adv.* **4**, 3974–3983 (2014).
11. Kim, K. J. *et al.* Antifungal activity and mode of action of silver nano-particles on *Candida albicans*. *BioMetals* **22**, 235–242 (2009).
12. Chudasama, B., Vala, A. K., Andhariya, N., Upadhyay, R. V. & Mehta, R. V. Antifungal activity of multifunctional Fe<sub>3</sub>O<sub>4</sub>-Ag nanocolloids. *J. Magn. Magn. Mater.* **323**, 1233–1237 (2011).



13. Kulthong, K., Srisung, S., Boonpavanitchakul, K., Kangwansupamonkon, W. & Maniratanachote, R. Determination of silver nanoparticle release from antibacterial fabrics into artificial sweat. *Part. Fibre Toxicol.* **7**, 2–10 (2010).
14. Liu, J., Wang, Z., Liu, F. D., Kane, A. B. & Hurt, R. H. Chemical transformations of nanosilver in biological environments. *ACS Nano* **6**, 9887–9899 (2012).
15. Le Monnier, A., Abachin, E., Beretti, J. L., Berche, P. & Kayal, S. Diagnosis of *Listeria monocytogenes* meningoencephalitis by real-time PCR for the *hly* gene. *J. Clin. Microbiol.* **49**, 3917–3923 (2011).
16. Gelosia, A., Baldassarri, L., Deighton, M. & Van Nguyen, T. Phenotypic and genotypic markers of *Staphylococcus epidermidis* virulence. *Clin. Microbiol. Infect.* **7**, 193–199 (2001).
17. Raho, R. *et al.* Photo-assisted green synthesis of silver doped silk fibroin/carboxymethyl cellulose nanocomposite hydrogels for biomedical applications. *Mater. Sci. Eng. C* **107**, 110219 (2020).
18. Chen, M. X., Alexander, K. S. & Baki, G. Formulation and Evaluation of Antibacterial Creams and Gels Containing Metal Ions for Topical Application. *J. Pharm.* **2016**, 1–10 (2016).
19. Mou, J. *et al.* Hydrogel containing minocycline and zinc oxide-loaded serum albumin nanoparticle for periodontitis application: preparation, characterization and evaluation. *Drug Deliv.* **26**, 179–187 (2019).
20. Correia, T. R. *et al.* 3D Printed scaffolds with bactericidal activity aimed for bone tissue regeneration. *Int. J. Biol. Macromol.* **93**, 1432–1445 (2016).
21. Balouiri, M., Sadiki, M. & Ibensouda, S. K. Methods for in vitro evaluating antimicrobial activity: A review. *J. Pharm. Anal.* **6**, 71–79 (2016).
22. Modo, M. Bioscaffold-Induced Brain Tissue Regeneration. *Front. Neurosci.* **13**, 1–26 (2019).
23. Fernández-García, L. *et al.* Safety and tolerability of silk fibroin hydrogels implanted into the mouse brain. *Acta Biomater.* **45**, 262–275 (2016).
24. Madhusudanan, P., Raju, G. & Shankarappa, S. Hydrogel systems and their role in neural tissue engineering. *J. R. Soc. Interface* **17**, (2020).
25. Assi, H., Candolfi, M., Lowenstein, P. R. & Castro, M. G. Rodent glioma models: Intracranial stereotactic allografts and xenografts. *Neuromethods* **77**, 229–243 (2012).
26. Richard, S. *et al.* USPIO size control through microwave nonaqueous sol-gel method for neoangiogenesis T2 MRI contrast agent. *Nanomedicine* **11**, 2769–2779 (2016).

27. Helmut, K., Hanisch, U. K., Noda, M. & Verkhatsky, A. Physiology of microglia. *Physiol. Rev.* **91**, 461–553 (2011).
28. Silver, J. & Miller, J. H. Regeneration beyond the glial scar. *Nature Reviews Neuroscience* vol. 5 146–156 (2004).
29. Coskun, V. *et al.* CD133<sup>+</sup> neural stem cells in the ependyma of mammalian postnatal forebrain. *Proc. Natl. Acad. Sci. U. S. A.* **105**, 1026–1031 (2008).
30. Samanta, P., Desai, A. V., Let, S. & Ghosh, S. K. Advanced Porous Materials for Sensing, Capture and Detoxification of Organic Pollutants toward Water Remediation. *ACS Sustain. Chem. Eng.* **7**, 7456–7478 (2019).
31. Lellis, B., Fávaro-Polonio, C. Z., Pamphile, J. A. & Polonio, J. C. Effects of textile dyes on health and the environment and bioremediation potential of living organisms. *Biotechnol. Res. Innov.* **3**, 275–290 (2019).
32. Ghosh, D. & Bhattacharyya, K. G. Adsorption of methylene blue on kaolinite. *Appl. Clay Sci.* **20**, 295–300 (2002).
33. Pourjavadi, A., Nazari, M., Kabiri, B., Hosseini, S. H. & Bennett, C. Preparation of porous graphene oxide/hydrogel nanocomposites and their ability for efficient adsorption of methylene blue. *RSC Adv.* **6**, 10430–10437 (2016).
34. Wang, S. *et al.* Preparation and characterization of graphene oxide/silk fibroin hybrid aerogel for dye and heavy metal adsorption. *Compos. Part B Eng.* **163**, 716–722 (2019).
35. Ling, S. *et al.* Design and function of biomimetic multilayer water purification membranes. *Sci. Adv.* **3**, 1–12 (2017).
36. Xiao, S., Wang, Z., Ma, H., Yang, H. & Xu, W. Effective removal of dyes from aqueous solution using ultrafine silk fibroin powder. *Adv. Powder Technol.* **25**, 574–581 (2014).
37. Umar, M., Min, K., Jo, M. & Kim, S. Ultra-thin, conformal, and hydratable color-absorbers using silk protein hydrogel. *Opt. Mater. (Amst).* **80**, 241–246 (2018).
38. Godiya, C. B., Cheng, X., Deng, G., Li, D. & Lu, X. Silk fibroin/polyethylenimine functional hydrogel for metal ion adsorption and upcycling utilization. *J. Environ. Chem. Eng.* **7**, 102806 (2019).
39. Sato, T., Abe, S., Ito, S. & Abe, T. Silk fibroin fiber for selective palladium adsorption: Kinetic, isothermal and thermodynamic properties. *J. Environ. Chem. Eng.* **7**, 102958 (2019).
40. Gore, P. M., Naebe, M., Wang, X. & Kandasubramanian, B. Progress in silk materials for integrated water treatments: Fabrication, modification and applications. *Chem. Eng. J.* **374**, 437–470 (2019).

41. Ania, C. O., Menéndez, J. A., Parra, J. B. & Pis, J. J. Microwave-induced regeneration of activated carbons polluted with phenol. A comparison with conventional thermal regeneration. in *Carbon* vol. 42 1383–1387 (Elsevier Ltd, 2004).
42. Luo, J., Zhang, N., Lai, J., Liu, R. & Liu, X. Tannic acid functionalized graphene hydrogel for entrapping gold nanoparticles with high catalytic performance toward dye reduction. *J. Hazard. Mater.* **300**, 615–623 (2015).
43. Wang, T. *et al.* Functional clay supported bimetallic nZVI/Pd nanoparticles used for removal of methyl orange from aqueous solution. *J. Hazard. Mater.* **262**, 819–825 (2013).
44. Wang, M. *et al.* Synthesis of Pt<sub>3</sub>Ni Microspheres with High Performance for Rapid Degradation of Organic Dyes. *Nanoscale Res. Lett.* **10**, (2015).
45. Vanaja, M. *et al.* Degradation of methylene blue using biologically synthesized silver nanoparticles. *Bioinorg. Chem. Appl.* **2014**, (2014).
46. Barroso-Martín, I. *et al.* Au and AuCu nanoparticles supported on SBA-15 ordered mesoporous titania-silica as catalysts for methylene blue photodegradation. *Materials (Basel)*. **11**, 1–17 (2018).
47. Begum, R. *et al.* Chemical reduction of methylene blue in the presence of nanocatalysts: a critical review. *Rev. Chem. Eng.* **0**, 749–770 (2019).
48. Perju, M. M., Dinu, M. V. & Dragan, E. S. Sorption of Methylene Blue onto Ionic Composite Hydrogels Based on Polyacrylamide and Dextran Sulfate: Kinetics, Isotherms, and Thermodynamics. *Sep. Sci. Technol.* **47**, 1322–1333 (2012).
49. Filho, C. M. C. *et al.* Synthesis, characterization and sorption studies of aromatic compounds by hydrogels of chitosan blended with  $\beta$ -cyclodextrin- and PVA-functionalized pectin. *RSC Adv.* **8**, 14609–14622 (2018).
50. Liang, B. *et al.* An artificially engineered ‘tumor bio-magnet’ for collecting blood-circulating nanoparticles and magnetic hyperthermia. *Biomater. Sci.* **7**, 1815–1824 (2019).
51. Sinha, V. & Chakma, S. Advances in the preparation of hydrogel for wastewater treatment: A concise review. *J. Environ. Chem. Eng.* **7**, 103295 (2019).
52. Putro, J. N., Kurniawan, A., Ismadji, S. & Ju, Y. H. Nanocellulose based biosorbents for wastewater treatment: Study of isotherm, kinetic, thermodynamic and reusability. *Environ. Nanotechnology, Monit. Manag.* **8**, 134–149 (2017).
53. Kang, S. *et al.* Removal of methylene blue from water with montmorillonite nanosheets/chitosan hydrogels as adsorbent. *Appl. Surf. Sci.* **448**, 203–211 (2018).
54. Foo, C. W. P. *et al.* Role of pH and charge on silk protein assembly in insects and spiders. *Appl. Phys. A Mater. Sci. Process.* **82**, 223–233 (2006).

55. Aziz, S., Sabzi, M., Fattahi, A. & Arkan, E. Electrospun silk fibroin/PAN double-layer nanofibrous membranes containing polyaniline/TiO<sub>2</sub> nanoparticles for anionic dye removal. *J. Polym. Res.* **24**, 0–6 (2017).
56. Rocher, V., Siaugue, J. M., Cabuil, V. & Bee, A. Removal of organic dyes by magnetic alginate beads. *Water Res.* **42**, 1290–1298 (2008).
57. Xie, J., Yang, X. & Xu, X. Wet chemical method for synthesizing 3D graphene/gold nanocomposite: catalytic reduction of methylene blue. *Phys. E Low-Dimensional Syst. Nanostructures* **88**, 201–205 (2017).
58. León, E. R., Rodríguez, E. L., Beas, C. R., Plascencia-Villa, G. & Palomares, R. A. I. Study of Methylene Blue Degradation by Gold Nanoparticles Synthesized within Natural Zeolites. *J. Nanomater.* **2016**, (2016).
59. Zhang, Y., Cui, X., Shi, F. & Deng, Y. Nano-gold catalysis in fine chemical synthesis. *Chemical Reviews* vol. 112 2467–2505 (2012).
60. Islam, M. T. *et al.* Sodium rhodizonate induced formation of gold nanoparticles supported on cellulose fibers for catalytic reduction of 4-nitrophenol and organic dyes. *J. Environ. Chem. Eng.* **5**, 4185–4193 (2017).
61. Šekuljica, N. *et al.* Decolorization of anthraquinonic dyes from textile effluent using horseradish peroxidase: Optimization and kinetic study. *Sci. World J.* **2015**, (2015).



## General conclusion

---

This work has focused on the design and characterization of silk-Au NPs, silk-Ag NPs and silk-IONPs bionanocomposites. The throughout study of the literature presented in the first chapter allowed a better comprehension of *Bombyx mori* silk structure and properties. In addition of its biocompatible, biodegradable and enhanced mechanical properties, the versatility of silk fibroin allows the obtaining of different materials; making it very easy to adapt the material with the desired application. This property is further enhanced by the synthesis of silk-based bionanocomposites, which raise a new world acquired properties derived from the nanocompotent. A detailed analysis of the literature showed the possibility of incorporating a variety of NPs into silk materials in an efficient way.

Two distinct ways to include NPs into silk materials have been found in the literature: *in situ* synthesis of NPs and addition of NPs synthetized upstream. *In situ* synthesis procedures allow the functionalization of the material by a one-step reaction. However, this procedure results in unevenly shaped and sized NPs from which surface chemistry is not controlled. These drawbacks can be overcome by previously synthesizing NPs in a conventional and well-controlled procedure. Silk materials can be further functionalized by adding these NPs into either the SF dispersion or the final SF material. Nevertheless, a special attention needs to be paid to the NPs surface chemistry to avoid SF gelation when in contact with such NPs. Moreover, in the case of hydrogels, a controlled crosslinking procedure is needed to control the addition of NPs within the final material. Although many different silk bionanocomposites have been found in the literature for applications, including the biomedical and the catalysis field, a thorough characterization of these materials is still lacking and the development of a unified methodology that allows the preparation of several silk scaffolds embedded with different type of NPs is still to be proposed.

In this work, we used the incorporation of upstream prepared NPs into silk materials with the aim to control their properties and stability within the SF dispersion and the produced materials. An in-depth characterization of the SF / NPs dispersion was conducted, and a variety of applications of these bionanocomposites were described. For this purpose, Au NPs, Ag NPs and IONPs have been chosen as model NPs due to their interesting applications in the biomedical field and well-known properties. The synthesis of such NPs has been carried in an aqueous media and with a controlled biocompatible ligand onto their surface. The presence of

such molecule allowed the perfect dispersion of NPs into the extracted SF. In addition, this molecule could be easily functionalized with other molecules to add additional properties to the bionanocomposite. We first evaluated the electrospinning of the SF / NPs mixture and produced NPs functionalized silk electrospun mats. These materials have also been successfully obtained by *in situ* NPs synthesis or posterior functionalization. However, a higher concern on NPs leaching to the environment exists when using these methodologies.

Silk hydrogels were as well obtained from the prepared SF / NPs mixture by an enzymatic crosslinking providing a good control over the hydrogel formation. Moreover the presence of NPs did not affect the enzymatic activity and the hydrogel could be formed in the same way. An in-depth *in situ* and *ex situ* characterization of these materials was presented in chapter 2. Fluorescent spectrometry allowed the *in situ* monitoring of the crosslinking reaction, and thus the gelation process, with and without NPs due to the fluorescence of dityrosine bonds formed during crosslinking. The obtained material was then characterized *ex situ*. Morphological studies proved no significant modification of silk structure due to NPs presence during the crosslinking process. These results were completed by the structure analysis of the material by FTIR and the evaluation of the mechanical properties by compression tests. Although no significant changes were seen within the silk conformation nor within the compression modulus, the swelling behavior of the resultant hydrogels was impaired when NPs were incorporated. The *in vitro* biocompatibility characterization of silk-NPs hydrogel bionanocomposites proved no cytotoxicity response and a good cellular adhesion to the material, suggesting a possible integration within the implanted tissue.

Although characterized to a much lesser extent, we have also shown the possibility to create silk sponges and 3D printed bionanocomposites from the same SF / NPs mixture. These results suggest the possibility to adapt our methodology to each silk material and provide a transposable protocol to obtain silk bionanocomposites. The possibility to produce multiple silk-based bionanocomposite materials in an easy manner allow a great adaptability of the material to the required application. Moreover, the use of different NPs seems feasible bringing in new properties.

The last chapter of this work has focused on the characterization and demonstration of the acquired NPs related properties by the silk material. Silk-Ag NPs hydrogel bionanocomposites showed an antibacterial effect against *E.coli* and *S. epidermidis*. Interestingly the results presented here suggest an antibacterial action by direct contact rather than by Ag<sup>+</sup> ion release as often suggested in the literature.



Silk-IONPs hydrogel bionanocomposites have proven the acquisition of superparamagnetic properties derived from IONPs. Furthermore, the incorporation of such NPs into silk hydrogels results in a decreased blocking temperature suggesting reduced NPs to NPs interaction within the silk material in comparison with the one found in the NPs aqueous dispersion. These materials have been then used for *in vivo* brain implants allowing a good MRI monitoring, at least up to 3 months after injection, suggesting no NPs release within the surrounding tissues. The evaluation of several strategies for hydrogel implantation showed that *in situ* crosslinking was the most well adapted procedure in our rodent model. This procedure showed decreased invasiveness into the brain resulting in reduced brain damage related to surgery. Histological studies revealed an acute inflammatory response coupled with a foreign body response as depicted by the enhanced presence of microglia and lymphocytes T CD8 within the injection area. Nevertheless, a good tissue regeneration process was observed with extremely activated astrocytes and stem cells at all time periods. Moreover, we have proven that part of the proliferating stem cells differentiate into neurons and endothelial cells forming new capillaries surrounding the hydrogel. Overall, a good biocompatibility of the material was observed and silk hydrogel had been partially removed by brain tissues after 3 months.

The last section of chapter III proves the use of silk materials as dye adsorbents for depollution application. Methylene blue (MB) has been chosen as model dye. A pseudo-second-order kinetic model best explained adsorption kinetics. The adsorption mechanism was found to better correlate to the Langmuir adsorption models suggesting a monolayer adsorption of MB into the silk surface. The nature of the adsorption was elucidated to be driven mainly by electrostatic interactions. The addition of ions into the solution (addition of salt) resulted in a decrease of the adsorption capacity. In addition, the change of silk overall charge induced by the pH variation resulted in an enhanced adsorption at pHs found over silk's pI and a reduced adsorption capacity at pH under this value. In neutral pH and deionized water, the maximum adsorption capacities of silk hydrogels were found to be of 25 mg of MB g<sup>-1</sup> silk. Although active carbons largely overcome these capacities, herein we have shown the possibility to reconstitute and recycle the adsorbent material by using acidic pHs. Finally, the introduction of Au NPs into the hydrogel allows the coupling of the adsorbent properties with Au NPs catalytic properties. The resultant nanocomposite successfully reduces MB to its nontoxic form, LMB, in a reduced time period.

Altogether, this work has provided a transposable method to produce silk-based bionanocomposites that can be used in many fields due to the adaptability of the material to the

desired application. We have performed an in-depth characterization of the dispersion of several NP types in silk fibroin dispersion and elucidated the influence of NPs within the formation and final structure of silk hydrogels. Finally, an application is provided as a proof of concept for each type of NP showing the acquisition of NP-related properties by the silk material.

## Perspectives

---

This work provides strong guidelines for silk bionanocomposite design and fabrication. The possibility to obtain easily such bionanocomposites materials in a transposable manner opens up new horizons. The diversity of silk materials (films, microspheres, foams...) and the possible combinations with different NPs enhances the adaptability of the material to meet specific requirements. The results obtained in this work provide guidelines for the development of new bionanocomposites with tailored properties and functions.

The use of silk nanocomposites for other applications may require further characterizations. For example, elucidating whether the impact of NPs into the swelling behavior of silk hydrogels is due to the nature of the embedded NPs or depends on their size may be interesting for drug release or relative humidity sensing applications. Similarly, further experiments should be conducted on the impact of the surface structure of 3D printed silk nanocomposites over cell adhesion or stem cell differentiation for biomedical applications. Moreover, the presence of NPs within the material could be used to provide mechanical, magnetic or electrical field stimuli, which have been shown to greatly impact stem cell differentiation for instance..

Further characterizations can be also conducted to better understand and optimize the performance of these materials for other applications, including those described in this work. In the case of antibacterial materials, an in-depth characterization of ion release should be conducted in the future for safety reasons. Moreover, further characterizations on the antibacterial action of these materials against biofilm formation could allow a better understanding of the mechanism by which the bionanocomposite produces an antibacterial effect.

For brain injections, the preliminary results presented herein are promising for further applications such as cavity filler after tumor removal or long-term drug delivery in a desired area. Nevertheless, before going further, controls should be performed to elucidate the origin of the inflammatory response. Moreover, hydrogel formulation and mechanical properties should be modified to better match the physiological conditions found in healthy brain tissue. These parameters can be modified by using smaller SF protein fragments, smaller SF concentrations or different crosslinking agents. These approaches may reduce the possible inflammatory response produced by different mechanical stimuli within the brain tissues. Silk

hydrogels can be functionalized as well with bioactive molecules as drugs or growth factors to enhance tissue regeneration. An in-depth, characterization and optimization of the material's degradation rate, and molecule release is required to successfully match the tissue regeneration requirements, avoiding a burst release of the molecule and providing a long-term dosage. In addition, the use of different crosslinking enzymes that do not require the presence of hydrogen peroxide but a different, less toxic, oxidizer will probably reduce the inflammatory response observed within this work.

The use of different enzymes to crosslink silk and form hydrogels could also find several applications within the depollution field. In fact, several enzymes, such as carbonic anhydrase, horseradish peroxidase or laccase, have been found to play an important role on the depollution of herbicides, dyes or drugs that are usually recalcitrant and have a great impact on the environment and human health. The NPs nature can also influence the selectivity of the degraded molecule increasing the materials action. Moreover, the requirement of sodium borohydride for the reaction used here is limiting due to its toxicity and the produced hydrogen, which is entrapped within the hydrogel resulting in its degradation over time. Therefore, further studies should focus in the possibility to avoid or replace sodium borohydride by a non-toxic reagent and using a reaction whom by products do not induce hydrogel degradation. Importantly, optimization of the adsorption rates should be conducted to become a competitive material with the gold standard: activated carbon.

In conclusion the results presented in this work constitute a solid base for further material development that matches the application requirements. The different type of NPs together with the versatility of silk materials opens up a vast number of applications, some of which may be unimaginable today. The sky is the limit.

# Accomplishments

---

The results contained within this work have been presented, published or submitted to the following:

## Articles

1. Iben Ayad, A.; **Belda Marín, C.**; Colaco, E.; Lefevre, C.; Méthivier, C.; Ould Driss, A.; Landoulsi, J.; Guénin, E. “water Soluble” Palladium Nanoparticle Engineering for C-C Coupling, Reduction and Cyclization Catalysis. *Green Chem.* **2019**, *21* (24), 6646–6657.
2. **Belda Marín, C.**; Fitzpatrick, V.; Kaplan, D. L.; Landoulsi, J.; Guénin, E.; Egles, C. Silk Polymers and Nanoparticles: A Powerful Combination for the Design of Versatile Biomaterials. *Front. Chem.* **2020**, *8* (December), 1–22.

## Submitted

- **Belda Marín, C.**; Egles, C; Humblot, V; Lalatonne, Y; Motte, L; Landoulsi, J; Guénin, E. Gold, Silver and Iron oxide Nanoparticle incorporation in silk hydrogels for biomedical applications: Elaboration, structure and properties. (submitted to ACS Biomaterials Science & Engineering, 2020)

## Oral communications

1. **Cristina Belda Marín**, Xuan Mu, Sarah Vidal Yucha, David L. Kaplan, Christophe Egles, Jessem Landoulsi, Erwann Guénin. *Silk based bionanocomposite engineering for medical applications*. Sixth International Conference on Multifunctional, Hybrid and Nanomaterials, Sitges (Barcelona, Spain) 11-15 Mars 2019.

## Poster presentations:

1. POSTER: **C. Belda Marín**, A. Essouiba, K. Belanger, C. Egles, J. Landoulsi, E. Guénin. *Nanoparticle embedded silk materials as new bionanocomposite*. Intechem Process, Compiègne, 7 et 8 mars 2018 (Poster, présentation flash, **Best poster price**).
2. POSTER : **C. Belda Marín**, A. Essouiba, K. Belanger, C. Egles, J. Landoulsi, E. Guénin. *Nanoparticle embedded silk materials as new bionanocomposite*. Journée thématique du GDR Bio-ingénierie des interfaces : biomatériaux, Paris, 6 avril 2018 (Poster).



# Annexes

---





## 1. Nanoparticle image analysis: Image J script

A script for Image J was developed in order to easily analyze a big number of images in an automated manner by using the Particle analysis plugin included in Image J software. The script code is found in Figure A.1

```

particle_analysis_200nm difscaleLOOPED.ijm
1 setBatchMode(true);
2 function action(input, output, filename) {
3     open(input + filename);
4     run("8-bit");
5     run("Enhance Contrast", "saturated=4 normalize");
6     run("Bandpass Filter...", "filter=160 filter=3 suppress=[None] tolerance=5 autoscale saturate");
7     setAutoThreshold("Yen");
8     run("Threshold...");
9     call("ij.plugin.frame.ThresholdAdjuster.setMode", "8&W");
10    //setTool("rectangle");
11    makeRectangle(129, 1770, 486, 171);
12    run("Cut");
13    run("Select All");
14    run("Set Measurements...", "area perimeter fit shape feret's display redirect=None decimal=5");
15    run("Set Scale...", "distance=389 known=200 pixel=1 unit=nm global");
16    run("Analyze Particles...", "size=100-900 circularity=0-1.00 show=[Overlay Masks] display exclude clear include");
17    saveAs("PNG", output+filename);
18
19    saveAs("Results", output+filename+"results.csv" );
20    run("Clear Results");
21
22    close();
23    // Do the processing here by adding your own code.
24    // Leave the print statements until things work, then remove them.
25    print("Processing: " + input + File.separator + filename);
26    print("Saving to: " + output);
27 }
28 input = getDirectory("Input Directory");
29 output = getDirectory("Output Directory");
30 list = getFileList(input);
31 for (i = 0; i < list.length; i++)
32     action(input, output, list[i]);
33 setBatchMode(false);
34
35 print("task Completed")

```

**Figure A.1.** Image J script used for analyze NPs diameter from TEM images. First, the image is converted into 8-bit image and contrast is enhanced. A band pass filter is applied followed by the thresholding of the image. Scale bar is previously adjusted for each set of images tested and included into line 15 of the script. An overlay mask image is created and each NPs counted is numbered. For each image, a CVS file is created containing all the measurements.

Briefly, TEM images are converted to 8-bit images, the contrast is enhanced, a band pass filter and a threshold are applied. Scale bar is previously measured in one of the images and set into line 15 within the code. A rectangle is placed around the scale bar found within the image to remove possible artefacts due to the numbers.

This script allows the user to select an input file from which all contained images will be analyzed. An output file is as well required to save the results. For each image analyzed and overlay masked image is created in which the counted NPs are numbered. This image allows a visual control of the procedure by the user. All the measurements of each NPs are then stored into a CVS file for each image. Herein each NPs can be easily identified due to its numbering allowing the user to remove any artefacts if necessary. Resultant images are found in Figure A.2.

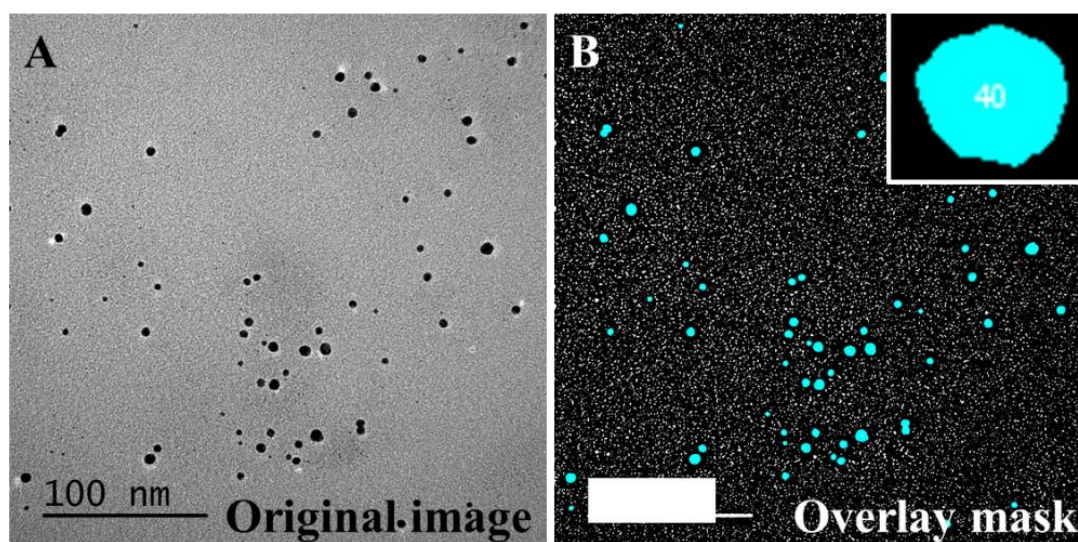


**Figure A.2.** Original TEM image of NPs (A) and the overlay mask created after image J analysis (B). Blue spots depict NPs analyzed each of them are numbered as show in the insert image (top right).

## 2. PDMS molds

Personalized PDMS molds with different sizes were prepared from 3D printed negative models (Figure A.3). Computer aided designs (CAD) were done using open source Onshape software. Molds were 3D printed in polylactic acid (PLA) material using a prusa MK3 (Prusa Research, Czech Republic) 3D printer with a 400  $\mu\text{m}$  resolution in the X and Y axis and a 20  $\mu\text{m}$  resolution in the Z axis. PDMS (Sylgard 184) components A and B were mixed in a 10:1 mass ratio. PDMS was poured into the 3D printed mold and placed under vacuum to remove air and avoid bubbles. PDMS was polymerized for at least 3 h at 50  $^{\circ}\text{C}$ . Higher temperature cannot be applied as the PLA glass transition temperature is 60  $^{\circ}\text{C}$ .

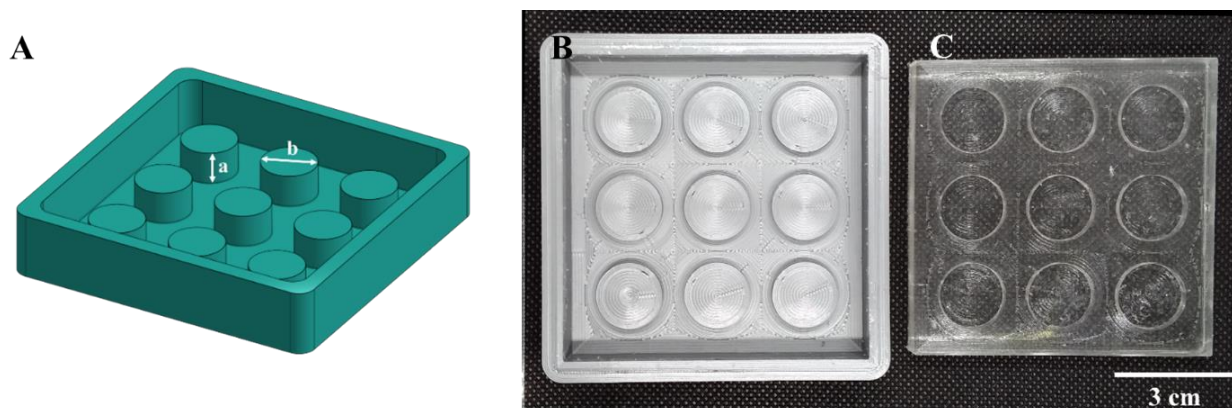


**Figure A.3.** CAD design (A) and PLA 3D printed (B) image of negative mold. PDMS mold (C) used for hydrogel preparation.

### 3. Compression tests: stress / strain curves

SF is an elastomeric material; therefore, the compression modulus is dependent on the strain as shown in Figure A.4. This behavior differs from other materials in which the stress is linearly correlated with the strain such as metals for example.

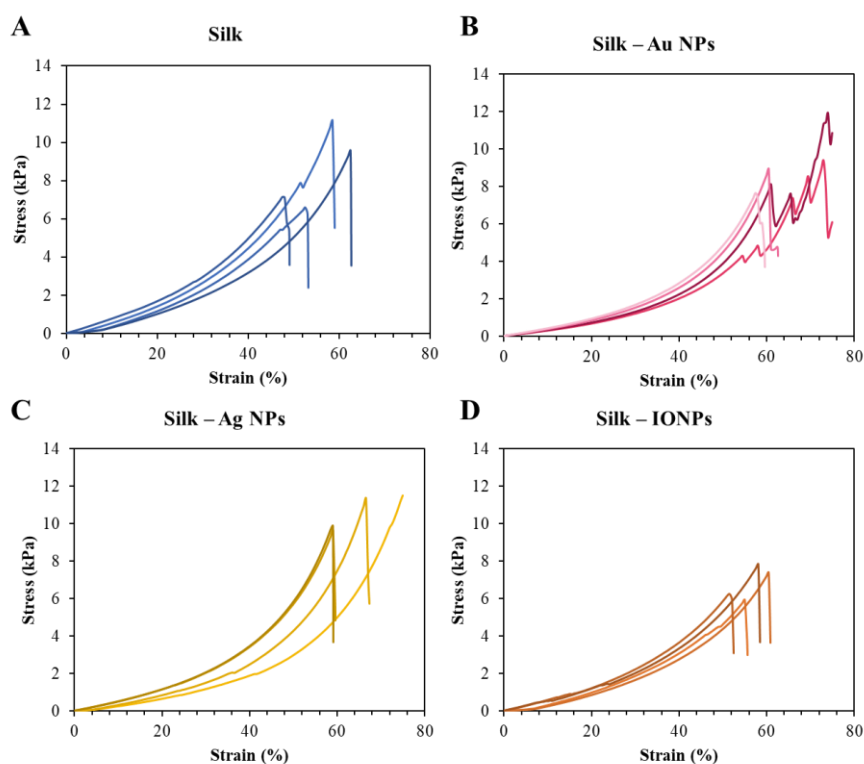


**Figure A.4.** Stress / Strain curves of silk (A), silk-Au NPs (B), silk-Ag NPs (C) and silk-IONPs (D) hydrogels. These curves show the elastomeric behavior of the tested materials as the compression modulus is dependent on the strain and no linear correlation is seen between stress and strain values. Four replicates are shown for each condition

## 4. Magnetic properties

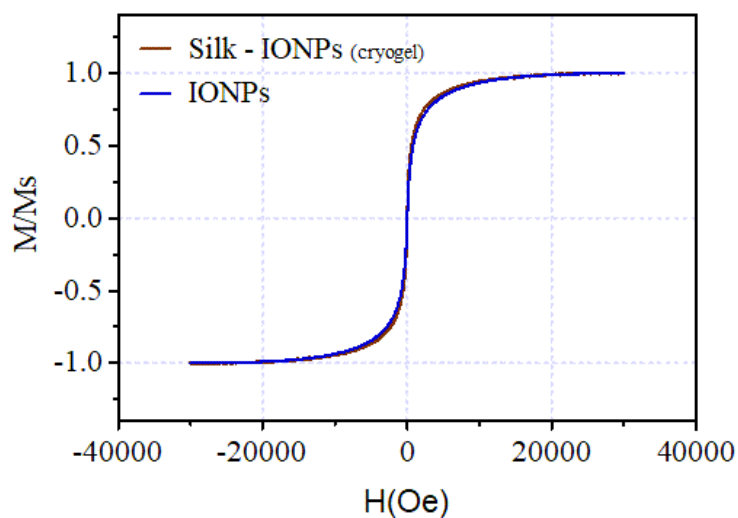


**Figure A.5.** Normalized magnetization as a function of the applied magnetic field for silk-IONPs cryogel bionanocomposites and IONPs aqueous dispersion

## 5. Immunostaining

### 5.1. Lymphocytes CD8

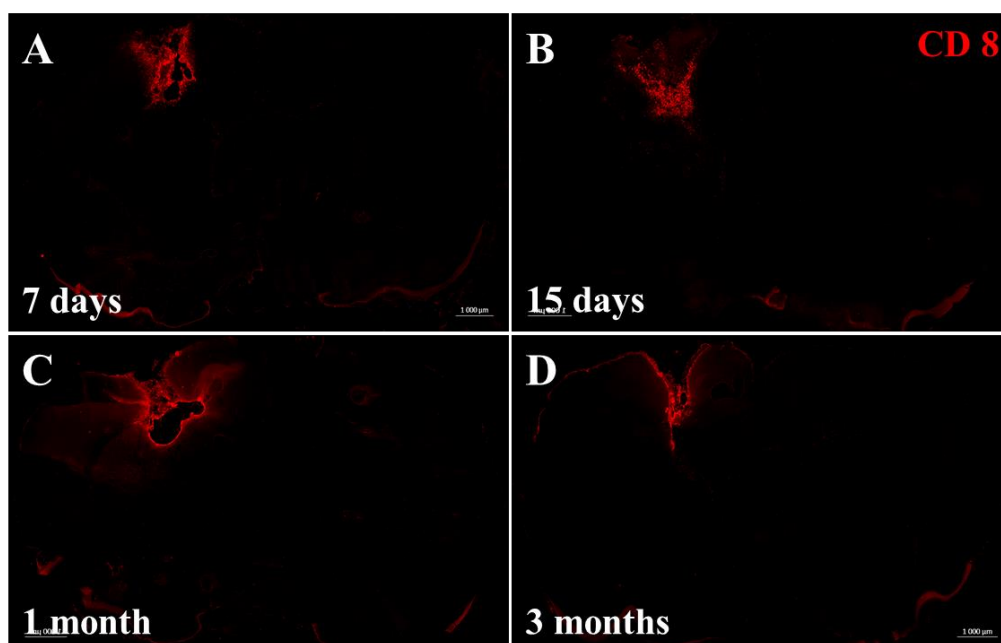


**Figure A.6.** Fluorescence microscopy images resulted from the immunostaining of lymphocytes T CD8<sup>+</sup> (red) 7, 15 days, 1 and 3 months after silk-IONPs hydrogel bionanocomposite injection. It is clearly seen from the images that lymphocytes T CD8<sup>+</sup> are present only within the injection area suggesting a local response up to 3 months.

## 5.2. Caspase

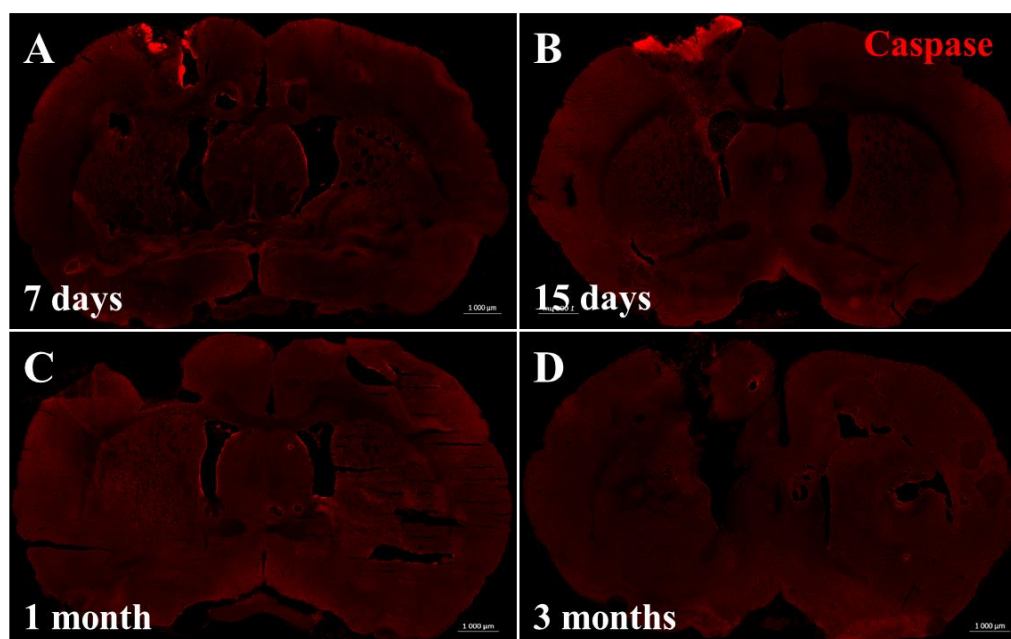


**Figure A.7.** Fluorescence microscopy images resulted from the immunostaining against caspase (red) depicting apoptosis procedures at 7, 15 days, 1 and 3 months after silk-IONPs hydrogel bionanocomposite injection. The higher intensity seen at 7 and 15 days within the top of the injection zone corresponds to the orange autofluorescence of the wax used to close the bone hole. A general apoptosis is found within the entire brain up to 3 months. Scale bar corresponds to 1000  $\mu\text{m}$ . © CEA-NeuroSpin Courtesy of S.Mériaux and F.Geffroy.





# Résumé

---

Les « bionanocomposites » à base de soie sont des matériaux qui suscitent un intérêt croissant dans de nombreuses applications, et en particulier dans le domaine biomédical, de par leur capacité à combiner les propriétés de la fibroïne (biodégradabilité, biocompatibilité et propriétés mécaniques intéressantes) et celles des nanoparticules (NP). L'objectif de ce travail est de (i) développer une méthode efficace, et « facile » à mettre en œuvre, permettant l'élaboration de plusieurs types de bionanocomposites de soie ; (ii) fournir une caractérisation approfondie pour une meilleure compréhension de l'interface soie/NP ; et (iii) présenter des applications pertinentes en relation avec les propriétés spécifiques de ces bionanocomposites.

Pour ce faire, les NP, d'or (Au NP), d'argent (Ag NP) et d'oxyde de fer (IONP) ont été utilisées en raison de leurs propriétés bien connues. L'élaboration de bionanocomposites à base de soie, tels que les tissus électrofilés, hydrogels, aérogels, éponges et structures imprimés en 3D est décrite. Une caractérisation approfondie, y compris des mesures *in situ* (pendant la formation du gel) et des analyses *ex situ* (une fois le gel formé), des hydrogels de soie montre qu'aucune différence significative n'est observée dans la structure de l'hydrogel, alors que la biocompatibilité des matériaux est préservée.

Enfin, une application potentielle pour chaque « bionanocomposite » est présentée. Dans une perspective biomédicale, les hydrogels soie-Ag NP montrent une activité antibactérienne significative. Les hydrogels soie-IONP, implantés dans le cerveau d'un rat et suivis par imagerie de résonance magnétique (IRM), montrent l'induction d'une procédure de régénération du cerveau pendant au moins 3 mois. Dans une perspective liée à la dépollution, les hydrogels soie-Au NP montrent des performances remarquables dans la catalyse de la réaction de réduction du bleu de méthylène par le borohydrure de sodium.

**Mots clé :** Fibroïne de soie, « bionanocomposite », nanoparticules, hydrogels, éponges, antibactérien, IRM, dépollution.



# Abstract

---

Silk-based bionanocomposites have attracted a growing interest in numerous applications, particularly in the biomedical field, owing to their ability to combine the specific properties of silk fibroin (biodegradability, biocompatibility and interesting mechanical properties) and nanoparticles (NPs). This work aims to (i) develop a straightforward, yet efficient, methodology to design various silk bionanocomposite materials; (ii) provide an in-depth characterization regarding the silk/NPs interface and (iii) provide potential applications which are relevant for the use of these bionanocomposites.

To this end, gold (Au NPs), silver (Ag NPs) and iron oxide (IONPs) NPs are used as model nanomaterials due to their well-known properties. The successful design of silk bionanocomposite electrospun mats, hydrogels, cryogels, sponges and 3D printed structures is described. An in-depth characterization, including *in situ* (during hydrogel formation) and *ex situ* (once hydrogel is formed), of silk hydrogel bionanocomposites do not reveal any noticeable structural changes of silk hydrogels, while their biocompatibility is not impacted by the incorporation of NPs.

Finally, a potential application for each bionanocomposite is presented. In a biomedical perspective, silk-Ag NPs hydrogels bionanocomposites show significant antibacterial activity. Silk-IONPs hydrogel bionanocomposites are implanted into rat's brain allowing a good monitoring of the implant by magnetic resonance imaging and inducing a brain regeneration process up to 3 months. In depollution perspective, silk-Au NPs hydrogel bionanocomposites show remarkable ability to adsorb and catalyze the reduction of methylene blue dye by sodium borohydride.

**Keywords:** silk fibroin, bionanocomposite, nanoparticles, hydrogels, sponges, antibacterial, MRI, depollution